Search for a bosonic decay of a charged Higgs at the LHC with the ATLAS detector

Waleed Syed Ahmed
Department of Physics
McGill University, Montreal

March 2023

CERN-THESIS-2023-068
//2023

A thesis submitted to McGill University in partial fulfilment of the requirements of the degree of Doctor of Philosophy

This page was intentionally left blank

Abstract

This thesis describes the search for a charged Higgs boson ($H^{\pm}$) decaying to a pseudoscalar particle (A) and a W boson in top-quark pair events. The analysis selects events with one electron and two muons in the final state and three or more jets, at least one of which is b-tagged. The signal model considers an H^{+} that is produced in top quark decays, while the A decays to muons. The mass range for the $H^{\pm}$ is between 100 GeV and 160 GeV, and that of the A is between 15 GeV and 75 GeV. This study uses 139 fb^{-1} of proton-proton collision data at $\sqrt{s} = 13$ TeV collected by the ATLAS detector during Run 2 of the LHC to search for an excess in the $\mu^{+}\mu^{-}$ invariant mass spectrum.

No significant excess above Standard Model predictions is observed in the signal region. The largest excess is found at a dimuon mass of 24 GeV and corresponds to a significance of 1.24σ. Upper limits are set at the 95% confidence level on the product of the branching ratios $t \to bH^{\pm}$, $H^{\pm} \to W^{\pm}A$ and $A \to \mu^{+}\mu^{-}$. The observed (expected) limits vary from $0.9\ (1.6) \times 10^{-6}$ to $6.9\ (9.9) \times 10^{-6}$, depending on the masses of the $H^{\pm}$ and A.

Résumé

Cette thèse décrit la recherche d'un boson de Higgs chargé se désintégrant en une particule pseudoscalaire A et un boson W dans des événements contenant $e\mu\mu$ dans les états finaux. La plage de masse cible de la particule A est comprise entre 15 GeV et 75 GeV. On suppose que H^+ est produit dans les désintégrations de quarks 'top' et que les A se désintègrent en muons. La plage de masse du H^+ est comprise entre 100 GeV et 160 GeV. Cette étude utilise 139 fb $^{-1}$ de données de collision proton-proton (pp) à $\sqrt{s} = 13$ TeV collectées par l'expérience ATLAS lors de la deuxième campagne du LHC.

Aucun excès significatif au-delà de la prédiction du Modèle Standard n'est observé dans la région de signal. Le plus grand excès se trouve à une masse de dimuons de 24 GeV et correspond à une significativité de 1,24 σ. Les limites supérieures à un niveau de confiance de 95% suivant la méthode CL_s sont déterminées pour BR ($t \to bH^{\pm}$, $H^{\pm} \to W^{\pm}A$, $A \to \mu^+\mu^-$). Les limites observées (prévues) varient de $0,9\ (1,6)\ \times 10^{-6}$ à $6,9\ (9,9)\ \times 10^{-6}$, selon les masses.

Acknowledgements

Exceptional challenges are taken on with the aid of exceptional individuals. I would not have been able to complete this dissertation without the assistance of some extraordinary people. While my words cannot do justice, I am grateful they were placed in my life exactly when I needed them and wish to thank them here:

My collaborators Lily Morvaj, Bill Murray and Adriana Milic to whom I am deeply indebted for their self-less support in the completion of this analysis. Lily for patiently teaching me how to do particle physics, often helping me at odd hours given our time differences. Bill for his deep knowledge and brilliant ability to resolve technical obstacles with simple solutions. Adriana for always offering technical help and sharing her analysis tools with me.

The leadership and reviewers of the ATLAS Higgs and Diboson Searches (HDBS) group for their oversight and guidance on this project over the years: Arnaud Ferrari, Katharine Leney, Christopher Hayes, Elliot Reynolds, Ben Nachman, Verena Martinez, Jana Schaarschmidt, Jianming Qian, Liron Barak, Andrew Haas.

Prof. Russell Steele for his unwavering commitment to student success, for his uncanny intuition, for believing in me and taking ownership to ensure I had the resources to complete my studies.

Faculty who have been excellent teachers and offered their time whenever requested: Robert Brandenberger, Tami Pareg-Barnea, Alex Maloney, Walter Reisner, Brigitte Vachon, Francois Corriveau, Keshav Dashgupta, Simon Caron-Huot.

The $ttX \rightarrow \tau\tau$ analysis team who gave me a chance to learn new physics by welcoming me to their fascinating project: Damiano, Jean, Nadav, Liron,Hernan, Tere.

Post-docs Heather, Jona and Tony for taking the time to answer any questions I had. Special thanks to Benoit for helping me with the qualification task.

My friends in the Department for helping me get through coursework and their companionship over the years: Kevin, Alessandro, Auriane, Andrea, Bryce, Tariq,

Matt Stubbs, Zach, Siggi, Vero, Hussein, Igor.

Student advocates Robyn McDougall, Nicole Whitmarsh and Carla Arbelaez from the LICM for guiding me through the University's administrative system.

The wonderful teachers at Continuing Education, Centre d'enseignement du français and Centre St-Louis whose flexibility allowed me to juggle both French & Physics.

All the kind souls in Geneva who made my stay at CERN comfortable: Sameed and Liana, Wasikul, Benoit. The warm community at the rue Vermont mosque; especially Hajj Yacine who gave generously of his time to teach me Arabic and fiqh. The volunteers at Croix-Rouge and Cartias-Geneve who welcomed me to their team. My neighbour Ayaz Ali who assisted me when I was injured and ill.

Amine El Kaouachi for offering me meaningful employment that served as a vital means of supporting myself. Abdoul Haqq and Hubert for patiently teaching me statistics and quantitative finance.

My dear friend Moshe Scheiner for helping me get through some tough days.

My mentors, teachers and guide: Sh.Faraz Rabbani, Sh. Ramzy Ajem, Sidi Arabi Benjami, Hajj Ismail Filali, Hafiz Munir Ahmad Khan; who taught me to have faith and stand firm during adversity.

The beautiful community and all the brothers at the Naqshbandi center who became family and nourished me both physically and spiritually; whose companionship helped me get through school. I am especially thankful to the elders: Sh. Omar Kone, Moulay Hassan, Sidi Ahmed Shawky who taught me recitation, Sidi Izzidine, Mohammadou.

I am eternally thankful to my family for being the pillars of support I needed during my doctoral studies. My mother for her incessant prayers and unconditional love, my father for encouraging me; for providing comfort and stability during the plague so I could focus on the physics. Moeed, Sunia and Farazia for always stepping up and offering support, for taking care of the house while I was away. All my extended family and cousins who cheered me on faithfully and believed in me; especially Ali khalu and my aunts Zuby, Rafia, Shabana & Farhana. Without all the love and prayers, I couldn't have gotten this far. Thank you.

Contribution to Original Knowledge

This thesis presents the first results [1] for the search of the $H^{\pm} \rightarrow W^{\pm}A$ process at the ATLAS experiment. Prior to this, there was only one study of this decay mode at the LHC and it was done by the CMS experiment using 36 fb^{-1} of data. This is the first search for this process using proton collision events collected by ATLAS during Run 2 of the LHC at $\sqrt{s} = 13$ TeV, corresponding to an integrated luminosity of 139 fb^{-1}. Using four times more data, the most stringent upper limits on the $H^{+} \rightarrow WA$ signal model are determined for the $e\mu\mu$ channel. The work also improves existing literature by providing two-dimensional exclusion limits for the signal model.

Contribution of Authors

The physics analysis presented in this thesis is part of the work, "Search for $H^{\pm} \to W^{\pm}A \to W^{\pm}\mu\mu$ in $pp \to t\bar{t}$ events using an $e\mu\mu$ signature with the ATLAS detector at $\sqrt{s} = 13$ TeV" [1]. This search is the combined effort of four analysts of the ATLAS collaboration. The author of the thesis, Waleed Ahmed, is the main analyst and contact editor for the project. He is responsible for the design and development of all elements of the analysis pipeline. This includes: signal Monte Carlo generation, signal selection and optimization studies, n-Tuple production, trigger studies, background estimation, designing the fit strategy, evaluation of systematics, authoring the technical support note and the conference note. The original work by the author is documented in chapters 5 to 10 of this thesis, while in chapters 1 to 4 he covers the background and context for this analysis. Contribution of the co-authors to this work are highlighted below:

• William John Murray: Contact editor. Contributed to sensitivity improvements (chapter 5), smoothing of systematic uncertainties (chapter 7), interpolated limit plots and tables (chapter 8), co-authoring publication and technical advising.

• Lily Morvaj: Provided mentorship and guidance on background modeling and fitting strategy (chapter 6), organized n-tuple generation, offered support for analysis tools.

• Adriana Milic: Responsible for framework development and support, dimuon trigger implementation, n-tuple generation, maintaining skimming code, writing scripts for data processing and signal interpolation.

ATLAS is an international experimental collaboration of over 3000 scientists. The work presented in this thesis relies on the extensive software and hardware infrastructure that has been developed by the experiment over the course of two decades. Members of the collaboration, the physics group Conveners in particular, have contributed actively by overseeing and reviewing this analysis project.


بسم الله الرحمن الرحيم

Contents

List of Figures

List of Tables

1

Introduction

This thesis documents the search for a neutral CP-odd scalar particle (A) produced in the decay of a charged Higgs boson (H^+) in $t\bar{t}$ events. The analysis targets the decay of A to a muon pair in events with $e^{\pm}\mu^+\mu^-$ and three or more jets, at least one of which is b-tagged. The di-muon mass spectrum between 15 GeV to 75 GeV, bounded by the masses of the Upsilon resonances and the Z boson, is used in the analysis. The corresponding mass range for the H^+ is between 100 GeV and 160 GeV.

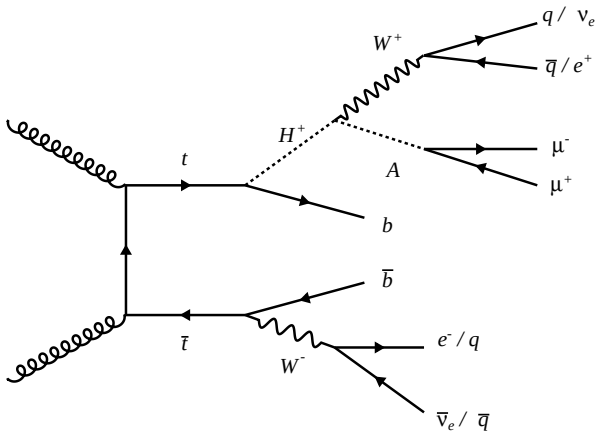

Figure 1.1 – Feynman diagram of the signal model: $H^+ \to WA$

The selection cuts are chosen by optimizing the signal-to-background ratio of various kinematic quantities in events with one electron and two opposite-sign muons in the final state. The backgrounds are then estimated in the kinematic region of interest by using Monte Carlo simulations normalized to data using profile likelihood fits. The primary background contributions arise from $t\bar{t}$, ttZ and Z+jets

productions. Experimental and theoretical uncertainties are assessed for the signal and background simulations.

The statistical analysis is performed in the framework of a two-Higgs-doublet model (2HDM) [2] where the pseudoscalar A is produced via $t \to H^+b \to W^+Ab$[1], as highlighted in Figure 1.1. The search is carried out by scanning across the di-muon mass spectrum and conducting counting experiments in single-bin windows with widths that maximize the sensitivity. The study uses 139 fb^{-1} of proton-proton (pp) collision data. This is the first time this search has been attempted in ATLAS at $\sqrt{s} = 13$ TeV.

The thesis is organized as follows. A review of the Standard Model of particle physics and the theory of proton-proton collisions is presented in Chapter 2. An overview of the experimental setup is provided in Chapter 3. Chapter 4 details the statistical techniques and analysis strategy used for this search. Chapter 5 outlines the procedures relevant for the signal event selection and optimization. Chapter 6 and Chapter 7 cover in detail the design of the analysis and the evaluation of systematic uncertainties. Finally, the results are presented in Chapter 8, followed by a discussion in Chapter 9.

1. Throughout this thesis charged Higgs bosons will be referred to as H^+, but the charge conjugate H^- mode is always implied.

2

Theory

2.1 The Standard Model

The Standard Model (SM) of particle physics is the most comprehensive theory which describes elementary particles and their interaction with the non-gravitational forces in Nature. In this formalism, point-like elementary particles are described as excitations of dynamical fields, while the forces are represented by gauge fields that mediate the interactions between the particles. More precisely, the SM is a spontaneously broken gauged quantum field theory based on the $SU(3) \times SU(2) \times U(1)$ symmetry group. The aim of this section is to elucidate the meaning of that statement. This will be done by reviewing the structure of the three dynamical theories which collectively make up the SM: Quantum Electrodynamics describing electromagnetism, Quantum Chromodynamics describing the strong force and the Glashow-Weinberg-Salam Theory describing the weak force. The material presented here is taken primarily from Ref. [3–11].

2.1.1 Particle Content

Elementary particles of the SM can be classified into two groups: half-integer spin particles called fermions and integer spin particles called bosons. Bosons have wavefunctions that are symmetric under interchange of any two particles, while fermions have antisymmetric wavefunctions. This leads to the Pauli exclusion principle for fermions that follow Fermi-Dirac statistics while bosons obey Bose-Einstein statistics. Fermions are further divided into two classes: leptons

and quarks. Leptons, quarks and mediating bosons are the building blocks of all understood forms of matter. A summary of the elementary particles and their properties can be found in Figure 2.1; a brief description is below.

Leptons are spin-$1/2$ particles that interact via the electromagnetic and weak force and do not participate in strong interactions. There are six leptons: the electron (e) and electron neutrino (ν_e), muon (μ) and muon neutrino (ν_μ), tau (τ) and tau neutrino (ν_τ). Anti-leptons corresponding to each of these particles brings the total number to twelve. The electrically charged leptons carry a charge of $-1e$ and their corresponding neutrinos have zero charge (and thus do not interact electromagnetically). Leptons also carry 'weak' charge which allows them to take part in weak interactions. The lightest lepton is the electron, followed by the muon and tau. Neutrinos are considered to be massless in the SM. The leptons are paired into three $generations$ with identical quantum numbers:

$$\begin{pmatrix} e \\ \nu_e \end{pmatrix} \begin{pmatrix} \mu \\ \nu_\mu \end{pmatrix} \begin{pmatrix} \tau \\ \nu_\tau \end{pmatrix} \tag{2.1}$$

Quarks are spin-half particles like the leptons but carry fractional charges. They partake in the strong interactions as well, in addition to electroweak interactions. The quarks are categorized into six $flavours$ which are classified as up (u), down (d), charm (c), strange (s), truth (t) and beauty (b). In addition to electric and 'weak' charge, the quarks carry a "colour" charge (referred to as red, blue and green). This additional property allows them to couple to the strong force. For example, a red quark carries one unit of redness and its anti-particle carries minus one unit of redness. After accounting for the anti-quarks and colour combinations, the total number of quarks comes to 36. Like leptons, they too are organized into three generations of increasing mass with each up-type quark (Q_e = + 2/3) paired with the down-type quark (Q_e = - 1/3):

$$\begin{pmatrix} u \\ d \end{pmatrix} \begin{pmatrix} c \\ s \end{pmatrix} \begin{pmatrix} t \\ b \end{pmatrix} \tag{2.2}$$

Hadrons are composite particles which are bound states of quarks; they are

colour neutral and take part in the strong interactions. Colour neutrality means that either the total amount of colour is zero or all the colours are present in equal amounts. For example, the proton is a hadron made of two up-quarks and a down-quark. There are two main types of hadrons: mesons and baryons. Mesons are made of two quarks (a quark and anti-quark) and carry integer spin, while baryons are made of either three quarks or three anti-quarks and carry half-integer spin. Due to the various possible combinations of quarks that can come together to form a bound state, the spectrum of hadrons is quite rich and a wide variety are created in particle accelerators such as pions (π), kaons (K) and B-mesons.

Gauge Bosons are spin-1 particles that are the force carriers of the SM. They number 12 in total and are responsible for mediating the interactions between the fermions of the theory. They are summarized below:

• The photon is a massless boson that mediates interactions between particles carrying the electromagnetic charge. It is electrically neutral and the force carrier in electromagnetism.

• The gluon is an electrically neutral, massless boson that is exchanged when particles interact via the strong force. They carry colour (like quarks), number 8 in total and do not exist as isolated particles. Evidence for gluons comes from deep inelastic scattering experiments which showed that roughly half the momentum of the proton was in its electrically neutral components. Their discovery was confirmed in 1980 by studies of three-jet events in e^+e^- collisions [12].

• $W^\pm$ and Z^0 bosons: The W and Z bosons mediate the weak interactions and are responsible for processes like nuclear beta decays (where a neutron transforms into a proton) and nuclear fusion which powers the Sun . Unlike gluons and photons, they are quite massive (80 and 91 GeV) and this explains the extremely short range of the weak force. Their discovery in 1983 was a triumph for the SM as their masses were found to be in excellent agreement with theoretical predictions.

Higgs boson This is the most recently discovered particle of the SM. It is the only scalar elementary particle (spin-0) and provides the mechanism by which the W and Z bosons acquire their masses. It is also responsible for the masses of the quarks and leptons as they have Yukawa couplings to the particle. As Higgs

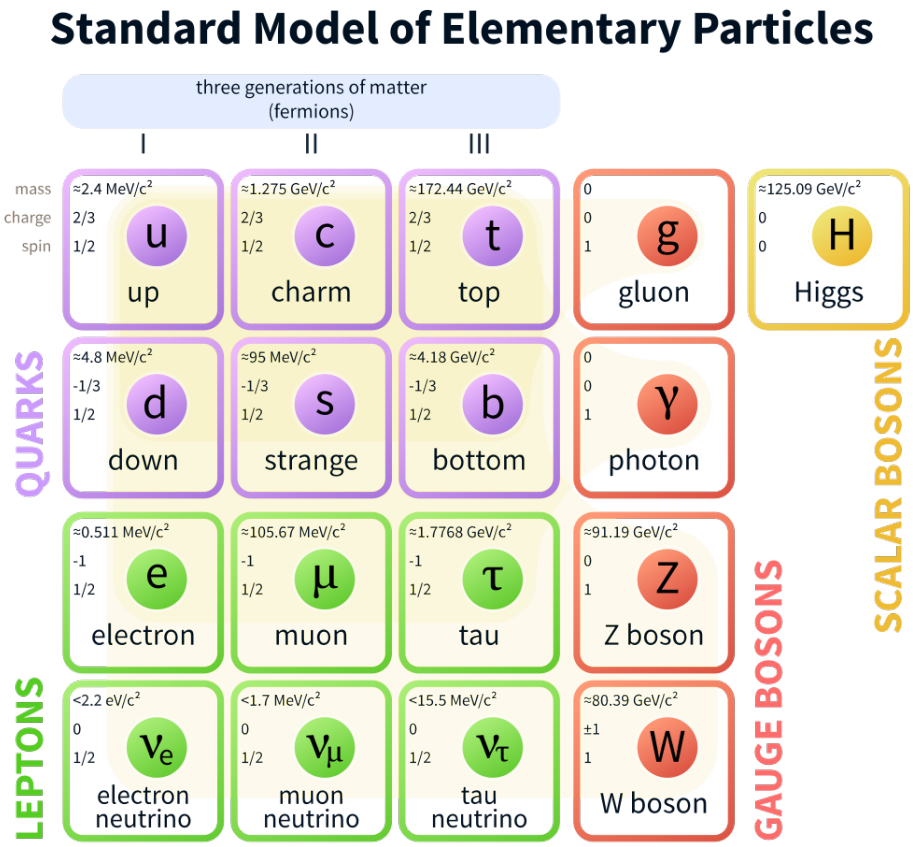

Figure 2.1 – A table summarizing the fundamental particles of the Standard Model [13].

couplings are proportional to mass, decay of Higgs to heavy particles is favoured over light ones.

A description of theories governing the forces associated with the gauge bosons is summarized below. The gravitational force does not have a quantum description and is explained by General Relativity instead.

2.1.2 Local Gauge Symmetry and Quantum Electrodynamics

Quantum Electrodynamics (QED) is the quantum field theory describing the interaction of particles that carry electrical charge. It respects local gauge transformations of the $U(1)$ symmetry group. In general, a symmetry is an operation that can be performed on a system that leaves it invariant. For example, a circle has rotational symmetry as it looks the same after it is rotated. For a square, the rotational symmetry is only partial as only rotations by 90° leave it invariant.

In the context of field theory, to be symmetrical under the group $U(N)$ means that the Lagrangian of the theory is unchanged under field transformations of the form

$$\psi \rightarrow U\psi, \tag{2.3}$$

where U is a set of $N \times N$ unitary matrices acting on the fields ψ which form an N-plet. A unitary matrix is one whose inverse is equal to its conjugate transpose i.e. $U^{-1} = U^{\dagger}$. QED is the simplest of gauge theories and its fields are invariant under a group of 1×1 matrices i.e. a number which is just the phase $e^{i\theta}$ with $0 \leq \theta < 2\pi$. $U(1)$ simply refers to the unitary matrices generated by phase transformations [14].

For a symmetry to be local means that it is parametrized by a function of space-time such as $\theta(x)$, while if the symmetry is only for a constant θ and independent of space-time, then it is called a global symmetry. According to the gauge principle [15], conserved quantities are required to be conserved both locally and globally. Global charge conservation would be satisfied if suddenly 20C of charge disappeared from Earth and appeared simultaneously on the Moon. However, this does not happen and notions of continuity require that the disappearance of charge be accompanied by a current which allows for its appearance at another point [8].

A continuous global symmetry can thus be promoted to a local symmetry. As will be seen, the cost of insisting that global invariance of the theory should hold locally is the introduction of a dynamical vector field A_{μ} called a $gauge$ field which couples to the matter fields. The requirement of local gauge invariance thus results in a force arising which is mediated by gauge fields. The number of gauge fields introduced in the theory corresponds to the generators of the sym-

metry group.

The power of the gauge principle can be seen [14] when it is applied to the free Dirac lagrangian for a fermion field ψ given by

$$\begin{aligned}\mathcal{L} &= \psi^\dagger \gamma^0 (i\gamma^\mu \partial_\mu - m)\psi, \\ &= \bar{\psi}(i\partial\!\!\!/ - m)\psi.\end{aligned} \tag{2.4}$$

This equation is invariant under the global phase transformation $\psi \to e^{iq\lambda}\psi$, where the parameter q indicates the relative magnitude of the change of phase caused by the gauge transformation. Requiring that this symmetry hold locally i.e. be space-time dependent, means that field should transform as

$$\psi \to e^{iq\lambda(x)}\psi. \tag{2.5}$$

Applying this transformation to 2.4 shows that the equation is not invariant and an additional term is introduced to the Lagrangian

$$\begin{aligned}\mathcal{L} &= \bar{\psi}e^{-iq\lambda}(i\gamma^\mu\partial_\mu - m)\psi e^{iq\lambda}, \\ &= \bar{\psi}e^{-iq\lambda}(i\gamma^\mu\partial_\mu(e^{iq\lambda}\psi) - m(e^{iq\lambda}\psi)), \\ &= \bar{\psi}e^{-iq\lambda}(i\gamma^\mu(iq(\partial_\mu\lambda)e^{iq\lambda}\psi + e^{iq\lambda}\partial_\mu\psi) - m(e^{iq\lambda}\psi)), \\ &= \bar{\psi}i\gamma^\mu\partial_\mu\psi - m\bar{\psi}\psi - q\bar{\psi}\gamma^\mu(\partial_\mu\lambda)\psi,\end{aligned} \tag{2.6}$$

$$\mathcal{L} \to \mathcal{L} - q(\bar{\psi}\gamma^\mu\psi)\partial_\mu\lambda. \tag{2.7}$$

This additional term appears as $\partial_\mu\psi$ does not have the same transformation rule as the field ψ itself i.e. the derivative does not transform $covariantly$. In order to make the $\mathcal{L}$ invariant under local phase transformations, something extra has to be added to soak up this term. This can be done by constructing a modified derivative D_μ which transforms just like field i.e. $D_\mu\psi \to UD_\mu\psi$. D_μ is called a

covariant derivative and is defined as

$$D_\mu \equiv \partial_\mu + iqA_\mu. \tag{2.8}$$

The new quantity A_μ is a vector field which transforms according to the rule

$$A_\mu \to A_\mu + \partial_\mu \lambda, \tag{2.9}$$

in order to compensate for the extra term in 2.7 involving $\partial_\mu \lambda$. By replacing every derivative ∂_μ in 2.4 by D_μ the invariance of $\mathcal{L}$ can be restored. This yields the modified $\mathcal{L}$ given by

$$\begin{aligned} \mathcal{L} &= \bar{\psi}(i\not{D} - m)\psi, \\ &= i\bar{\psi}\not{\partial}\psi - m\bar{\psi}\psi - q(\bar{\psi}\gamma^\mu\psi)A_\mu. \end{aligned} \tag{2.10}$$

This locally gauge invariant Lagrangian is no longer free and describes the interaction of fermions with the gauge field A_μ. The transformation rule for A_μ is the same as the one for the vector potential from Maxwell's electromagnetism and one identifies A_μ as the photon field. The full Lagrangian must also contain a free term for A_μ which can be obtained from the Maxwell Lagrangian. Adding this to the equation gives the complete Lagrangian for QED:

$$\begin{aligned} \mathcal{L} &= \mathcal{L}_\mathcal{A} + \mathcal{L}_\psi, \\ &= -\frac{1}{4}F_{\mu\nu}F^{\mu\nu} + i\bar{\psi}\not{\partial}\psi - m\bar{\psi}\psi - (q\bar{\psi}\gamma^\mu\psi)A_\mu, \\ \mathcal{L}_{\mathcal{QED}} &= -\frac{1}{4}F_{\mu\nu}F^{\mu\nu} + \bar{\psi}(i\not{D} - m)\psi, \end{aligned} \tag{2.11}$$

where $F_{\mu\nu} = \partial_\mu A_\nu - \partial_\nu A_\mu$ and denotes the electromagnetic field strength tensor. Important to note in this equation is that in order to preserve gauge invariance, the A_μ field has to be massless. The mass term would take the form $m^2 A^\mu A_\mu$ which is not invariant under 2.9 i.e. $A^\mu A_\mu \neq (A_\mu + \partial_\mu\lambda)(A_\mu + \partial_\mu\lambda)$.

In summary, the requirement of local gauge invariance to the free Dirac lagrangian results in an interacting theory between a vector field (photon) and fermion fields (electrons, positrons, quarks) which is identified as the theory of electrodynamics. The interactions between the fermions due to the exchange of a photon gives rise to the electromagnetic force. The parameter q is the coefficient of the coupling to the photon and represents the charge that determines the strength of the interaction between the fermion and gauge field. Thus, the particles in electromagnetism described by the various fields carry electric charges $\pm q$.

2.1.3 The Strong Force and Quantum Chromodynamics

Quantum Chromodynamics (QCD) is the theory of nuclei and their constituents; it describes the interaction of particles that carry colour charge. It is the $SU(3)$ component of the SM and accounts for the strong nuclear force. QCD contains several types or $flavours$ of Dirac fermions (quarks) and each flavour comes in three colours - red, blue and green. A quark, an up quark for example, is thus really a collection of three quark field components of equal mass. Following from 2.4, the free Lagrangian for one quark flavour can be written as [4]:

$$\mathcal{L} = \bar{\psi}_r(i\partial\!\!\!/ - m)\psi_r + \bar{\psi}_g(i\partial\!\!\!/ - m)\psi_g + \bar{\psi}_b(i\partial\!\!\!/ - m)\psi_b. \tag{2.12}$$

To simplify the equation, the Dirac fields can be grouped into a column vector

$$\Psi = \begin{pmatrix} \psi_r \\ \psi_g \\ \psi_b \end{pmatrix}, \tag{2.13}$$

which results in a more compact Lagrangian given by

$$\mathcal{L} = \bar{\Psi}(i\partial\!\!\!/ - m)\Psi. \tag{2.14}$$

This equation is identical to the original Dirac Lagrangian, however Ψ now is a column vector with three components and each element of this vector is a four-component Dirac spinor. While the single particle Dirac Lagrangian had $U(1)$ gauge symmetry, this theory exhibits $U(3)$ symmetry i.e. transformations of the form $\Psi \rightarrow U\Psi$ leave it invariant. However, U is now a 3×3 unitary matrix. Exploiting this larger symmetry group using a similar strategy used for QED can yield the full interacting theory of quarks. However, the group elements are generated in a more complicated way and require some explanation.

Consider unitary matrices in more detail. Similar to the way any complex number with modulus 1 can be written in the form $e^{i\theta}$ with real θ, any unitary matrix can be written in the form

$$U = e^{iH}, \tag{2.15}$$

where H is hermitian i.e. it is equal to its own conjugate transpose ($H^\dagger = H$). Furthermore, $U(N)$ can be expressed in terms of the subgroups $SU(N)$ and $U(1)$. SU stands for $special\ unitary$ and refers to unitary matrices with determinant 1, while $U(1)$ is the group of phase rotations. For example, for $N = 3$, any element of $U(3)$ can be expressed as an element of $SU(3)$ times an appropriate phase-factor

$$\begin{aligned} U(3) &= e^{i\theta} e^{i\alpha^a T^a}, \\ &= U(1) \otimes SU(3), \end{aligned} \tag{2.16}$$

where α^a are real numbers parametrizing the group elements and T^a are hermitian matrices called the group $generators$, which are 3×3 matrices in this case. As the matrix $e^{i\alpha^a T^a}$ has determinant 1, it belongs to $SU(3)$. The number of generators for an $SU(N)$ group is given by $N^2 - 1$. Thus, there are 8 generators for $SU(3)$. A gauge theory is called $Abelian$ if the group generators commute, while it is $non\text{-}Abelian$ or a $Yang-Mills$ theory if they do not commute. Thus, QED is considered an Abelian gauge theory while QCD is non-Abelian.

Having already explored $U(1)$ phase transformations, the invariance under

$SU(3)$ symmetry is what is new in 2.16 and relevant for QCD. In order to make the global $SU(3)$ invariance of the free Lagrangian in 2.14 to be local i.e. $\alpha^a \rightarrow \alpha^a(x)$, the field transformations take the form

$$\Psi \rightarrow S\Psi, \text{where } S \equiv e^{ig_s\alpha^a(x)\lambda^a}, \tag{2.17}$$

where g_s is the coupling constant in analogy with charge q from QED and λ^a are the $SU(3)$ group generators referred to as the Gell-Mann matrices. Inserting this in the free $\mathcal{L}$ would show that the theory is not invariant under this local gauge transformation. Similar to the previous derivation, the remedy to this is the introduction of a modified derivative which transforms like the fields i.e. $D_\mu\psi \rightarrow SD_\mu\psi$. The covariant derivative is now given by

$$D_\mu \equiv \partial_\mu - ig_sG^a_\mu\lambda^a, \tag{2.18}$$

where G^a_μ are the gauge fields of the theory, referred to as gluons. There are eight of them, corresponding to the number of generators of $SU(3)$ and therefore $a = 1..8$. In order to ensure the Lagrangian remains unchanged after introduction of this covariant derivative, a transformation rule for G^a_μ is needed (in analogy with 2.9). However, it is not trivial to deduce this as the matrices involved do not commute. Considering an infinitesimal transformation, it can be shown that G^a_μ has to obey

$$G^a_\mu \rightarrow G^a_\mu + \frac{1}{g_s}\partial_\mu\alpha^a(x) - f^{abc}\alpha^b(x)G^c_\mu, \tag{2.19}$$

in order to leave the Lagrangian invariant. f^{abc} are referred to as the structure constants of the $SU(3)$. Plugging the $covariant\ derivative$ into the free $\mathcal{L}$ yields

$$\begin{aligned}\mathcal{L} &= \bar{\Psi}(i\not{D} - m)\Psi, \\ &= i\bar{\Psi}\gamma^\mu\partial_\mu\Psi - m\bar{\Psi}\Psi + g_sG^a_\mu(\bar{\Psi}\gamma^\mu\lambda_a\Psi).\end{aligned} \tag{2.20}$$

The last term of this gauge invariant Lagrangian indicates the theory is no longer free and an interaction term between gauge fields and fermions has now arisen. The cost of requiring local $SU(3)$ symmetry is the introduction of 8 gluon fields. To complete the exercise, a kinetic term for the gluons needs to be added which would take the form of $G^a_{\mu\nu}G^{a\mu\nu}$ similar to QED. The field strength tensor for QCD is given by

$$G^a_{\mu\nu} = \partial_\mu G^a_\nu - \partial_\nu G^a_\mu + g_s f^{abc} G^b_\mu G^c_\nu. \tag{2.21}$$

This gives the final QCD Lagrangian for a single quark flavour

$$\begin{aligned} \mathcal{L}_{\mathcal{QCD}} &= -\frac{1}{4} G^a_{\mu\nu} G^{a\mu\nu} + \bar{\Psi}(i\not{D} - m)\Psi, \\ &= -\frac{1}{4}(G^a_{\mu\nu})^2 + \bar{\psi}_i(i\delta_{ij}\gamma^\mu\partial_\mu + g_s\gamma^\mu G^a_\mu \lambda^a_{ij} - m\delta_{ij})\psi_j, \end{aligned} \tag{2.22}$$

where the last line is expanded in component form and i is colour index with i = $1, 2, 3$. This $\mathcal{L}$ describes the phenomenon of strong interactions observed in Nature. The requirement of invariance under $SU(3)$ has given rise to the gluons which interact with three equal-mass fermions (i.e. colours of a given quark flavour) and mediate the strong force. This symmetry results in the conservation of colour charge which is preserved in all QCD interactions. Unlike the mediator of QED, the gluons themselves carry colour charge as well. This is a result of the gluon field strength tensor in 2.21 having the term $g_s f^{abc} G^b_\mu G^c_\nu$ which indicates that the gluons couple to themselves and thus carry colour-charge. In the fundamental interaction vertex $q \to q + g$, the flavour of incoming and outgoing quark are the same but the colour may change. Thus, gluons have to carry the difference and are 'bi-coloured', carrying one unit of positive and negative colour.

2.1.4 The Weak Force and Glashow-Weinberg-Salam Theory

A complete theory of weak interactions has to account for the following:

• Flavour change of quarks and leptons. The weak force is responsible for phenomena such as nuclear β decay i.e. $n \to p + e + \bar{\nu}$. At a fundamental level, this process involves flavour change described by $d \to u + e^{-} + \bar{\nu}$.

• Violation of parity and charge conjugation symmetry. The weak force is not invariant under the spatial inversion $x \to -x$. While the electromagnetic and strong forces treat left and right handed particles identically, this is not the case for weak interactions.

• Heavy mediators. The particles mediating the weak force must be very heavy (unlike massless photons or gluons) as the force is extremely short range.

The theory proposed by Sheldon Glashow, Steven Weinberg and Mohammad Abdus Salam (GWS) [16–18] was able to successfully account for the above and made a number of precise and successful predictions. Moreover, their model remarkably was able to unify the weak and electromagnetic interactions into a larger gauge theory. It is their work which eventually came to be called the $Standard\ Model$ [7, 19]. The derivation presented in this section has been adapted from Ref. [6,8,9,20].

Part 1: SU(2)$_L \otimes$ U(1)$_Y$ Theory

To build the gauge theory for weak interactions, one starts with the fermions which are represented by Dirac spinors. As seen previously, for a single lepton the free Lagrangian is given by

$$\begin{aligned} \mathcal{L} &= \bar{\psi}(i\partial\!\!\!/ - m)\psi, \\ &= i\bar{\psi}\gamma^{\mu}\partial_{\mu}\psi - m\bar{\psi}\psi. \end{aligned} \tag{2.23}$$

As the weak force violates parity and the charged currents (W bosons) couple only to left-handed fermions (i.e. their spin and momentum are opposed), it is

instructive to separate the fermions into left and right handed chiral states. This can be accomplished by using the projection operators P_L and P_R which act on an unpolarized Dirac spinor and separate left and right states

$$P_R = \frac{1}{2}(1+\gamma^5) \quad P_L = \frac{1}{2}(1-\gamma^5), \tag{2.24}$$

$$\begin{aligned} \psi_R = P_R\psi = \frac{1}{2}(1+\gamma^5)\psi, \\ \psi_L = P_L\psi = \frac{1}{2}(1-\gamma^5)\psi. \end{aligned} \tag{2.25}$$

Re-writing the $\mathcal{L}$ in terms of the different chiral states gives

$$\mathcal{L} = i(\bar{\psi}_L \partial\!\!\!/ \psi_L + \bar{\psi}_R \partial\!\!\!/ \psi_R) - m(\bar{\psi}_R\psi_L + \bar{\psi}_L\psi_R). \tag{2.26}$$

This equation suffers from a problem. The mass term involves fermions of both chiralities, coupling the left to right. Because the ψ_L and ψ_R fields in the SM carry different gauge charges, such a term is not gauge invariant and cannot be included in the Lagrangian [21]. Thus to start off, the theory will have no mass terms for the fermions. The mechanism to generate masses will be discussed in the subsequent section.

In the spirit of the original construction of this model [17], consider a free Dirac Lagrangian in terms of chiral lepton fields, only with a neutrino ν_e and an electron e, given by

$$\mathcal{L} = i(\bar{\psi}_{Le} \partial\!\!\!/ \psi_{Le} + \bar{\psi}_{Re} \partial\!\!\!/ \psi_{Re} + \bar{\psi}_{L\nu} \partial\!\!\!/ \psi_{L\nu}), \tag{2.27}$$

where ψ_{Le} and ψ_{Re} are the left and right chiral states of the electron, respectively.

As neutrinos are left-handed $\psi_{L\nu}$, a right-handed term for them has not been included above. Recall that in QCD the effect of a gauge boson interacting with the gluon is a change in the colour of the incoming and outgoing quark. One can expect that a gauge boson mediating the weak force could also change an up quark into a down quark at one vertex, and convert an electron into a neutrino at the other [20]. The matrices representing the fermions in such a theory should contain at least two elements (as one particle gets turned into a different one at a vertex). The leptons and quarks are thus packaged as doublets, allowing for the possibility of mixing between e and ν for example. Introducing the new notation to indicate a left-handed doublet L_i and right-handed singlet R_i $(i = e, \mu, \tau)$:

$$L_i = \frac{1}{2}(1-\gamma^5)\begin{pmatrix}\psi_\nu \\ \psi_i\end{pmatrix} \quad R_i = \frac{1}{2}(1+\gamma^5)\psi_i, \tag{2.28}$$

the free lepton Lagrangian can now be re-written as

$$\mathcal{L} = i\bar{L}_e \not{\partial} L_e + i\bar{R}_e \not{\partial} R_e. \tag{2.29}$$

The underlying symmetry group for this theory is $SU(2)_L \otimes U(1)_Y$, subgroups of $U(2)$. The $'L'$ subscript indicates that $SU(2)$ transformations involve left-handed states only, while $'Y'$ is a reference to the generator of the $U(1)$ group which is called the $weak\ hypercharge$ and is used to distinguish the group from the low-energy $U(1)$ of QED. The $SU(2)_L$ is a local symmetry and its associated conserved charge is called $weak\ isospin$ denoted by I. The local gauge transformations of the fields that leave the $\mathcal{L}$ invariant then take the form

$$\begin{aligned} L_e &\to e^{\frac{i}{2}\alpha^a(x)\tau^a} L_e, \\ R_e &\to e^{i\beta(x)\hat{Y}} R_e, \end{aligned} \tag{2.30}$$

where $\tau^a = \frac{\sigma^a}{2}$ and $\hat{Y} = Y$ (a constant) is the generator of $U(1)$ group. The σ^a are the 2×2 Pauli matrices that generate $SU(2)$ and they number $2^2 - 1 = 3$ in total. $SU(2)$

is a rotation symmetry and $\alpha^a(x)$ are the angles of rotation in the abstract isospin space which has 3-dimensions (I_1, I_2, I_3) or (I_x, I_y, I_z). The notation τ^a, rather than σ^a, is used to emphasize that the matrices are acting on a state with two sorts of fermions $\bar{\Psi} = (\bar{f}\ \ \bar{g})$, rather than on the spin state of single fermion. Thus, τ^a are sometimes called the Pauli isospin matrices [6].

The machinery used to describe spin in quantum mechanics can be used directly for isospin. The eigenstates of spin for a particle are represented by $|s, m\rangle$, where s is the spin of the particle and m is the eigenvalue of S_z, representing the measurement of the spin angular momentum along the z-axis. While s is fixed for a particle, m goes as $-s, -s+1, ..., s-1, s$. Similarly, a particle's isospin state can be specified by the isospin I and the eigenvalue of I_3, the third-component of the isospin generators.

It should be noted that this weak isospin is analogous but different from the $isospin$ in nuclear physics which is a global $SU(2)$ symmetry. An example of the (strong) isospin is the nucleon which carries $I = \frac{1}{2}$ and the I_3 eigenvalue of $+\frac{1}{2}$ represents a proton (isospin-up) and $-\frac{1}{2}$ is a neutron (isospin down) i.e. $p = |\frac{1}{2}, \frac{1}{2}\rangle$ and $n = |\frac{1}{2}, -\frac{1}{2}\rangle$. These particles can be arranged in a two-component object called an isospin doublet representing a nucleon:

$$\Psi = \begin{pmatrix} p \\ n \end{pmatrix}. \tag{2.31}$$

When families of closely related particles such as these are found in Nature, it hints that there is an $internal$ symmetry relating the particles. The idea is that these particles are a single physical entity but there is an internal dial which could be rotated to turn one family member into another. A symmetry such as $SU(2)$ is called internal because it doesn't relate to space and time, but rather to relations between different particles. For example, a rotation through 180° about the I_x axis of isospin space converts a proton into a neutron, and vice-versa. Note the symmetry is only approximate in this case as the masses of the two particles are not the same [4,6].

Returning to the derivation after this digression, the $SU(2) \otimes U(1)$ theory

can now be gauged following the same procedure as done previously for QED and QCD. Gauging $SU(2)$ means introducing three gauge fields W_μ^a (one for each generator) which act on the isospin doublet L_i ($I = \frac{1}{2}, I_3 = \pm\frac{1}{2}, Y = -1$). Gauging $U(1)$ introduces the potential B_μ which acts on both L_i and $R_i (I = 0, Y = -2)$. The covariant derivative is now defined as

$$\hat{D_\mu} = \partial_\mu - \frac{i}{2} g \hat{\tau^a} W_\mu^a - \frac{i}{2} g' \hat{Y} B_\mu, \tag{2.32}$$

where g is the $SU(2)$ coupling constant and g' is for $U(1)$. The field strength tensors are now given by

$$\begin{aligned} W_{\mu\nu}^a &= \partial_\mu W_\nu^a - \partial_\nu W_\mu^a + g \epsilon_{abc} W_\mu^b W_\nu^c, \\ B_{\mu\nu} &= \partial_\mu B_\nu - \partial_\nu B_\mu, \end{aligned} \tag{2.33}$$

which can be used to write the kinetic terms for the gauge fields. Re-writing the free Lagrangian in terms of the covariant derivatives now gives the locally gauge invariant theory under $SU(2)_L \otimes U(1)_Y$

$$\begin{aligned} &\mathcal{L}_{SU(2)\otimes U(1)} = -\frac{1}{4} W_{\mu\nu}^a W^{a\mu\nu} - \frac{1}{4} B_{\mu\nu} B^{\mu\nu} + \bar{L}_e i \not{D} L_e + \bar{R}_e i \not{D} R_e, \\ &= -\frac{1}{4} W_{\mu\nu}^a W^{a\mu\nu} - \frac{1}{4} B_{\mu\nu} B^{\mu\nu} + \bar{L}_e i \gamma^\mu (\partial_\mu - \frac{i}{2} g \tau^a W_\mu^a + \frac{i}{2} g' B_\mu) L_e + \\ &\bar{R}_e i \gamma^\mu (\partial_\mu + i g' B_\mu) R_e, \end{aligned} \tag{2.34}$$

where $a = 1, 2, 3$. Once again, demanding local gauge symmetry to the free $\mathcal{L}$ has yielded an interacting theory and the introduction of gauge fields. These four gauge fields will ultimately correspond to the physical mediators of the weak and electromagnetic force, as will be seen. While this is a good start, this theory is not complete as it does not fully describe the weak force. The weak force has massive mediators, but gauge invariance prohibits this and the leptons are also still massless. These issues will be addressed by the introduction of symmetry breaking in the next section.

Interlude: Spontaneous Symmetry Breaking and the Goldstone Theorem

The ground state, or the lowest energy state, in a canonically quantized field theory is called the $vacuum$. It is the state with no particles, and excitations about the vacuum $|0\rangle$ are interpreted as particles and anti-particles. An excitation is denoted by the operation of the creation operator $a_p^\dagger$ on $|0\rangle$

$$a_p^\dagger|0\rangle = |\overrightarrow{p}\rangle, \tag{2.35}$$

where $|\overrightarrow{p}\rangle$ is an eigenstate of the free Hamiltonian and is interpreted as a single particle of momentum $\overrightarrow{p}$ and energy $\omega_p = \sqrt{|\overrightarrow{p}|^2 + m^2}$. Multiple particles can be created with repeated application of the creation operators on the vacuum e.g. $a(p_1)^\dagger a(p_2)^\dagger|0\rangle$ represents a two particle state. In other words, if one applies energy $\omega_p = \sqrt{|\overrightarrow{p}|^2 + m^2}$ and momentum $\overrightarrow{p}$ in some region of spacetime, a particle is created as an excitation of the underlying field [22].

The quantization procedure assumes that the system has a ground state that is annihilated by a_p i.e. $a_p|0\rangle = 0$, where a_p is the annihilation operator for the field quanta. Classically, the ground state is an equilibrium point where the force vanishes and is thus obtained by minimizing the potential energy. In the quantized theory, the value of the field that minimizes the potential is interpreted as the $vacuum\ expectation\ value$ or vev of the quantum field and is denoted by v such that

$$\begin{aligned} \langle 0|\phi|0\rangle &= v, \\ \langle\phi\rangle &= v. \end{aligned} \tag{2.36}$$

As the vev is the value of the field at the lowest energy, fluctuations about this value correspond to dynamical degrees of freedom which are associated with the particles in the quantized theory. The Lagrangian of the theory describes the nature of these excitations.

In quantizing the free (scalar) theory, the potential takes the form $V = m\phi^2$ and is unique and stable. The minimum is trivially at the origin $\phi = 0$ and thus

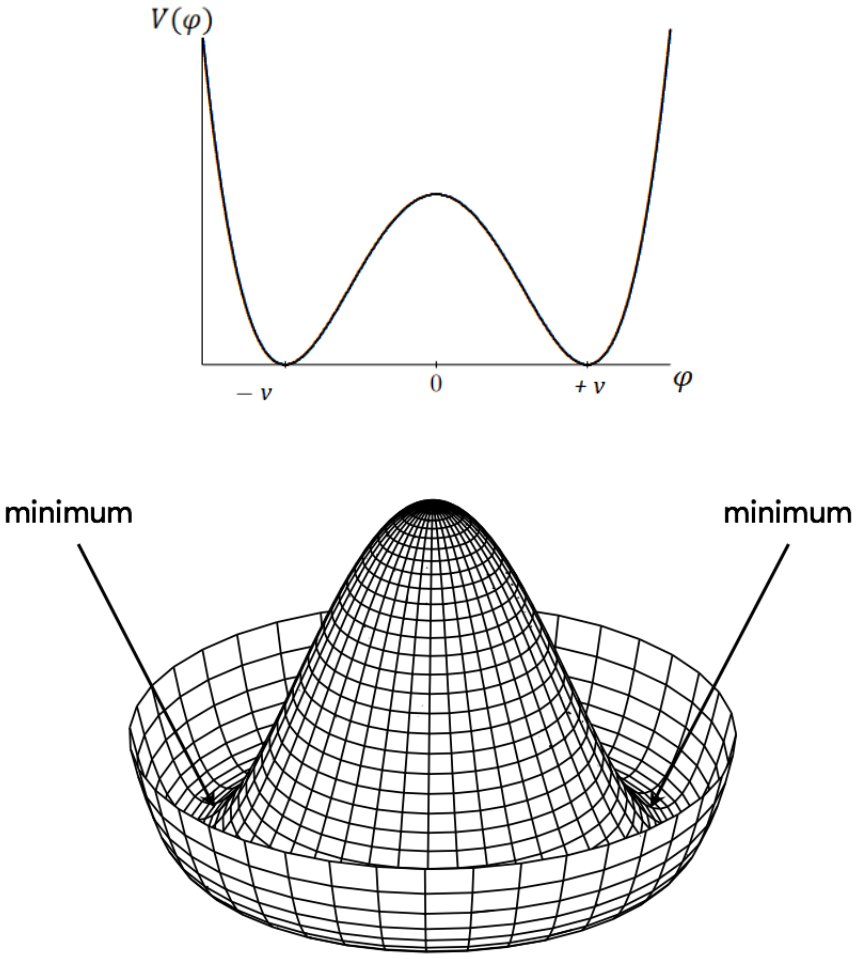

Figure 2.2 – The shape of the potential in a theory with a discrete symmetry (top) and the one with continuous symmetry (bottom). When a continuous symmetry is broken, excitations along the pit of the valley where the potential is flat are massless and are referred to as the Goldstone bosons.

$\langle 0|\phi|0\rangle = 0$, as the quantum field is composed of creation and annihilation operators that vanish in the vacuum. However, this is not always the case and it is possible to have a theory with degenerate vacua which can result in the vev having a non-zero value. Consider the following ϕ^4 theory with the 'wrong sign' for the mass term:

$$\begin{aligned}\mathcal{L} &= \frac{1}{2}\partial^\mu\phi\partial_\mu\phi - V(\phi), \\ &= \frac{1}{2}(\partial^\mu\phi)(\partial_\mu\phi) - (-\frac{1}{2}\mu^2\phi^2 + \frac{\lambda}{4!}\phi^4), \\ &= \frac{1}{2}(\partial^\mu\phi)(\partial_\mu\phi) + \frac{1}{2}\mu^2\phi^2 - \frac{\lambda}{4!}\phi^4.\end{aligned} \tag{2.37}$$

The shape of this potential is shown in Figure 2.2. The equilibrium points can be found by $\frac{\partial V}{\partial\phi} = 0$ and are $(0, \pm\sqrt{\frac{6\mu^2}{\lambda}})$. The point $\phi = 0$ is a local maximum while the global minima are at $\phi = \pm\sqrt{\frac{6\mu^2}{\lambda}}$. There are thus two potential ground states for the theory which can be denoted as $|\Omega_+\rangle$ and $|\Omega_-\rangle$. The vacuum expectation value for ϕ is a non-vanishing constant now given by

$$\begin{aligned}\langle\Omega_+|\phi|\Omega_+\rangle &= +v = \left(\frac{6\mu^2}{\lambda}\right)^{1/2}, \\ \langle\Omega_-|\phi|\Omega_-\rangle &= -v = -\left(\frac{6\mu^2}{\lambda}\right)^{1/2}.\end{aligned} \tag{2.38}$$

Note that the second derivative $\frac{\partial^2 V}{\partial\phi^2}$ is negative for $\phi = 0$ and thus the point is unstable. Quantizing the theory about it will lead to problems. For example, perturbing the field about $\phi = 0$ will lead to a particle spectrum that contains a tachyon, a particle with the imaginary mass $m = i\mu$. Furthermore, the Feynman rules for the theory will be derived by doing a perturbative expansion of the S-matrix, and this technique will also not work about an unstable point. The theory thus has to be reformulated such that fluctuations around the true vacuum are considered.

The system could choose to settle in either of the two stable degenerate minima of the theory, both are equivalent. Choosing $|\Omega_+\rangle$ would mean considering excitations about the point $\phi = \phi_0 = +v$. To solve the theory and identify the correct mass terms, the potential $V(x)$ can be approximated in the vicinity of its minimum ϕ_0 as a harmonic oscillator potential. Taylor expanding the potential about the minimum gives

$$\begin{aligned} V(\phi - \phi_0) &= V(\phi_0) + \left(\frac{\partial V}{\partial \phi}\right)_{\phi_0} (\phi - \phi_0) + \frac{1}{2!}\left(\frac{\partial^2 V}{\partial \phi^2}\right)_{\phi_0} (\phi - \phi_0)^2 + ... \\ &= V(\phi_0) + \mu^2(\phi - \phi_0)^2 + ... \end{aligned} \tag{2.39}$$

Defining a new shifted field $\eta = \phi - \phi_0 = \phi - v$, which represents oscillations about the stable minimum, and ignoring the constant term $V(\phi_0)$, the Lagrangian in 2.37 can be rewritten in terms of η

$$\mathcal{L} = \frac{1}{2}\partial^\mu \eta \partial_\mu \eta - \mu^2 \eta^2 + \mathcal{O}(\eta^3), \tag{2.40}$$

where η obeys $\langle \Omega_+ | \eta | \Omega_+ \rangle = 0$. This Lagrangian represents the same physical system in 2.37 that is written in terms of ϕ, there has only been a change of variables indicating the ground state has moved 'off-center'. However, the particle excitations now have a sensible mass of $\sqrt{2}\mu$. This version is also suitable for the purposes of deriving the Feynman rules and will give a perturbative expansion which is convergent.

This exercise of reformulating the theory about a stable ground state demonstrates the concept of *spontaneous symmetry breaking*. A symmetry is described as being spontaneously broken when the ground state of the theory does not share a symmetry which is found in the equations of motion. The original $\mathcal{L}$ in 2.37 was symmetrical under the operation $\phi \to -\phi$ (called a Z_2 symmetry), but in the version in 2.40, the symmetry is no longer apparent as there are cubic terms in the field. The process of the system settling from an unstable to a stable ground state through an arbitrary choice of vacuum is said to have broken the Z_2 symmetry. Note that the symmetry has not disappeared all together, but is rather hidden in

the re-written version of the theory.

The previous example considered a discrete symmetry, with only two ground states. Consider now a theory with a continuous symmetry which leads to more interesting results:

$$\mathcal{L} = \frac{1}{2}[(\partial_\mu \phi_1)^2 + (\partial_\mu \phi_2)^2] + \frac{\mu^2}{2}(\phi_1^2 + \phi_2^2) - \frac{\lambda}{4!}(\phi_1^2 + \phi_2^2)^2. \tag{2.41}$$

The shape of the potential $V(\phi_1, \phi_2)$ is shown in Figure 2.2 and resembles a Mexican hat. The system has global $SO(2)$ symmetry: it is symmetric with respect to rotations in the $\phi_1(x) - \phi_2(x)$ plane. The minima of $V(\phi_1, \phi_2)$ lie on a circle now and are infinite. They form a set of degenerate vacua which are related to each other by rotation. The equation of this circle can be shown to be

$$\phi_{1min}^2 + \phi_{2min}^2 = \frac{6\mu^2}{\lambda} = v^2. \tag{2.42}$$

The physical fields, which are excitations about the stable vacuum, are then realized by doing perturbations about the circle $|\phi|$ of radius $\sqrt{\frac{6\mu^2}{\lambda}}$ (not about ϕ = 0). The symmetry of the system will be broken when it randomly chooses to settle in a particular ground state. For simplicity, one can choose $(\phi_1, \phi_2) = (+\sqrt{\frac{6\mu^2}{\lambda}}, 0)$. The new field variables representing the deviations from this minimum are

$$\begin{aligned} \eta = \phi_1 - \sqrt{\frac{6\mu^2}{\lambda}} = \phi_1 - v, \\ \rho = \phi_2. \end{aligned} \tag{2.43}$$

Taylor expanding the potential $V(\phi_1, \phi_2)$ about this point as done previously, and

reformulating the $\mathcal{L}$ in terms of η and ρ would give

$$\mathcal{L} = \frac{1}{2}[(\partial_\mu \eta)^2 + (\partial_\mu \rho)^2] - \mu^2 \eta^2 + \text{higher order terms} \tag{2.44}$$

Similar to the example with discrete symmetry breaking, this equation shows that particles of the field η have a mass$\sqrt{2}\mu$. However, there are no quadratic terms of the ρ field. In other words, excitations of ρ are massless. This massless excitation is called a $Goldstone$ boson. According to Goldstone's theorem, the spontaneous breaking of a global continuous symmetry is always accompanied by the appearance of a massless particle.

This phenomenon can be understood intuitively by looking at the shape of the potential. Oscillating up and down along the ϕ_1 direction will require energy to go up the walls of the potential and overcome the restoring forces; the particles thus have a mass. However, displacements in the ϕ_2 direction corresponds to rolling in the bottom of the circular valley with no opposing forces and costs no energy. The excitations in this direction are thus massless.

In summary, these examples show that the correct mass terms in a theory can be disguised and they can be identified by locating the global minimum and re-writing the Lagrangian as a function of the deviation from this point. As will be seen in the next section, when applied to a locally gauged theory, the phenomenon of spontaneous breaking of global symmetries will play a key role in generating masses for gauge bosons.

Part 2: SU(2)$_L \otimes$ U(1)$_Y \rightarrow$ U(1)$_{EM}$ and Electroweak Unification

Equipped with the idea of spontaneously symmetry breaking, it became possible to not only come up with a description of the weak force but also to unify it with electromagnetism. Weinberg's seminal 1967 paper motivates this when he starts by stating that, "Leptons interact only with photons, and with the intermediate bosons that presumably mediate weak interactions. What could be more natural than to unite these spin-one bosons into a multiplet of gauge fields?" [17].

With this goal in mind, this section continues with Part 2 of the derivation of a theory that not only describes the weak force but also hopes to unify it with electromagnetism.

In order to break the symmetry of the theory described by 2.34 (and generate masses for the particles), a complex scalar field called the $Higgs\ field$ is added to it. It has four components which are arranged into a two component-vector, or a doublet, given by

$$\begin{aligned}\Phi &= \begin{pmatrix}\phi^+\\ \phi^0\end{pmatrix},\\ &= \frac{1}{\sqrt{2}}\begin{pmatrix}\phi_3 + i\phi_4\\ \phi_1 + i\phi_2\end{pmatrix},\end{aligned} \tag{2.45}$$

$$\Phi^\dagger\Phi = (\phi^+)^*\phi^+ + (\phi^0)^*\phi^0 = \frac{1}{2}(\phi^1 + \phi^2 + \phi^3 + \phi^4), \tag{2.46}$$

where $\phi_1..\phi_4$ are real. Φ is an isospin doublet ($I = \frac{1}{2}, I_3 = \pm\frac{1}{2}$) and consists of a positively charged (ϕ^+) and a neutral spin-zero (ϕ^0) particle(the superscripts indicate electromagnetic charges). The doublet configuration will allow for the field to couple the left-handed L_i and right-handed R_i fermions in a Yukawa coupling; this will allow for mass generation of the fermions. Introduction of the Φ to the theory will result in an addition to $\mathcal{L}_{SU(2)\otimes U(1)}$ in the form of

$$\begin{aligned}\mathcal{L}_\Phi &= (D^\mu\Phi)^\dagger(D_\mu\Phi) - V(\Phi^\dagger\Phi) + \mathcal{L}_{Yukawa},\\ &= (D^\mu\Phi)^\dagger(D_\mu\Phi) + \mu^2\Phi^\dagger\Phi - \lambda(\Phi^\dagger\Phi)^2 - G_e(\bar{L}_e\Phi R_e + \bar{R}_e\Phi^\dagger L_e),\end{aligned} \tag{2.47}$$

where $(\Phi)^\dagger = (\phi^{(+)*}, \phi^{(0)*})$ denotes the hermitian conjugate and G_e is the coupling strength. The form of the potential is the most general allowed by gauge invariance and renormalizability [21]. Note that unlike the example of spontaneous symmetry breaking discussed in the previous section, the kinetic term for Φ has covariant derivatives D^μ, indicating the theory is locally gauged. Furthermore,

symmetry breaking will now be applied to a non-Abelian theory. Adding $\mathcal{L}_\Phi$ to 2.34, the full Lagrangian of the theory before symmetry breaking becomes

$$\begin{aligned}\mathcal{L}_{unbroken} &= \mathcal{L}_{SU(2)\otimes U(1)} + \mathcal{L}_\Phi, \\ &= -\frac{1}{4}W^a_{\mu\nu}W^{a\mu\nu} - \frac{1}{4}B_{\mu\nu}B^{\mu\nu} + \bar{L}_e i\not{D} L_e + \bar{R}_e i\not{D} R_e \\ &+ (D^\mu\Phi)^\dagger(D_\mu\Phi) + \mu^2\Phi^\dagger\Phi - \lambda(\Phi^\dagger\Phi)^2 - G_e(\bar{L}_e\Phi R_e + \bar{R}_e\Phi^\dagger L_e).\end{aligned} \tag{2.48}$$

The symmetry of the theory can now be broken. This is accomplished when the Higgs field goes from an unstable to a stable state and acquires a vacuum expectation value. This event, called the electroweak phase transition, is believed to have occurred about 10^{-12} seconds after the Big Bang when the Universe cools to below 10^{16} K and its ground state breaks the $SU(2) \otimes U(1)$ symmetry.

The minimum of the Higgs potential $V(\Phi^\dagger\Phi)$ is not at the origin, but found at $(\Phi^\dagger\Phi)_0 = v^2 = \mu^2/\lambda$. Similar to the previous example, the Higgs field can pick one of the infinite number of equivalent vacua. One can choose to break the symmetry with the new ground state at $(\phi_1, \phi_2, \phi_3, \phi_4) = (\sqrt{2}v, 0, 0, 0)$. The vacuum expectation value of Φ then becomes

$$\langle\Omega|\Phi|\Omega\rangle = \Phi_0 = \begin{pmatrix} 0 \\ v \end{pmatrix}. \tag{2.49}$$

The motivation of choosing this form of a vacuum expectation value is the following. When a non-abelian gauge symmetry is broken, it is possible that that the vacuum state is still invariant under a subset of the original symmetry i.e. those symmetries remain unbroken [6]. This form of the vacuum will ensure that the ground state is invariant under the $U(1)$ transformation $U = e^{iQ\alpha(x)}$ where

$$Q = I_3 + \frac{1}{2}Y. \tag{2.50}$$

This equation is called the Gell-Mann-Nishijima relation. It states that generator Q is a linear combination of the generator I_3 of $SU(2)$ and Y of $U(1)_Y$. The $SU(2)_L \otimes$

$U(1)_Y$ symmetry generated by (I_a, Y) is spontaneously broken or 'Higgsed' down to $U(1)_{EM}$ generated by Q. Q remains unbroken in the final theory and will be identified as the generator of electromagnetic charge and the associated gauge boson will be the photon. This choice of vacuum thus allows one to recover Maxwell's electromagnetism in a symmetry broken Universe (note also that giving a vev to ϕ_3 or ϕ_4 would break electromagnetism, so ϕ_1 and ϕ_2 are the only options).

In analogy with the previous example, the potential can be expanded about the ground state. The shifted field representing the fluctuations about the vacuum is now made of

$$\begin{aligned} \eta = \phi_1 - \sqrt{\frac{\mu^2}{\lambda}} = \phi_1 - v, \\ \rho = \phi_2, \\ \chi = \phi_3, \\ \xi = \phi_4. \end{aligned} \tag{2.51}$$

However, re-writing the Lagrangian in terms of these fields will give vector-scalar cross terms which will be difficult to interpret. As the symmetry of the theory is local, a different isospin rotation can be performed at each point in space-time. By applying a combined hypercharge and isospin gauge transformation, the components ϕ_2, ϕ_3, ϕ_4 can be set to zero and the excitations above the ground state can be expressed under the $unitary\ gauge$, also called the $physical\ gauge$ as in this gauge the physical particles of the theory become apparent. The ground state takes a simpler form now

$$\phi = \frac{1}{\sqrt{2}} \begin{pmatrix} 0 \\ v + h \end{pmatrix}, \tag{2.52}$$

where the physical field $h(x)$ has a vanishing expectation value $< h >= 0$ and its quanta is called the $Higgs\ boson$. The unbroken theory from 2.48 can now be reformulated about the stable ground state. To see the physics of the broken theory,

different parts of the Lagrangian can be evaluated. The first four terms that don't involve the Higgs field remain intact. Expanding out the kinetic part for Φ in terms of the new ground state would give [6]:

$$\begin{aligned} D_\mu\phi &= \partial_\mu\phi - \frac{i}{2}g\tau^a W_\mu^a\phi - \frac{i}{2}g'B_\mu\phi \\ &= \frac{1}{\sqrt{2}}\begin{pmatrix}0\\ \partial_\mu h\end{pmatrix} - \begin{pmatrix}\frac{ig}{2}\begin{pmatrix}W_\mu^3 & W_\mu^1 - iW_\mu^2\\ W_\mu^1 + iW_\mu^2 & -W_\mu^3\end{pmatrix} + i\frac{g'}{2}B_\mu\end{pmatrix}\frac{1}{\sqrt{2}}\begin{pmatrix}0\\ v+h\end{pmatrix}, \end{aligned} \tag{2.53}$$

$$\begin{aligned} (D^\mu\phi)^\dagger(D_\mu\phi) &= \frac{1}{2}(\partial_\mu h)^2 + \frac{g^2v^2}{8}(W_\mu^1)^2 + \frac{g^2v^2}{8}(W_\mu^2)^2 \\ &+ \frac{v^2}{8}(gW_\mu^3 - g'B_\mu)^2 + \text{higher order terms.} \end{aligned} \tag{2.54}$$

Expansion of the kinetic terms shows that the Lagrangian now has quadratic terms in the gauge fields W_μ^1, W_μ^2 and linear combination $gW_\mu^3 - g'B_\mu$. In other words, the gauge fields have now acquired mass! From the coefficient of these terms, it can be seen that the mass for W_μ^1, W_μ^2 is given by $M_W^2 = \frac{g^2v^2}{4}$. The mass of the linear combination of the gauge fields depends on the relative strength of the coupling constants g and g'.

This extraordinary phenomenon of mass generation through spontaneous symmetry breaking in a gauge theory is the famous $Higgs\ mechanism$ [23–27]. The Higgs field that was introduced acquires a vev and tends to a minimum value Φ_0; it is the interactions of the vector fields with Φ_0 that induces the particles to act as if they had mass [9]. The massless Goldstone bosons which appeared in the previous example of symmetry breaking are no where to be found. The Higgs field started out with four scalar fields, of which three disappear and the last remaining massive scalar is the Higgs boson. Those degrees of freedom have now gone into giving mass to the vector bosons (a massive vector field has three degrees of freedom, while a massless has just two polorization states). This is often described as the gauge fields 'eating' the Goldstone bosons and acquiring mass.

To relate the fields W_μ^1, W_μ^2, W_μ^3, B_μ to the physical observed fields, the mat-

rix in the equation above can be diagonalized. The normalized eigenstates, called the mass eigenstates, and the eigenvalues representing the masses are given by

$$\begin{aligned} W_\mu^\pm &= \frac{1}{\sqrt{2}}(W_\mu^1 \mp iW_\mu^2) & M_W^2 &= \frac{g^2v^2}{4} \\ Z_\mu &= W_\mu^3 \cos\theta_\mathrm{W} - B_\mu \sin\theta_\mathrm{W} & M_Z^2 &= \frac{v^2(g^2+g'^2)}{4} \\ A_\mu &= W_\mu^3 \sin\theta_\mathrm{W} + B_\mu \cos\theta_\mathrm{W} & M_A^2 &= 0 \end{aligned} \tag{2.55}$$

where $\cos\theta_\mathrm{W} = \frac{g}{\sqrt{g^2+g'^2}}$ and $\sin\theta_\mathrm{W} = \frac{g'}{\sqrt{g^2+g'^2}}$. The first three states correspond to the $W^\pm$ and Z bosons. The last mass eigenstate A_μ has an eigenvalue of 0. It is identified as the photon and is orthogonal to Z_μ. This occurs because in the broken theory there remains one unbroken $U(1)$ symmetry group and it is identified the gauge symmetry of QED (this can be seen more explicitly by re-writing the gauge kinetic terms in terms of the mass eigenstates).

Similarly, the mass for the leptons can be seen by inserting the vev into the Yukawa coupling terms in 2.48 [21]:

$$\begin{aligned} & G_e(\bar{L}_e\phi R_e + \bar{R}_e\phi^\dagger L_e) \\ &= G_e(\bar{\psi}_{L\nu} \quad \bar{\psi}_{Le})\frac{1}{\sqrt{2}}\begin{pmatrix} 0 \\ v+h \end{pmatrix}\psi_{Re} + G_e\bar{\psi}_{Re}\frac{1}{\sqrt{2}}(0 \quad v+h)\begin{pmatrix}\psi_{L\nu}\\ \psi_{Le}\end{pmatrix} \\ &= \frac{G_e}{\sqrt{2}}[(v+h)\bar{\psi}_{Le}\psi_{Re} + (v+h)\bar{\psi}_{Re}\psi_{Le}] \\ &= \frac{G_e}{\sqrt{2}}(v+h)\bar{\psi}_e\psi_e \\ &= \frac{G_e v}{\sqrt{2}}\bar{\psi}_e\psi_e + \frac{G_e}{\sqrt{2}}h\bar{\psi}_e\psi_e \end{aligned} \tag{2.56}$$

where ψ_e is the electron spinor. Once again, a mass term for the lepton is generated due to the vev and its value is given by $m_e = \frac{G_e v}{\sqrt{2}}$. Note that the neutrino drops out and remains massless even after symmetry breaking. The equation above also indicates that Higgs boson couples to the matter fields. The strength of the coup-

ling can be written in terms of the mass, and is shown to be $G_e \propto m/v$. Thus, the Higgs boson couples to other particles in proportion to their masses and decays preferentially into the heaviest particles kinematically allowed.

Lastly, the potential in 2.48 can be expanded in terms of the vev to see the properties of the Higgs boson [11]:

$$\begin{aligned} &\mu^2\Phi^\dagger\Phi - \lambda(\Phi^\dagger\Phi)^2, \\ &= -\mu^2 h^2 - \lambda v h^3 - \frac{1}{4}\lambda h^2, \\ &= -\frac{1}{2}m_h^2 h^2 - \sqrt{\frac{\lambda}{2}} m_h h^3 - \frac{1}{4}\lambda h^4, \end{aligned} \tag{2.57}$$

where the last line has been re-written to show explicitly the mass of the Higgs boson which is given by $m_h = \sqrt{2}\mu = \sqrt{2\lambda}v$. The Higgs mass thus has a magnitude which is controlled by the vev and a new coupling constant λ. The cubic and quartic terms in the equation also highlight that the Higgs boson couples to itself.

The program of building a theoretical framework for the weak force, and unifying it with electromagnetism is now complete. The model presented here only considered one generation of leptons for simplicity, but it can be extended to quarks as well. In this unified theory, the weak and electromagnetic forces are not unrelated phenomenon but different manifestations of the fundamental 'electroweak' interaction. The photon and Z boson are both mixtures of W_μ^3 and B_μ, different aspects of the same underlying fields. It should be noted that while this unification attempt involves combining the two forces into the $SU(2)_L \otimes U(1)_Y$ group with different coupling constants g and g', a more complete unification would involve only a single gauge group with one coupling constant. The mathematical structure of the theory presented here is summarized pictorially in Figure 2.3.

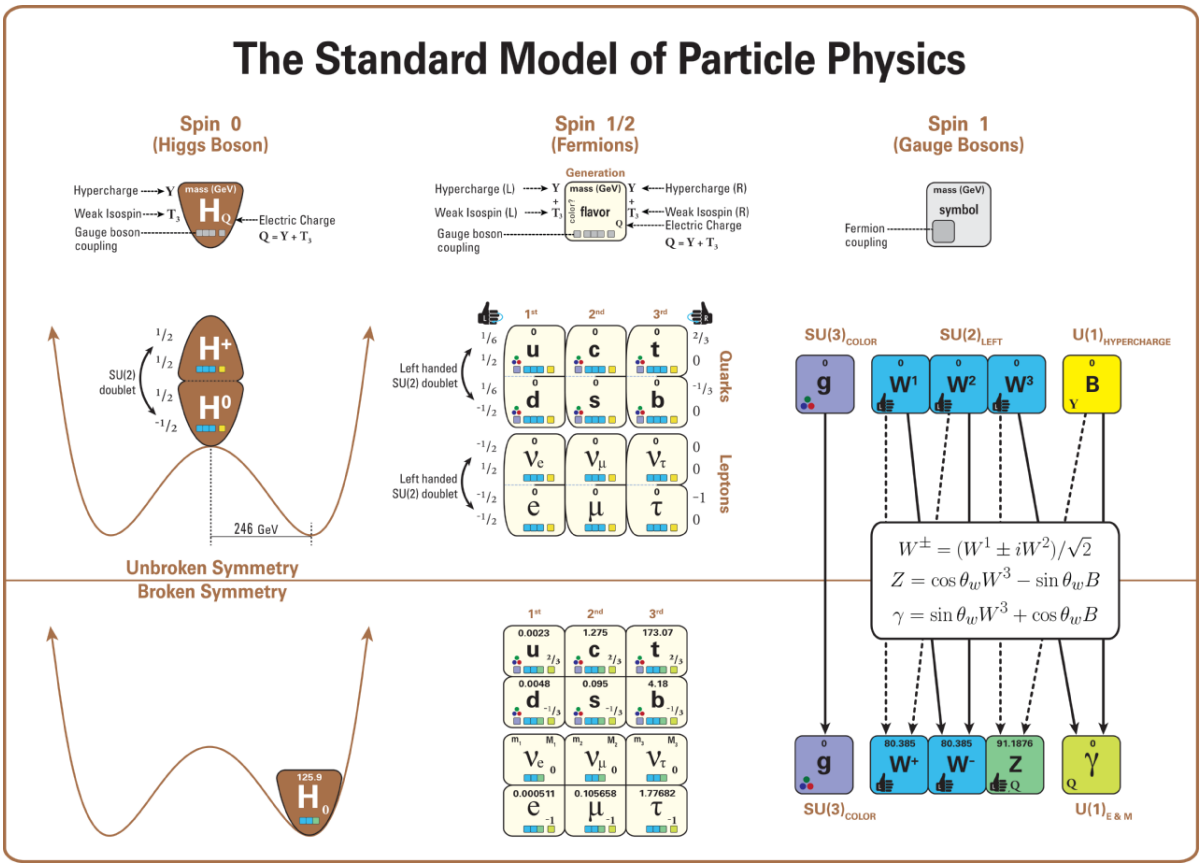

Figure 2.3 – The mathematical structure of the Standard Model [28].

2.2 Motivation: Extending the Standard Model Higgs Sector

The discovery of the Higgs boson by the ATLAS and CMS collaborations [29, 30] in 2012, nearly 50 years after the GWS theory was first proposed, served as an outstanding validation of the Standard Model. The measured properties of this particle to date all agree within theoretical predictions: it is spin-0, it has been observed in five decay channels ($\gamma\gamma, \tau\tau, ZZ, WW, bb$) with a statistical significance of greater than 5σ and the branching ratios are in good agreement with SM predictions [31].

Despite this success of the SM, it might not be the full story. There is strong motivation to believe that the SM Higgs is only one particle of a larger scalar sector and more spin-0 particles are yet to be found. As the fermion sector of the SM has three generations (i.e. is $non\text{-}minimal$), it could be expected that a scalar sector would also contain a large family of particles. Similar to the fermions, the structure of this sector is ad-hoc and there is nothing fundamental that forbids a richer spectrum of Higgs particles [32]. Particularly relevant for this search is the fact that both spin-1 and spin-1/2 particles have been observed in charged and neutral states. However, a charged spin-0 elementary particle is yet to be discovered.

Furthermore, there are a number of observed phenomena which the SM fails to explain. The nature of dark matter (DM), which is believed to make up 26 % of the critical density in the Universe, is not understood in this theory [33]. Neutrinos in the SM are massless and this does not account for observed neutrino oscillations which would require a neutrino mass. Additionally, the origin of matter-antimatter asymmetry of the Universe (baryonic asymmetry) cannot be explained by the theory. The SM also does not describe the gravitational force, which has a separate theoretical framework. All these shortcomings indicate that there must be an extension of this theory, referred to as Beyond the Standard Model (BSM) physics, to describe Nature in a more complete way.

In order to explain these anomalies, numerous new physics models have been proposed. Among these include the Minimal Supersymmetric Standard Model

(MSSM) [34–36], Next to Minimal Supersymmetric Standard Model (NMSSM) [37, 38] and Axion models [39, 40]. These theories generally involve an extension or modification of the SM Higgs structure. It is also possible that a non-minimal Higgs sector mediate interactions with DM particles through a 'Higgs portal', or that DM itself is composed of scalar particles [41]. CP-odd scalars have also been proposed as a possible explanation of the diffuse gamma-ray excess from the galactic centre [42]. Additionally, the recent measurement of a_μ by the g$-$2 collaboration finds a value $4.2\ \sigma$ higher than theoretical calculations which can be explained in the context of light BSM Higgs particles [43, 44]. Searching for additional Higgs particles is thus well-motivated and discovery of such a state would solve many of the outstanding problems in modern physics.

New physics theories that involve adding another Higgs doublet to the SM are amongst the most popular. These Two-Higgs-Doublet Models (2HDMs) [45,46] are a large class of models that appear in many theoretical frameworks (e.g. supersymmetry) that are designed to address shortcomings of the SM. The signal model used in this thesis employs a 2HDM as well. The theory is one of the simplest extensions of the SM and contains two complex $SU(2)$ Higgs doublets (Φ_1 and Φ_2) which can generate masses for all the gauge bosons and fermions. There are thus 8 degrees of freedom at the start, and after symmetry breaking 3 are eaten up by the $W^\pm$ and Z gauge bosons which acquire mass. The Higgs sector of the 2HDM then ends up with five remaining scalars : two CP even Higgses (H and h, with $m_h < m_H$), one CP odd Higgs (A) and a pair of charged ($H^\pm$) Higgs bosons. In general, most higher Higgs representations predict in their spectrum a charged Higgs boson [47].

In hadron colliders such as the LHC, there are several ways that the charged Higgs boson can be produced. Searches can generally be classified into those for heavy ($m_{H^+} > m_{Top}$) and light ($m_{H^+} < m_{Top}$) charged scalars. This search targets a light charged Higgs as it has been shown that the particle can be copiously produced at colliders in proton-collisions via top quark decay. When kinematically allowed, $pp \to t\bar{t} \to b\bar{b}H^-W^+ + c.c.$ provides the most important source of light charged Higgs bosons, well above the yield of various direct production modes: $gb \to tH^-, gg \to t\bar{b}H^-, gg \to W^\pm H^\mp, b\bar{b} \to W^\pm H^\mp, gg \to H^\pm H^\pm, q\bar{q} \to$

$H^{\pm}H^{\pm}, c\bar{b}/c\bar{s} \to H^{+}, qb \to q'H^{+}b, q\bar{q}' \to H^{+}\phi$ [47].

The light charged Higgs can in principle decay to a fermion-antifermion pair ($H^{+} \to c\bar{s}/c\bar{b}/\tau\nu$), to gauge bosons ($H^{+} \to W^{+}\gamma$) or to a gauge boson and a neutral Higgs boson ($H^{+} \to W^{+}A$) [48]. There are strong theoretical motivations to study the $H^{\pm} \to W^{\pm}A$ mode. Most searches to-date focus on H^{+} decays to fermions, either leptons ($H^{+} \to \tau\nu$) or hadrons ($H^{+} \to c\bar{s}/c\bar{b}$). The bosonic modes are largely neglected and have been described as the 'forgotten channels' [49]. However, if a light neutral Higgs (A) exists such that the $H^{+} \to WA$ channel is kinematically allowed, the branching fractions into the conventional final states $\tau\nu$ and cs can be strongly suppressed [50]. The bosonic decays of the H^{+} can then compete with, or even dominate, the fermionic modes [49, 51–53]. Searching for a charged Higgs in this channel is thus well justified and especially needed given that it has been neglected at colliders.

2.2.1 Summary of past results

A number of past experimental searches at colliders have placed exclusion limits for light charged Higgs bosons. For the fermionic modes, both CMS and ATLAS experiments have searched for $H^{+} \to \tau\nu$, $H^{+} \to cs$ and $H^{+} \to cb$ at the LHC. The most recent results are summarized here: For $BR(t \to bH^{+}) \times BR(H^{+} \to \tau\nu)$, ATLAS has placed exclusion limits between 0.25% and 0.031% in the mass range 90–160 GeV, while CMS set limits between 0.36% and 0.08% for a mass range of 80–160 GeV; both searches use $\sqrt{s} = 13$ TeV data [54, 55]. For the $H^{+} \to c\bar{s}$ searches, limits are placed on $BR(t \to bH^{+})$ assuming $BR(H^{+} \to c\bar{s}) = 100\%$: ATLAS placed upper limits varying between 5 % and 1 % for H^{+} masses between 90 GeV and 150 GeV using $\sqrt{s}$ = 7 Tev data , while CMS set limits in the range 1.68-0.25% for masses between 80 and 160 GeV using $\sqrt{s} = 13$ TeV data [56, 57].

For the $H^{+} \to c\bar{b}$ searches: ATLAS obtained limits on $BR(t \to bH^{+}) \times BR(H^{+} \to c\bar{b})$ in the range 0.15 % to 0.42 % for masses between 60 and 160 GeV using $\sqrt{s} = 13$ data, while CMS placed limits on $BR(t \to bH^{+})$ assuming $BR(H^{+} \to c\bar{b}) = 100\%$ of 0.8–0.5% for a mass range of 90–150 GeV using $\sqrt{s} = 8$ TeV data [58, 59]. The ATLAS result for cb decays is notable as it reports a local ex-

cess of 3σ significance (1.6σ global) for m_H^+ = 130 GeV. Prior to the LHC, the LEP-II also searched for a light charged Higgs boson. Assuming decays to only the fermionic modes $H^+ \to \tau\nu$ and $H^+ \to cs$, they placed a lower bound on the mass of about 80 GeV [60].

For the bosonic decays of the H^+, the first results came from the CDF experiment at the Tevatron. They searched for a light pseudoscalar a in the next-to-minimal Supersymmetric extension of the Standard Model (NMSSM) [61] and set upper limits on $\mathcal{B}(t \to bH^+ \to bW^+a \to bW^+\tau^+\tau^-)$ between 8% and 50% for a charged Higgs boson mass between 90 and 160 GeV and m_a between 4 and 9 GeV [62]. Then, at LEP-II, the DELPHI and OPAL experiments placed a lower bound on the H^+ of 72 GeV for a 2HDM type-I with m_A between 12 and 70 GeV assuming the bosonic channel dominates [60]. At the LHC, the first results for $H^+ \to W^+A$ come from the CMS collaboration using 36 fb^{-1}of pp collision data. No significant excess was reported and they placed limits on the decay chain $t \to bH^+ \to bW^+A \to bW^+\mu^+\mu^-$ of 1.9×10^{-6} to 8.6×10^{-6} for an H^+ between 100 and 160 GeV and A between 15 and 75 GeV [63]. ATLAS and CMS have also searched for another bosonic decay, $H^+ \to WZ$, using $\sqrt{s} = 13$ data [64,65]. Prior to the study presented in this thesis, no results from ATLAS were available for the W^+A decay channel.

2.3 Physics of pp collisions

The LHC acts as a discovery machine designed to collide protons at the TeV scale to probe physics at high energies - or equivalently, short distances ($\approx 10^{-19}$m) - with hopes of uncovering new particles that arise in these interactions. This section aims to provide a description of the underlying theory of hadron collisions and proton structure in order to aid the interpretation and analysis of data coming from the collider.

2.3.1 Proton structure and Parton Distribution Functions

The 'parts' making up the proton are called partons. According to the parton model [66–68], first advanced by Richard Feynman and James Bjorken, the proton is made up of three valence quarks (uud), gluons and a 'sea' of virtual quark-antiquark pairs which are perpetually being created and annihilated due to fluctuations of gluon fields. These partons are the point-like constituents of the proton and interact like free particles at high energies (small distance scales) but are strongly interacting and tightly bound at low energies. This arises due to the QCD asymptotic freedom regime [69] which is a result of the self-interaction of gluons discussed earlier. One can think of masses connected by springs as displaying asymptotic freedom: at short distances they interact weakly but as the springs are pulled apart and the length scale increases, the interactions get stronger and stronger [6].

The exact composition of the partons inside the proton is dynamic and quite complex; only a probabilistic description is possible. Parton Distribution Functions (PDFs) describe the probability of finding a parton of a particular flavour and momentum inside the proton [70]. The mixture of partons that makeup the proton depends on:

• the Bjorken-x : the fraction of the proton's momentum P^μ which is carried by the parton i. It is denoted by x with $0 < x < 1$, the parton momentum is therefore given by $p_i^\mu = xP^\mu$

• the Q^2 : the 4-momentum transfer scale of the scattering process. It repres-

ents the invariant mass of the virtual photon probe exchanged in the interaction and can be expressed in terms of the Mandelstam variable such that $\hat{t} = -Q^2$.

These two variables parameterize the PDF $f_i(x, Q^2)dx$ which gives the probability of finding a parton of type i, with a momentum fraction between $x + dx$ of the full proton momentum, when the hadron is probed at the scale Q^2. Parton densities are governed by low energy (long distance) physics, where the relevant distance scale is that of the hadron (10^{-15} m), and the strong coupling constant is large. Thus, PDFs are non-perturbative functions and cannot be calculated $a\ priori$; they are determined by fits to data from deep inelastic scattering experiment which probe the inside of hadrons using leptons.

The total amount of momentum carried by the quarks, gluons and antiquarks must sum to the total proton momentum. The PDF thus has the constraint that

$$\sum_i \int_0^1 dx x[f_i(x, Q^2)] = 1. \tag{2.58}$$

Additionally, the PDFs are to be normalized in a way that reflects the quantum number of the proton. As the proton is a bound state of uud and some mixture of quark-antiquark pairs, it should contain an excess of two u quarks and one d quark over the corresponding antiquarks. This implies the constraints:

$$\int_0^1 dx[f_u(x, Q^2) - f_{\bar{u}}(x, Q^2)]) = 2, \tag{2.59}$$

$$\int_0^1 dx[f_d(x, Q^2) - f_{\bar{d}}(x, Q^2)]) = 1, \tag{2.60}$$

$$\int_0^1 dx[f_s(x, , Q^2) - f_{\bar{s}}(x, Q^2)]) = 0. \tag{2.61}$$

At low energies ($Q^2 < 1$ GeV^2), the proton predominantly acts as a single particle and indistinguishable from an elementary fermion such as the muon. In the medium energy range ($1 < Q^2 < 10^4$ GeV^2), the proton behaves like a com-

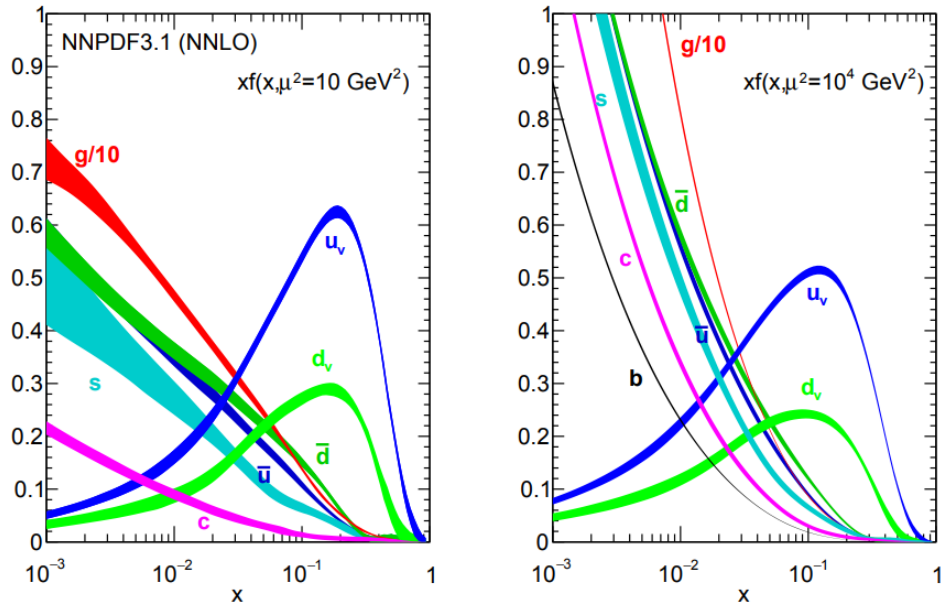

Figure 2.4 – Example of parton distribution functions from the NNPDF Collaboration showing the momentum density of partons [71]. The distributions of valence quarks, gluons and sea-quarks can be seen for two different energy scales. The PDFs are weighted by the momentum fraction and vertical axis corresponds to $xf(x, Q^2)$. The gluon PDF is divided by 10.

posite particle and its structure is dominated by the valence quarks. At higher energies, valence quarks play a smaller role and the gluon-and sea-quark PDFs are dominant; this pattern can be see in example PDFs in Figure 2.4. About 38 % of the proton momentum is contained in the valence quarks (u and d), the gluon content ranges from 35 - 50 % depending on scale, and the remainder is in sea-quarks (i.e. s, c, b or $\bar{d}, \bar{u}, \bar{c}, \bar{s}, \bar{b}$) [5, 72, 73].

2.3.2 Hadronic cross-sections and Luminosity

The parton model assumption is that the total cross-section for a process when two hadrons collide could be obtained by weighting the sub-process cross-section of the partons with the PDFs. Thus, the master formula for a given final

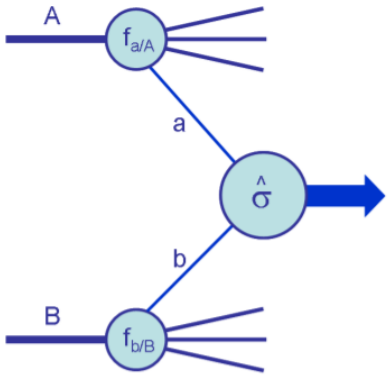

Figure 2.5 – An illustration of two partons from hadrons interacting in a collision [74].

state X in pp collisions is expressed as [74]:

$$\sigma_{pp\to X} = \int_0^1 dx_a dx_b f_a(x_a, Q^2) f_b(x_b, Q^2) \hat{\sigma}_{ab\to X}(x_a, x_b, Q^2) \tag{2.62}$$

where $f_a(x_a, Q^2)$ is the PDF and $\hat{\sigma}_{ab\to X}$ is the parton level cross-section of the hard scatter of parton a and b (partonic quantities are indicated with a hat). The $\hat{\sigma}$ is proportional to the matrix-element squared for the scattering event; the process is illustrated in Figure 2.5. This technique of combining non-perturbative objects (PDFs), which represent long-distance physics, with short-distance calculations in perturbative QCD is achieved due to the factorization theorem. It should be noted that the partonic center-of-mass energy $\sqrt{\hat{s}}$ of the interaction is smaller than $\sqrt{s}$, the proton-proton center of mass energy. This is a result of parton carrying only a fraction of the proton momentum. It is given by $\sqrt{\hat{s}} = \sqrt{x_a x_b s}$ where x_a and x_b are the momentum fractions of the interacting partons. The partonic cross-section in the expression above is calculated in a perturbative expansion in the QCD strong coupling constant α_S. The equation then becomes

$$\sigma_{pp\to X} = \int_0^1 dx_a dx_b f_a(x_a, \mu_F^2) f_b(x_b, \mu_F^2) \times [\hat{\sigma}_0 + \alpha_S(\mu_R^2)\hat{\sigma}_1 + ..]_{ab\to X}. \tag{2.63}$$

The scale dependence on the production rate can be seen clearly in the equation above. The $\hat{\sigma}$ term calculated using QCD gives rise to perturbative corrections of $\mathcal{O}(\alpha_S^n)$ where α_S depends on the renormalization scale μ_R at which it is evaluated. The scale at which the PDFs are evaluated is referred to as the factorization scale μ_F and can be thought of the scale that separates the nonperturbative and perturbative physics [73,74]. The factorization and renormalization scale are typically chosen to be equal to the momentum transfer involved, i.e. $\mu_F \approx \mu_R \approx Q^2$.

The uncertainty on the cross-section thus arises from three main sources: missing higher order terms in the perturbative expansion of the partonic cross section (this is usually evaluated by varying μ_R and μ_F), PDF uncertainties associated with experimental determination of these functions and the errors associated with the measurement of α_S. The procedure for determining these uncertainties for this analysis is detailed in Chapter 7; the predicted cross-section for some important processes at the LHC can be seen in Figure 2.6.

The cross-section can be converted to an event rate R using the instantaneous $luminosity$ $\mathcal{L}$ of the collider which characterizes the collision rate. The R is expressed as [72]:

$$R = \frac{dN}{dt} = \mathcal{L}\sigma, \tag{2.64}$$

where $\frac{dN}{dt}$ is the number of collision events per second and σ is the cross-section of the physics process. The cross-section has units of area and is typically given in barns (1 barn = 10^{-24} cm^2) while the instantaneous luminosity has units of [1 / cross-section $\times$ time] (e.g. cm^{-2}s^{-1}). The instantaneous luminosity is related to some of the key parameters of the accelerator and can be approximated as:

$$\mathcal{L} = f\frac{n_1 n_2}{4\pi\sigma_x\sigma_y} \approx f\frac{n_b N_p^2}{4\pi\sigma_x\sigma_y}, \tag{2.65}$$

where f is the frequency of the collisions (40 MHz for the LHC), n_1 and n_2 are the number of protons in each of the colliding bunches (instead of colliding single protons, colliders use bunches of protons at the same time to maximize the probability of rare interactions), σ_x and σ_y represents the beam size that has a Gaussian

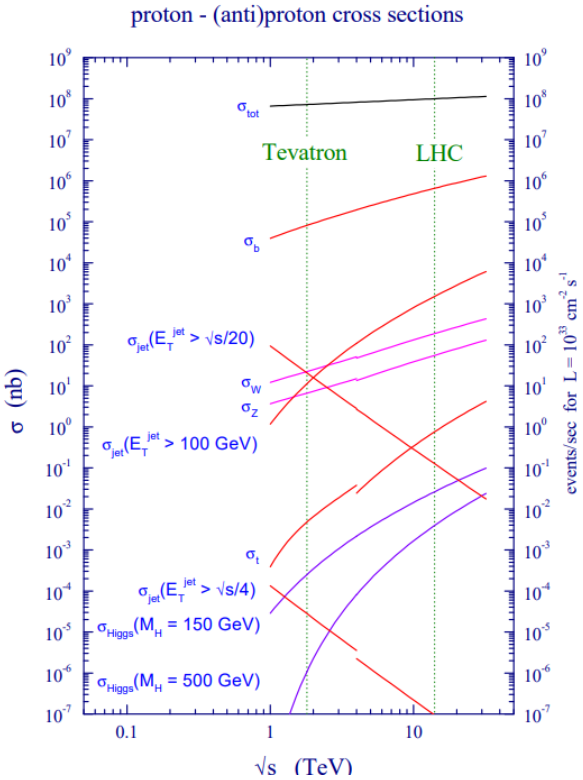

Figure 2.6 – Standard Model cross sections at the Tevatron and LHC colliders [74].

density profile ($\approx 15\mu$m), n_b is the number of bunches (≈ 2800 per beam) and N_p is the number of particles per bunch ($\approx 1 \times 10^{11}$). Thus, to increase luminosity and gather more data, one needs to squeeze a large number of protons in a small transverse beam spot. The design luminosity of the LHC is about 10^{34} cm^{-2}s^{-1}. To get the number of events produced, the luminosity can be integrated over time to get the *integrated luminosity* which carries units of inverse area (e.g. fb^{-1})

$$N_{produced} = \sigma \times \int \mathcal{L} dt. \tag{2.66}$$

The ATLAS detector does not actually observe the number of events given by this equation. This is because the detector suffers from a number of inefficiencies which prevents it from detecting all the events that are produced at the interaction point. These inefficiencies can arise due to limitations on particle iden-

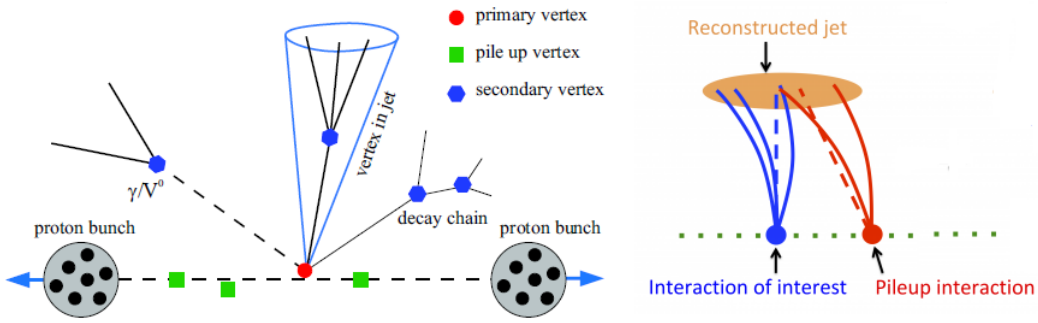

Figure 2.7 – An illustration of pile-up events. Multiple proton-proton interactions occur in each collision event which results in many vertices in addition to main high energy primary vertex. This leads to a degradation of the resolution of measured quantities for the final state particles. Adapted from [75,76].

tification, reconstruction of tracks, detector acceptance and the ability to trigger on events of interest. The observed number of events thus has to account for the detector's efficiency ϵ of selecting events and is given by

$$N_{obs} = \sigma \times \int \mathcal{L} dt \times \epsilon. \tag{2.67}$$

While the high luminosity of a collider is advantageous to collect large amounts of data, it also leads to a challenge. As there are a large number of protons being smashed together in each collision ($\approx 10^{11}$), it becomes very probable that more than one interaction occurs each time. This phenomenon of several proton-proton collisions occurring simultaneously is called $pile\text{-}up$. The interaction of interest involving a head-on collision is called the $hard\text{-}scatter$ event and its vertex is the most energetic one. The other interactions involve lower energy $soft$ scattering processes (occurring at distance scales larger than the hadron) and are called pile-up events.

Pile-up events are classified as $in\text{-}time$ pile-up and $out\text{-}of\text{-}time$ pile-up. The pp collision events at the LHC occur in proton bunches which are separated by 25 ns. In-time pile up refers to soft-interactions that occur within the same bunch crossing (i.e. the same 25 ns window), while out-of-time pileup refers to pile-up events from another bunch crossing that leave behind their signatures in the

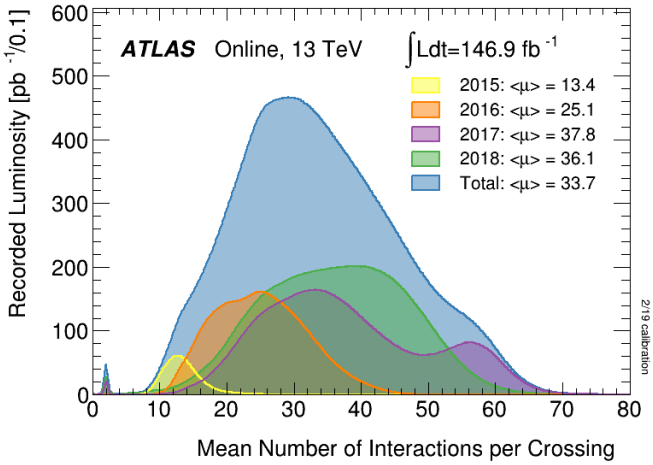

Figure 2.8 – The distribution of the mean number of interactions per crossing $< \mu >$ during Run 2 of the LHC (2015 - 2018). The $< \mu >$ corresponds to the mean of the Poisson distribution of the number of interactions per crossing calculated for each bunch [77].

collision of interest. The average pile-up multiplicity $< \mu >$, used to quantify the amount of pile-up, is the mean number of proton-proton interactions occurring per bunch crossing. It is directly related to the luminosity and is given by

$$< \mu >= \frac{\mathcal{L}_{bunch}\sigma_{inelastic}}{f}, \tag{2.68}$$

where $\mathcal{L}_{bunch}$ is the instantaneous luminosity per bunch, $\sigma_{inelastic}$ is the cross-section (about 80 mb for Run 2) for inelastic pp events i.e. events where the protons disintegrate in the collision and the final state particles are different from the initial state. During Run-2 of the LHC with a frequency f of about 40 MHz, there were an average of 33.7 interactions per bunch crossing [77].

As a result of the pile-up interactions, unwanted collisions overlap in the detector and hide the rare processes that one is searching for. The final-states observed in the detector are not only products of the hard-scatter event, but the superposition of these products with those from the other simultaneous soft collisions as well. As seen in Figure 2.7, the pileup essentially consists of a large number of soft hadrons which are spread over the whole detector and this complicates the reconstruction of the interesting events. The net result is that pile-up

biases and smears the reconstructed quantities and distributions of the final states of hard collisions [78]. In ATLAS analyses the effect of pileup is accounted for by using sophisticated tracking and object reconstruction algorithms, modeling additional vertices in Monte Carlo simulations from soft collisions and assigning systematic uncertainties related to this effect.

2.3.3 Structure of a Collision

The collision of hadrons in a particle accelerator is a complex process involving a number of intermediate stages before the final products are observed and recorded by the detector. Understanding the anatomy of the collision is not only needed for sifting through the hundreds of final state particles produced, but it also plays a critical role for Monte Carlo event generators used to simulate the processes being studied. The structure of a collision can be approximated into various steps as seen visually in Figure 2.9 and a summary of these stages is given below [79–84]:

• Hard-scatter: two protons made of a bag of partons (quarks, gluons) are moving towards each other on a collision course at a very high speed. While the protons are a spherical bound state in their own rest frame, they are like extremely flat discs due to Lorentz contraction in the lab frame and the internal interactions are time dilated. The PDFs encode the partonic substructure of these incoming particles. One parton from each of the protons enters the hard process, they interact at high Q^2 and produce a number of outgoing partons (usually two) at high angles with respect to the beam axis. A short lived resonance could be produced in this high energy interaction (such as a top, W or Z) and is considered a part of the process. This process involving high momentum transfers can be calculated using perturbative QCD based on the recipe outlined in equation 2.62.

As the two protons are complex bound states of strongly interacting partons, it is possible that multiple parton interactions (MPI) take place during the same collision. These secondary interactions in addition to the hard scattering process are called the $underlying\ event$ (UE) (This should not be confused with pile-up events, where several protons collide in the same bunch crossing). The

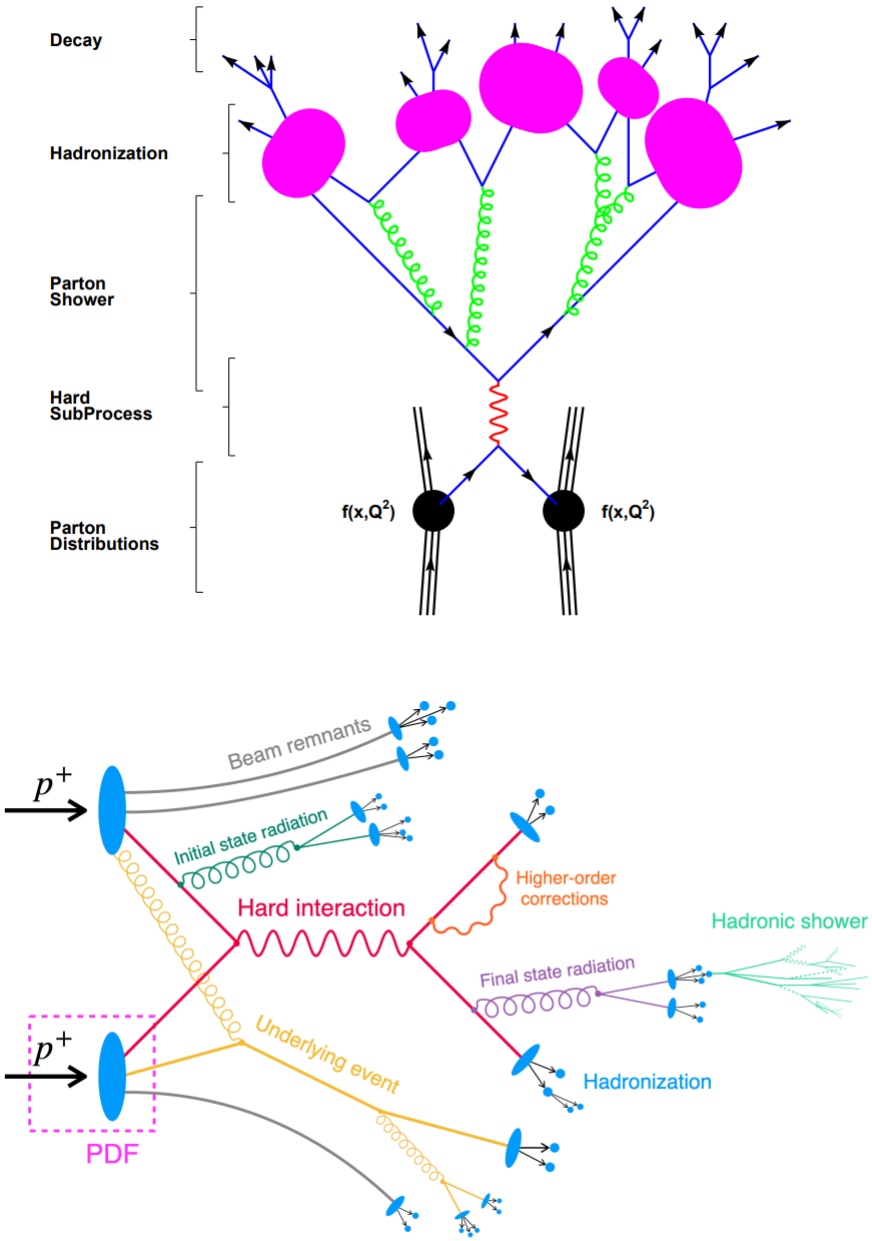

Figure 2.9 – An illustration of the structure of a proton-proton collision. Top: An overview of the various stages of the collision starting from the incoming protons to the final decays. Bottom: The various elements of the hard scatter process in a hadron collision. Adapted from Ref. [81, 85].

UE produces soft hadrons which contaminate and overlie the hard event. The remains of the proton which are not 'pulled out' during the scattering are called the $beam\ remnants$. They continue to travel in the original direction and carry the remainder of the energy and colour difference.

• Parton showers: The partons entering and exiting the hard scattering event can radiate gluons via QCD Bremsstrahlung. A high energy emission associated with the incoming parton is called initial-state radiation (ISR) and for the outgoing parton is called final-state radiation (FSR). These gluons can radiate further and also split into quark-antiquark pairs, thus creating a cascade of partons called a $parton\ shower$. The original hard partons are thus dressed with clusters of QCD radiation which can eventually form into QCD jets.

• Hadronization: As the partons recede from each other, confinement forces become significant and the quarks and gluons transform into color-neutral hadrons. This step is called $hadronization$ or $jet\ fragmentation$. Many of these hadrons are unstable and decay further at various time-scales. These decays can be visible to the detector and the information from these final states can be used to reconstruct what happened during the core process.

3

Experimental Apparatus

This chapter covers an overview of the Large Hadron Collider (LHC) and the ATLAS experiment. The experimental setup outlined in this chapter is taken primarily from the ATLAS Technical Design Report [86].

3.1 The LHC

Located in an underground tunnel near Geneva, Switzerland at the foothills of the Jura mountains is the Large Hadron Collider (LHC) [87]. The LHC is a two-ring superconducting hadron accelerator with a circumference of 26.7 km. It rests 100m below the ground and accelerates two counter-rotating beams of protons. The accelerator is the world's most powerful and is designed to collide protons at a centre-of-mass energy $\sqrt{s}$ of 14 TeV. The beams collide at four experiments positioned along the LHC ring: ALICE, LHCb, CMS and ATLAS.

Electric and magnetic fields play a key role in operating the LHC. The dynamics of charged particles in an electromagnetic field are described by the Lorentz-Newton force

$$\overrightarrow{F} = e(\overrightarrow{E} + \overrightarrow{v} \times \overrightarrow{B}), \tag{3.1}$$

where e is the particle charge, $\overrightarrow{E}$ is the electric field, $\overrightarrow{v}$ is the instantaneous velocity of the particle and $\overrightarrow{B}$ is the magnetic field. The electric field is used to accelerate the particles and is parallel to the direction of motion. The magnetic field controls the transverse motion of the particles and is perpendicular to the direction of motion. This setup at the LHC of using electromagnetic fields to steer beams

of opposing particles to provide colliding beam experiments is significantly more advantageous than the alternative of fixed target experiments. This can be seen when comparing the center-of-mass energies of two colliding beams. For equal mass particles of momentum p and energy E, the energy of the system is given by [33]:

$$E_{cm} = \sqrt{s} = \sqrt{(E_1 + E_2)^2 - (\vec{p_1} + \vec{p_2})^2} \tag{3.2}$$

For a fixed target experiment, $\vec{p_2} = 0$ and the expression reduces to $\sqrt{s} = \sqrt{2m^2 + 2E_1 m}$. For a colliding experiment, $\vec{p_1} = -\vec{p_2}$ and the expression becomes $\sqrt{s} = E_1 + E_2$. Thus, despite being more challenging, the LHC configuration provides $\sqrt{s}$ equal to 2 times the beam energy, while for a fixed target arrangement the collision energy goes as $\sqrt{2E_{beam}}$.

At the start of the LHC acceleration chain is a metal cylinder filled with hydrogen gas. The hydrogen molecules are passed to a machine called the duoplasmatron which is surrounded by an electric field that is used to strip off their electrons. The resulting protons are then accelerated to an energy of 50 MeV by radio-frequency (RF) cavities in a linear accelerator called LINAC2. LINAC2 is made of cylindrical conductors which are alternately charged positive or negative. As the protons pass through them, they are pushed by the conductors behind and pulled by the conductors ahead [88,89].

Next, the beam of protons is injected into the Proton Synchrotron Booster (PSB) which accelerates them to an energy of 1.4 GeV. In the PSB, proton "bunches" are formed as the protons are made to synchronize with the RF cavity acceleration frequency. The bunches are then sent to the Proton Synchrotron (PS) where they are arranged into trains to be accelerated to an energy of 26 GeV. The next step is the Super Proton Synchrotron (SPS) which is the second-largest machine in the accelerator complex. It provides both clockwise and anticlockwise-circulating bunches to the LHC at 450 GeV. Lastly, the proton beams are brought to an energy of 6.5 TeV inside the LHC ring (during Run-2 this was the maximum energy achieved). The proton beams can contain up to 2808 bunches with 10^{11} protons in each bunch. The beams have a bunch spacing of 25 ns, producing the collision

frequency of 40 MHz [72, 90].

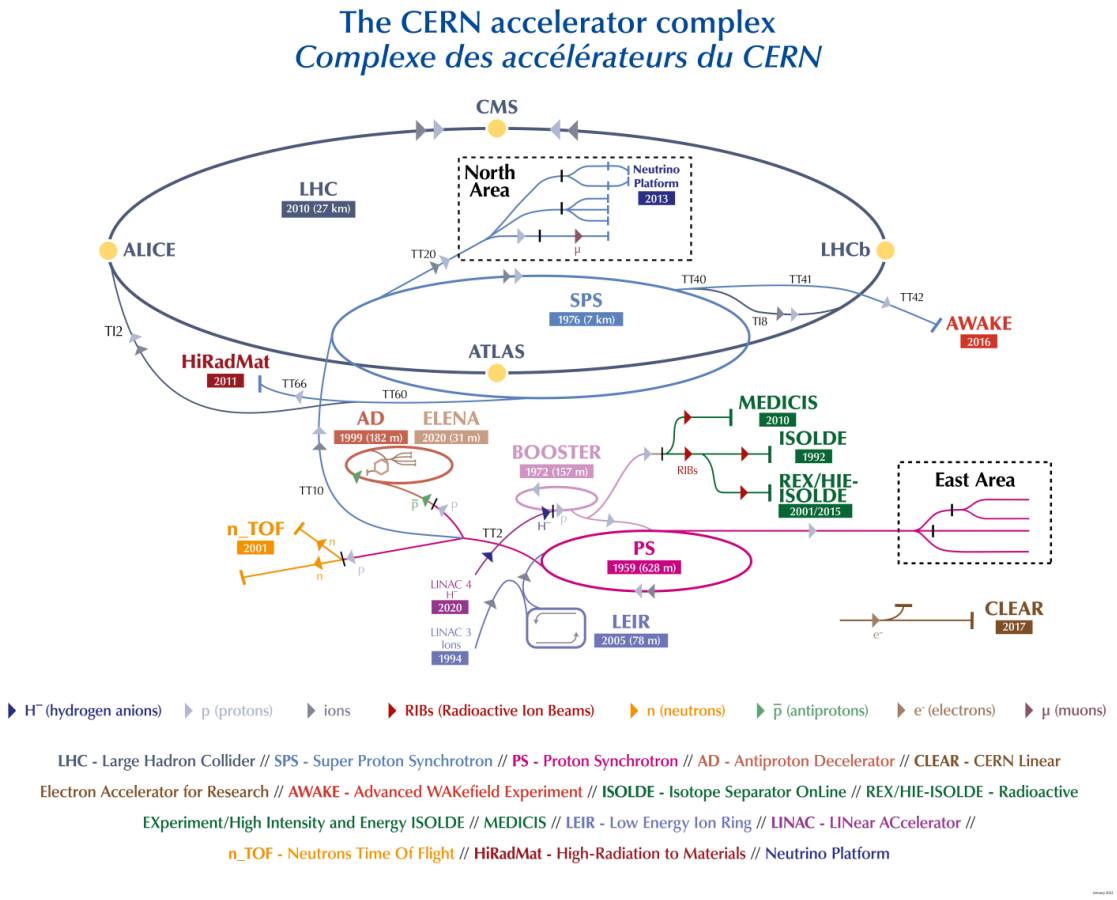

Figure 3.1 – The acceleration chain for protons at the LHC [72].

Once the LHC is filled, magnets are used to steer the beams and keep them in orbit. The LHC superconducting magnets operate at 1.9 K and produce a magnetic field of 8.3 T. There are 1232 dipole magnets which bend the beams and keep them in their circular path. Additionally, 392 quadrupole magnets are used to focus them. The beam pipes are about 3 cm in diameter and under a ultrahigh vacuum (10^{-13} atm) to prevent protons from colliding with particles outside the designated points. As the beams circulate over the course of a run, the luminosity degrades since the number of protons in each bunch decreases due to collisions. They are thus eventually dumped and refilled in order to ensure the luminosity requirements are maintained.

3.2 The ATLAS Experiment

ATLAS (A Toroidal LHC ApparatuS) is a general purpose detector designed to identify and measure the momenta and energies of particles produced in proton-proton collisions at the LHC [86]. It is the largest detector on the LHC ring, having a diameter of 25 meters, a length of 44 meters and weighing 7000 tons.

The detector has a cylindrical geometry with collisions taking place at the center, referred to as the Interaction Point (IP). As particles produced in the collisions at the IP traverse the detector, they interact with the numerous sub-detector systems of ATLAS (shown in Figure 3.3). Through these interactions, the particles are identified and their properties measured and recorded. The ATLAS detector can generally be categorized into three parts: the Inner Detector, the Calorimeters and the Muon system. As searching for the $H^+ \to WA$ process involves studying muons, electrons and jets in the final state, all these components play a vital role for the analysis. A brief description of the various components of the detector is below.

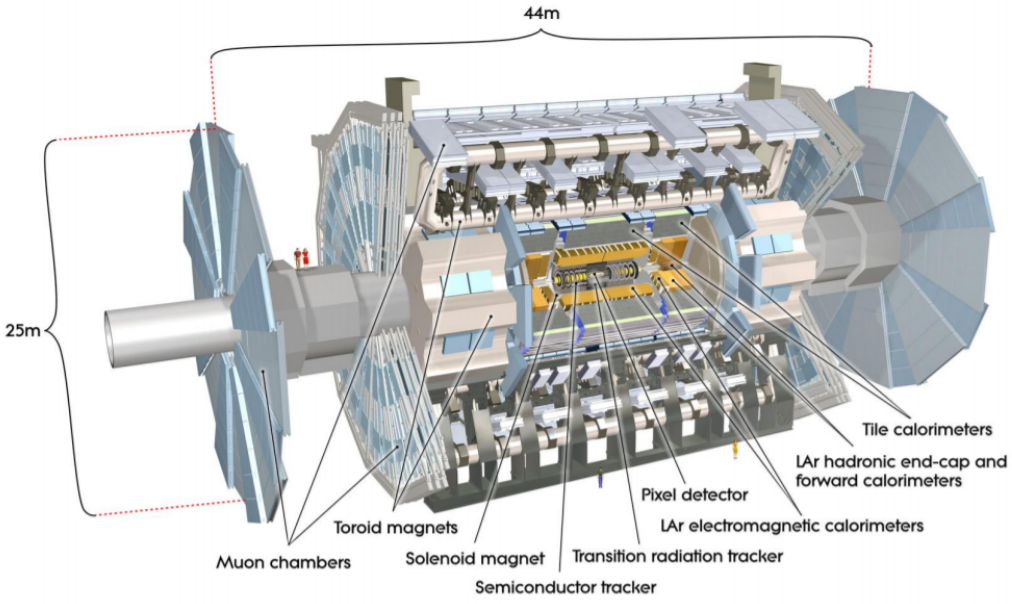

Figure 3.2 – A schematic of the ATLAS detector [86].

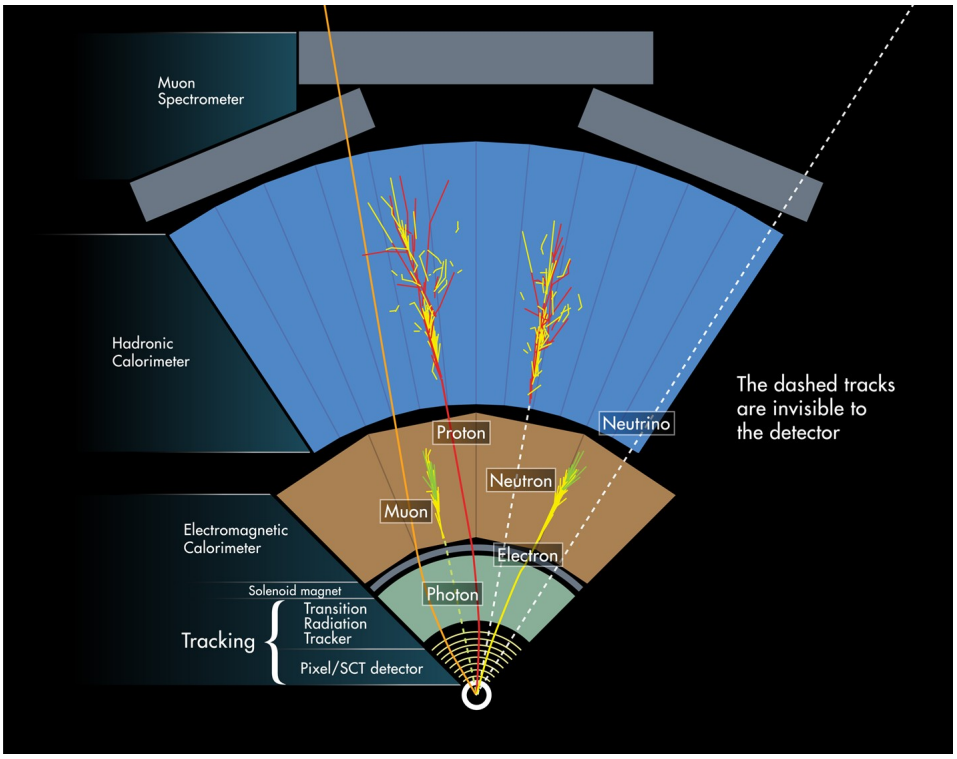

Figure 3.3 – The trajectories of particles as they traverse through the subsystems of the ATLAS detector [91].

3.2.1 Coordinate System

ATLAS uses a right-handed coordinate system as shown in Figure 3.4. The origin is at the nominal interaction point (IP) in the center of the detector and the z-axis is along the beam pipe. The x-axis points from the IP to the center of the LHC ring, and the y-axis points upwards towards the surface. Cylindrical coordinates (r, ϕ) are used in the transverse plane, ϕ being the azimuthal angle around the z-axis. Transverse quantities are used as visible p_z is not conserved while visible p_T is conserved to a good approximation (recall the interactions happen between partons whose full initial state is not known exactly). The pseudorapidity represents the angle with respect to the axis of the colliding beams. It is defined in terms of the polar angle θ as

$$\eta = -\ln \tan(\theta/2). \tag{3.3}$$

A value of $\eta = 0$ denotes particle trajectories perpendicular to the beam and η approaches infinity for trajectories parallel to the beam. Angular separation between particles is measured in units of ΔR defined as

$$\Delta R \equiv \sqrt{(\Delta\eta)^2 + (\Delta\phi)^2}. \tag{3.4}$$

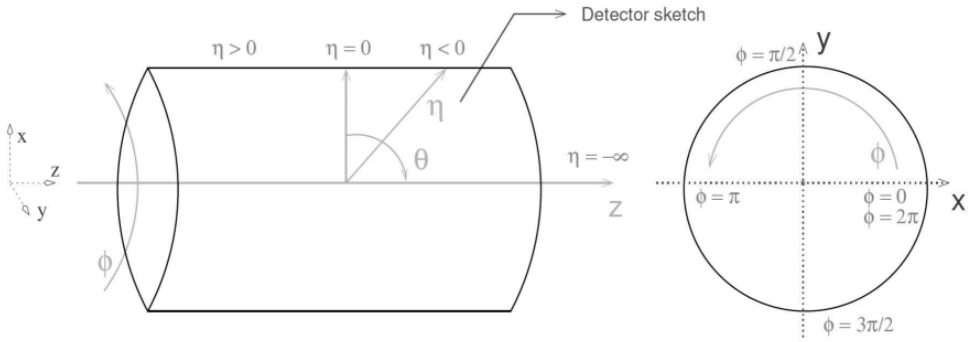

Figure 3.4 – The coordinate system of the ATLAS detector [92].

3.2.2 Inner Detector and Solenoid

The inner detector (ID) [93,94] is the inner most part of the ATLAS detector and closest to the IP. It consists of four detector systems: insertable B-layer (IBL), pixel detector, semiconductor tracker (SCT) and transition radiation tracker (TRT). The ID is designed to measure the momenta of charged particles, their trajectories (tracks) and identify the location of the interaction vertices. Since about a 1000 particles emerge from the collision point every 25 ns, the detector is designed to operate in a very large track density environment. It has a cylindrical geometry (Figure 3.5) with a diameter of 2.1 m and a length of 6.2 m. The design track momentum resolution for the ID degrades with p_{T} and is given by $\frac{\sigma_{p_{\mathrm{T}}}}{p_{\mathrm{T}}} = 0.05\% p_{\mathrm{T}}$ (GeV) $\oplus 1\%$, where $\oplus$ denotes a sum in quadrature. The transverse impact parameter resolution is 10 μm.

The ID is surrounded by a superconducting solenoidal magnet [95] providing a 2T axial field which bends the particle tracks in the ϕ direction. Operating a

temperature of 4.5 K, it is 5.8m long in the direction of the beam-line with a diameter of 2.5m. As charged particles move inside the magnetic field, their tracks curve with a radius of curvature proportional to their momentum and inversely proportional to their electric charge. Using the charge, momentum and track information, the particle can be identified and its interaction vertex can be reconstructed. For a particle with Lorentz factor γ moving in the transverse plane with a radius of curvature R and a magnetic field B, the transverse momentum p_T is given by:

$$\begin{aligned} F &= qvB, \\ \frac{\gamma m v^2}{R} &= qvB, \\ p_T &= qBR. \end{aligned} \tag{3.5}$$

The IBL, pixel and SCT are silicon-based solid-state detectors and work based on the excitation of pn-junctions in silicon. As charged particles traverse the semiconductor detector, they ionize valence electrons in the material and electron-hole pairs are created. Under the application of an electron field, these pairs drift towards the strip or pixel readout elements and generate a hit signal. The current generated depends on the energy of the incoming particle and higher momentum particles deposit more energy [72, 96, 97].

IBL The IBL [98] is the sub-detector that is closest to the interaction point. It was introduced during the first LHC shutdown due concerns of radiation damage to electronics in the inner most layer for Run-2 which was to have twice the instantaneous luminosity. This insertable layer helps minimize the risk of damage and improves the tracking and vertexing performance for the new run. It is positioned at an average radial distance of 35.7 mm and covers 332 mm on each side from the center in the z-direction. The IBL is made up of 14 staves instrumented with planar and 3D silicon pixel sensor technology. The staves are grouped around the beam axis, arranged in turbine like fashion with an overlap in ϕ [99].

Pixel Detector Immediately after the IBL lies the silicon pixel detector. It is made of 3 cylindrical layers positioned at radial distances of 50.5 mm, 88.5 mm and

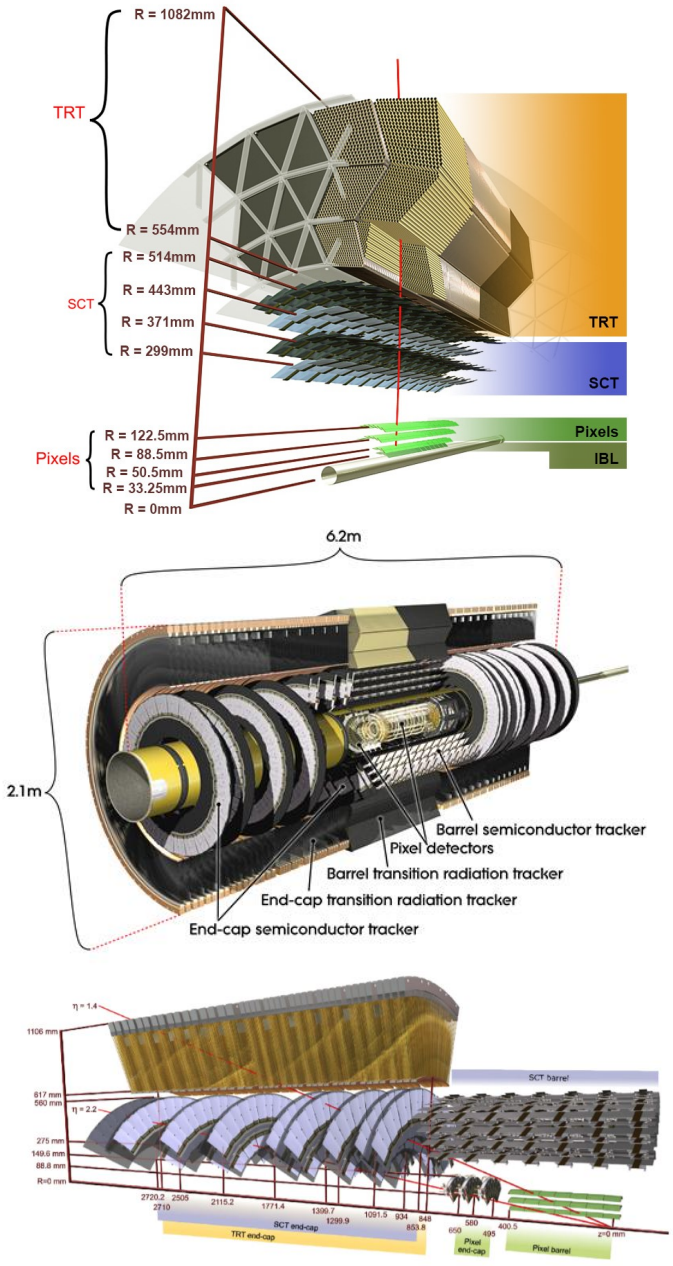

Figure 3.5 – The cross sectional views of the different subsystems in the Inner Detector [99–101].

122.5 mm, and two end caps which have three disks each. The detector consists of 1744 silicon pixel modules; each module covers an active area of 16.4 mm $\times$ 60.8 mm and contains 47 232 pixels, most of size 50 μm $\times$ 400 μm. The detector

provides high granularity measurements for vertex reconstruction and has a hit resolution of 10 μm ($R-\phi$) x 115 μm (z) in the barrel [94].

SCT The semiconductor tracker is made of silicon strips with a geometry similar to the pixel detector. It consists of 4088 modules arranged in four concentric cylindrical layers and two endcaps with nine disks each. The detector spans radial distances from 299 mm to 560 mm and provides coverage of $|\eta| < 2.5$; most SCT module consists of four silicon-strip sensors. Its operation principle is similar to the pixel detector but the design includes long strips of silicon rather than a pixelated structure. As a result, it has a lower precision of 17 μm ($R-\phi$) $\times$ 580 μm (z).

TRT The Transition Radiation Tracker is the outer most subsystem of the inner detector and operates as a drift chamber. Its unique design provides both tracking capability and particle identification based on transition radiation (TR). TR is released when a highly relativistic charged particle ($\gamma \geq 10^3$) crosses the boundary between materials with different dielectric constants. The TRT is made of about 300,000 straw drift tubes of 4 mm diameter filled with a Xenon-based gas mixture. It covers radial distances from 563 mm to 1066 mm and has a track resolution of 130 μm ($R-\phi$). In the centre of each tube is a 31 μm gold-plated tungsten wire, at ground potential, acting as the anode while the walls are kept at -1.5 kV. The space between the drift tubes is filled with polypropylene fibres which acts as the radiator material and allows for the emission of TR photons [102].

When a charged particle traverses the straws, it ionizes the gas and produces ionization charges (electrons and ions). A signal, proportional to the amount of ionization, is produced when the charges drift towards the anode wire due to the strong electric field. The signal is discriminated against two thresholds; a low threshold (LT) of about 300 eV is used for tracking purposes and a high threshold (HT) for particle identification of 6 -7 kV. Relativistic electrons emit TR as they traverse through the detector which is absorbed by the Xenon gas and produce additional ionization; this results in a larger signal associated with electrons and is used to distinguish them from heavier pions [103].

3.2.3 The Calorimeter System

The ATLAS calorimeter system is designed to measure the energy of the particles produced at the IP. It is made up of the electromagnetic (ECAL) and hadronic calorimeters (HCAL), shown in Figure 3.6. The ECAL measures the energy of electrons and photons while the HCAL measures energies of hadrons. Unlike the tracking detectors which aim to make a measurement without disturbing the trajectories of the particles, the calorimeter is designed to stop and fully absorb the incoming particle. The absorption of the particle generates a signal in the detector which is calibrated such that its energy can be inferred.

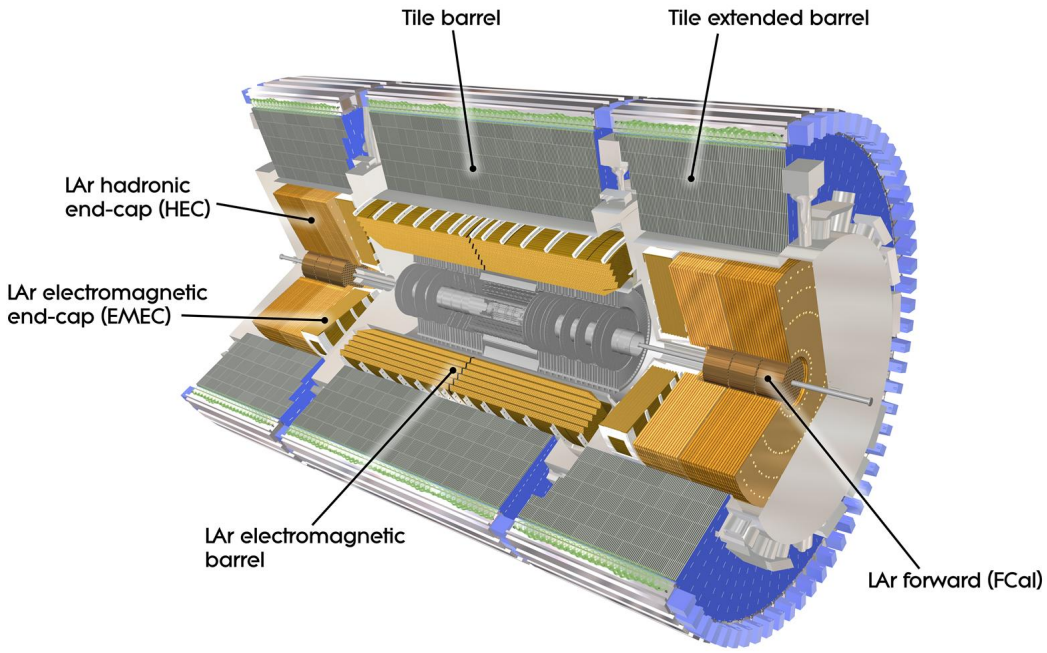

Figure 3.6 – A cross-sectional diagram of the ATLAS calorimeter system highlighting the electromagnetic and hadronic sub-systems [86].

Sampling calorimeters are used in the ATLAS design which are made of alternating layers of absorbing and active material. Incident particles will interact with the dense absorber material that degrade its energy and produces a cascade of secondary lower energy particles (showers) which ionizes the active medium. The energy deposited by these showers is longitudinally "sampled" at regular in-

tervals in the active region which is instrumented and thus provides a detectable signal [104]. A description of the ECAL and HCAL is below.

Electromagnetic calorimeters The EM calorimeter is a sampling lead-liquid Argon (LAr) calorimeter and provides coverage in the barrel ($|\eta| < 1.475$) and endcap ($1.375 < |\eta| < 3.2$) regions [105]. It uses lead as the absorber material and liquid argon (LAr) as the active material. LAr is used because of its linear response behaviour, stability of response over time and intrinsic radiation- hardness. The absorbing and active layers are interleaved and organized in an accordion−like geometry which allows for complete coverage in ϕ (Figure 3.7); the absorber plates are about 1.5 mm in thickness. The ECAL is divided into the EM barrel calorimeter (EMB) and the endcap calorimeters (EMEC). The EMB consists of two half barrels with a small gap of 4 mm at z = 0 while the EMECs are divided into two coaxial wheels; the outer wheel (OW) covers $1.375 < |\eta| < 2.5$ and the inner wheel (IW) covers $2.5 < |\eta| < 3.2$. The total thickness of EM calorimeter is > 22 radiation lengths (X_0) [1] in the barrel and > 24 X_0 in the end-caps. The relative energy uncertainty (or resolution) for the detector decreases with the energy (i.e. the resolution improves with E) and is given by $\frac{\sigma_E}{E} = \frac{10\%}{\sqrt{E(\mathrm{GeV})}} \oplus 0.7\%$.

Incident particles generate EM showers in the absorber material which ionizes the LAr. The ions and electrons then drift due to the influence of the electric field between the grounded absorber and the electrode, which are kept at a high-voltage potential. The electrons induce a triangular pulse on the electrodes that is measured. The height of the induced pulse is proportional to the energy deposited, while the arrival time of the incident particle can be inferred from the pulse peaking time. In the barrel for example, the size of the drift gap on each side of the electrode is 2.1 mm and this gives an electron drift time of about 450 ns for a nominal voltage of 2000 V. The calorimeter can provide good discrimination between photons and jets with a leading π^0, which decays primarily to a photon pair. It can also reconstruct the direction of neutral particles, such as unconverted photons, for which the ID can't be used [105].

1. The energy of the incoming particles decreases exponentially with $E(x) = E_0 e^{-x/X_0}$, where X_0 is the radiation length and represents the average distance over which a high energy electron loses $1/e$ of its original energy via Bremmstrahlung.

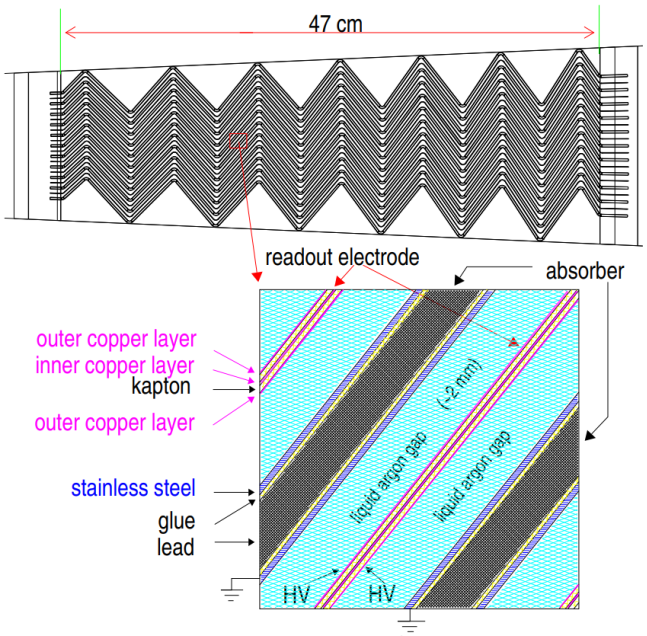

Figure 3.7 – Schematic of the EMCAL showing accordion−like geometry [105].

Hadronic Calorimeters The HCAL measures the energy of hadrons (made of coloured particles) that produce hadronic showers through inelastic strong interactions with the nuclei of the detector material. These showers are more complicated and contain many particles such as pions, neutrons and kaons. The neutral pions decay into photons which can induce electromagnetic cascades; hadronic showers thus have both an electromagnetic and hadronic component. They are characterized by the interaction length λ which is much longer for a material than its radiation length X_0, and are thus more diffuse than EM showers. The HCAL surrounds the ECAL and is designed to contain these complex showers in order to make the energy measurement. It is made of three subsystems: the tile calorimeter in the barrel, two hadronic end-cap calorimeters (HEC) and two forward calorimeters (FCal).

• The tile calorimeter covers up to $|\eta| < 1.7$ and uses steel as the absorber and scintillating plastic tiles as the active material. It radially extends from an inner radius of 2.28 m to an outer radius of 4.25 m; the radial depth is approximately 7.4 interaction lengths (λ). The modules of the detector (64 in total) are assembled in a periodic steel-scintillator structure as shown in Figure 3.8; the scintillator tiles

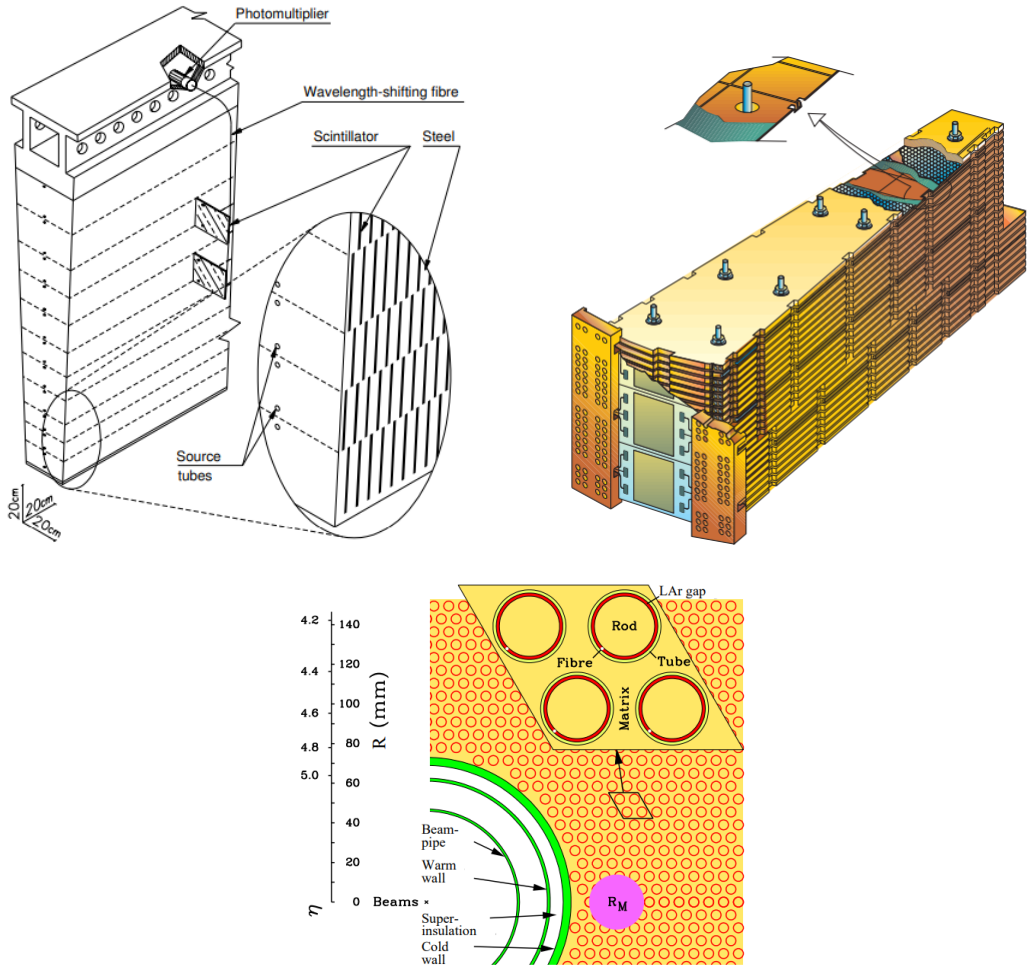

Figure 3.8 – Different parts of the hadronic calorimeter are shown: a module of the tile calorimeter (top left), a wedge of the HEC (top right) and a module of the FCal (bottom) [86].

are 3mm thick and are separated by 14 mm steel plates. Wavelength shifting fibres attached to two separate photomultiplier tubes are used to readout the scintillator tiles. As a hadron passes through the scintillating tiles, ultraviolet light is emitted which is optimized for detection by the wavelength shifting guides. The light travels to photo-multiplier tubes where it is converted to an electric signal which allows for the energy measurement [106, 107].

- The LAr Hadronic End-cap Calorimeter (HEC) is made of two independ-

ent wheels at each end-cap and is situated behind the EMECs as shown in Figure 3.6. It covers the region $1.5 < |\eta| < 3.2$ and uses copper plates as the absorber material that are interleaved with 8.5 mm liquid argon gaps which serve as the active medium. Each of the HEC wheels consists of 32 identical wedge-shaped modules, shown in Figure 3.8. The wheels closest to the IP are made of 25 mm parallel copper plates, while 50 mm copper plates are used for those further away. The inner radius of the copper plates is 0.475 m while the outer radius is 2.03 m [108].

• The LAr Forward Calorimeter (FCal) covers the region $3.1 < |\eta| < 4.9$ and is located at a distance of approximately 4.7 m from the interaction point. It is designed to measure both electromagnetic and hadronic energy in this region. The FCal is made of three modules in each end-cap: the first is made of copper and is optimized for EM measurements, while the last two are made of tungsten and predominantly measure the energy of the hadronic interactions. Each module is parallel to the beam pipe and consists of an absorber matrix with cylindrical electrodes extending its full length (≈ 45 cm). These electrodes have a "rod" (anode) inside a "tube" (cathode) with a narrow annular gap between the two, as seen Figure 3.8. This gap is filled with LAr which is the active medium. The total depth of the FCal is about 10 interaction lengths [109].

The design resolution for the HCAL in the barrel and end cap is $\frac{\sigma_E}{E} = \frac{50\%}{\sqrt{E(\mathrm{GeV})}} \oplus 3\%$, while in the forward region it is $\frac{\sigma_E}{E} = \frac{100\%}{\sqrt{E(\mathrm{GeV})}} \oplus 10\%$.

3.2.4 The Muon Spectrometer and Toroidal Magnets

The muon spectrometer (MS) [110] is the outermost part of ATLAS and serves to trigger on muons and measure their tracks. Muons are about 200 times heavier than electrons and very penetrating, they do not create showers in the calorimeters and thus deposit very little energy in them. The MS is thus placed after the calorimeters and works as a tracking detector to identify muons. Its subsystems are made of gas ionization detectors - muons ionize the gas as they traverse through and this results in the ionized charges drifting under an electric field to electrodes which register a signal. Toroidal magnets deflect the muon tracks in the $R-z$ plane; the curvature of the tracks is used to infer the transverse momenta

of the particles. Tracks from the MS can be extrapolated and matched with tracks in the inner detector for muon reconstruction and identification.

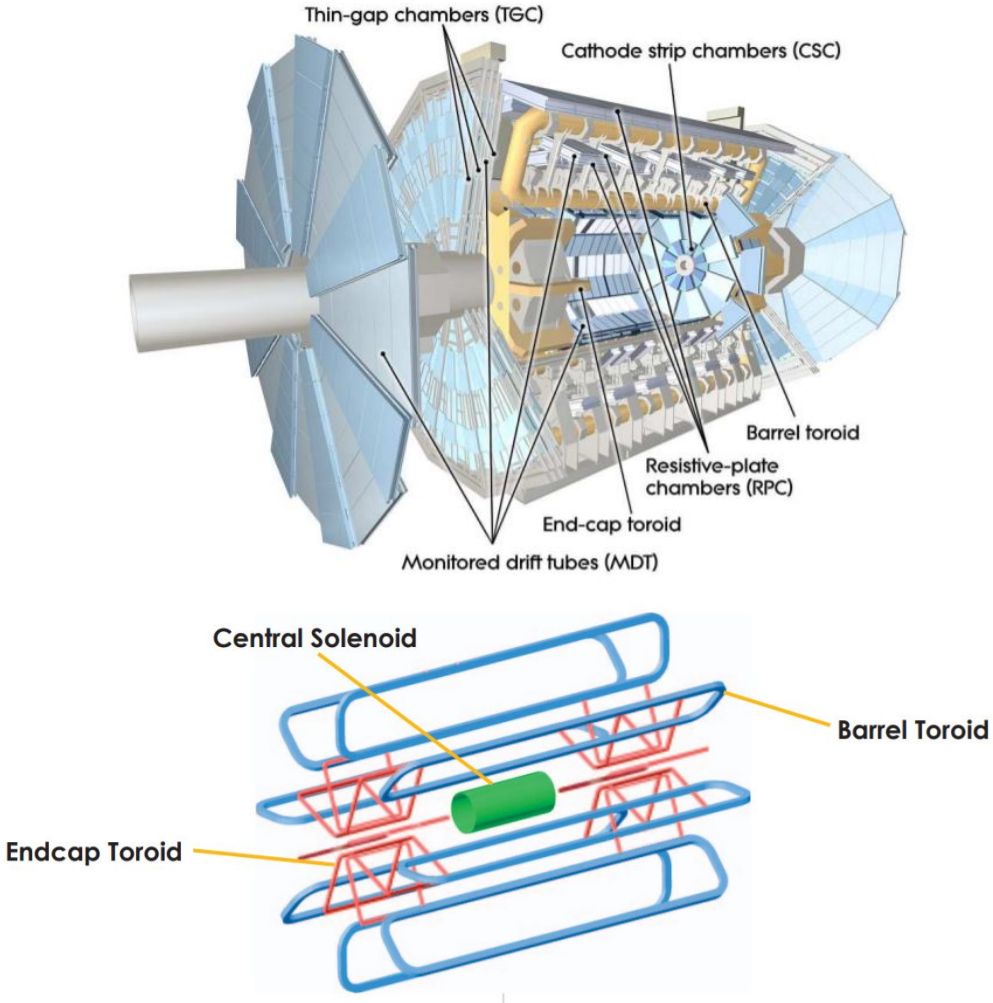

Figure 3.9 – A cut-away showing the various parts of the ATLAS muon spectrometer (top) and a layout of the magnet system of the detector (bottom) [86, 111].

The subsystems of the MS, referred to as 'chambers', can be divided based on their functionality: precision tracking or triggering. The precision-tracking chambers are designed to determine the coordinate of the muon tracks in the bending plane. A set of precision chambers with three stations of Monitored Drift Tubes (MDT's) [112] perform momentum measurement for $|\eta| < 2.7$ and have an average

track resolution of 35 μm. Each chamber consists of 3 to 8 layers of drift tubes that have a diameter of 30mm and are kept at a pressure of 3 bar. At large pseudo-rapidities ($2 < |\eta| < 2.7$), tracking is provided by the Cathode Strip Chambers (CSC's) [113]. The CSC's replace the MDT's in the inner-most endcap layer where their performance degrades due to high background conditions. CSC's are multi-wire proportional chambers with a high granularity and a resolution of 40 μm.

The trigger chambers of MS complement the tracking chambers and provide capability to trigger on muon tracks. The Resistive Plate Chambers (RPC's) [114] are used in the barrel and cover $|\eta| < 1.05$, while Thin Gap Chambers (TGC's) [115] are employed in the end-caps and cover $1.05 < |\eta| < 2.4$. RPC's are gaseous parallel electrode-plate detectors while the TGCs are multiwire chambers. They have a high timing resolution and can deliver track information within tens of nanoseconds after the particle traverses the detector; this allows for the ability to tag the beam-crossing. The RPCs and TGCs measure both coordinates of the track i.e. in both the bending (η) and non-bending (ϕ) planes.

The magnetic field in the MS is provided by superconducting air-core toroid magnets; one in the barrel and two in the end-cap as shown in Figure 3.9. They produce a field of 0.5 T in the central region and 1 T in the end-cap region. The barrel toroid is made of eight individual coils with a length of 25.3 m, and inner and outer diameters of 9.4 m and 20.1 m respectively; this makes it one of the largest superconducting magnet systems ever built. The system provides magnetic fields in the ϕ direction and bends the muons trajectories in the $R - z$ plane.

The layout of the MS is shown in Figure 3.9. In the barrel, the chambers are divided into three concentric circles around the beam line and are located at radii of approximately 5 m, 7.5 m, and 10 m. In the two end-caps, the chambers are perpendicular to the beam direction and form large wheels which are located at $|z| \approx$ 7.4 m, 10.8 m, 14 m, and 21.5 m from the interaction point. The momentum resolution of the MS is given by $\frac{\sigma_{p_T}}{p_T} = 10\%$ at p_T = 1 TeV.

3.2.5 Trigger and Data Acquisition

The ATLAS Trigger and Data Acquisition (TDAQ) system is responsible for the selection and storage of physics events arising from pp collisions. With bunches crossing every 25 ns and several dozen pp collisions happening in each crossing (pile-up), a collision rate of about 1 billion (10^9) per second is expected. It is thus not feasible (or useful) to permanently record every event. Most events are low-energy inelastic collisions that contain known physical processes. The trigger system is thus designed to make quick decisions about which events should be stored and potentially contain the rare processes which the experiment is built to search for.

The ATLAS trigger system is able to reduce the raw event rate from the LHC of 40 MHz down to 1.2 kHZ which is written out for physics analyses [116]. It is made of a two-level trigger system: the Level-1 (L1) Trigger and High-level Trigger (HLT). For an event to be permanently recorded by ATLAS, it has to pass the requirements of both the L1 and HLT triggers.

Level-1 The L1 trigger is hardware-based and uses a subset of detector information to reduce the event rate from 40 MHz to about 100 kHz. It is able to make decisions in less than 2.5 μs; only a few parts of the detector can read out information at such a fast rate. The L1 system looks for high p_{T} muons, electrons, photons, jets, hadronically decaying τ-leptons, as well as large missing and total transverse energy. The sub-systems of the trigger rely on information from the calorimeters (LICalo) and the muon detectors (L1Muon). LICalo selections use granularity information from the ECAL and HCAL, while the L1Muon uses hit information from the RPCs and TGCs [117].

High Level Trigger The HLT is a software-based trigger which uses complex algorithms to further reduce the data rate from 100 kHz to about 1 kHZ, with an average physics throughput to permanent storage of 1.2 GB/s. The HLT objects such as jets and leptons are only reconstructed after the L1 trigger has accepted an event. Dedicated trigger algorithms are executed on a computing farm of approximately 40,000 selection applications called Processing Units (PUs); these PUs can make decisions within a few milliseconds [116].

The collection of all the L1 and HLT triggers is called the trigger menu [117]. This menu is made of various combinations of trigger configurations referred to as trigger chains. These chains are made of an L1 trigger item and a series of HLT algorithms that reconstruct physics object and require kinematic cuts on them. The trigger chains follow a specific naming scheme which allows for easy identification of the event selection criteria. For example, the chain HLT_2MU14_L12MU10 requires at least two muons with $p_{\mathrm{T}} \geq 10$ GeV identified by the L1 trigger, followed by a requirement of at least two $p_{\mathrm{T}} \geq 14$ GeV muons from the HLT.

4

Statistical Methods and Fitting Techniques

Profile likelihood fits are an effective method to incorporate systematic uncertainties as part of a likelihood fit. They are ubiquitous today in particle physics analyses at the LHC. This analysis exploits their power for the purposes of background modeling, hypothesis testing and evaluation of uncertainties. Described in this chapter are the fitting techniques and statistical methods used in this search. The material presented here is taken primarily from Ref. [33, 118–127].

4.1 Probability Models and Likelihood

In order to make a quantitative assessment about the existence of a new particle, statistical tests are constructed that allow one to make probabilistic statements on the observed data. The probability model is the center piece of statistical inference and assigns a probability to each possible outcome of an experiment. A simple example in particle physics is the Poisson model which describes a counting experiment

$$P(N|\nu) = \frac{\nu^N e^{-\nu}}{N!}. \tag{4.1}$$

This model defines the probability of observing N events for a random process in a fixed time interval given the hypothesis ν which represents the number of expected events. The notation $P(N|\nu)$ can be verbalized as "the probability of N given ν". Given ν, the Poisson distribution fully specifies the probability of each possible outcome of a counting experiment. The model is one of the most common in particle physics as it describes the outcomes of a counting analysis

with any type of event selection. For example, the probability to observe 7 events in a counting experiment under the background-only hypothesis of ν = 3 and a signal+background hypothesis of ν = 7 is given by:

$$\begin{aligned} P(N|H_{\text{bkg}}) &= 0.022, \\ P(N|H_{\text{sig+bkg}}) &= 0.149. \end{aligned} \tag{4.2}$$

The statement $P(N = 7|H_{S+B}) = 0.15$ is interpreted to mean that 15 % of future counting experiments can expect to give $N = 7$ under the assumption of the signal + background hypothesis. In general, the hypothesis H specifies the probability $P(x|H)$ for each data outcome of an experiment x. If the data x is considered to be fixed, then the probability to observe it is regarded as a function of the hypothesis H, and the equation is called the $Likelihood$ of H denoted by $L(H)$. The hypothesis is often characterized by a number of parameters θ in which case $L(\theta) = P(x|\theta)$ is called the likelihood function and it describes how probable the observed data is for different values of θ [33, 124].

Many particle physics analyses are not counting experiments but involve studying the distributions of an observable. Thus, a probability model has to be built for the whole distribution. While in some cases the distributions of an observable can be determined analytically from first principles, they are derived from simulations in most analyses. The outcome of these simulations are histograms describing the observables of interest. An example of a Monte Carlo simulation (MC) prediction for a fictitious signal and background process is shown in Figure 4.1. The statistical model for a binned distribution, such as the one shown, is effectively a series of counting experiments that can be described with a Poisson distribution for each bin:

$$L(\vec{N}|H_B) = \prod_i \text{Poisson}(N_i|b_i), \tag{4.3}$$

$$L(\vec{N}|H_{S+B}) = \prod_i \text{Poisson}(N_i|s_i + b_i), \tag{4.4}$$

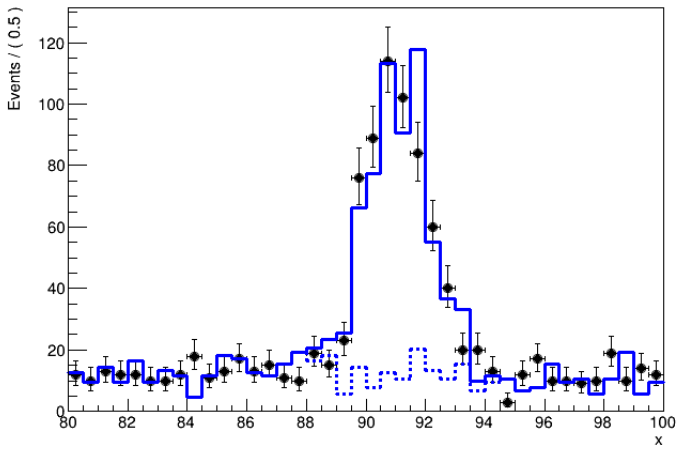

Figure 4.1 – Expected binned distribution of an observable x under the background and signal+background hypothesis, obtained from MC simulation [118].

where b_i and s_i are the predicted event counts for the background and signal process in bin i respectively. $L(\vec{N}|H_B)$ is the probability to observe the precise (binned) distribution of the recorded data under a given model [118].

In the case of a continuous variable, the concept of a probability model can be extended into the concept of a Probability Density Function (PDF), $f(x)$, where $\int f(x)dx \equiv 1$. The probability to observe an event in the observable range $a < x < b$ is then given by the integral $\int_a^b f(x)dx$. The term PDF can loosely refer to either the probability or the probability density [33].

4.2 Profile Likelihood Fits

To determine the probability of observing the $H^+ \to WA$ process, a statistical model needs to be built describing the expected distribution from signal and background processes in the observable being studied. If one measures a variable x and constructs a histogram from it, the expected event count in bin n_i of the

distribution can be written as [120]:

$$E[n_i] = \mu s_i + b_i, \tag{4.5}$$

where s_i and b_i are the mean number of entries from the signal and background processes in the phase space under study. The variable μ is the signal strength and the parameter of interest (POI), with $\mu = 0$ meaning the signal is turned off (background-only hypothesis), while $\mu = 1$ represents the nominal signal rate for the theory under consideration. The expected contribution from signal and backgrounds in the i_{th} bin is given by

$$\begin{aligned} s_i &= s_{tot} \int_{bin\ i} f_s(x)\ dx, \\ b_i &= b_{tot} \int_{bin\ i} f_b(x)\ dx, \end{aligned} \tag{4.6}$$

where $f_s(x)$ and $f_b(x)$ are the PDFs of the discriminating variable x for signal and background events. The total mean number of signal and background events are given by s_{tot} and b_{tot}. The model describing the data in this analysis is built from binned signal and background histogram distributions. The likelihood function can thus be written as the product of the Poisson probabilities in each bin:

$$L(\mu) = \prod_{j=1}^{N} \frac{(\mu s_j + b_j)^{n_j}}{n_j!} e^{-(\mu s_j + b_j)} \tag{4.7}$$

This model can be further improved by accounting for systematic uncertainties that affect the distributions being studied and assess their impact on the parameter(s) of interest. The prediction for the background and signal yields are subject to multiple sources of error, such as the Jet Energy Scale and trigger efficiency. These uncertain degrees of freedom are introduced into the model as new parameters $\vec{\theta}$, referred to as $nuisance\ parameters$ (NPs). The signal and background rates then become functions of the NPs i.e. $s(\theta)$ and $b(\theta)$, and the likelihood becomes $L(\mu) \rightarrow L(\mu, \theta)$. The model now describes the distribution of the observ-

ables for values of both μ and θ. Instead of the classical approach of studying the impact of the systematics on the POI by repeating the likelihood fit for each source of error separately, the uncertainties are now included in the model and are a part of the fitting procedure [128].

Information about the NPs is usually available from prior measurements, for example, from a calibration measurement for an experimental systematic uncertainty. A separate likelihood function $L_{subs}(\tilde{\theta}_{obs}|\theta)$ can be constructed to encode this information, where $\tilde{\theta}_{obs}$ represents the data of this $subsidiary\ measurement$, often done by a physics performance group, and θ is the NP representing the source of error. The updated model can be expressed as a joint likelihood of the original physics measurement L_{phys} and L_{subs} in the form [123, 125]:

$$\begin{aligned} L(\mu,\theta) &= L_{phys}(\text{data}|\mu,\theta) \times L_{subs}(\tilde{\theta}|\theta), \\ L(\mu,\theta) &= \prod_i \text{Poisson}(\text{data}|\mu s(\theta) + b(\theta)) \times p(\tilde{\theta}|\theta), \end{aligned} \tag{4.8}$$

where $data$ refers to the experimental observation or pseudo-data from a sampling distribution and $p(\tilde{\theta}|\theta)$ is the PDF of the auxiliary measurement. L_{subs} typically takes the form of a unit Gaussian. The θ parametrization is such that it is described by a normal distribution centered at $\theta^0 = 0$, with $\theta = \pm 1$ corresponding to one sigma up and down variations from the nominal value. Counting uncertainties, such as MC statistical uncertainties, are described by Poisson probability terms instead.

A commonly used approach to reduce the effect of systematic errors in LHC analyses is to constrain the NPs with data in background-enriched kinematic regions called $control\ regions$. The procedure of determining the best-fit values $\hat{\theta}$ of the NPs (written with a hat) using data is referred to as $profiling$ [122]. This approach can provide stronger constraints on θ for the phase space under study than the subsidiary measurement alone. As shown in Figure 4.2, the $\hat{\theta}$ are values of the parameters that maximize the likelihood function $L(\mu,\theta)$, or minimize the

negative log-likelihood:

$$-\frac{\partial \ln L}{\partial \theta}|_{\theta=\hat{\theta}} = 0. \tag{4.9}$$

The profiling procedure entails adjusting the probability model in a continuous way, in comparison with data, according to the effects of systematic uncertainties in order to yield a configuration that gives the best compatibility with the data. This can result in the NPs being 'pulled' from their nominal value of 0 or 'constrained' i.e. the estimated uncertainty on the NP can be less than 1 [128]. The behaviour of the fit can be investigated by looking at the $pulls$ of the NPs, defined as the difference between the true and measured value divided by the uncertainty [129]:

$$pull = \frac{\hat{\theta} - \theta_0}{\Delta\theta}, \tag{4.10}$$

where $\hat{\theta}$ is the best-fit value of the NP, θ_0 is the nominal value and $\Delta\theta$ is the estimated uncertainty.

In addition, it is also very useful to understand which systematic uncertainties have the largest impact on the final result. A $ranking$ of the NPs is thus generated for this purpose which highlights the impact of each uncertainty on the parameter of interest. The impact on the POI, $\Delta\mu$, due to an individual NP is calculated by fixing the parameter to its best-fit value and associated uncertainty. All other parameters are allowed to vary and the magnitude of the shift in the fitted μ, in comparison to a nominal fit, is a measure of the impact of the NP on the result [130]. Furthermore, it is useful to decompose the total uncertainty on the POI into its statistical and systematic components. The statistical uncertainty is obtained by doing the fit to data with the all the NPs fixed to their best-fit values. The total systematic uncertainty can then be determined by subtracting in quadrature the statistical uncertainty from the total uncertainty [31].

Finally, all this allows one to define the $profile\ likelihood$ as [119]:

$$L_p(\mu) = L(\mu, \hat{\hat{\theta}}(\mu)), \tag{4.11}$$

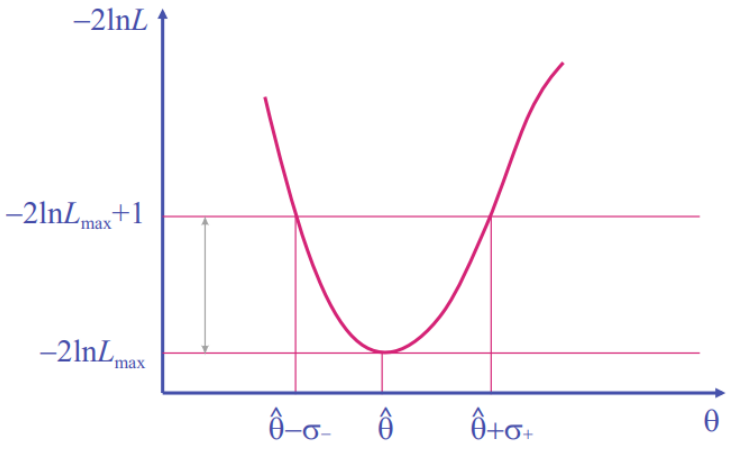

Figure 4.2 – Parameter estimation: The best-fit values of a parameter is determined by minimizing the negative log likelihood. The uncertainty interval can be found by looking around the minimum and finding the values where ln L increases by one unit (or n^2 for a $n\sigma$ interval). The error from this approach can be asymmetric if the curve is asymmetric [126].

where $\hat{\hat{\theta}}(\mu)$ are the best-fit values of θ for a specified value of μ, also called a conditional maximum likelihood estimate (MLE). Thus, the profile likelihood depends only on the parameters of interest μ and the NPs are replaced by their profiled values. This modified likelihood will be useful when constructing a test statistic for the purposes of hypothesis testing, as discussed in the following section. In high energy physics jargon, the joint likelihood of the form in Equation 4.8 with a normalized Gaussian term is generally referred to as the profile likelihood [125, 131].

4.3 Hypothesis Testing

A hypothesis test addresses the question of whether the observed data is consistent with the null-hypothsis (H_0) or an alternative hypothesis (H_1). A claim of discovery can be made when the data is found to be incompatible with the predictions of the model being tested. A p-value is calculated to quantify the degree of agreement of the data with predictions. It is the probability to obtain the observed data, or more extreme, under a given a hypothesis in future repeated experiments.

Using the same example as before, the probability to observe 7 events or more under the background prediction of μ = 3 in a Poisson counting experiment is given by the p-value

$$p(H_B) = \sum_{N=7}^{\infty} P(7|\mu = 3) = 0.23. \tag{4.12}$$

A hypothesis can be considered excluded if the p-value is found to be below a specific threshold. Low p-values correspond to high significance i.e. the smaller the p-value, the stronger the evidence that the hypothesis being tested should be rejected. In particle physics, a p-value of less than 2.87×10^{-7}, corresponding a 5σ significance, is need to reject the background-only hypothesis and claim discovery. To exclude a signal hypothesis, a p-value of 0.05 (i.e. 95% confidence level) is commonly used, corresponding to a significance of 1.64σ.

In addition to defining the H_0 (background-only) and H_1 (signal + background), a test statistic is needed for the purposes of hypothesis testing. A $test\ statistic$ is a variable computed from the data sample used to discriminate between the two hypotheses; it represents a 'summary' of the information available in the data [126]. It is a function of the data x and is often denoted by $t(x)$. In the previous examples, the event count was the test statistic (i.e. $t(x) = x$) used to discriminate between two hypotheses. When analyses are not counting experiments and one is working with distributions, a test statistic is needed to quantify if a histogram of the observed data is more extreme than another. A commonly used test statistic for this purpose is the likelihood ratio defined as:

$$t(x) = \lambda(x) = \frac{L(x|H_{S+B})}{L(x|H_B)}. \tag{4.13}$$

This is the optimal discriminator when comparing two hypotheses according to the Neyman–Pearson lemma [132]. The ratio λ orders the dataset according to signal extremity; it conventionally tends to have large values if H_{S+B} is true and small values if H_B is true. As the test statistic now maps the dataset x into a single number λ, the p-value is now an integral over the expected test statistic distribution. It is equal to the probability of calculating λ_{obs} or greater on the data events

and is given by:

$$p = \int_{\lambda_{\text{obs}}}^{\infty} f(\lambda|H_i)d\lambda, \tag{4.14}$$

where $f(\lambda|H_i)$ is the PDF representing the expected distribution of the test statistic λ under the hypothesis H_i.

In this analysis, hypothesized values of the parameter of interest μ need to be tested, but the statistical model also contains nuisance parameters θ. The likelihood ratio suitable in this case is called the $profile\ likelihood\ ratio$ defined as [120]:

$$\lambda(\mu) = \frac{L_p(\mu)}{L(\hat{\mu}, \hat{\theta})}, \tag{4.15}$$

$$= \frac{L(\mu, \hat{\hat{\theta}})}{L(\hat{\mu}, \hat{\theta})}. \tag{4.16}$$

The denominator is the maximized likelihood function where $\hat{\theta}$ and $\hat{\mu}$ are best-fit values (ML estimators) which are fit simultaneously. The numerator is the L_p defined earlier, with $\hat{\hat{\theta}}(\mu)$ being the value which maximizes the likelihood for the fixed value of μ under test. This ratio will be $0 \leq \lambda \leq 1$, with λ near 1 implying good agreement between the data and the hypothesized value of μ. It is thus useful to define test statistic for the search as:

$$t_\mu = -2 \ln \frac{L(\mu, \hat{\hat{\theta}})}{L(\hat{\mu}, \hat{\theta})}, \tag{4.17}$$

$$= -2 \ln \lambda(\mu). \tag{4.18}$$

The test statistic t_μ is used as a measure of discrepancy between the data and the hypothesis; higher values of t_μ represent increasing disagreement, in contrast to λ. The p-value quantifying the level of disagreement with data can now be

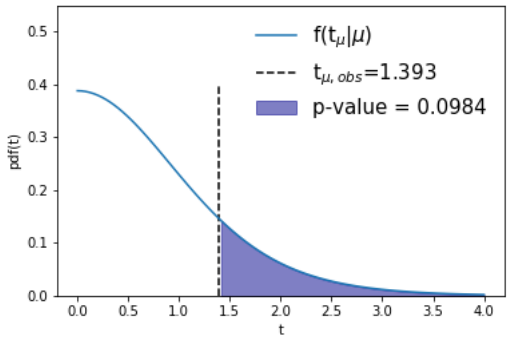

Figure 4.3 – An example distribution of a test statistic. The p-value is calculated as the integral from the observed value of t_μ to infinity [118].

defined as:

$$p_\mu = \int_{t_{\mu,obs}}^{\infty} f(t_\mu|\mu) dt_\mu, \tag{4.19}$$

where $t_{\mu,obs}$ is the observed value of the likelihood ratio calculated on the data events and $f(t_\mu|\mu)$ is the PDF of t_μ under the assumption of signal strength μ. An example distribution for $f(t_\mu|\mu)$ used for calculating p-values can be seen in Figure 4.3.

If one were to repeat the experiment many times, $t_{\mu,obs}$ would take on different values and it thus conceptually has a distribution that is encoded in $f(t_\mu|\mu)$. However, the sampling distribution of the test statistic is usually not known and needs to be determined in order to calculate the p-values (in contrast to the example earlier where the event count was the test statistic and its distribution was Poisssonion). One method to estimate these distributions is through conducting multiple pseudo-experiments with toy Monte Carlo simulations that randomize the number of observed events. However, this approach is computationally very expensive and takes a long time. As a result, a simplification is made using asymptotic formulas due to Wilk's theorem [133] which allows for the test statistic sampling distribution to be modelled as an analytic χ^2 distribution.

4.4 Limit Setting

In order to establish discovery of signal, the background-only hypothesis with $\mu = 0$ needs to be rejected. The test statistic then takes the form [120]:

$$q_0 = \begin{cases} -2\ln\lambda(0) & \hat{\mu} \geq 0, \\ 0 & \hat{\mu} < 0, \end{cases} \tag{4.20}$$

where λ is the profile likelihood ratio defined previously with $\mu = 0$. This equation simplifies to the following asymptotic form with sufficient data statistics:

$$q_0 = \begin{cases} \frac{\hat{\mu}^2}{\sigma^2} & \hat{\mu} \geq 0, \\ 0 & \hat{\mu} < 0, \end{cases} \tag{4.21}$$

where $\hat{\mu}$ is the best-fit value obtained by the log-likelihood minimization and it follows a Gaussian distribution with a mean μ' and standard deviation σ. Large values of q_0, obtained when $\hat{\mu}$ is increasing as a result of the event rate rising above the expected background, indicate incompatibility with the background-only hypothesis. The constraint of $\hat{\mu} \geq 0$ represents the physics assumption that the signal rate is non-negative and it can only increase the mean event rate above the background. While a negative $\hat{\mu}$ may represent discrepancy with data, it is not a disagreement which indicates the presence of a signal. Thus, in the case of a negative estimate of μ i.e. $\hat{\mu} \leq 0$, the q_0 is set to zero as only positive $\hat{\mu}$ can be used to reject the background-only hypothesis. For this test statistic, the significance using an asymptotic approximation is given by $Z \approx \sqrt{q_0}$. The associated p-value is called the discovery p-value denoted by p_0. It should be noted that rejecting the background-only hypothesis is only a part of establishing a discovery. This would also include other factors such as the degree to which the data can describe the new signal hypothesis.

In the case no significant excess is found in the data and it is generally compatible with theory predictions, testing for discovery is not very relevant. Exclud-

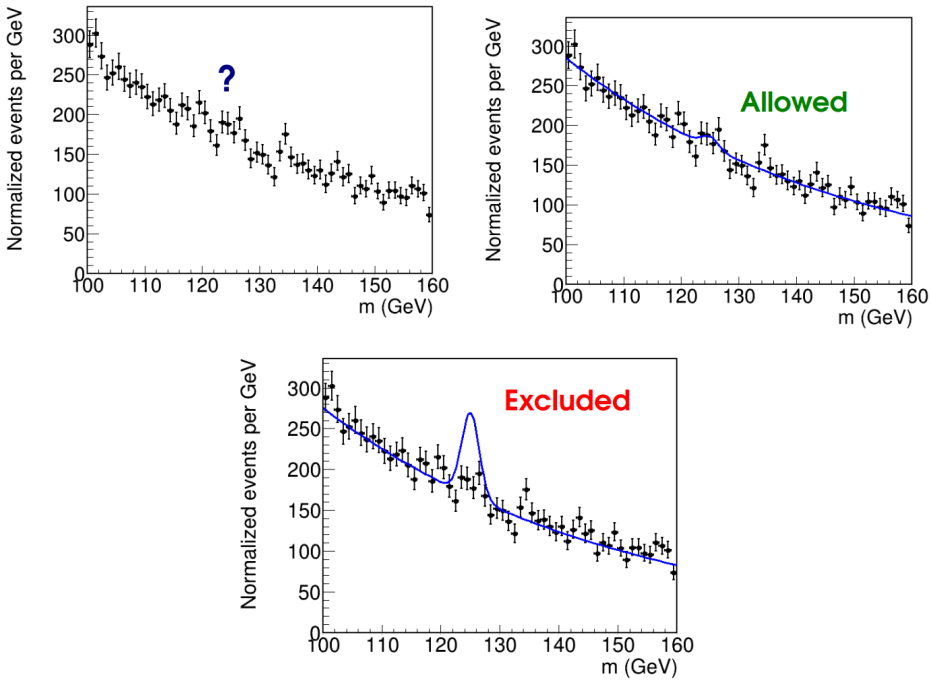

Figure 4.4 – In addition to looking for an excess, the data can be used to set exclusion limits. Theories that predict that large signals should have appeared in the data can be excluded, while models predicting small signal rates remain allowed. Adapted from Ref. [134].

ing the presence of a large signal by setting an *upper limit*, or an exclusion limit, is more interesting instead. An upper limit is a statement about the largest amount of signal that could have been present in the analysed background-like data, with a particular degree of confidence. Any signal model which predicts a larger cross-section than the upper limit on the signal rate can be rejected, for if such a large signal were truly present, it would have appeared in the dataset. This idea can be seen visually in Figure 4.4 and Figure 4.5. The test statistic to set an upper limit on μ is given by:

$$q_\mu = \begin{cases} -2\ln\lambda(\mu) & \hat{\mu} \leq \mu, \\ 0 & \hat{\mu} > \mu. \end{cases} \tag{4.22}$$

As before, for large enough data samples q_μ can be approximated to take the

following asymptotic form:

$$q_\mu = \begin{cases} \frac{(\mu-\hat{\mu})^2}{\sigma^2} & \hat{\mu} \leq \mu, \\ 0 & \hat{\mu} > \mu. \end{cases} \tag{4.23}$$

This test statistic can be used to discriminate the hypothesis of a signal being produced at rate μ from an alternative hypothesis of the signal at a lesser rate $\mu' < \mu$. Large values of q_μ represent increasing incompatibility between the hypothesized value of μ and the data. The constraint of $q_\mu = 0$ for $\hat{\mu} > \mu$ means that μ is not excluded in cases where the estimate on the signal rate is larger than the assumed value. Such as estimate would indicate an upward fluctuation of the data, and it is not taken to mean incompatibility with the signal + background hypothesis, so it doesn't count against it. The constraint is thus designed to protect the limits from upward fluctuations. The $p-$value to determine upper limits for a hypothesized μ then becomes:

$$p_\mu = \int_{q_{\mu,obs}}^{\infty} f(q_\mu|\mu) dq_\mu. \tag{4.24}$$

Using the statistic q_μ the upper limit μ_{up} (i.e. the largest value of μ not rejected) can be determined at a confidence level of 1 - α by setting p_μ = α and solving for μ. Setting an upper limit is therefore also called an inverted hypothesis test as it is determined by varying the POI until the p-value falls below the α threshold. The confidence region at CL = 1 – α is the allowed region containing the values of μ that are not rejected. In this analysis $\alpha = 0.05$ i.e. the upper limits are determined at the 95 % confidence level. This means that the true value of the parameter of interest μ is covered by the allowed region 95% of the time; 5 % of the time the hypothesis being tested is wrongly excluded. The significance using an asymptotic approximation is given by $Z_\mu \approx \sqrt{q_\mu}$.

Instead of determining upper limits by setting p_μ = 0.05 and solving for μ, a modified approach is used in LHC analyses called CL$_s$ in order to avoid $spurious$

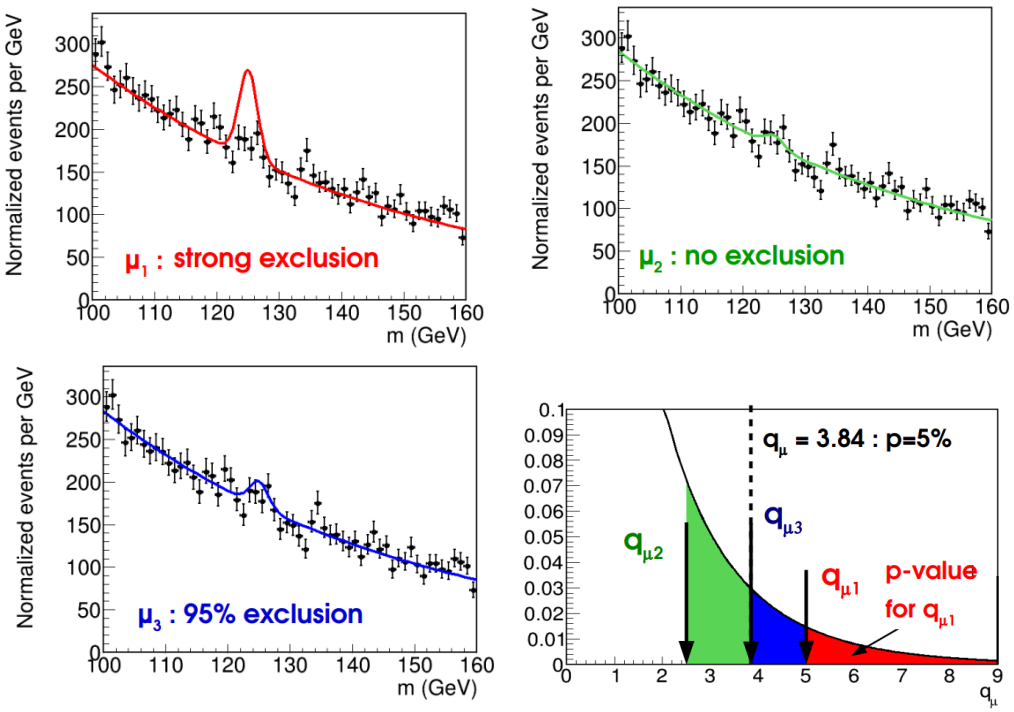

Figure 4.5 – The limit setting procedure entails calculating the test statistic for various signal hypotheses and determining the p-value using each one. In this example, signal strengths that give value of larger than $q_\mu = 3.84$ are incompatible with the signal + background hypothesis and can be rejected with 95 % confidence. Adapted from Ref. [134].

exclusions [118]. A spurious exclusion can happen when the event rate fluctuates substantially below the background-only expectation. This can result in arbitrarily small and even a negative value for the upper limit, a quantity which should intrinsically be positive. The CL_s method was proposed [135] to address this issue of excluding signal models to which one has no experimental sensitivity. As α is typically taken to be 0.05, this issue can be expected in one out of every twenty searches.The CL_s value is defined as:

$$\begin{aligned} CL_s &= \frac{P(q \geq q_{obs}|s+b)}{P(q \geq q_{obs}|b)}, \\ &= \frac{\int_{q_{obs}}^{\infty} f(q|s+b)dq}{1 - \int_{-\infty}^{q_{obs}} f(q|b)dq}, \\ &= \frac{p_{s+b}}{1-p_b}, \\ &= \frac{CL_{s+b}}{CL_b}, \end{aligned} \tag{4.25}$$

where p_{s+b} is the p-value for a signal + background hypothesis, while p_b is the p-value for the background-only hypothesis. Thus, to exclude a signal hypothesis, the μ is varied until the CL_s value reaches ≤ 0.05 (instead of using the CL_{s+b} value obtained from p_{s+b} alone as done previously).

In this approach, the p_{s+b} value is penalized by the divisor 1 - p_b. As seen in Figure 4.6, if the distributions of the test statistic are well separated for the two hypotheses (indicating good sensitivity to the signal), then $1 - p_b \approx 1$ and $CL_s \approx p_{s+b}$. However, if the two distributions largely overlap (indicating poor experimental sensitivity to the signal), then if p_b is large due to a statistical fluctuation, then $1 - p_b$ becomes small and the p_{s+b} value is penalized (increases). In summary, the CL_s method helps prevent spurious rejection of signal models in cases of low sensitivity by making the α threshold difficult to reach and is thus more conservative.

Finally, expected limits are a useful quantity to calculate in order to characterize the sensitivity of the search. Intuitively, this is the upper limit on the signal one would obtain with a dataset in agreement with the background-only hypothesis (i.e. SM prediction). It is thus determined by using the p-value corres-

ponding to the median of the q_μ distribution under the $\mu = 0$ hypothesis (instead of using q_{obs} in 4.24), as shown in Figure 4.7. The error bands for the median significance are the points at which the distribution crosses the quantiles of 16 % and 84% (defining $\pm 1\sigma$), and the crossings of 2.5% and 97.5% (defining $\pm 2\sigma$). As $\hat{\mu}$ is Gaussian distributed, the error bands map onto the variation of $\hat{\mu}$ of $\pm\sigma$ and $\pm 2\sigma$ about the central value of μ'. To avoid producing an extensive ensemble of simulated datasets using toy Monte Carlo, the median values of the test statistics are in practice determined using a single representative dataset called an $Asimov$ dataset. This artificial dataset is obtained by setting the data yields of the observables to their expected values.

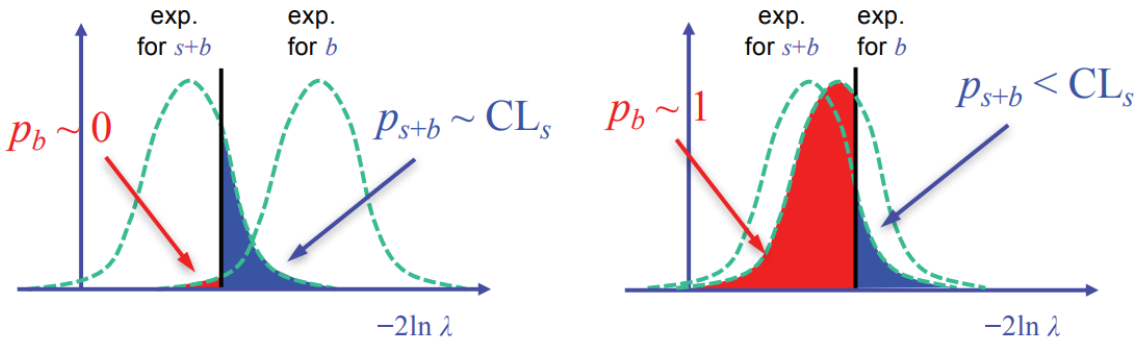

Figure 4.6 – Illustration of the CL_s method. The sampling distribution of the test statistic - 2 ln λ under the signal + background and background-only hypotheses is shown; the black line is the value measured in data. The overlapping distributions (right) indicate low sensitivity to the hypothesized signal model. In this case the CL_s approach gives a more conservative limit due to the penalty from CL_b term. When the distributions are well separated, the CL_s value approaches CL_{s+b} [126].

Look-elsewhere Effect

In searches where the position of the signal peak is not known $a\ priori$, the p-values computed are local in the sense that they are based on a single statistical test of a given mass hypothesis. However, since a wide range is being scanned, the significance calculations must take into account the possibility of a background fluctuation occurring anywhere in the search range. This is known as the "look

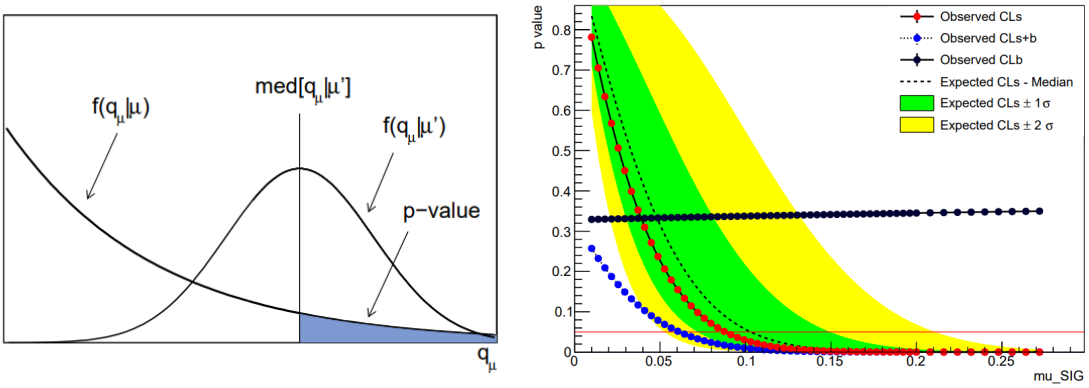

Figure 4.7 – Left: Median of the test statistic distribution under the alternative hypothesis is used to calculate the expected sensitivity [120]. Right: Example calculation of the upper limits for a signal model. The signal strength is raised until p-values dip below the 0.05 mark (redline) which indicates 95 % CL exclusion is reached.

elsewhere effect" [136].

Global p-values are the relevant quantities which account for background fluctuations occurring in the entire mass range. According to ATLAS recommendations, global p-values need to be calculated if a local of excess of greater than 2σ is observed. The prescribed method for this calculation is given by the formula:

$$p_{global} = p_{local} + N_{up} e^{-\frac{1}{2}(Z^2_{local} - Z^2_{ref})}, \tag{4.26}$$

where N_{up} is the number of times the p-value curve crosses a specified reference level. Z_{ref} is the significance corresponding to the chosen reference p-value level,often taken to be $p = 0.5$ ("0σ" level). Figure 4.8 shows an example of counting p-value downcrossings.

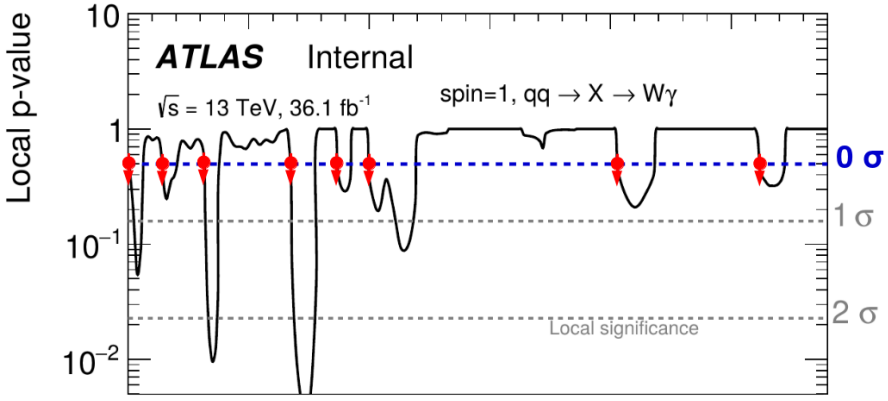

Figure 4.8 – Example of counting p-value down crossings at the 0σ level [137].

4.5 Methodology and Workflow

Profile likelihood fits are performed using the `HistFitter` [121] framework; it is often referred to as 'the fit' in this thesis. The package is used to construct a parametric model describing the data using binned histograms as inputs. The model describes the nominal prediction of the signal and background processes, and associated systematic variations, for the regions under study.

The statistical data analysis proceeds by defining three regions of the phase space. The *signal region* (SR) is where a particular signal model predicts an excess of events over the background. To estimate the backgrounds in the SR, a *control region* (CR) is defined where the dominant background (and systematic uncertainties) can be constrained by comparison to the data. CRs are designed to have a high purity for one type of background and free of signal contamination. The last component is the *validation region* (VR). The VR is placed kinematically in between the CR and the SR in order to validate the assumptions involved in the background estimation and has limited signal contamination.

The fit constructs a probability density function with adjustable parameters using HistFactory [124] to extract accurate and quantitative information from the data. The inputs to create this come in the form of histograms which can be obtained from MC simulations or be user-defined. The CRs and SRs are modelled by separate PDFs and combined into a simultaneous fit. An important feature of

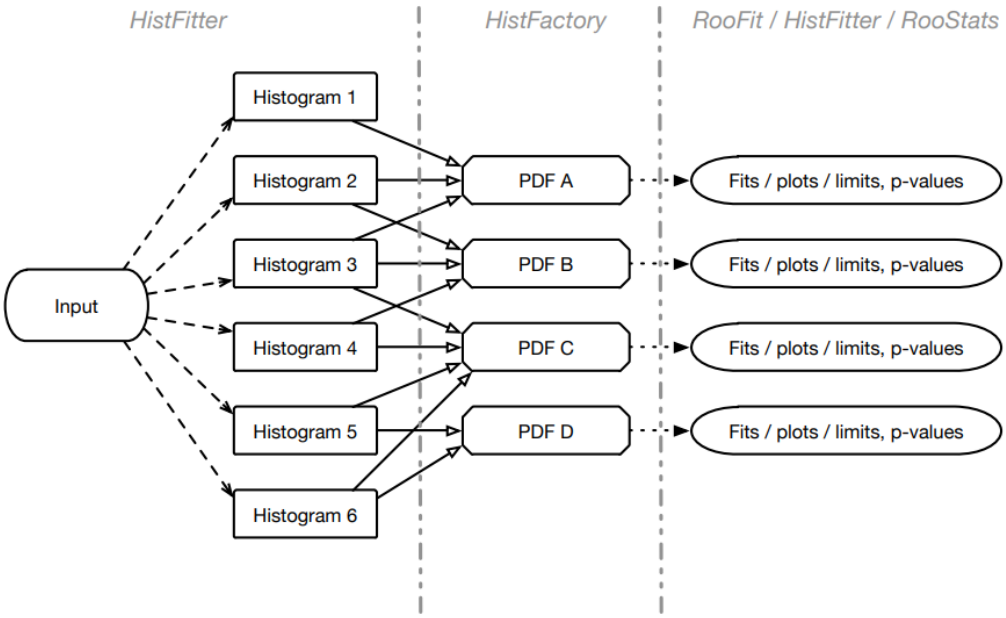

Figure 4.9 – The processing sequence used by Histfitter to build and test data models [121].

this strategy is that the PDF parameters in all the three regions are shared, thus allowing for the use of information from signal, backgrounds and systematics uncertainties consistently in all regions. The PDFs generated are used to perform fits to data using RooFit [138], carry out statistical tests using RooStats [139], and generate tables and plots. This processing sequence used by the HistFitter framework is summarized in Figure 4.9.

The PDF constructed describes the POI (signal strength), the normalization factors for background processes as estimated from the data, and the nuisance parameters that encode the impact of systematic uncertainties. The likelihood for the analysis is then the product of Poisson distributions of event counts in the SRs and CRs, and takes the form [121]:

$$L(n, \theta^0 | \mu_{sig}, b, \theta) = P_{SR} \times P_{CR} \times C_{syst}, \tag{4.27}$$

$$= P(n_s | \nu_s(\mu_{sig}, b, \theta)) \times \prod_i P(n_i | \nu_i(\mu_{sig}, b, \theta)) \times C_{sys}(\theta^0, \theta). \tag{4.28}$$

where n_s and n_i represents the number of observed events in the signal and each control region i respectively. The Poisson expectations ν_s and ν_i for the signal and control regions are functions that depend on the normalization factors μ_i contained in the expected background rate b, the signal strength μ and the nuisance parameters θ. Constraints on the systematic uncertainties are included using the probability density function $C_{sys}(\theta^0, \theta)$, where θ^0 is the nominal value around which θ can be varied.

To estimate the backgrounds, the observed event rate in the CRs is used to coherently normalize the predicted background in all kinematic regions through a likelihood fit to the observed data. As MC simulations are used to model the background in this analysis, their initial predictions ('pre-fit' values) are scaled to levels observed in the CRs using normalization factors computed by the fit. This results in what are called *normalized background predictions*. The normalized predictions are then extrapolated from the CRs into the VRs and SRs as shown schematically in Figure 4.10. This procedure assumes that the kinematic distributions used to differentiate the SR from the CRs are well modelled after fitting the PDF to data in the CRs. Post-fit modifications to PDF parameters obtained from the CRs are extrapolated to the VR to validate this assumption. A discussion on the use of CRs, as opposed to a side-band fit to constrain backgrounds, is found in Section 6.4.2.

Once good agreement is found between the extrapolated background predictions and observed data in the VR, the predicated backgrounds are only then compared to the observed data in the SR. This process is called 'unblinding' and statistical tests can be performed on the data once it has taken place. This approach validates the performance of the extrapolations prior to unblinding and prevents analysers from using premature SR predictions that could bias the physics result. This workflow summarized in Figure 4.11.

An important part of the fitting procedure are the $transfer\ factors$ (TFs) used to convert the observations in the CRs into the background estimates in the SRs. The TFs are the ratios of the expected event counts as highlighted in the

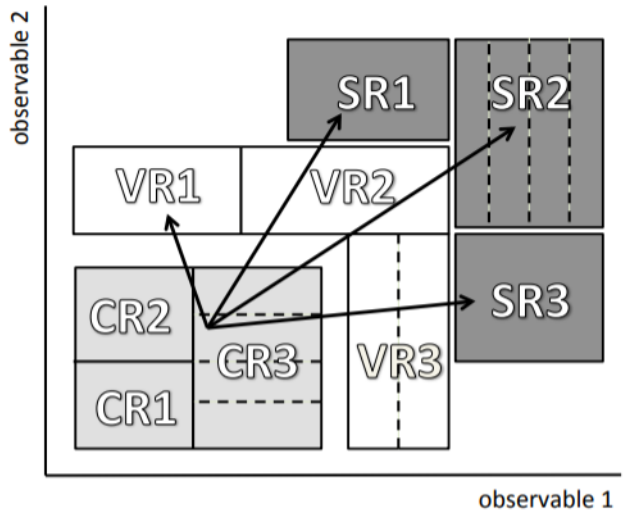

Figure 4.10 – A schematic view of an analysis strategy with multiple control, validation and signal regions. The regions can have one bin or multiple bins (indicated by the dashed lines). The extrapolation from the CR to the SR is verified in the validation regions [121].

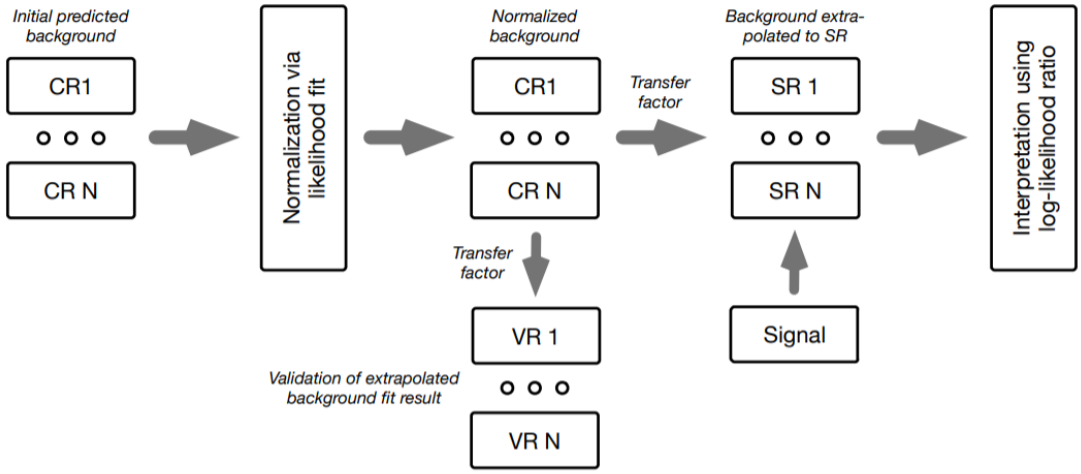

Figure 4.11 – Overview of the background estimation approach and analysis workflow [121].

following equation [121]:

$$N_p(\text{SR, est.}) = N_p(\text{CR, obs.}) \times \underbrace{\frac{N_p(\text{SR, pre-fit})}{N_p(\text{CR, pre-fit})}}_{\text{TF}} = \mu_p \times N_p(\text{SR, pre-fit}), \tag{4.29}$$

where N_p(SR, est.) is the predicted number of background events for the physics process p in the SR, N_p(CR, obs.) is the observed data events in the CR, N_p (SR, pre-fit) and N_p(CR, pre-fit) are the estimates on the event rates for the process directly from the MC without being normalized in a fit to the data. As indicated, the TF is the ratio of the expected events in the SR and CR. The TF $\times$ N_p(CR, obs.) term can be re-written as the normalization factor μ_p, obtained from a fit to the data, multiplied by the nominal background prediction. The two formulations are equivalent to the fit i.e. they contain a normalization quantity derived from data and then multiplied by a fixed constant. One of the advantages of using TFs is that systematic uncertainties on the estimated backgrounds can be cancelled in the extrapolation if they affect the CR and SR in the same way. The total uncertainty on the SR background estimate is then made of the statistical uncertainties in the CRs and the residual systematic uncertainties of the extrapolation [140].

5

Event Selection

A collision $event$ is defined as the set of recorded digitized signals in the ATLAS detector produced from products of proton bunch collisions in the LHC [31]. To conduct a search for the $H^+ \to WA$ process, events have to be optimally selected in order to maximize the performance of the analysis. As seen in the Feynman diagram for the decay in Figure 5.1, the selection would entail picking out top-quark pair events which contain leptons and jets in the final states. This chapter summarizes details about the datasets, object reconstruction methods and optimization procedures relevant for selecting events for this search.

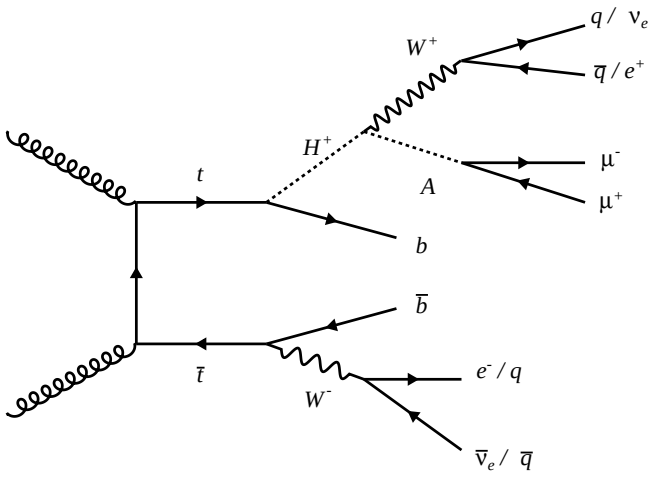

Figure 5.1 – Feynman diagram of the signal model: $H^+ \to WA$ (same as Figure 1.1)

5.1 Dataset and Monte Carlo event simulations

5.1.1 Dataset

The data used in this analysis was collected during the 2015–2018 data-taking period of the LHC (Run 2) with a center-of-mass energy of pp collisions of $\sqrt{s} = 13$ TeV. During this period, the collider delivered 156 fb^{-1} of data, of which 147 fb^{-1} were recorded and 139 fb^{-1} met the quality requirements needed for physics analyses (Figure 5.2). The data from the Good Runs List (GRL) was used. This list excludes defective data compromised by anomalous conditions such as the non-operation of subcomponents, a surge in noise from detector electronics or a high-voltage trip [141].

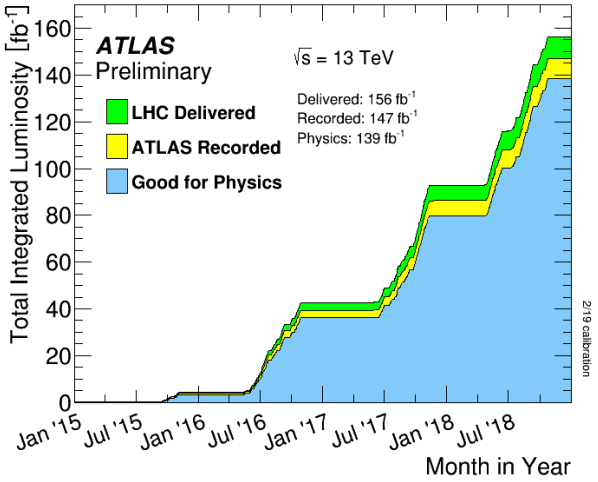

Figure 5.2 – Cumulative luminosity versus time delivered to ATLAS during Run 2 of the LHC. The recorded luminosity reflects the inefficiencies related to the DAQ caused by factors such as the high voltage ramp-up time for the detector subsystems. 'Good for physics' (blue) refers to the criteria of requiring all reconstructed physics objects to meet the data quality conditions set by the experiment [77, 141].

5.1.2 Background event simulations

Event simulations generated using Monte Carlo (MC) techniques have been extensively used to design this analysis. They were employed for estimating the

backgrounds, studying the kinematics of the signal process, optimizing the sensitivity and evaluating uncertainties. The ATLAS MC simulation production is carried out in three main stages [142]:

• Event generation: This step entails the production of a set of particles (their four-momenta) and subsequent decays. The matrix element calculation is performed for the probability of the hard-scatter at the required order of accuracy using an event generator package. The Parton Distribution Functions (PDFs), describing the substructure of the proton, are used by the event generator as an external input; a number of PDF libraries are available for this purpose. The event generators also have a set of pre-defined parameters for the simulations. However, these are not tuned for use at the LHC; tuning parameter sets are made available based on run conditions to create simulations that can better describe the collision data. The parton shower and hardonization are also simulated at this stage.

• Detector simulation: The particles produced by the event generator are passed through a geometric simulation of the detector. The interaction of the particles with the physical material is simulated and the energy deposited in the detector's sensitive regions is recorded.

• Digitization: The simulated energy deposits by the particles are converted to voltages and currents to mimic the raw output data from the detector.

The background samples used in the analysis employ various event generator packages. The $t\bar{t}$ and single top-quark samples are generated with POWHEG-BOX v2 [143–147] using the NNPDF3.0 [148] set (at next-to-leading-order (NLO) accuracy) and then interfaced to PYTHIA 8.230 [149] for modelling of the parton shower (PS). The Powheg `hdamp` parameter is set to $1.5 \times m_t$, where m_t is the top-quark mass and is set to 172.5 GeV. For the underlying event description the A14 set of tuned parameters [150] is used, along with the NNPDF2.3 LO PDF [151]. The $t\bar{t}$ + vector boson processes, $t\bar{t}$+V (V=W, Z), are generated with MADGRAPH5_AMC@NLO v2.3.3 [152] interfaced to PYTHIA 8.210 for the PS.

For the $(W \rightarrow \ell\nu)/(Z \rightarrow \ell\ell)$+jets ($l$ = e, μ, τ) and di-boson backgrounds, SHERPA v2.2.1 [153,154] with the NNPDF3.0 set (at next-to-next-to-leading-order (NNLO)) accuracy is used. SHERPA is a multi-parton matrix element and PS gener-

ator including hadronization [155–159]. For the V+jets background, SHERPA uses NLO matrix elements for up to two partons, and LO matrix elements for up to four partons calculated with the Comix [160] and OpenLoops libraries [161, 162]. They are matched with the SHERPA parton shower using the MEPS@NLO prescription [156–159] using the tune developed by the SHERPA authors. For di-boson processes, matrix elements are at NLO accuracy for up to one additional parton and at LO accuracy for up to three additional partons. EVTGEN [163] is used to model the properties of the bottom and charm hadron decays in all the simulated samples, except those simulated with SHERPA. The effects of pile-up are modeled for all events by overlaying additional pp collisions generated with PYTHIA 8.186.

5.1.3 Signal event simulations

MC simulations are used to generate signal events in which a charged Higgs boson is produced in top quark decays and subsequently decays to an A and W boson. The samples were generated using MADGRAPH5_AMC@NLO v2.3.3 [152] interfaced with PYTHIA 8.186 using the A14 set of tuned parameters. This leading order simulation uses the NNPDF2.3 LO PDF [151] set. Both H^+ and A are simulated using a narrow width assumption as the width is always smaller than the detector resolution for the investigated parameter space. The simulated signal samples include the charge conjugate states of the H^+. The charged Higgs production in top-quark pairs was simulated under assumption it is conservative to ignore small contributions from other production modes and interference [164]. Inclusive decays of the on-shell W bosons are simulated and a lepton filter is used requiring three charged leptons in the generated events. A 2D mass grid was generated for the (H^+, A) masses targeting the search range of the analysis. Mass points were generated in steps of 15 GeV for the A and 20 GeV for the H^+: (160,75), (160, 60), (160, 45), (160, 30), (160, 15), (140, 45), (140, 30), (140, 15), (120, 30), (120, 15), (100, 15) GeV.

All the backgrounds simulated by the event generators are processed through the ATLAS detector full simulation [142] based on GEANT4 [165]. The signal samples, however, are processed through a fast simulation [166] in order

to reduce computing time. The same software used to reconstruct the data is also used for the signal and background simulations. A list of the simulated event samples is tabulated in Appendix A.6.

5.2 Object Reconstruction Methods

All of the particles created in collisions need to be reconstructed and identified from the signals they leave in the ATLAS detector with a high efficiency. The object reconstruction methods relevant for this analysis are summarized below.

5.2.1 Track and Vertex Reconstruction

The reconstruction of tracks and vertices are a key part of reconstructing the full collision event. A $track$ is the trajectory of a charged particle in the detector [167]. It is used as an input in the reconstruction of other objects, such as muons and electrons, and the identification of the vertex location. Charged particles are measured at multiple points (hits) on the inner detector (ID) and this information is then used to reconstruct their trajectories. The sign of the charge and the momentum of the particle is determined by the curvature of the track.

The sequence of algorithms used to reconstruct the tracks of primary particles is outlined in Ref. [167, 168]. These tracks are required to have $p_T > 400$ MeV and $|\eta| < 2.5$. The reconstruction process entails taking the hits recorded by the ID and grouping them into clusters. These clusters are transformed into three-dimensional space-points representing the volume through which the charged particle has passed. An iterative procedure is then used, starting with three space-points, to identify various track candidates. The track candidates are evaluated individually and are ranked in terms of the likelihood with which they describe the real trajectories of particles. The candidate with the highest score is chosen and is fitted with a high-resolution fit using all the information from the ID to extract the final track parameters. The particle moves in a helix trajectory and the final reconstructed tracks are described by five parameters, shown in Figure 5.3 [169,170]:

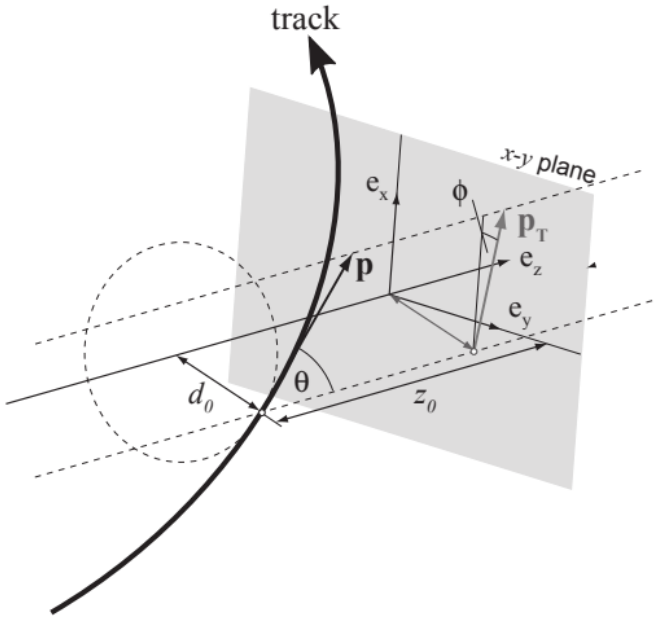

Figure 5.3 – Track reconstruction: The trajectory of a charged particle is characterized by the transverse and longitudinal impact parameters, d_0 and z_0, the azimuthal angle ϕ, and the polar angle θ of the track.

• The transverse (longitudinal) impact parameters d_0 (z_0): These are defined as the point of closest approach of the track in the transverse (longitudinal) plane to the reference point. The reference is taken to be the average position of the pp interactions, or the beamspot position.

• The azimuthal angle ϕ and the polar angle θ of the track momentum at the reference point.

• The factor q/p which is the ratio of the charge of the reconstructed track over the magnitude of its momentum.

The reconstructed tracks serve as inputs into the reconstruction of primary vertices. Primary vertices (PV) are defined as the points in space where pp interactions have taken place [171]. A PV has at least two tracks with $p_T > 400$ MeV. An event will typically have many PVs which arise from both the hard-scatter interaction and the pile-up from soft-QCD interactions. Secondary vertices are those that arise from the decays of primary particles and interactions with detector material;

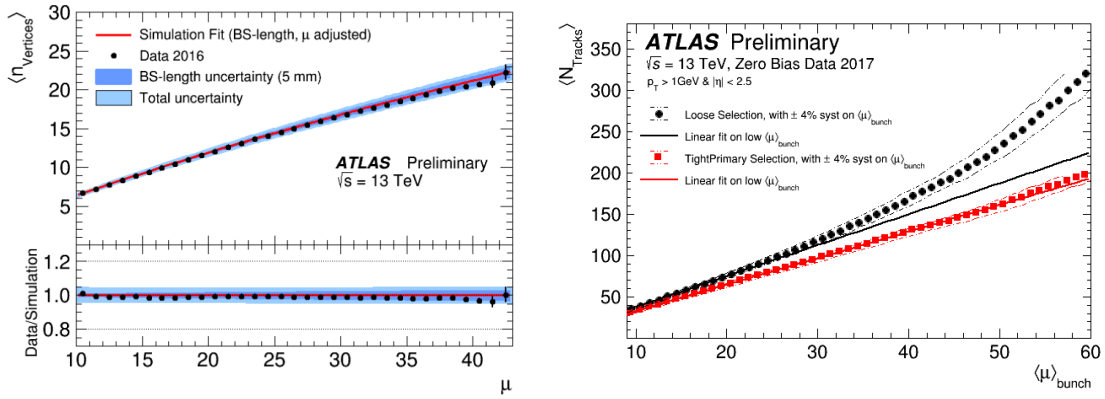

Figure 5.4 – Vertex reconstruction: (Left) The mean number of primary vertices N_{PV} as a function of the average number of interactions per bunch crossing $< \mu >$. μ is the Poisson mean per bunch while the brackets $<>$ indicate the average over colliding bunches. A strong correlation can be seen between the two variables. (Right) The average number of reconstructed charged particle tracks that pass preselection in as a function of the $< \mu >$. The solid lines show a linear fit to the data in the region $9 << \mu >< 16$, and extended to higher $< \mu >$ [173, 174].

they are further away from the primary ones.

The hard-scatter primary vertex is defined as the primary vertex with the highest sum of transverse momentum squared $\sum p_T^2$ of the tracks associated to it [171]. This means that the vertex is at the location of the largest momentum exchanged where the particles of interest are likely to be created. While there can be many primary vertices in the event, one is identified as the hard-scatter vertex. Although not all of the vertices are reconstructed in the event, the reconstruction efficiency of hard-scatter PV is higher than 99% [170]. A measure of the in-time pile-up activity can be obtained from the total number of reconstructed primary vertices (N_{PV}) with 2 or more tracks. As seen in Figure 5.4, N_{PV} is strongly correlated with the average pile-up multiplicity $< \mu >$. However, $< \mu >$ is sensitive to both in-time and out-of-time pile-up as it is obtained by measuring the instantaneous luminosity [172].

Reconstruction of the vertices takes places in two stages: vertex finding and vertex fitting [171]. Vertex finding is a pattern recognition process that involves associating tracks to vertex candidates. The vertex fitting entails calculation of the actual vertex position and its associated error matrix. The reconstruction al-

gorithm starts by identifying the seed position for the first vertex candidate using its z-position, i.e. the longitudinal position, of the reconstructed tracks passing the selection criteria. The tracks and the seed are used to estimate the best vertex position with a χ^2 fit. Each track carries a weight which quantifies its compatibility with the fitted vertex [175]. The fit is an iterative procedure and less compatible tracks are down-weighted in each iteration. Tracks incompatible with the vertex are removed and used to seed a new vertex. This process is repeated until no additional vertices can be found. The $beam\ spot$ position is used as a three-dimensional constraint in the algorithm. It is the area where most collisions take place and during the 2018 run of the LHC its size measured about 7 μm x 7 μm x 34 mm [176]. The wider dimension of the beam spot in the longitudinal direction allows the vertices to be better distinguished in the z-direction, explaining why this axis is used to seed the vertex initially.

5.2.2 Muons

Muons have a high lifetime of 2.2 μs and travel far into the detector before decaying. They are distinguished from other particles as they leave a very clean track and deposit little energy in the calorimeters. These particles are very penetrating and traverse all the subsystems. Their presence is evidenced by tracks in the ID and MS; they also leave a characteristic energy deposit in the calorimeters. These properties allow muons to be reconstructed with a high efficiency and offer precise momentum measurements.

Track information from the muon spectrometer (MS) and the inner detector (ID) is used to reconstruct muons; information from the calorimeters also supplements these inputs. The tracks are first identified independently in the two detector systems and then combined. The combination can occur in several ways and results in five 'types' of muons due to the different reconstruction strategies [177]:

• Combined (CB) Muons: These are reconstructed by matching tracks from the MS to the tracks from the ID and performing a combined track fit based on hit information from the two subsystem. Energy losses in the calorimeters is also taken into account.

• Inside-out combined (IO) Muons: These are reconstructed by using an $inside\text{-}out$ algorithm which extrapolates ID tracks to the MS and searches for at least three loosely-aligned MS hits. The approach does not use an independently reconstructed track from the MS. The combined fit uses the ID tracks, the energy loss from the calorimeters and the MS hits. This approach can help recover efficiency for low-p_{T} muons which may not reach the middle MS station.

• Muon-spectrometer Extrapolated (ME) Muons: When an MS track can't be matched to an ID track, its parameters are extrapolated to the beamline and this results in an ME muon. These are used to extend the acceptance outside the ID and help exploit the full MS coverage upto $|\eta| = 2.7$.

• Segment-Tagged (ST) Muons: These are reconstructed with the condition that an ID track extrapolated to the MS satisfies tight angular matching requirements to at least one reconstructed MS segment. A segment is a short straight-line local track built from hits in an individual MS station (e.g. a chamber of MDT or CSC). Once an ID track is successfully matched, it is identified as a muon candidate and the muon parameters are taken from the ID track fit.

• Calorimeter-tagged (CT) Muons: These are reconstructed by extrapolating ID tracks through the calorimeters and searching for energy deposits which are consistent with that of a minimum-ionising particle (MIP). MIPs are relativistic particles with a mean energy loss rate close to the minimum; a muon is a MIP at ≈ 0.35 GeV/c. Such a deposit is used to tag the ID track as a muon and the ID track fit is used to get the muon parameters.

Muon Identification

A set of additional $identification$ requirements are used to select high quality muon candidates for physics analyses. A given set of requirements is called a $working\ point$ (WP). WPs are designed to meet the diverse needs of ATLAS physics analyses which could have specific requirements on prompt-muon identification, resolution of the momentum measurement, and rejection of background due to non-prompt muons.

The identification muon WPs have a particular focus on rejecting non-prompt and mis-identified muons, also known as $fakes$. Leptonic decay of hadrons often

produce soft muons inside of a jet. If the hadron gives enough of its energy to the muon, it can appear isolated and be reconstructed as a prompt muon. Very energetic hadrons (e.g. kaons or pions) may also 'punch-through' the hadronic calorimeters and reach the MS, and could be reconstructed as a muon.

The track quality of the muons is exploited to increase the purity of candidates used in physics analyses. Non-prompt muons coming from the decay of hadrons produce poor quality tracks due to a change in trajectory (kink) mid flight. This also results in incompatibility between the momentum measurements between the ID and MS. It should be noted that this is particular for non-prompt decays from light hadrons. Muons arising from decays of heavy hadrons containing charm and bottom quarks (heavy flavours) produce good quality tracks. These can be distinguished from the prompt muons which tend to be more isolated in the ID and calorimeters [177].

The identification WPs for muons used in ATLAS are five and defined as follows:

• Medium: This WP accepts only CB and IO muons within the ID acceptance of $|\eta| < 2.5$. It is suitable for a large variety of analyses as it provides a good efficiency and purity, while keeping systematic uncertainties in the prompt-muon efficiency and background rejection small.

• Loose: All the muons passing the $Medium$ WP are accepted by the $Loose$ WP. Additionally, it includes CT and ST muons in the range $|\eta| < 0.1$. This WP was optimized for the reconstruction of Higgs boson decays in the four-muon final state and benefits from a high reconstruction efficiency, at the cost of lesser purity and larger uncertainties.

• Tight: This WP accepts CB and IO muons passing the Medium WP with at least two $precision\ stations$. A precision station of a muon is defined as the number of MS stations in which the muon has at least three hits in the MDT or CSC detectors. This WP offers the highest purity of muons at the expense of loss in efficiency.

• Low-p_{T}: Only the CB and IO muons are used in this selection WP. It targets the lowest-p_{T} muons which are less likely to be constructed as full tracks in the MS.

As the non-prompt background can be large for low momenta muons, the WP exploits a set of variables to provide good separation between prompt muons and light-hadron decays. This results in an optimal background rejection and ensures high reconstruction efficiency.

• High-p_{T}: Only CB and IO muons that pass the Medium WP requirements are used for this identification requirement. This WP is ideal for momentum measurement for muons with p_{T} over 100 GeV and was optimized for the heavy W' and Z' searches.

Muon Isolation

In addition to imposing muon identification requirements, background can be further reduced by using $isolation$ requirements. Prompt muons originating from the hard-scatter can be discriminated from muons of secondary sources by measuring the amount of hadronic activity around them. They are well-separated without any particles in the vicinity i.e are more isolated, compared to non-prompt muons which are surrounded by jet constituents.

Isolation can be measured using either ID tracks, calorimeters or a combination of both (a $particle\ flow$ approach). Track-based isolation variables are defined using the scalar sum of the p_{T} of the ID tracks for a given PV in an η-ϕ cone of a given ΔR size (typically 0.2 or 0.3) around the muon. Calorimeter-based isolation variables use the sum of the energy in calorimeter clusters in a cone of size ΔR = 0.2 around the muon. Various isolation working points used in ATLAS can be found in Ref. [177].

The requirements placed on the muon candidates used in this analysis are listed in Table 5.1. In summary, they have to satisfy $p_{\mathrm{T}} > 5$ GeV, $|\eta| < 2.7$ and pass the $LowPt$ identification requirement discussed earlier. They also have to be isolated from surrounding detector activity by requiring that the scalar sum of p_{T} of additional ID tracks and the sum of the transverse energy E_{T} of calorimeter topological clusters, both within a cone of size $\Delta R = 0.2$ around the muon, be less than 15% and 30%, respectively, of the muon p_{T}. Lastly, to further reduce muons from hadron decays, pile-up interactions and cosmic rays, selection requirements are imposed on the impact parameters of the muon track. Where

an ID track is present, it is required to have a longitudinal impact parameter $|z_0 \sin\theta| < 0.5$ mm to ensure it is compatible with originating from the PV, where θ is the polar angle of the muon track. The transverse impact parameter significance has to be $|d_0|/\sigma_{d_0} < 3$, where σ_{d_0} is the uncertainty on d_0.

Cut	Value/description
ID	LowPt
Acceptance	$p_{\mathrm{T}} > 5$ GeV, $\lvert\eta\rvert < 2.7$
IP	$z_0 \sin\theta < 0.5$ mm
	$\lvert d_0\rvert/\sigma_{d_0} < 3$

Table 5.1 – Summary of the muon selection criteria. "IP" stands for the impact parameter.

5.2.3 Electrons

The signature of an electron in the detector is a track in the ID, an energy deposit in the electromagnetic calorimeter and a shower shape which is consistent with an electromagnetic shower. It leaves little or no energy in the hadronic calorimeters. Showers are a cascade of particles produced when a high energy incident electron loses energy by radiating a photon (bremsstrahlung). The photon, if energetic enough, will create electron-positron pairs (pair production) which will radiate again. This repeating process creates a cascade of particles which continues until the energy becomes low enough that energy losses via pair production and bremsstrahlung no longer dominate. The photons, positrons and electrons are emitted in a very collimated fashion and are reconstructed as part of the same electromagnetic cluster [72, 178].

A reconstructed electron is thus defined as an object consisting of a cluster built from energy deposits in the calorimeter with a matched track [179]. If there is no track pointing to the cluster of energy, it is considered a candidate for a photon. If the matched track to the cluster points to a secondary vertex, it is a $converted\ photon$ candidate i.e. an electron resulting from a photon converting to an electron–positron pair before reaching the EM calorimeter. An electron can also be wrongly constructed as a photon due poor matching between the track and

cluster. As electrons and photons deposit similar showers in the EM calorimeter, their reconstruction occurs in parallel. The incoming particles deposit energy in both longitudinal and lateral directions in many connected calorimeter cells. The sum of the total energy in all these cells can be determined by using clustering algorithms that group these cells together.

The reconstruction algorithm starts with preparing tracks and clusters for identification [179]. Clusters of energy deposits measured in spatially connected EM and hadronic calorimeter cells called $topological\ clusters$, or topo-clusters, are first selected. Topological clustering entails grouping into clusters neighboring cells that have significant energies compared to the expected noise [180]. The cell initiating the cluster, or $seed$ cell, is required to have a cell energy significance, defined as the signal to noise ratio, of greater than 4. This dynamical algorithm iteratively adds to the cluster the neighbor of a cell already in the cluster, provided the new cell meets the noise threshold set (normally a cell significance of 2 is used). This approach of building clusters following the shape of the energy deposits results in clusters with a variable number of cells, in contrast to fixed-size clusters produced by alternative algorithms.

These clusters are then matched with tracks from the ID. As electrons are likely to radiate photons via bremsstrahlung due to interactions with the detector, the ID tracks are re-fitted to account for this using a Gaussian-sum Filter algorithm. In the final step, the topo-cluster matched to the re-fitted track is used to seed a $supercluster$. Building a supercluster is a new technique which allows one to recover radiative losses from bremsstrahlung to improve the energy measurement of the primary electrons. As seen in Figure 5.5, constructing a supercluster helps connect the primary cluster from the electron shower ($seed\ cluster$) with a nearby secondary cluster formed from the radiated photon shower ($satellite\ cluster$). The term supercluster refers to the seed and satellite system together, and their use significantly improves the energy resolution. Once the supercluster is built, an energy calibration is applied to it and the tracks are matched to it in the same way as done for the topo-clusters. The four-momentum of the final electron object is then computed using the matched tracks and superclusters [181].

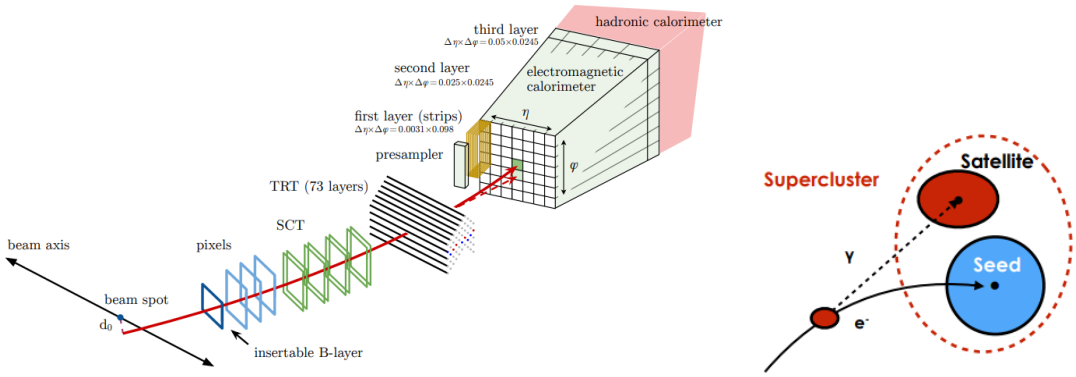

Figure 5.5 – Electron Reconstruction: (Left) An electron traversing through the detector, shown in red. It first passes the tracking system and then enters the EM clorimeter. The dashed line is the bremsstrahlung photon produced due interaction with material in the tracking system. (Right) Illustration of a supercluster formed by combining seed and satellite clusters arising from the incident electron and radiated photon, respectively [178, 181].

Electron Identification and Isolation

Similar to muons, further identification and isolation requirements are placed on electrons to increase their purity. Misidentified and non-prompt electrons can arise in heavy hadron decays (e.g. $b \to cl\nu$ where the b-quark is inside a hadron) and light hadron decays (including $\pi^0 \to \gamma\gamma$) that can fake an electromagnetic shower. They can also arise from non-prompt tau decays and conversions in which a photon pair-produces before reaching the EM calorimeter while giving most of its energy to the electron.

A likelihood-based identification is used for the quality criteria of the electrons selected for the analysis [178]. The likelihood discriminant (LH) is built from quantities measured in the ID and calorimeter that assist in distinguishing prompt isolated electrons from energy deposits of hadronic jets mimicking electrons, converted photons and non-prompt electrons from hadron decays. These variables can be classified based on properties of the electron track, the lateral and longitudinal development of the EM shower and the spatial compatibility of the primary electron track with the reconstructed cluster in the calorimeter. The values of the LH are used to define the quality working points for electrons which are: `Loose`, `Medium` , `Tight` as outlined in Ref. [179]. These three levels offer a trade-off between increasing purity at the cost of decrease in reconstruction efficiency.

Prompt electrons are expected to be well isolated from other tracks with little calorimeter activity around them. An isolation criteria is thus applied to further suppress mis-identified electrons. Similar to muons, track-based and calorimeter-based variables are used to impose isolation cuts. These cuts are catered to the various needs of physics analyses and results from a compromise between a highly-efficient identification of prompt electrons and good rejection of fake electrons. There are four isolation working points used in ATLAS: `Gradient`,`Loose`, `Tight`, `HightPtCaloOnly`.

In summary, the electrons in this analysis are reconstructed using information from energy deposits in the electromagnetic calorimeter (ECAL) geometrically matched to a track in the ID; they must satisfy $p_{\mathrm{T}} > 5$ GeV and $|\eta| < 2.47$. Clusters in the transition region ($1.37 < |\eta| < 1.52$) between the barrel and the end-caps of the ECAL are excluded. A *Medium Likelihood* requirement is used for electron identification. Electrons are required to be isolated from the surrounding detector activity by requiring that the scalar sum of p_{T} of additional inner detector tracks (calorimeter clusters) within a cone of size $\Delta R = 0.3$ (0.2) around the electron be less than 10% (20%) of the electron p_{T} if that p_{T} is less than 200 GeV. For higher p_{T} electrons, the only requirement is that the scalar sum of p_{T} of additional calorimeter clusters within a cone of size $\Delta R = 0.2$ around the electron be less than 35% of the electron p_{T}. Track quality cuts are also placed to further reduce background from fake electrons. Like muons discussed previously, electron tracks must also fulfil $|z_0 \sin\theta| < 0.5$ mm and $|d_0/\sigma_{d_0}| < 5$ to ensure that the candidates originate from the primary vertex. Table 5.2 summarizes the details of electron ID and reconstruction.

Cut	Value/description
ID	MediumLLH
Acceptance	$p_{\mathrm{T}} > 5$ GeV, $\lvert\eta\rvert < 2.47$
IP	$z_0 \sin\theta < 0.5$ mm
	$\lvert d_0/\sigma_{d_0\lvert} < 5$

Table 5.2 – Summary of the electron selection criteria. "IP" stands for the impact parameter.

5.2.4 Jets

The final states of proton-proton collisions are characterized predominantly by $jets$, or collimated sprays of charged and neutral hadrons created by the hadronization of a single parton [182]. Jets are created when a quark or gluon is produced during a particle collision. Due to QCD colour confinement, isolated partons from the proton do not propagate through the detector but transform into colour neutral hadrons instead. These hadrons decay and fragment into many particles in a tight collimated cone around the original direction of the parton. This spray of particles which leave topologically related energy deposits in the calorimeters is the experimental signature of the original gluon or quark. Kinematic information about the original parton that initiated the particle shower can be inferred by reconstructing the jet and measuring its properties [72].

The jet reconstruction algorithms aim to group the particles from the hadronization process together and measure the energy of the incident parton. They can be divided into two classes: cone algorithms and sequential algorithms. Cone algorithms work by grouping particles within a specific conical angular region, such that the momentum sum of the particles in the cone corresponds with the cone axis. Such a cone is considered $stable$ and is physically close in direction and energy to the original partons. Sequential algorithms identify the pair of particles that are closest in some distance measure, recombine them and repeat the procedure continually until a pre-defined stopping criteria is reached [183].

Calorimeter cells are first clustered into three-dimensional topological clusters which are used to create jet objects. The jets used in this analysis are reconstructed using the anti-k_T sequential clustering algorithm [184] implemented in the FASTJET package [183] with a radius parameter $R = 0.4$. The distance measure d_{ij} between two objects i and j, and between an object i and the beam B is defined as:

$$\begin{aligned} d_{ij} &= min(\frac{1}{k_{Ti}^2}, \frac{1}{k_{Tj}^2})\frac{\Delta_{ij}^2}{R^2}, \\ d_{iB} &= \frac{1}{k_{Ti}^2}, \end{aligned} \tag{5.1}$$

where $\Delta_{ij}^2 = (y_i - y_j)^2 + (\phi_i - \phi_j)^2$ and k_{Ti}, y_i, ϕ_i and R are respectively the transverse momentum, rapidity, azimuth of object i and the radius parameter. The distance measure changes based on the algorithm being used. For example, for the k_T algorithm, the k_{Ti}^2 factor has a power of 1, the Cambridge-Aachen approach has power 0, while the 'anti-k_T' method uses a power of -1 [90].

Inputs into the algorithm are four-vector objects that may be stable particles defined by MC generators, charged-particle tracks, calorimeter energy deposits (topo-clusters), or algorithmic combinations of the latter two [182]. The anti-k_T algorithm works by finding the distances d_{ij} and d_{iB} for all objects i, j. If d_{iB} is the smaller of the two, then object i is defined as the final jet and removed from list of entities. If d_{ij} is smaller, then the object i and j are merged into a new object whose momentum is p_i + p_j, often called a 'pseudo-jet'. The procedure is repeated and the distances are re-calculated until no objects are left to be assigned.

Jets reconstructed only using energy information from the calorimeters are called $EMTopo\ jets$. This was the main jet definition used in the experiment prior to the end of Run 2 and provided robust energy scale and resolution characteristics across a wide kinematic range. An improved method for hadronic final state measurements used during Run 2 is the $particle\ flow$ or $PFlow$ algorithm [185]. This approach combines information from both the tracker and the calorimeter to form the input signals representing individual particles. The algorithm removes calorimeter energy deposits from charged hadrons and instead relies on information of their momenta from the inner tracker. This improves the charged-hadron measurement as the double-counting of charged-hadron signals between the tracker and calorimeter is minimized. The jet reconstruction is then carried out on an ensemble of $particle\ flow\ objects$ consisting of the remaining calorimeter energy and tracks that are matched to the hard scatter interaction (while a large fraction of tracks and energy deposits from pile-up are removed). PFlow jets are used in this analysis and offer improved energy and angular resolution, and reconstruction efficiency [182, 185].

For additional suppression of pile-up jets, the jet-vertex-tagger (JVT) [186] is also used. This multivariate technique is used for jets with $p_{\mathrm{T}} < 60$ GeV and $|\eta| < 2.4$. It uses the jet track and vertex information to differentiate between pile-

up and hard scatter jets. Finally, all selected jets for analysis purposes are required to have $p_{\mathrm{T}} > 20$ GeV, $|\eta| < 2.5$ and must pass quality requirements defined to minimise the impact from beam and cosmic ray particles and detector effects.

b-jet tagging

Jets containing b-hadrons are called b-jets and the procedure to identify them is called b-tagging. The algorithms for b-tagging exploit the experimental signatures of this particle: a long lifetime, high mass and high multiplicity. Their lifetime is relatively long of about 1.5 ps ($< c\tau > \approx 450\mu m$) and they decay further away from the primary vertex which leads to the creation of a secondary vertex. The mean flight length $< l >= \beta\gamma c\tau$ for a b-hadron with p_T of 50 GeV is on average 3 mm and its decay results in topologies with displaced vertices that are not expected to point back to the primary vertex like prompt tracks. The tracks of b-jets thus also have large transverse and longitudinal impact parameters d_0 and z_0; tracks in light jets have impact parameter significances that are typically consistent with zero. b-tagging therefore entails finding signatures of displaced vertices and also identifying soft leptons (muons and electrons) inside the jet which result from semi-leptonic b-decays [72, 90, 187–189].

A multivariate algorithm, referred to as MV2c10, is used for b-tagging in this analysis [190, 191]. The algorithm utilises a Boosted Decision Tree (BDT) with a dedicated optimisation for Run-2 to take advantage of the newly installed IBL. The input parameters into this method consist of a likelihood-based combination of the transverse and longitudinal impact parameter significances, identification of a secondary vertex and associated properties, and the reconstruction of the b-hadron decay chain with a Kalman filter. Additionally, the p_T and η of the jet are used for training the BDT to take advantage of correlations with other variables. The training is conducted using simulated $t\bar{t}$ samples where the b-jets are used as signal while the c-jets and light-flavour jets are used as background. This tagger provides several working points which correspond to the identification efficiency for selecting jets; a 77% b-jet identification efficiency (ϵ_b) was used. Table 5.3 summarises the jet selection criteria for the search.

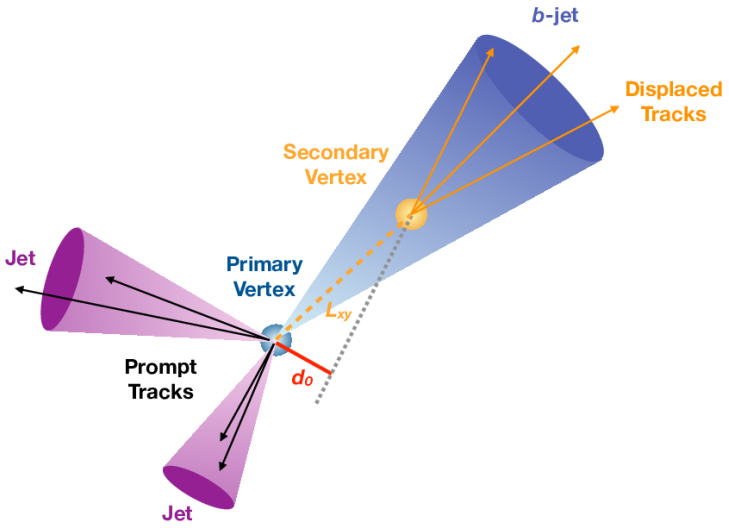

Figure 5.6 – A diagram showing the distinct decay geometry of a b-jet. The long lifetime of b-hadrons results in a large transverse decay length L_{xy} which produces displaced tracks originating from a secondary vertex. The transverse impact parameter d_0 is typically large for tracks coming from the decay of b-hadrons. Jets that are initiated by lighter quarks or gluons don't have these characteristics and consist of mostly prompt tracks from the primary vertex [188].

Cut	Value/description
Acceptance	$p_{\mathrm{T}} > 20$ GeV, $\lvert\eta\rvert < 2.5$
JVT	`Tight` WP, JVT > 0.5 for $\lvert\eta\rvert < 2.4$ and $20 < p_{\mathrm{T}} < 60$ GeV
b-tagging	MC2c10 $\epsilon_b = 77.53\%$

Table 5.3 – Summary of jets selection criteria. For b-tagging MV2c10 discriminant is used, with the tagging efficiency (ϵ_b) WP at 77.53%.

5.2.5 Overlap Removal

It is possible that the tracks or energy deposits from a single particle be reconstructed as two different objects. An overlap removal procedure is thus implemented to avoid the double-counting of analysis objects. If electrons, muons or jets overlap with each other, all but one object must be removed from the event. The removal happens as follows:

- If the same ID track is shared between two electrons, the most energetic of

them is kept.

• If a reconstructed electron and muon share a track in the ID, the electron is removed. However, if the muon sharing the track with the electron is calorimeter-tagged (CT), then the muon is removed instead of the electron.

• If a jet (which is not b-tagged) and an electron are reconstructed within $\Delta R' = 0.2$ [1] of each other, then the jet is removed.

• If a jet (which is not b-tagged) and a muon are within $\Delta R'$ = 0.2 of each other, and the jet has less than three tracks (with $p_{\mathrm{T}} > 500$ MeV) or carries less than 50% of the muon p_{T}, then the jet is removed; otherwise, the muon is removed.

• Electrons or muons separated from the remaining jets by $\Delta R' < 0.4$ are removed.

5.3 Trigger

The target signature of the search is a scalar boson decaying to a muon pair. The single and dimuon triggers were thus chosen to collect the events and provided a competitive sensitivity for the analysis. These triggers also offered a better signal selection efficiency than the electron triggers. Single muon triggers require the transverse momentum of the muon to be above 20 or 26 GeV, while the dimuon trigger requires both muons to be above 14 GeV. As the threshold of the single lepton trigger is quite high, addition of the dimuon triggers with lower p_{T} thresholds helps recover the efficiency losses for lower mass particles. As per ATLAS recommendations, an offline cut of 1 GeV above the trigger threshold p_{T} is applied in the selection to ensure that events are on the trigger plateau.

The list of triggers used per run period is shown in Table 5.4. The naming scheme of the trigger is made of various components separated by underscores. For example, in `HLT_mu20_iloose_L1MU15`, HLT stands for High level trigger, `mu20` is the lepton type (muon) and p_{T} threshold (20) in GeV, `iloose` is the name of the isolation working point, `L1MU15` means that atleast one muon with p_{T} over

1. The distance metric used to define overlapping objects is $\Delta R' = \sqrt{(\Delta y^2) + (\Delta \phi^2)}$ where Δy^2 represents the rapidity difference.

15 GeV is required by the L1 trigger.

Trigger Name
HLT_mu20_iloose_L1MU15 HLT_mu26_ivarmedium
HLT_2mu10 HLT_2mu14

Table 5.4 – List of triggers per run used to collect events for the analysis.

5.4 Signal Region Cuts and Optimization

The signal model for this analysis is characterized by two top quark decay chains. One is given by $t \to bW^-$ and the other is $t \to bH^+ \to bW^+A \to bW^+\mu^+\mu^-$. The search is thus conducted by looking for a signal in the $\mu^+\mu^-$ invariant mass spectrum. In principle, the H^+ spectrum could have been searched for as well, but this was not used due to its poor resolution. This results both from the ambiguity in the association of one of the two W bosons in the event to the H^+ candidate, and the difficulties in accurately reconstructing either the leptonic or the hadronic W boson momentum (see Section 9.1 for a discussion).

The $A \to \mu^+\mu^-$ decay mode was chosen as muons provide a clean signature, good momentum resolution and identification efficiency. The selection is optimized for the semi-leptonic decays of the W bosons with electrons ($WW \to e\nu q\bar{q}$). The final states thus contain three leptons: $e\mu\mu$. The semi-leptonic decay was chosen due to the exceedingly large backgrounds and poor sensitivity in the hadronic W channel.

The optimal cuts were determined by studying the difference in the signal and background shapes for various kinematic distributions using Monte Carlo simulations. At first, a loose selection was used which captures the scope of this search. It is defined as follows:

• **SR0**: exactly 2 opposite-sign (OS) muons and 1 electron, $12 < m_{\mu\mu} < 77$

Various distributions with SR0 cuts are shown in Figure 5.7. The jet requirements were optimized in the first step. The optimal value for the cut was chosen

such that it maximizes the signal-to-background ratio as shown in Figure 5.10. It was found that ≥ 3 jet and ≥ 1 b-tagged jet provided the best performance. A stricter selection was then applied as follows:

• **SR1**: exactly 2 OS muons and 1 electron, $12 < m_{\mu\mu} < 77$, ≥ 3 jets, ≥ 1 b-tagged jet

The kinematic distributions with SR1 cuts are shown in Figure 5.8. The electron p_{T} and muon p_{T} fraction , $p_{\mathrm{T}}(\mu_2)/p_{\mathrm{T}}(\mu_1)$, were determined to be good discriminating variables in this step. The optimal value for the electron p_{T} was determined to be ≥ 20 GeV and for the $p_{\mathrm{T}}(\mu_2)/p_{\mathrm{T}}(\mu_1)$ it was ≥ 0.2. It was also found that the muon p_{T} fraction cut can provide better sensitivity when it is applied in events where the sub-leading muon and electron have the same sign. The kinematic distributions with the finalized cuts are shown in Figure 5.9.

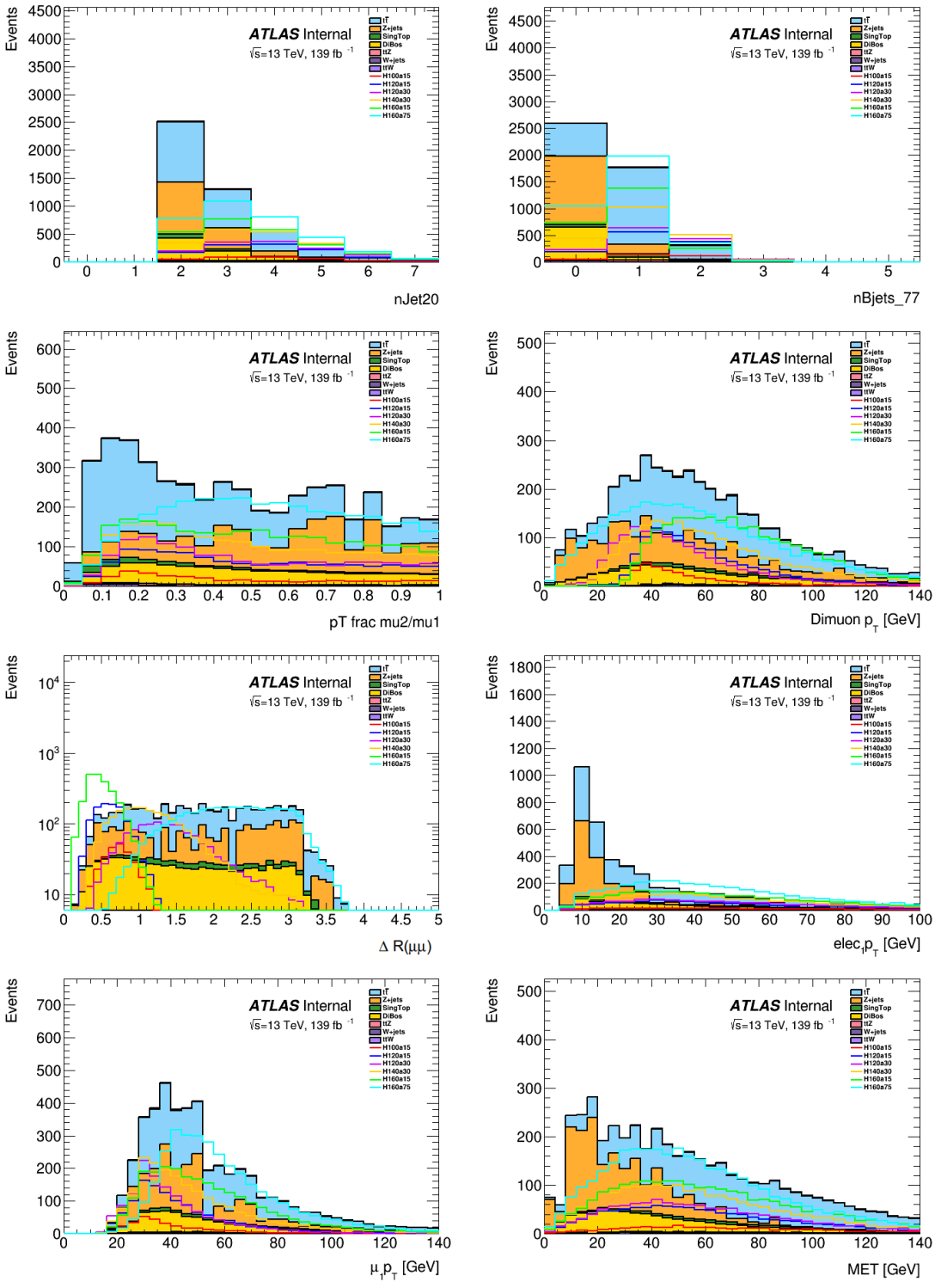

Figure 5.7 – Signal Selection Optimization: A selection of the numerous shape distributions that were studied to optimize the signal selection. SR0 cuts have been applied for these plots.

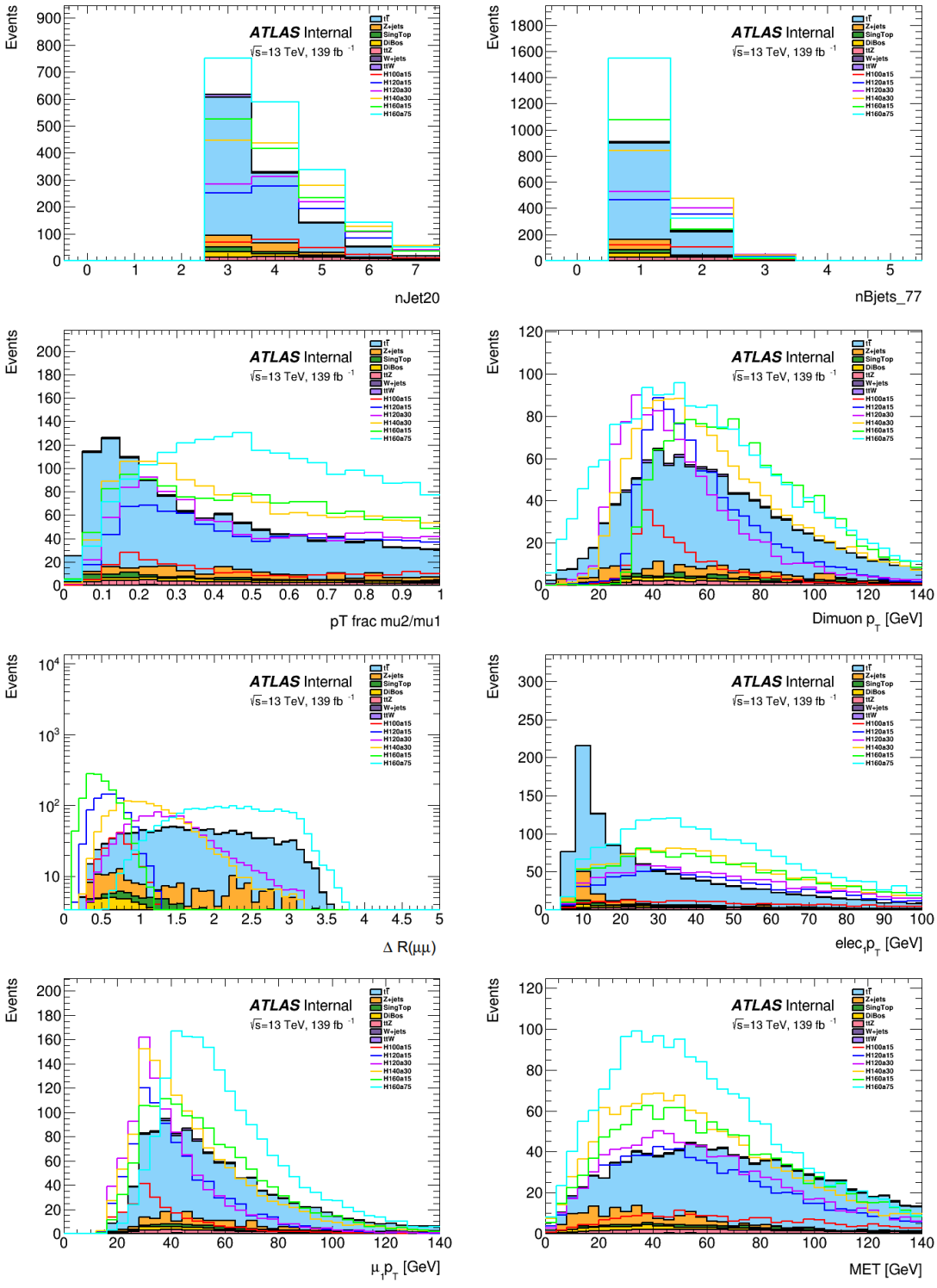

Figure 5.8 – Signal Selection Optimization: A selection of the numerous shape distributions that were studied to optimize the signal selection. SR1 cuts have been applied for these plots.

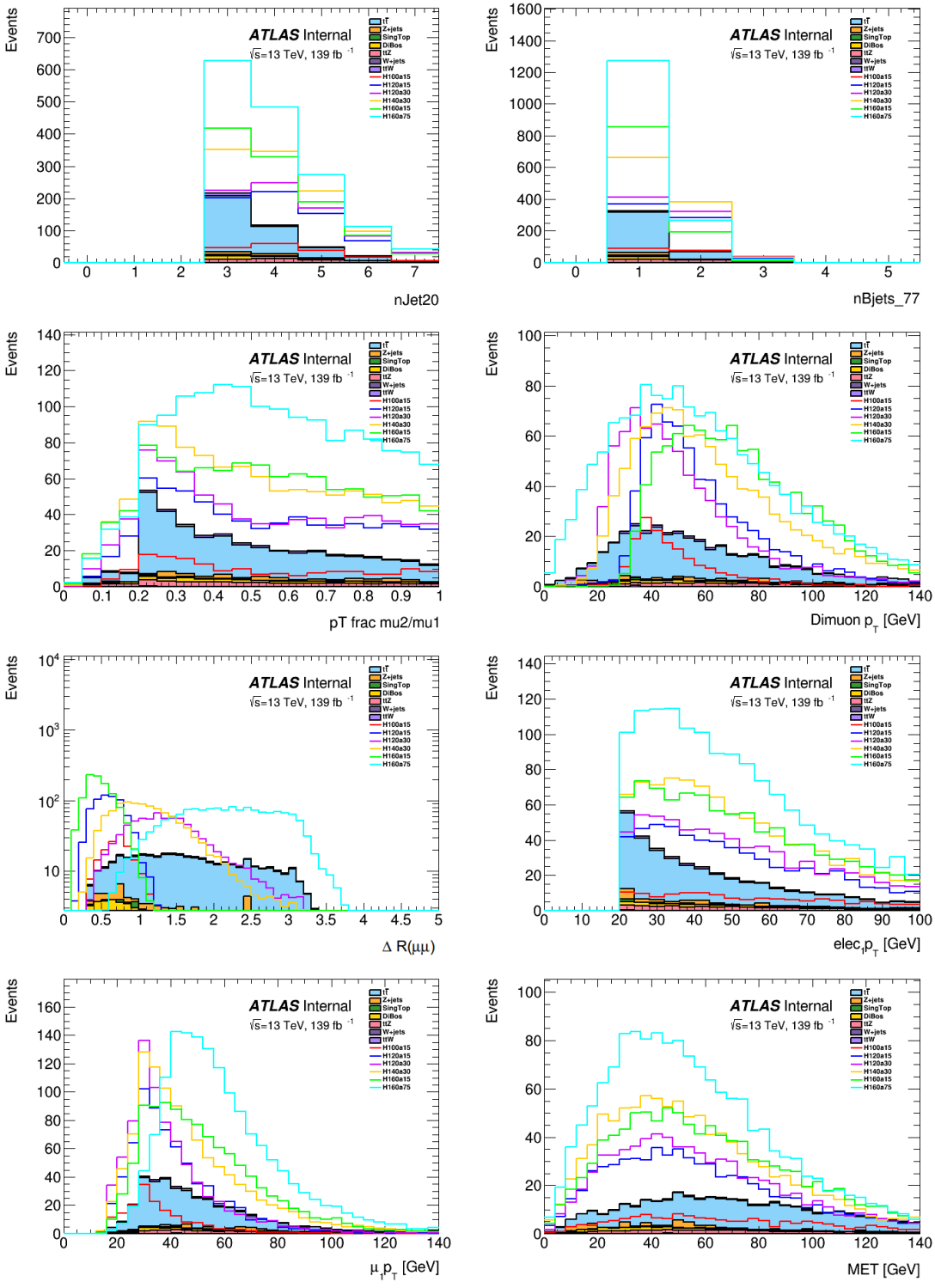

Figure 5.9 – Signal Selection Optimization: A selection of various kinematic distributions after applying all the signal selection cuts.

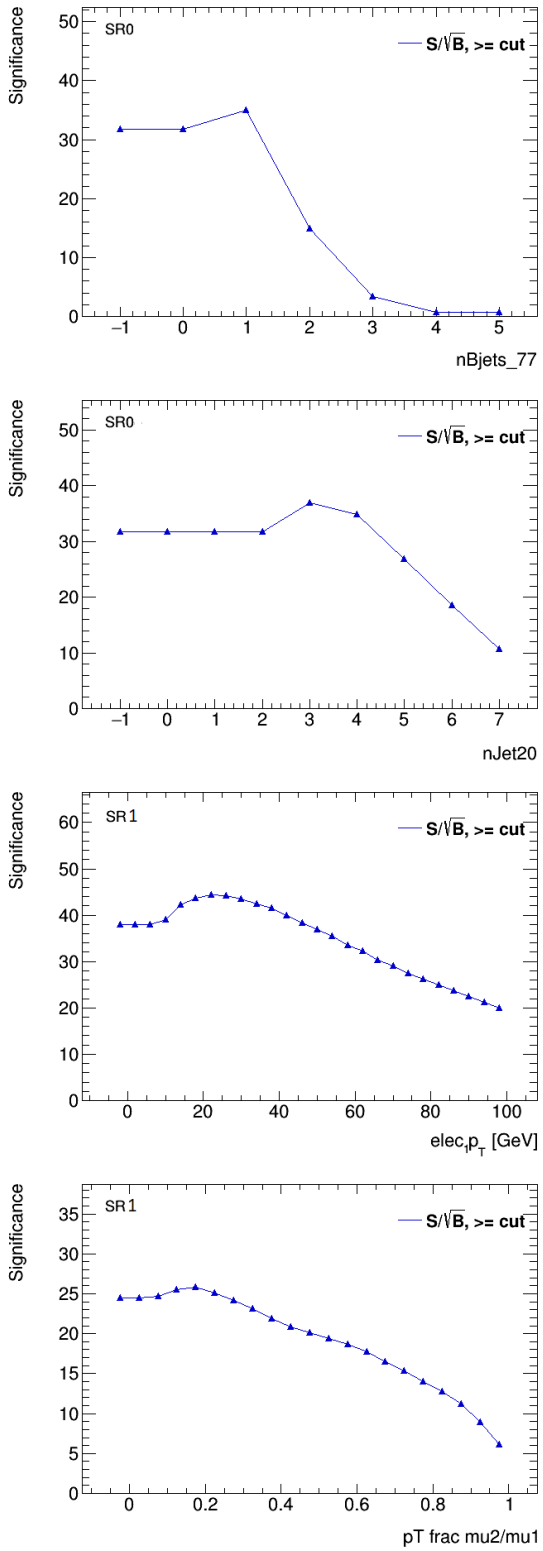

Figure 5.10 – Signal Selection Optimization: Signal-to-background ratio for various distributions using the m_A = 15 GeV signal sample.

The final selection cuts for the analysis are summarized in Table 5.5. This selection criteria is also referred to as the inclusive signal region or 'SRInclusive' in this thesis. It represents the target phase-space of the search, before this region is further split into small $m_{\mu\mu}$ windows for hypothesis testing as will be explained in Chapter 6. The selection efficiencies for the signal mass points using this criteria is shown in Figure 5.11. Details of the efficiency calculation can be found in Appendix A.1.

The shape of the signal and the di-muon mass resolution in the SR can be seen in Figure 5.12. The di-muon mass resolution depends roughly linearly on the mass of the A boson, going from 0.35 GeV at 15 GeV to 1.6 GeV at 75 GeV.

	Event selection	
Trigger	single muon	di-muon
Muons	$p_{\mathrm{T}}^{\text{leading}} > 27$ GeV, $p_{\mathrm{T}}^{\text{subleading}} > 5$ GeV	$p_{\mathrm{T}}^{\text{leading}} > 15$ GeV, $p_{\mathrm{T}}^{\text{subleading}} > 15$ GeV
	exactly 2, opposite sign $12 < m_{\mu\mu}$ [GeV] < 77 $p_{\mathrm{T}}(\mu_2^{SS})/p_{\mathrm{T}}(\mu_1^{OS}) > 0.2$[1]	
Electrons	exactly 1, $p_{\mathrm{T}} > 20$ GeV	
Jets	≥ 3, $p_{\mathrm{T}} > 20$ GeV ≥ 1 b-tagged jet	

Table 5.5 – Summary of the final signal region cuts. [1]The OS and SS in the p_{T} fraction refer to the muons having opposite-sign or same-sign with respect to the electron in the event.

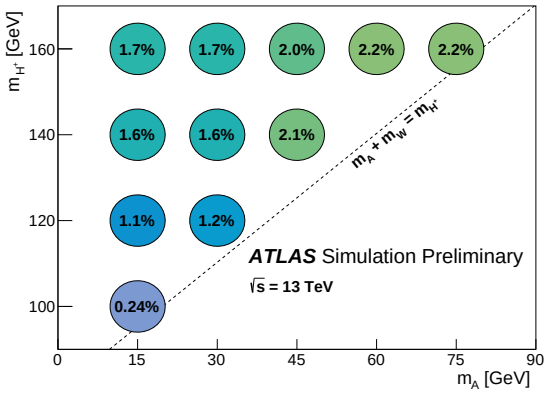

Figure 5.11 – The grid of simulated signal mass points with the final selection efficiency inscribed, as discussed in Appendix A.1. The dotted line shows the kinematic limit below which on-shell decay of $H^+ \to WA$ is not possible.

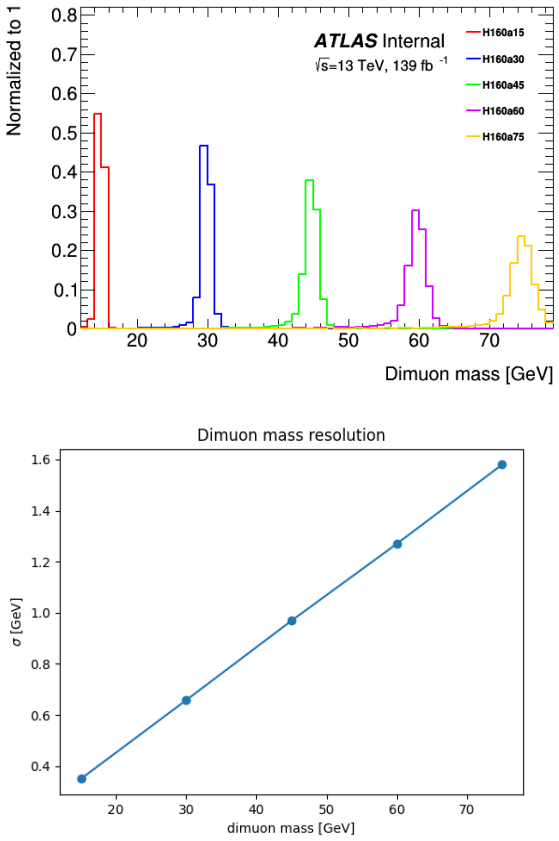

Figure 5.12 – Distribution of the dimuon spectrum with the simulated signal samples at 1 GeV binning(top). Dimuon mass resolution at various points in the signal region (bottom).

6

Analysis Design

6.1 General Strategy

The search for the $H^+ \to WA \to W\mu\mu$ process is carried out by looking for an excess in the opposite-sign $m_{\mu\mu}$ spectrum in the range of 15 to 75 GeV. It is assumed that the signal has a localized peak which would appear above the non-resonant background. The wide signal region is therefore divided into small windows and the background event yield in each window is compared with data to determine if a significant deviation from the SM prediction is observed. The background prediction in each window is determined from simulations using the method detailed in this section. The signal is estimated either using the generated signal samples or through interpolation for the mass points where no MC sample exists. Single-bin counting experiments are conducted to look for an excess in each mass window, and are used to set upper limits at the 95% confidence level. The mass windows have bin widths that optimize the sensitivity.

6.2 Overview of Background Model

The dominant background expected in the signal region is from $t\bar{t}$ pair-production ($\approx$ 75%), while the sub-dominant backgrounds are from ttZ ($\approx$ 10%) and Z+HF jets ($\approx$ 10%), where HF stands for Heavy Flavour and indicates that the associated jets contain at least a b or c hadron. The $t\bar{t}$ background events can have two real leptons from the W, but must consist of atleast one non-prompt or fake lepton, which is predominantly the sub-leading muon. The fake leptons arise from

heavy flavored hadron decays in b, c quark originated jets in the $t\bar{t}$ semi-leptonic processes, as shown in Figure 6.1. Smaller contributions from other background sources include: single-tops, ttW, dibosons and W+jets and Z + LF, where LF stands for Light Flavour and indicates that none of the associated jets contain a b or c hadron. The change in the $t\bar{t}$ background due to top decay to H^+ is neglected. The expected distribution of the background in the SR is shown in Figure 6.2.

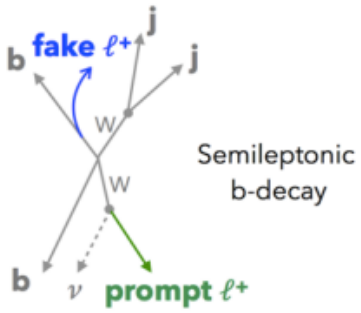

Figure 6.1 – Example of prompt and fake leptons from heavy flavour decays [192].

The main backgrounds ($t\bar{t}$, ttZ, Z+HF) are estimated using a semi-data driven approach. High statistic MC samples are used as a base template for the backgrounds and their overall yield is normalized to the data using a profile likelihood fit in background-enriched control regions (CRs). A free-floating normalization factor (NF), μ, is associated with each of the CRs and represents the scaling of the background sample to the nominal cross-section. An estimate of the backgrounds in the SR can be obtained by applying these NFs to the simulation using the CR-only fit procedure described below.

The minor backgrounds do not have any normalisation parameters assigned, their yields can vary only as constrained by their cross section uncertainties. The multijet background is expected to be small since three leptons are required; this follows the ttW and ttH analyses [193]. Any unforeseen multijet fake contribution will populate the CRs in a similar way to the signal region, and thus the background modelling would account for it. Contributions from rare processes such as triboson events were also found to be negligible. The MC templates in the analysis could be further split and reorganized based on the fake composition. However, this was deemed unnecessary given the good Data/MC agreement seen

in the background validation studies documented in the next section. Additionally, the lack of simulation statistics visible in the Z+jets simulation is addressed by replacing the MC distribution with a smooth function; the details are given in Appendix A.2.1.

To check the robustness of this method, a validation region is defined which has similar kinematics and background composition as the signal region. Data/MC agreement in this region is used to further validate the background model.

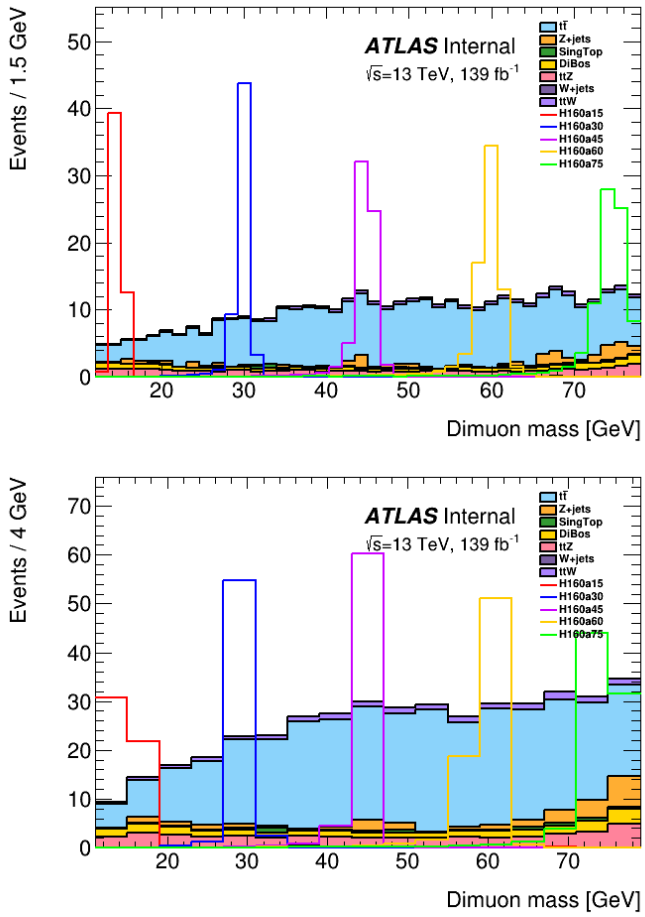

Figure 6.2 – Expected distribution of the backgrounds, overlaid with the signal, after selection cuts. Fit parameters are set to their nominal values (i.e. pre-fit). Both narrow binning (1.5 GeV) and wide binning (4 GeV) are shown, bracketing the range used in the analysis. Signal has been scaled to show good visibility in the plot, assumption for normalization are: σ = 831.76 pb, $BR(t \to H^+b)$ = 5%, $BR(H^+ \to WA)$ = 1, $BR(A \to \mu\mu) = 3 \times 10^{-4}$.

6.3 Control and Validation Regions

	Shared Cuts				
muons	Exactly 2 $p_{\mathrm{T}}^{\mathrm{leading}} > 27$ GeV, $p_{\mathrm{T}}^{\mathrm{subleading}} > 5$ GeV (single-mu trig) $p_{\mathrm{T}}^{\mathrm{leading}} > 15$ GeV, $p_{\mathrm{T}}^{\mathrm{subleading}} > 15$ GeV (dimuon trig) $p_{\mathrm{T}}(\mu_2^{SS})/p_{\mathrm{T}}(\mu_1^{OS}) > 0.2$				
electrons	Exactly 1				
jets	At least three, $p_{\mathrm{T}} > 20$ GeV, of which at least one is a b-tagged jet				
	CRZ	CRtt$Z$	CR$t\bar{t}$	SRIncl	VR
M$\mu\mu$ [GeV]	[78,102]	[78,102]	[12,77]	[12,77]	No M$\mu\mu$ cut
Electron p_{T} [GeV]	< 20	> 20			
dimuon charge	OS		SS	OS	No charge cut
M$e\mu$ [GeV]	No M$e\mu$ cut				$30 < Me\mu_1 <$110

Table 6.1 – Summary of the Control, Validation and Signal Regions. SRInclusive refers to the signal region before the dimuon mass cuts have been applied to it in order to split it into small windows.

The control regions (CRs) in the analysis serve to validate the event modeling kinematics of the background MC and to determine the overall normalization factors. They are defined in Table 6.1. Each control region is designed to enrich the background being constrained and is orthogonal to the SR; the signal contamination in the CRs was found to be negligible (less than 0.1 %). Description of the CRs are as follows:

• **CR$t\bar{t}$:** This region is used to constrain the primary background i.e. $t\bar{t}$ events with a fake muon. The region differs from the signal region in only one aspect: same-sign (SS) muons are required instead of opposite-sign (OS) muons. The modeling of the $t\bar{t}$ simulation in this region serves as a good indicator of the type of modeling that can be expected in the SR.

• **CRtt$Z$:** This region is simply in the side-band of the signal region and the dimon mass range is $78 < M_{\mu\mu} < 102$ GeV. The idea is to use the Z-peak to constrain the ttZ background.

• **CRZ:** This region is used to constrain the Z+HF background. The Z + jets

background is split into HF and LF components and only the HF component has a floating cross-section. HF refers to jets that contain a b or c hadron. Such jets make up 84% of the Z events in this region. This region is the same as CRtt$Z$ except the high-p_{T} electron cut is inverted to enrich the contribution from fake electrons in Z+jets which dominate in the SR.

A validation region (VR) is defined to test the fitting procedure; it serves to validate the extrapolation method from the CR to the SR. The VR is designed to be in between CR$t\bar{t}$ and SR. While the SR and CR$t\bar{t}$ are completely orthogonal (one has OS muon requirement while the other has SS muons), there are no sign requirements on the muons in this region. A subset of tri-lepton events, with both opposite-sign and same-sign di-muon pairs, is selected by requiring a dilepton mass of 30 GeV $< m_{e\mu} <$ 110 GeV, where $e\mu$ represents the electron and leading muon. The result is a diluted, signal-depleted region which has similar statistics, kinematics and background composition as the SR and thus can be used to test the fitting procedure. One-third of the events are same-sign while the rest are opposite-sign in this region. To ensure this region could be studied reliably, the signal contamination was checked and found to be only 0.8 % on average in this region assuming a $BR(t \to H^{+}b)$ of 1 % , $BR(H \to WA)$ = 1 and $BR(A \to \mu\mu)$ of 3×10^{-4}.

6.4 Fit Configurations

As discussed previously, profile likelihood fits for the analysis are carried out using the `HistFitter` [121] package. The likelihood is a product of Poisson probability density functions and Gaussian distributions that constrain the nuisance parameters associated with the systematic uncertainties. These fits are used to determine the normalization factors for the dominant backgrounds, and to calculate p-values and exclusion limits. The fit configurations in this analysis are described below.

6.4.1 CR-only Fit

The purpose of this configuration is to determine the normalization factors, estimate the expected events in the SR and validate the background simulation.

In this mode, a fit to the data is done simultaneously in the three single-bin CRs and the free floating NFs corresponding to each of the backgrounds is measured: $\mu_{t\bar{t}}$, μ_{ttZ}, μ_Z. A value of unity for these parameters represents the nominal SM rate for the process. These NFs are determined by maximizing the likelihood function such that it tends towards a configuration which gives the best possible compatibility between the yields in the simulation and the data in the CRs.

The SR and signal samples are not included in this setup, as the fit name suggests. The NFs are applied to the pre-fit yields in the SR to get the expected background estimates. Data/MC agreement post-fit is studied in the CRs to determine the accuracy of the background MC simulation.

This configuration is also used to test the extrapolation process. Once the NFs are obtained from the fit in the CRs, they are applied directly to the VR. The VR is not included in the fit, i.e. this region is not used to constrain the backgrounds. Good Data/MC agreement in the CR and VR would indicate the soundness of the background model.

6.4.2 Signal + Background Fit

The signal+background mode of the fit is used to test for the presence of new phenomena; it calculates p-values and sets upper limits on the signal model.

In this mode, the fit is done simultaneously in four regions: CR$t\bar{t}$, CRttZ, CRZ and an SR window. The SR window is a part of the SRInclusive region; this 65 GeV wide region, $12 \leq m_{\mu\mu} \leq 77$ GeV, is split into smaller sections to improve the signal-to-background ratio for each mass hypothesis test. The window is centered around the mass hypothesis being tested. The signal region outside the window is not used by the fit. The optimized widths of the $m_{\mu\mu}$ windows for this analysis are summarized below:

- 1.5 GeV for $15 \leq m_{\mu\mu} \leq 30$ GeV;
- 2 GeV for $30 < m_{\mu\mu} \leq 45$ GeV;
- 3 GeV for $45 < m_{\mu\mu} \leq 60$ GeV;
- 4 GeV for $60 < m_{\mu\mu} \leq 75$ GeV.

These bin widths were chosen by optimizing the expected limit calculation. The limits were calculated in various parts of the spectrum with a different binning and the width providing the best sensitivity was chosen. Details of the study can be found in Appendix A.3.

To carry out the search, a series of likelihoods fits are performed as the SR window scans across the dimuon spectrum. A test statistic based on the profile likelihood ratio [120] is used to test hypothesized values of the signal strength μ_{sig} for each mass point. The statistical tests are performed in steps of 1 GeV for 15 GeV $\leq m_{\mu\mu} \leq 45$ GeV and 2 GeV for 46 GeV $\leq m_{\mu\mu} \leq 75$ GeV; this ensures that the SR windows partially overlap. The final limits are derived based on the compatibility between the observed and predicted yields in each mass window. Upper limits on the μ_{sig} are interpreted as limits on $BR(t \to H^+b) \times BR(H^+ \to WA) \times BR(A \to \mu\mu)$.

The analysis does not use a functional form fit; an approach commonly used for narrow resonance searches with smoothly falling backgrounds. This fitting strategy is often recommended when the statistics of the MC histogram templates are insufficient, the sidebands of the resonances are wide enough to ensure systematics from background subtraction are small or there are concerns of large uncertainties due to extrapolation from a CR [194]. The methodology presented here, which compares event yields within a narrow $m_{\mu\mu}$ mass window, was first motivated by two dimuon resonance searches [63, 195] relying on the same approach using partial Run-2 data. Both these techniques have been used in the past to carry out resonance searches, each offering its advantages and challenges.

The use of a cut-and-count approach (i.e. counting experiments in a mass window), rather than fitting a shape, has an important advantage for this analysis: the dependence on the H^+ mass enters only through the selection efficiency, without needing to parametrise a di-muon mass spectrum which would be a weak function of the H^+. This in turn means that the p-value calculation is independent

of the charged Higgs boson mass and depends only on the A mass. This simplifies the analysis design and the scan over a 2D-mass grid, allowing for limits to be easily interpolated over the (m_{H^+}, m_A) plane. The one-dimensional dependence on p-values also helps reduce the look-elsewhere effect [136] in case of a significant excess.

The side-bands of the individual mass points have not been used in these fit configurations to constrain the total background; although the side-band of the inclusive signal region is used to constrain the Z+jets and ttZ backgrounds. This could potentially improve the sensitivity by reducing the effect of systematic uncertainties; the precise improvement would depend on the treatment of the generator theory systematic (see Section 7.3.1) as this is one of the major sources of error. However, blinding constraints and concerns of signal contamination made it difficult to study this region as a CR. The same-sign region which is orthogonal with negligible contamination was thus chosen to constrain and study the primary background.

As will be seen in the breakdown of uncertainties in the following section, the systematic error on the background predictions is generally less than the statistical one, so the gain from using the side-bands would not be exceptional. They would also come with shape systematics which would be most important in the high background regions - exactly where the current systematics become more important. The use of CRs instead of a sideband fit gives background composition detail and simplifies the analysis by making the evaluation of the p-value independent of the charged Higgs boson mass. As will be seen in the validation studies presented in Section 6.7, the CR also offers a very good prediction of the background rates and modeling of the kinematic variables.

6.5 Signal Interpolation

To conduct the search across the entire SR, signal yields have to be determined for masses that were not generated in the MC signal samples (see Figure 5.11 for the generated mass points). These yields are interpolated using order-3

splines which produce a smooth curve connecting the known yields. The values obtained from the spline interpolation are used as nominal yields for the intermediate masses when conducting the analysis. Since the SR is split into windows of various widths, the interpolation procedure is repeated for the widths used: 1.5 GeV, 2 GeV, 3 GeV and 4 GeV.

The splines demonstrating the interpolation between various H^+ masses are shown in Figure 6.3 and Figure 6.4. These plots show that the splines are well-behaved and the simulated mass points provide the appropriate knots to create a smooth interpolation. A closure test was conducted to validate the accuracy of the interpolation procedure and can be found in Appendix A.4.

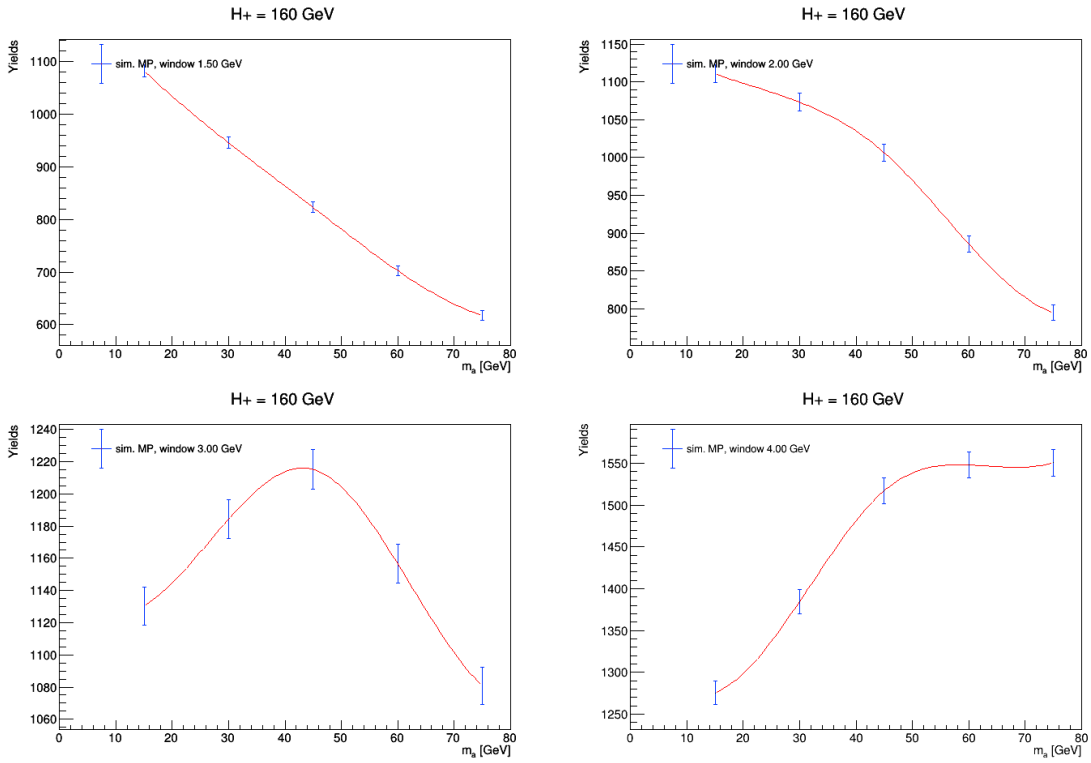

Figure 6.3 – Signal Interpolation: Plots showing the interpolation of yields between simulated mass points using cubic splines for H^+ = 160 GeV masses, assuming $BR(H \rightarrow AW = 1)$ and $BR(A \rightarrow \mu\mu = 3 \times 10^{-4})$. These figures show that the splines are well-behaved and the simulated mass points provide the appropriate knots to create a smooth interpolation.

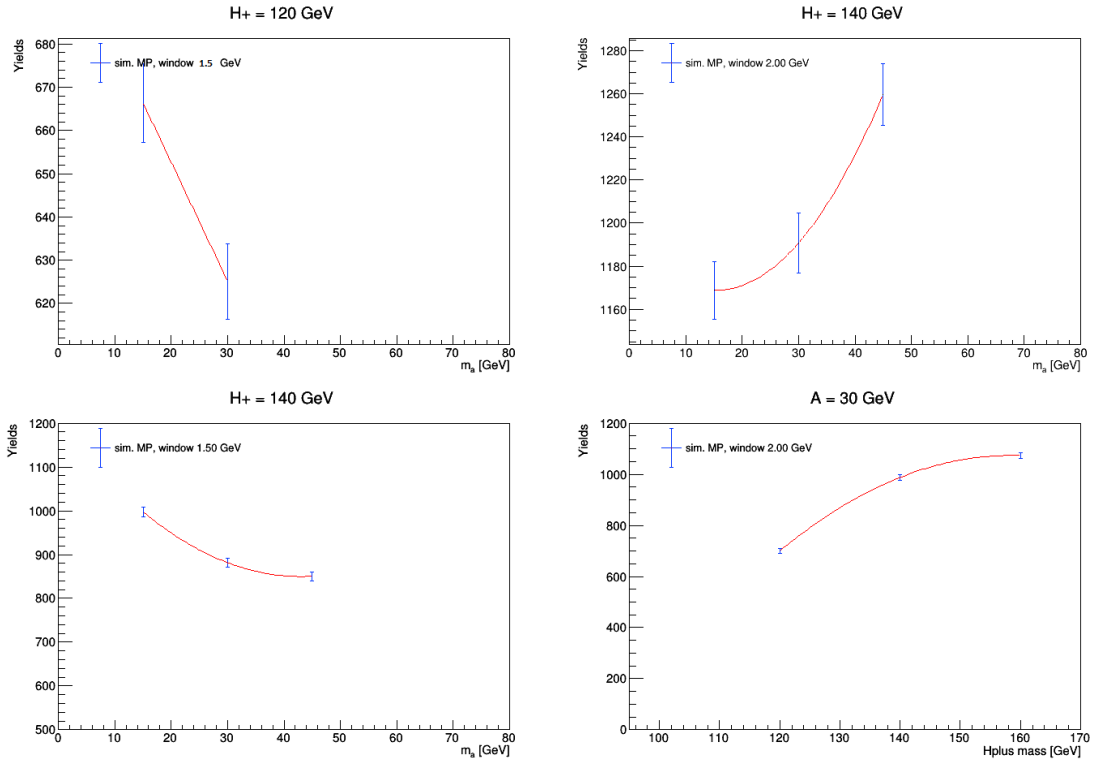

Figure 6.4 – Signal Interpolation: Plots showing the interpolation of yields between simulated mass points using cubic splines for H^+ = 140, 120 GeV masses assuming $BR(H \to AW = 1)$ and $BR(A \to \mu\mu = 3 \times 10^{-4})$. These figures show that the splines are well-behaved and the simulated mass points provide the appropriate knots to create a smooth interpolation.

6.6 Blinding Strategy

In order to avoid experimenter's bias in conducing the search, data in the signal region was entirely blinded during the design of the analysis as per standard practice. Only the data in control and validation regions was used prior to unblinding. In consultation with ATLAS Conveners of the Higgs to Light Resonance Searches (HLRS) physics group, the unblinding of the data to establish presence (or absence) of signal was done in three stages:

• Stage 1: Key kinematic variables such as p_{T} and η in the SR, with exception of the dimuon mass spectrum, were unblinded. This step was taken after the design of the background model was complete and it had been tested with data in the control regions. This step helped build confidence that the MC would accurately predict the shapes and scales in the SR.

• Stage 2: The data yields in only the inclusive signal region were unblinded at a more advanced stage with the finalized selection cuts. Using typical $BR(t \to H^+b)$ of 1 % , $BR(H^+ \to WA)$ = 1, $BR(A \to \mu\mu)$ of 3×10^{-4} and a signal efficiency of 2.5% showed an expectation of about 19 signal events for a sample signal mass point of m_A = 45 GeV against an expected background of about 470 events. Thus, the signal was less than the total uncertainty on the inclusive yield ($\approx \pm 40$) and one wouldn't be sensitive to it in this diluted region.

• Stage 3: The entire dimuon spectrum was unblinded in the final stage of the review process. This step was taken after all aspects of the design were completed and the analysis had been thoroughly reviewed by Editorial Board members, designated Technical Reviewers and all the Conveners of the Higgs and Diboson Searches (HDBS) physics group.

6.7 Background Model Validation

The section documents the studies carried out using the CR-only fit procedure to validate the background model. In summary, they show that the Monte Carlo simulations agree with the data and can be used to reliably estimate back-

grounds.

These studies proceed by measuring the NFs in the control regions and then comparing the data with simulation post-fit. After executing the fit, the NFs were found to be:

- $\mu_{t\bar{t}} = 1.04 \pm 0.10$
- $\mu_{Z} = 1.03 \pm 0.21$
- $\mu_{ttZ} = 1.61 \pm 0.41$

Two of them are compatible with one, indicating that the simulation predicts background rates reliably even in the regions dominated by fake leptons. The normalization factor for ttZ deviates from unity, but is compatible with the previous ATLAS measurement [196].

The post-fit yields in the various kinematic regions can be seen in Table 6.2. By construction, the fit forces the total background rate in the CRs to match the data, fixing the total error and introducing anti-correlations between the components. The fitted yields in the VR and SRInclusive show good agreement with the predicated event rates, providing evidence that the background modelling is reliable. This is also supported by distributions of kinematic quantities in the inclusive signal region, shown later in Figure 6.7.3.

Regions	CRZ	CR$t\bar{t}$	CRttZ	VR	SRIncl
Observed events	803	190	635	529	465
Fitted bkg events	803 ± 28	190 ± 14	635 ± 25	541 ± 43	470 ± 37
Fitted $t\bar{t}$	136 ± 21	170 ± 14	97 ± 19	388 ± 46	320 ± 39
Fitted Z+HF	491 ± 49	0.72 ± 0.16	43 ± 8	18 ± 6	29 ± 6
Fitted Z+LF	84 ± 29	0.41 ± 0.14	12 ± 4	2.82 ± 0.98	13 ± 4
Fitted $t\bar{t}Z$	52 ± 14	6.40 ± 1.64	327 ± 83	76 ± 19	64 ± 16
Fitted diBoson	34 ± 17	0.58 ± 0.29	147 ± 73	32 ± 16	22 ± 11
Fitted W+jets	0.01 ± 0.01	0.40 ± 0.39	0 ± 0	0.08 ± 0.07	0.49 ± 0.48
Fitted Single top	4.13 ± 0.29	4.38 ± 0.23	2.39 ± 0.12	9.00 ± 0.46	6.17 ± 0.33
Fitted $t\bar{t}W$	1.06 ± 0.15	7.43 ± 0.97	6.42 ± 0.83	14 ± 2	16 ± 2
Pre-Fit MC bkg events	762 ± 93	181 ± 9	505 ± 76	497 ± 31	433 ± 23
Pre-Fit $t\bar{t}$	131 ± 15	163 ± 9	93 ± 14	373 ± 22	308 ± 18
Pre-Fit Z+ HF	475 ± 79	0.69 ± 0.08	42 ± 6	18 ± 7	28 ± 3
Pre-Fit Z+ LF	84 ± 30	0.41 ± 0.14	12 ± 4	2.82 ± 0.99	13 ± 4
Pre-Fit $t\bar{t}Z$	32 ± 2	3.97 ± 0.12	202 ± 3	47 ± 1	40 ± 1
Pre-Fit Diboson	34 ± 17	0.58 ± 0.29	147 ± 74	32 ± 16	23 ± 11
Pre-Fit. W+jets	0.01 ± 0.01	0.40 ± 0.40	0 ± 0	0.08 ± 0.07	0.49 ± 0.49
Pre-Fit Single top	4.13 ± 0.29	4.38 ± 0.23	2.39 ± 0.12	9.00 ± 0.47	6.17 ± 0.33
Pre-Fit $t\bar{t}W$	1.06 ± 0.15	7.43 ± 0.97	6.42 ± 0.84	14 ± 2	16 ± 2

Table 6.2 – CR-only Fit studies: Pre-fit and post-fit yields in the CRs, SRInclusive and VR with uncertainties. By construction the fit only affects $t\bar{t}$, Z+HF and $t\bar{t}Z$ and forces the total background yield in the three CRs to match the data, fixing the total error and introducing anti-correlations between the components. In contrast, the agreement in the VR and SRInclusive validates the background estimation method. The pre-fit error in CR$t\bar{t}$ appears smaller than post-fit because $t\bar{t}$ has no pre-fit cross-section uncertainty applied, while the dominating uncertainty post-fit is the normalization uncertainty. Note that the SRInclusive is treated as a VR by the fit for this study.

6.7.1 Data/MC in Control Regions

The plots in this section show the Data/MC agreement post-fit for various kinematic variables using the CR-only mode of the fit. Figure 6.5 shows the mass spectrum in various regions while Figures 6.6, 6.7, 6.8 and 6.9 highlights the modeling of p_{T}, η and other variables in the control regions. All the plots show good modeling and agreement with data.

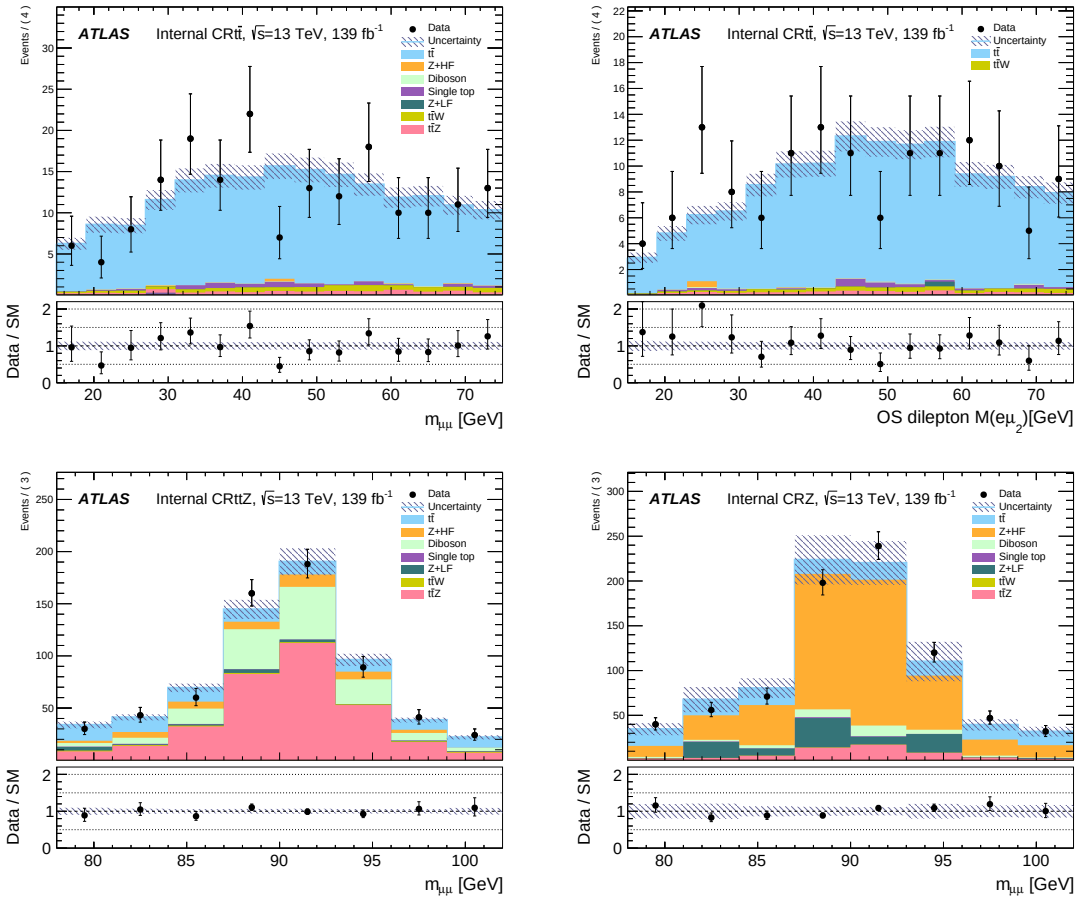

Figure 6.5 – CR-only Fit studies: Post-fit MC distributions of various mass variables in comparison to data are shown in the CRs. Since CR$t\bar{t}$ has SS muons, unlike the SR, the OS M$e\mu$ spectrum is also shown to check modelling of OS leptons.

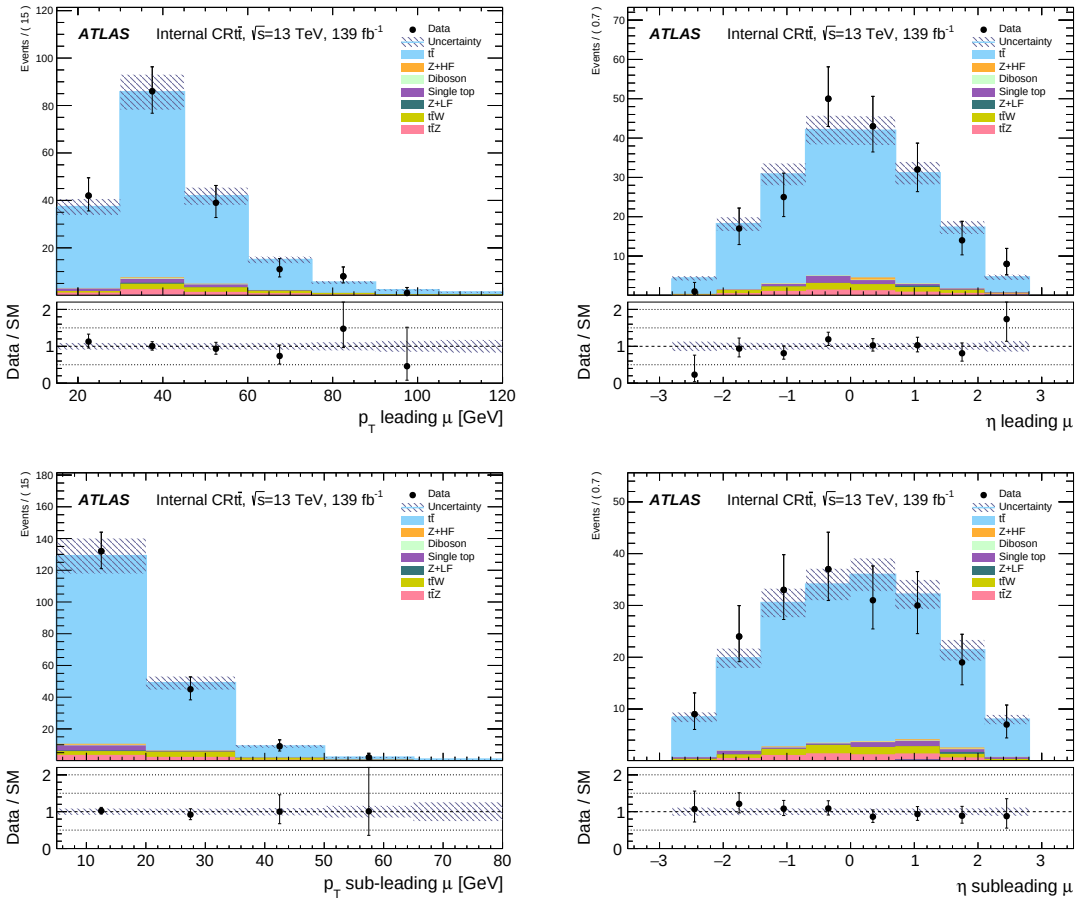

Figure 6.6 – CR-only Fit studies: Modeling of the η and p_{T} variables for the leptons in CR$t\bar{t}$.

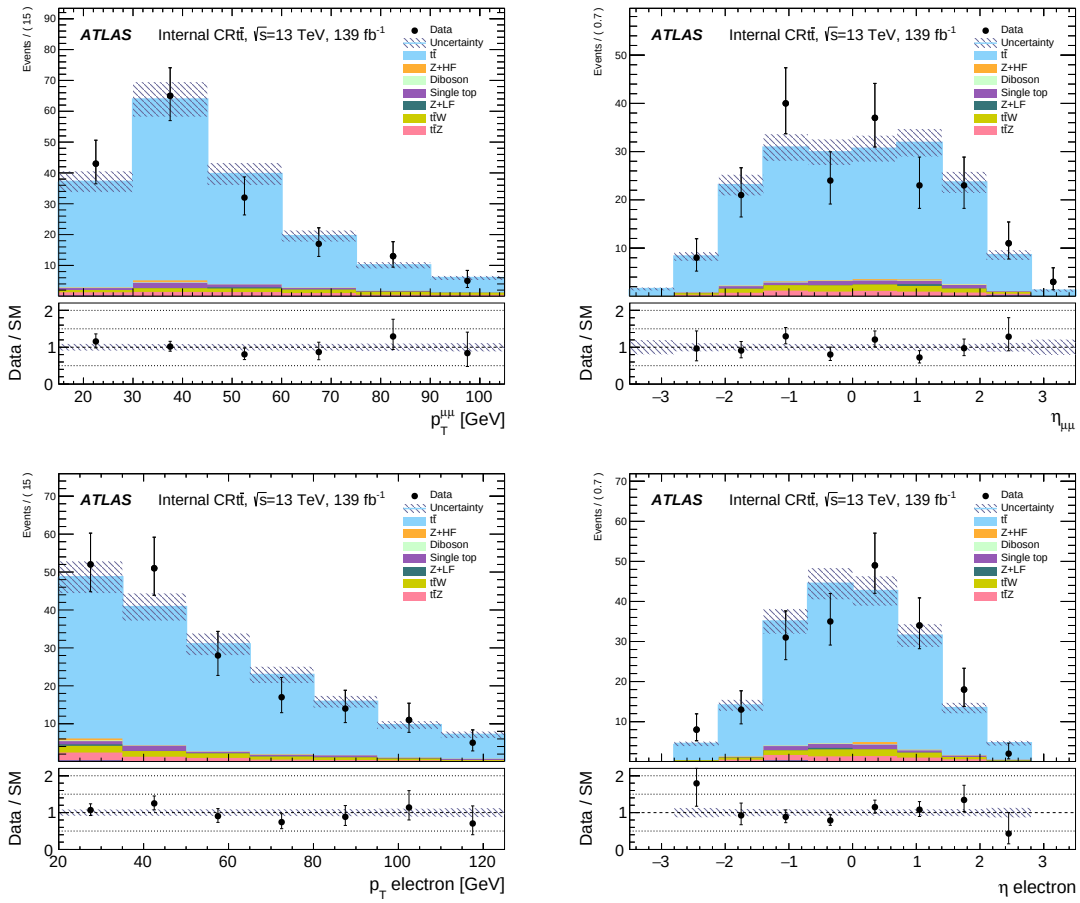

Figure 6.7 – CR-only Fit studies: Data/MC comparisons for various kinematic variables for the leptons in CR$t\bar{t}$.

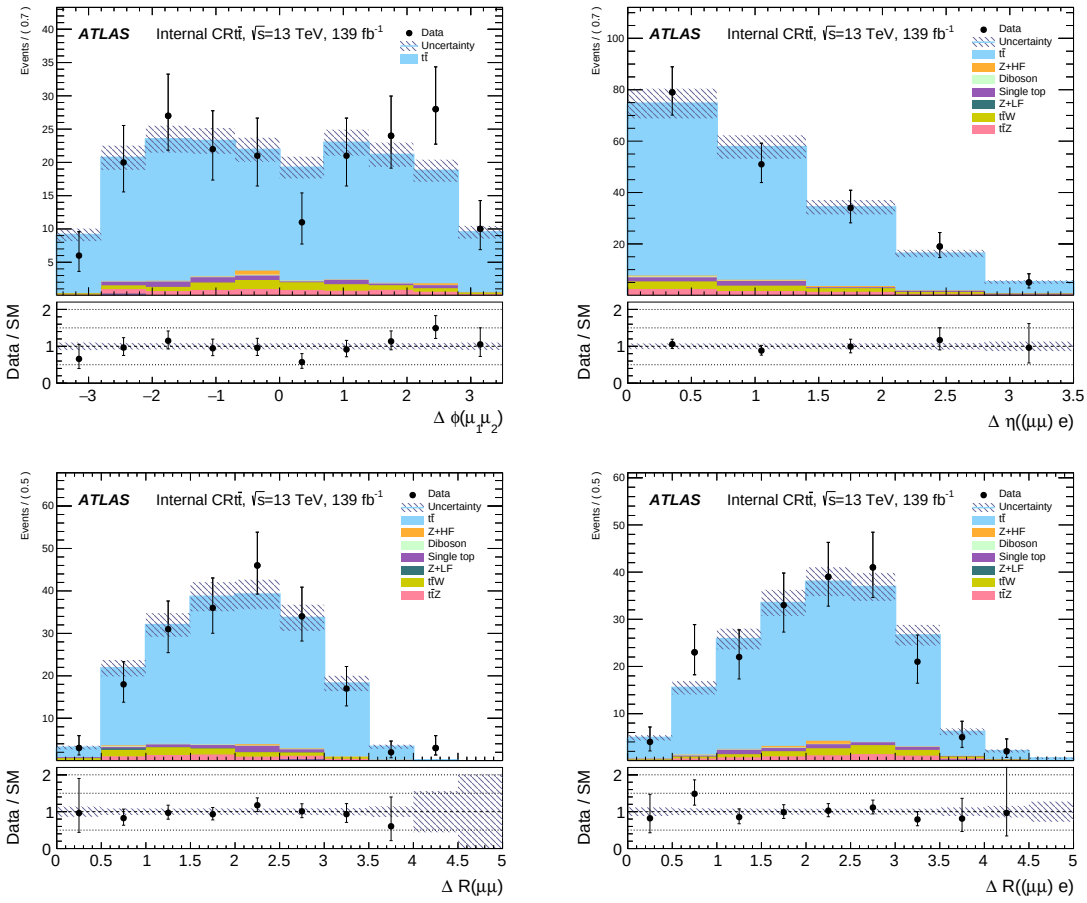

Figure 6.8 – CR-only Fit studies: Data/MC comparisons for dilepton kinematics in CR$t\bar{t}$.

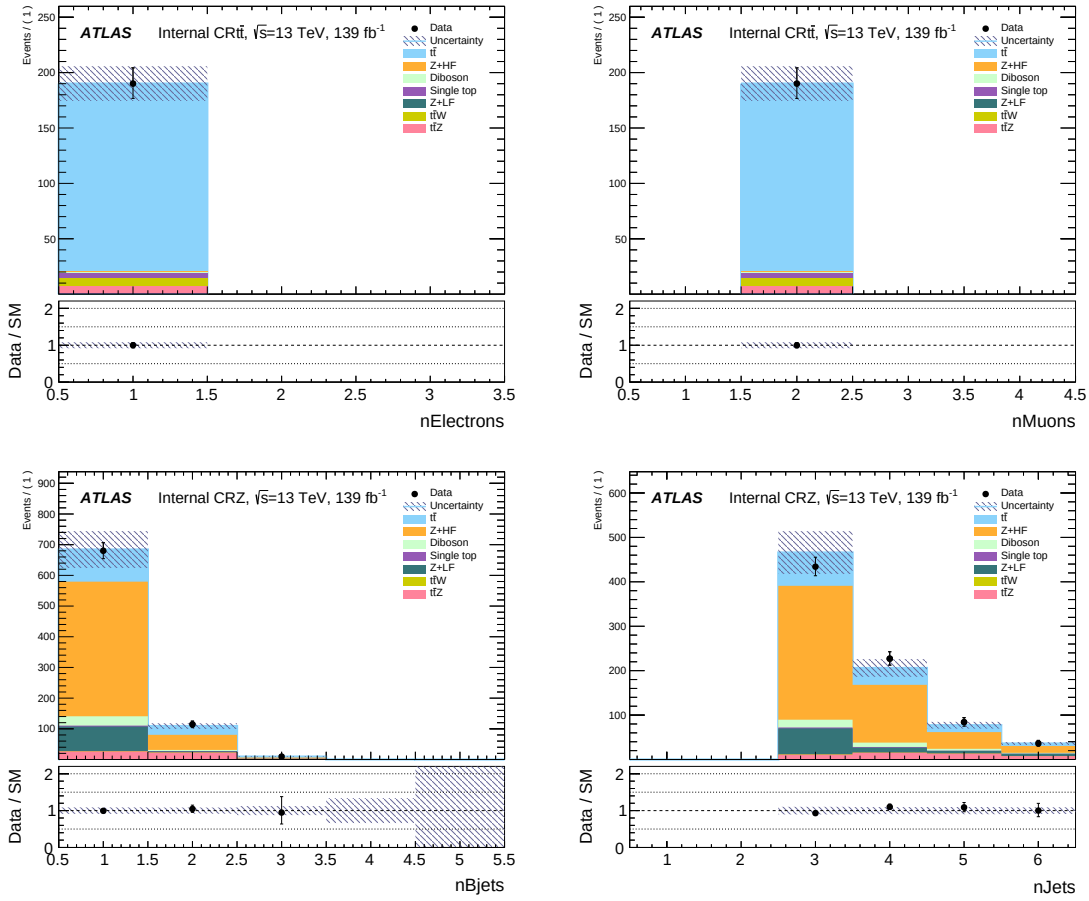

Figure 6.9 – CR-only Fit studies: Data/MC comparisons for lepton and jet multiplicities in CR$t\bar{t}$ and CRZ.

6.7.2 Data/MC in Validation Region

To validate the fitting procedure, various distributions are shown from the VR in Figures 6.10, 6.11, 6.12, 6.13. The CR-only mode of the fit is used and the VR is not used to constrain the background. All the plots show good modeling and agreement with data.

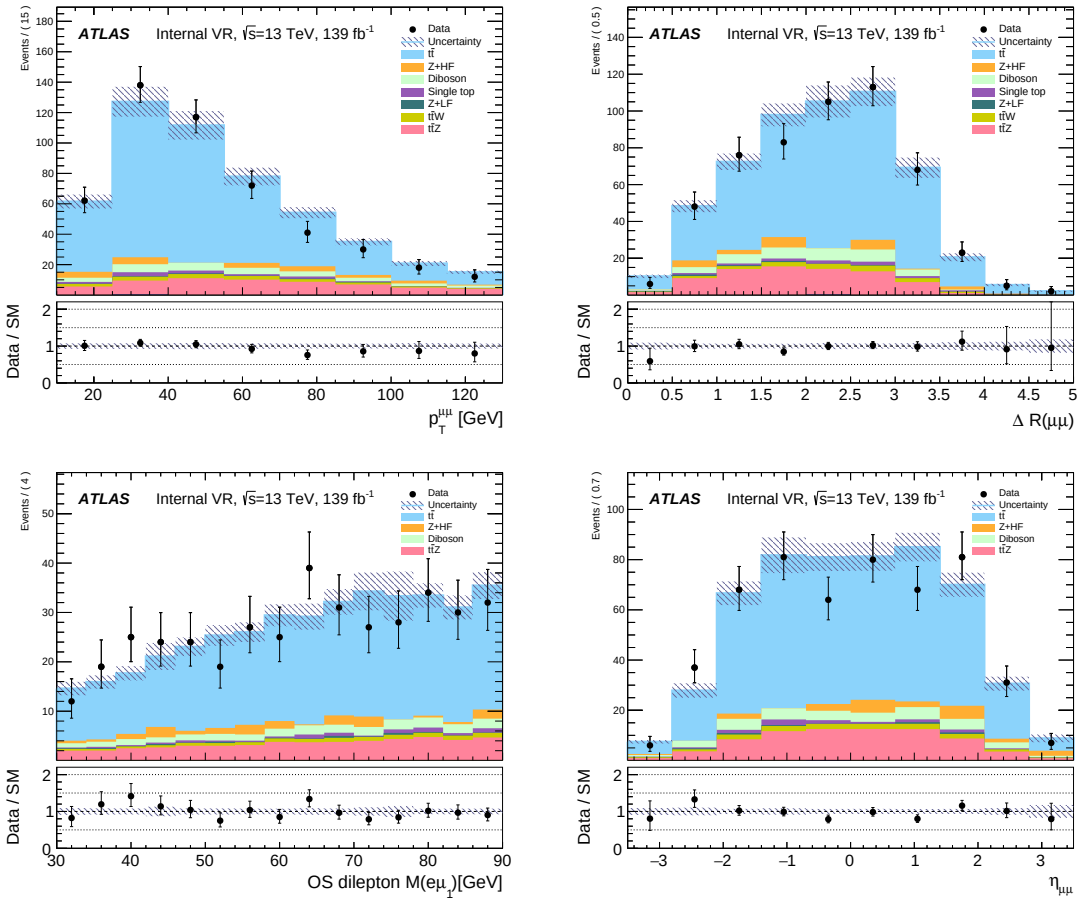

Figure 6.10 – CR-only Fit studies: To validate the fit and test the shape modelling, various distributions for the dimuon kinematics are shown from the VR. Recall that the VR is a mixture of OS and SS dimuon events. These plots thus show that both OS and SS events are modelled well by simulation.

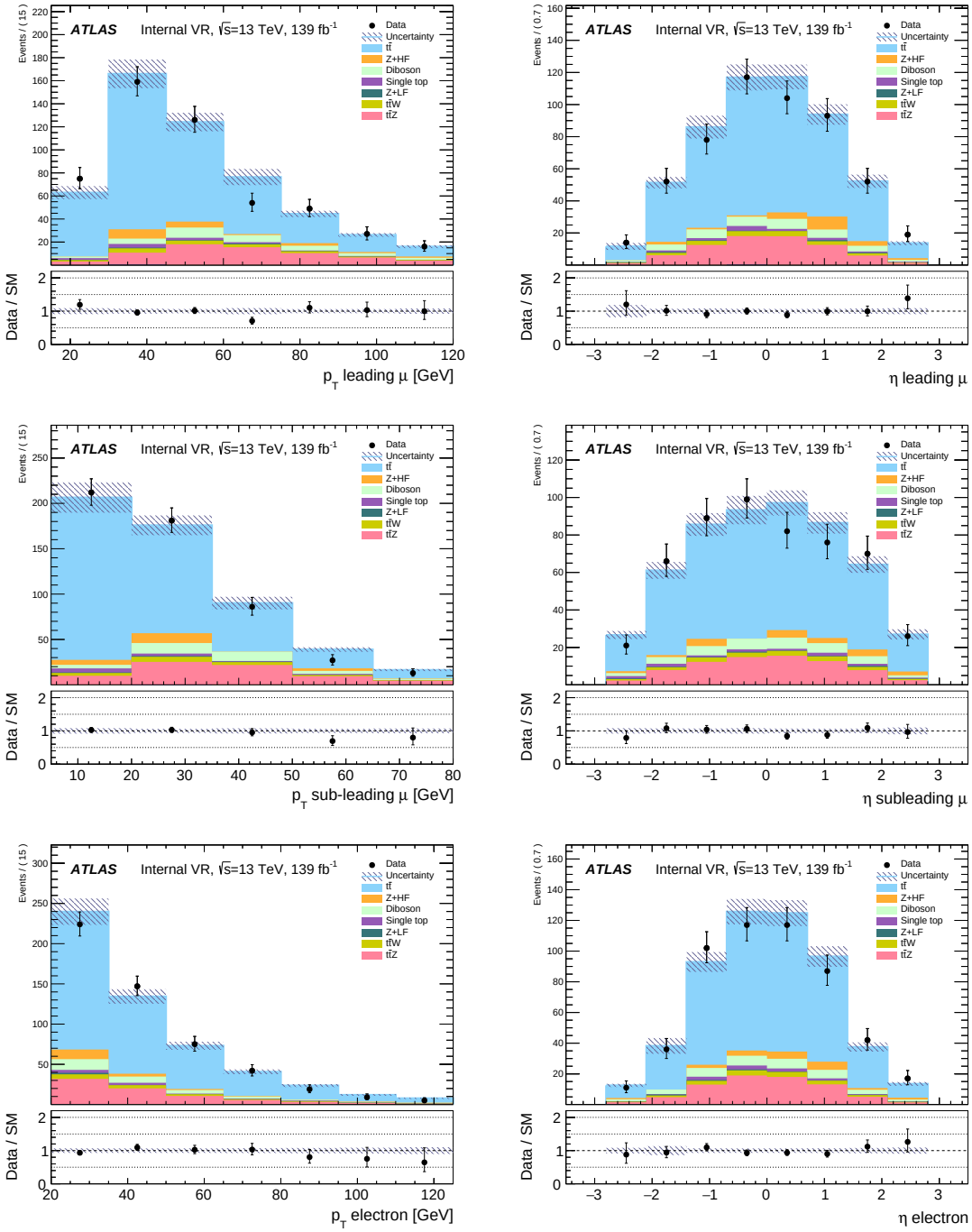

Figure 6.11 – CR-only Fit studies: Data/MC comparison of the η and p_{T} of the leptons in the VR indicating good modelling of the kinematics.

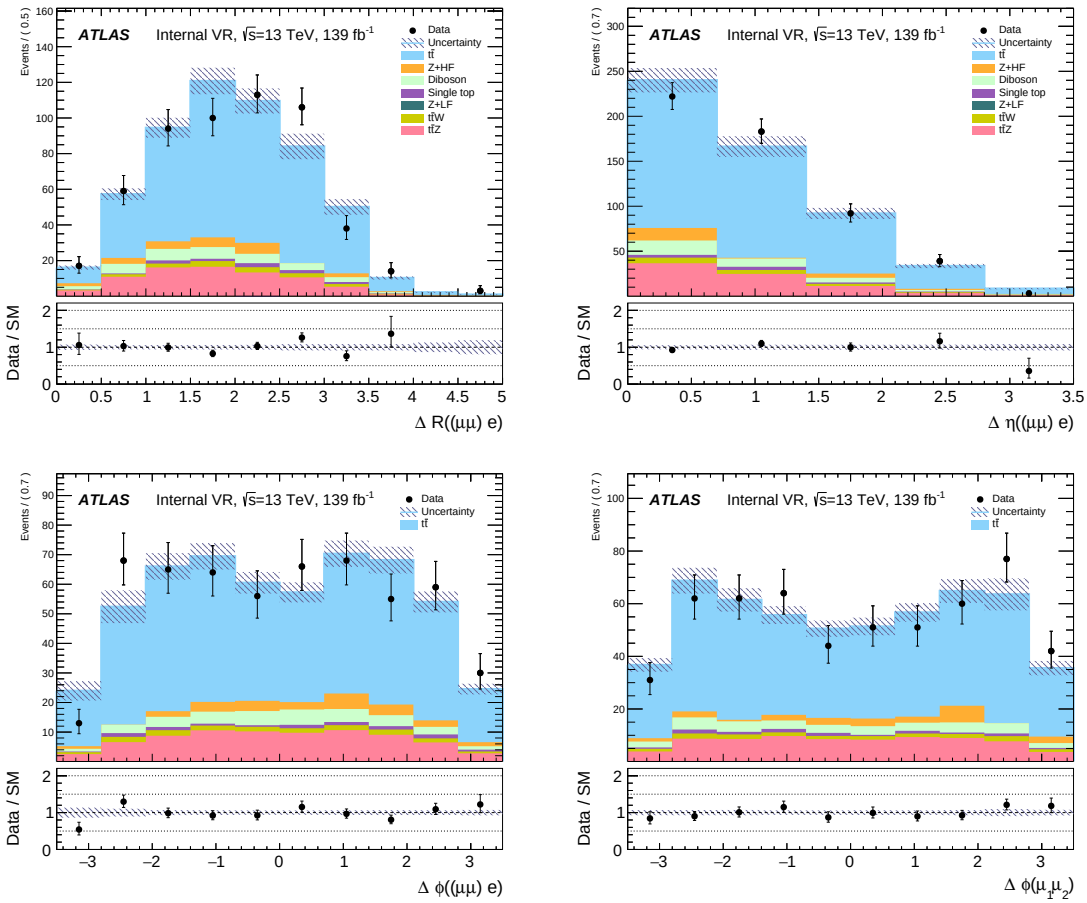

Figure 6.12 – CR-only Fit studies: Data/MC comparisons for dilepton kinematic variables shown for the VR. Good modelling is observed in this region.

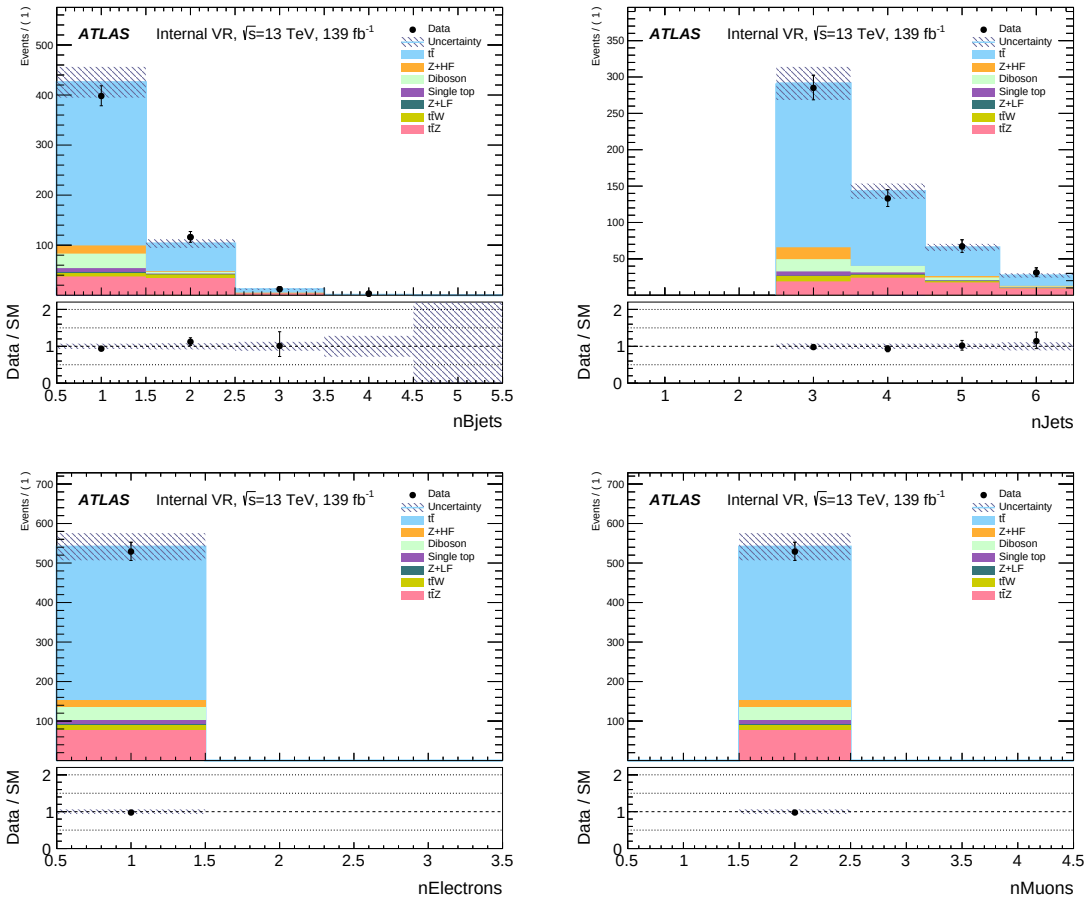

Figure 6.13 – CR-only Fit studies: Lepton and jet multiplicities in the VR post-fit.

6.7.3 Data/MC in SRInclusive

Modeling of the various kinematic variables is shown for the inclusive SR in Figures 6.14, 6.15, 6.16, 6.17. Note the SR is not used to do the likelihood fit in this configuration; only the CRs are used to constrain the background using the data. In this mode, the SR is treated as a VR. All the plots show good agreement with data and indicate that extrapolation method from the CR to SR is sound.

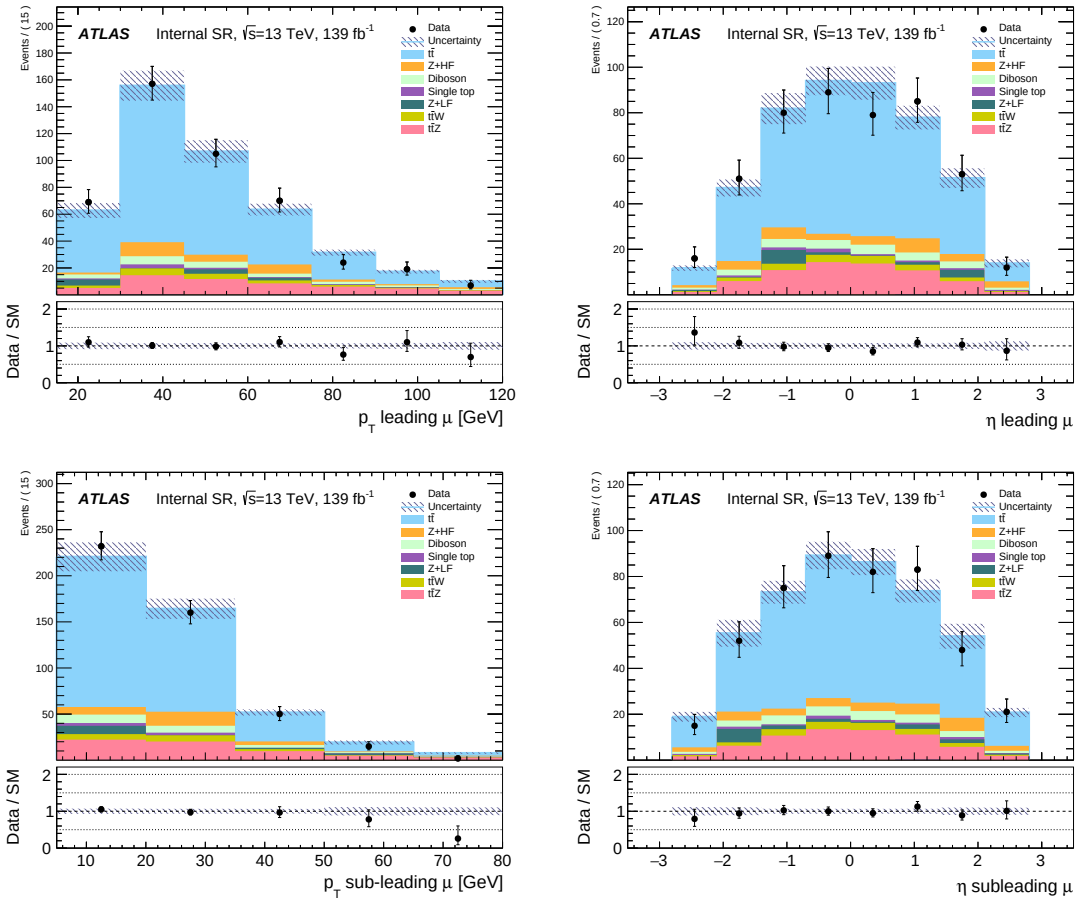

Figure 6.14 – CR-only Fit studies: Comparison of the modelling of the η and p_{T} of the muons in the inclusive signal region. These plots show that the MC is modeling the kinematics quite well and the extrapolation procedure is sound.

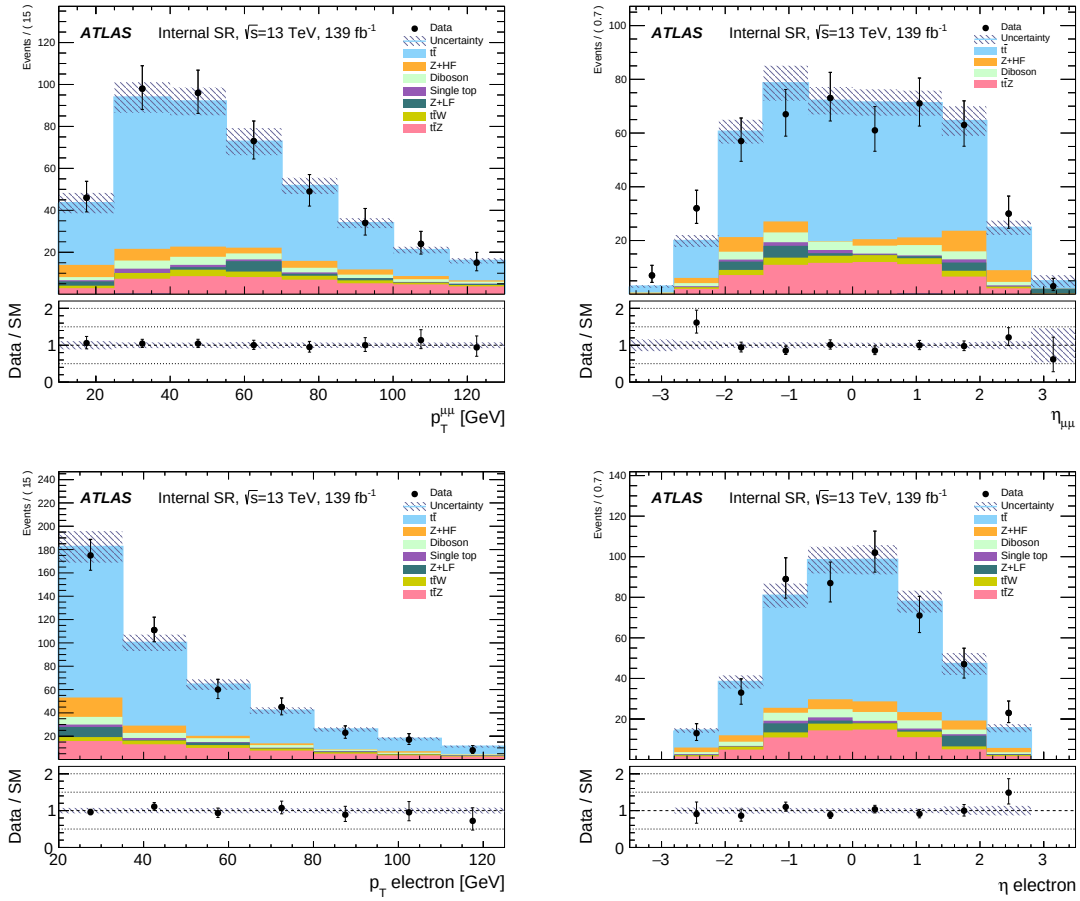

Figure 6.15 – CR-only Fit studies: Data/MC comparison of the modelling of the lepton kinematics in the inclusive signal region. Good modelling is observed in this region.

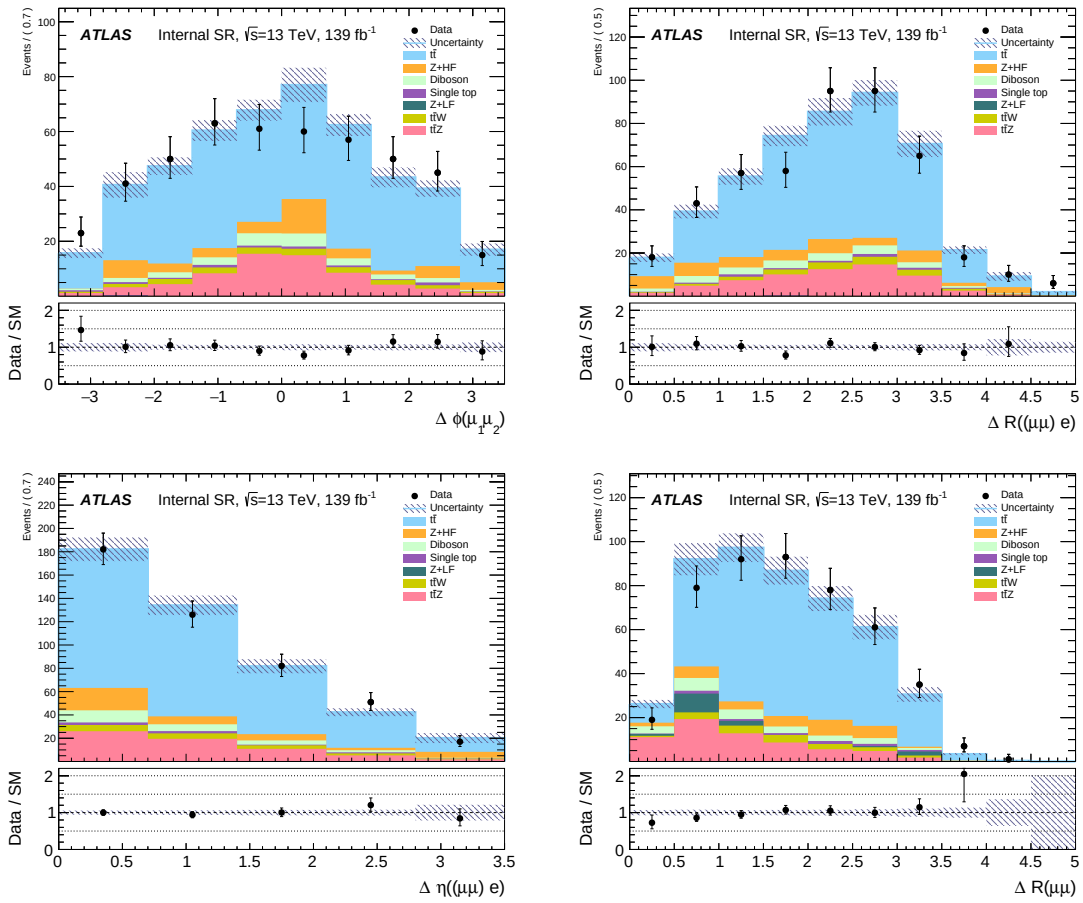

Figure 6.16 – CR-only Fit studies: Data/MC comparisons for dilepton kinematic variables shown for the SR.

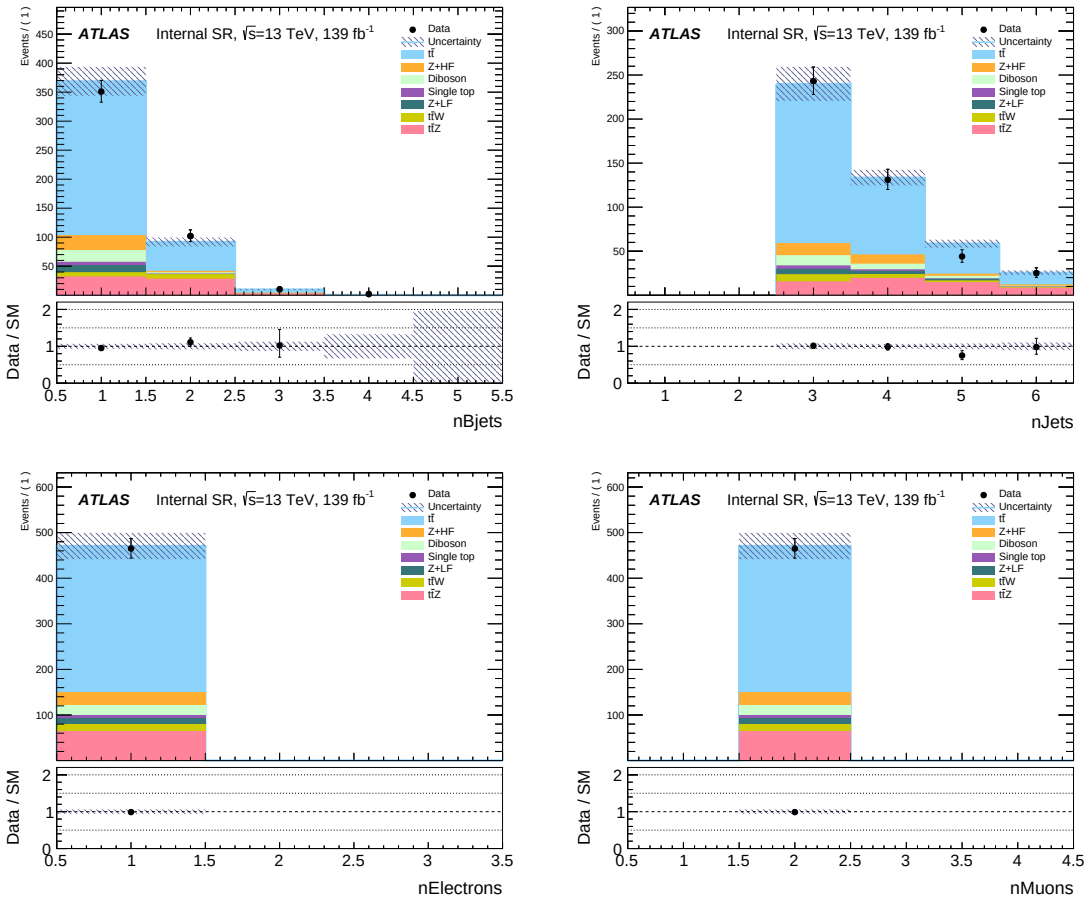

Figure 6.17 – CR-only Fit studies: Lepton and jet multiplicities in the SRInclusive post-fit.

7

Uncertainty Analysis

Systematic uncertainties affect the event yields in the signal and control regions in this analysis. These arise from experimental and theoretical sources, modelling errors and limited simulation statistics. The experimental sources relate to the reconstruction and identification of physics objects while theoretical uncertainties relate to assumptions made on the cross-sections or choice of modeling parameters used for the Monte Carlo samples. This section describes in detail the uncertainty analysis carried out in this thesis.

7.1 Transfer Factor Systematics

The systematic uncertainties in the analysis affecting the shapes of the kinematic distributions are propagated as the uncertainties on the transfer factors (TF) i.e. the ratio of the MC yields in the SR and CR. They are incorporated into the likelihood fit as nuisance parameters (NPs). The NPs are usually constrained by a Gaussian PDF with a width corresponding to the size of the uncertainty as determined from auxiliary measurements. The effect of the uncertainties on the event yields is obtained by varying the NP parameters by one sigma up and down in comparison to the nominal yields. The background prediction in the SR, for $t\bar{t}$ for example, is given by:

$$\text{N(SR est.)}^{t\bar{t}} = \mu_{t\bar{t}} \times \text{N(SR pre-fit)}^{t\bar{t}}, \tag{7.1}$$

$$= \text{N(CR obs)}^{t\bar{t}} \times \underbrace{\frac{\text{N(SR pre-fit)}^{t\bar{t}}}{\text{N(CR pre-fit)}^{t\bar{t}}}}_{\text{TF}}, \tag{7.2}$$

where N(SR est.) is the estimated yield in the SR, N(CR obs) is the number of observed events in the CR for the process, and the TF is defined as the ratio of the MC pre-fit yields. A useful feature of the TF method is that systematic uncertainties on the predicted background processes can be (partially) cancelled in the extrapolation if they affect the control region and signal region equally [140]. Thus, only the relative change in the systematic uncertainty between the SR and CR has an effect. To optimize these cancellations, the CRs are chosen to be as similar as possible to the SR by inverting few cuts in the selection and also have larger event statistics. The systematic uncertainty due to a particular source, $t\bar{t}$ for example, in some region X can be calculated as a relative uncertainty on the transfer factor as:

$$\Delta\text{TF(X)}^{sys}_{t\bar{t}} = \frac{\text{TF}_{t\bar{t}}(X)^{sys} - \text{TF}_{t\bar{t}}(X)^{nom}}{\text{TF}_{t\bar{t}}(X)^{nom}}. \tag{7.3}$$

7.2 Experimental Uncertainties

The experimental uncertainties that were evaluated follow a set of recommendations from the ATLAS experiment which are common to all analyses. These uncertainties depend on factors such as calibration techniques, methods for object identification and reconstruction, and data taking conditions. A description of the uncertainty sources affecting the measurement is summarized below; the corresponding nuisance parameters in the fit are summarized in Table 7.1.

Jets: These uncertainties arise from the calibration of the energy scales and resolution of the reconstructed jet objects. The jet energy scale (JES) calibration seeks to restore the jet energy to that of jets reconstructed at the particle level [182]. Precise knowledge of the jet energy resolution (JER) is needed for any search for BSM physics involving jets. JER also affects the missing transverse momentum, and is thus relevant for searches involving particles that decay into neutrinos and require a well-reconstructed missing momentum. Both these uncertainties depend on the p_{T} and η of the jet, and are measured by considering the differences in response between simulations and data.

Flavour tagging: The uncertainties associated with the tagging of different flavours of jets, such as b-tagging, are estimated as uncertainties on the scale factors applied to the jets in the simulation. These scale factors are applied to MC events in order to account for flavour tagging algorithm efficiency differences between simulation and data. The uncertainties on the scale factors come from a variety of sources which include the generator choice, the parton shower fragmentation model, jet energy scales and background cross-section uncertainties [197].

Leptons: The uncertainties arising from muon and electron identification efficiency, energy scale and resolution are considered. Scale factors are applied to the lepton efficiency to correct the MC predictions to the observed data using J/ψ and Z-boson decays [177, 179]. The uncertainty is evaluated by the varying the central values of the scale factors and determining the final impact on the yields.

Trigger: The efficiency scale factors for the single and dimuon triggers are calculated as a function of the p_{T} of the muon and account for the difference in trigger efficiency between simulation and data. Trigger related uncertainties are evaluated by varying the systematic sources which affect these scale factors.

Luminosity and Pile-up: The uncertainty on the combined Run 2 integrated luminosity is 1.7% and is obtained by using the LUCID-2 detector for the primary luminosity measurement. This error is dominated by uncertainties related to the calibration of the absolute luminosity using the van der Meer method [198]. The uncertainty due to pile-up re-weighting is also included. The effect of pileup is accounted for in the MC by overlaying additional pp collisions; however, the amount of pileup in each event might not agree with what is measured in data. Scale factors are thus applied to account for pile-up reweighting and the uncertainty is derived from variations on these correction factors.

MC statistics: The predictions on event rates are affected by a statistical uncertainty due limited simulation statistics in the Monte Carlo samples. The MC statistical error is described by a Poisson probability term in the fit, instead of a Gaussian as is the case for the other systematic sources. It is included as one nuisance parameter per bin (denoted by γ), using the Beeston-Barlow technique [199].

7.3 Theory Uncertainties

Theory uncertainties arise due to the differing methods used to calculate the cross-sections and the procedures used to simulate the proton-proton collisons at the LHC. A summary of the theoretical sources of uncertainties which can affect the observables used in the analysis is below.

Hard-scatter generation: The dependence on the choice of the Monte Carlo generator to simulate the hard-scatter for the background was considered. The $t\bar{t}$ nominal sample which uses POWHEG was compared to a sample generated using MADGRAPH5_AMC@NLO v2.3.3 to evaluate this uncertainty.

Parton shower modelling: The impact of the hadronization and fragmentation uncertainties in the parton shower modelling are included. This is evaluated by comparing the nominal $t\bar{t}$ sample showered with PYTHIA 8.230 to the alternative sample showered with HERWIG 7.0.4 [200, 201].

Initial-state and final-state radiation (ISR and FSR): ISR and FSR can affect the recoil of a system and refers to the radiation emitted by partons before and after the scattering event, respectively. These are assessed by varying the internal PYTHIA 8.230 showering parameters to increase or decrease the amount of radiation as per the prescription in Ref [202].

Renormalisation and factorisation scales: The cross-section prediction for a process in pp collisions depends on the renormalisation (μ_R) and factorisation (μ_F) scales. These refer to the momentum transfer scale at which the process is measured and enters the matrix element calculations as seen in equation 2.62. The uncertainty is determined by varying μ_R and μ_F by a factors of 2 and assessing the impact on yields.

Parton Distribution Function (PDF): Calculation of the production cross-section requires knowledge of the fraction of the proton momentum carried by the partons in the collision. This is encapsulated in the parton density functions (PDFs) which are parametrized as a function of momentum transfer. PDFs are obtained from global fits to data from deep-inelastic scattering (DIS), Drell-Yan and jet measurement data. Uncertainty due to choice of the PDF is evaluated by com-

paring the impact on the yields from two different PDF sets as per the PDF4LHC recommendations [203].

A flat uncertainty on the production cross-sections is used for the small backgrounds that don't have a free-floating normalization parameter. The uncertainties used are based on the recommendations from the ATLAS physics modelling group and are summarized below:

- single-Top: 5%
- W+jets : 50%
- di-Bosons: 50%
- ttW: 13%

7.3.1 Smoothing systematics

The $t\bar{t}$ generator, shower and radiation theory uncertainty was fluctuating between the neighbouring bins in the SR windows due to low statistics of the MC samples used. It was found to vary as much as 15 % between bins, a jump not expected from the physics. Smoothing was thus applied to the entire SR by doing a linear fit to the relative difference between the nominal and varied spectrum. A constant error of 17 % for generator, 22 % for shower and 4% radiation systematics was used for all the signal windows as shown below in Figures 7.1, 7.2,7.3.

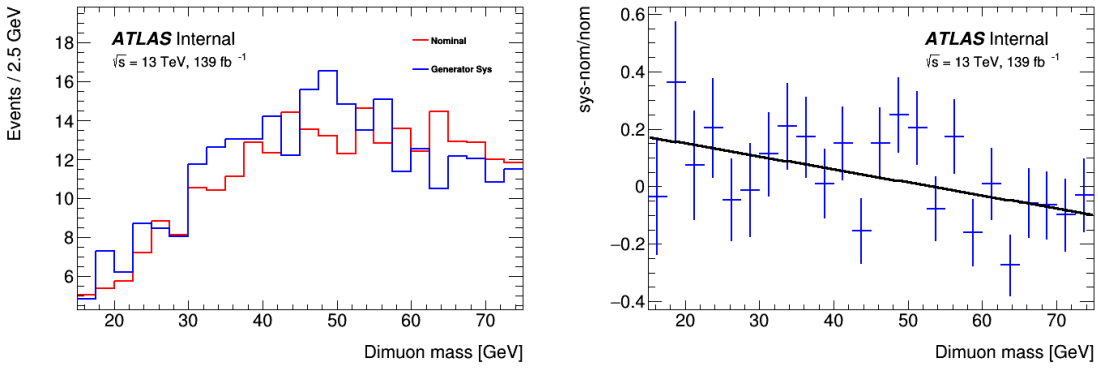

Figure 7.1 – Smoothing of $t\bar{t}$ generator theory systematic. A constant error of 17 % was used across the SR bins.

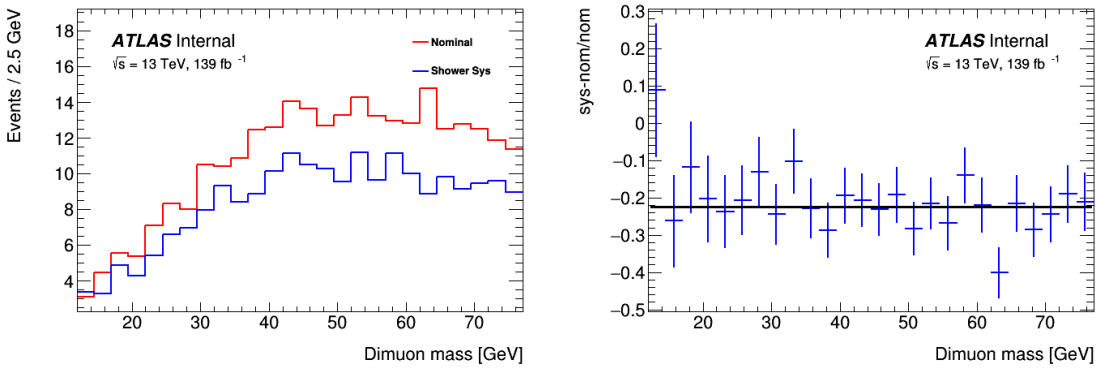

Figure 7.2 – Smoothing of $t\bar{t}$ shower theory systematic. A constant error of 22 % was used across the SR bins.

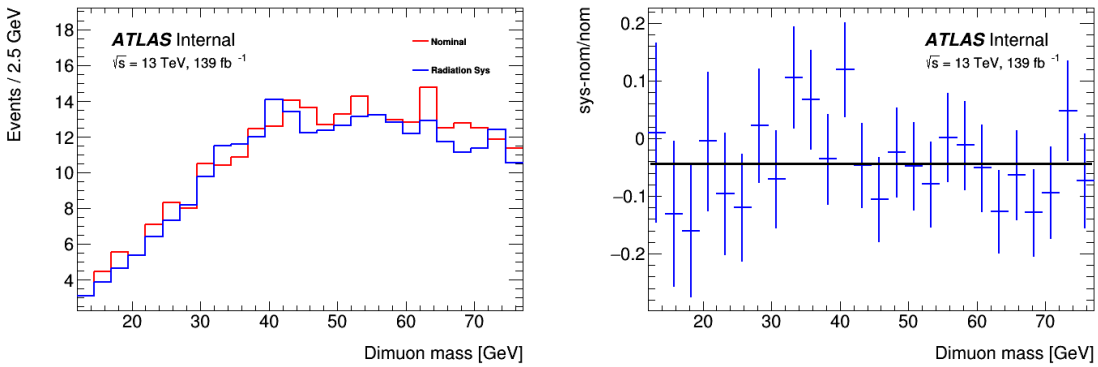

Figure 7.3 – Smoothing of $t\bar{t}$ radiation theory systematic. A constant error of 4 % was used across the SR bins.

Object	Nuisance Parameter Name
Jets	JET_EtaIntercalibration_NonClosure_highE
	JET_EtaIntercalibration_NonClosure_negEta
	JET_EtaIntercalibration_NonClosure_posEta
	JET_Flavor_Response
	JET_GroupedNP_1
	JET_GroupedNP_2
	JET_GroupedNP_3
	JET_JER_DataVsMC
	JET_JER_EffectiveNP_1
	JET_JER_EffectiveNP_2
	JET_JER_EffectiveNP_3
	JET_JER_EffectiveNP_4
	JET_JER_EffectiveNP_5
	JET_JER_EffectiveNP_6
	JET_JER_EffectiveNP_7restTerm
	JET_JvtEfficiency
Flavour tagging	FT_EFF_B_systematics
	FT_EFF_C_systematics
	FT_EFF_Light_systematics
	FT_EFF_extrapolation_systematics
	FT_EFF_extrapolation_from_charm_systematics
Muons	leptonWeight_MUON_EFF_BADMUON_STAT
	leptonWeight_MUON_EFF_BADMUON_SYS
	leptonWeight_MUON_EFF_ISO_STAT
	leptonWeight_MUON_EFF_ISO_SYS
	leptonWeight_MUON_EFF_RECO_STAT
	leptonWeight_MUON_EFF_RECO_SYS
	leptonWeight_MUON_EFF_RECO_STAT_LOWPT
	leptonWeight_MUON_EFF_RECO_SYS_LOWPT
	leptonWeight_MUON_EFF_TTVA_STAT
	leptonWeight_MUON_EFF_TTVA_SYS
	MUON_SAGITTA_RESBIAS
	MUON_SAGITTA_RHO
	MUON_ID
	MUON_SCALE
	MUON_MS
Electrons	leptonWeight_EL_EFF_ID_TOTAL_1NPCOR_PLUS_UNCOR
	leptonWeight_EL_EFF_Iso_TOTAL_1NPCOR_PLUS_UNCOR
	leptonWeight_EL_EFF_Reco_TOTAL_1NPCOR_PLUS_UNCOR
	EG_RESOLUTION_ALL
	EG_SCALE_ALL
Trigger	SF_SLORDLMUON_EFF_TrigStatUncertainty
	SF_SLORDLMUON_EFF_TrigSystUncertainty
Theory	ttbar_genSysNominal
	ttbar_showerSysNominal
	ttbar_radSysNominal
	Syst_PDFset909xx

Table 7.1 – A list of the nuisance parameters in the fit associated with the various uncertainty sources.

7.4 Signal

The experimental uncertainties used for the signal MC are the same as those for the background MC, as described above. Additionally, the following uncertainties were also applied for the signal.

7.4.1 Cross-Section

The signal in this analysis is produced from top quark pairs. Thus, the uncertainty on the production cross-section is that for the $t\bar{t}$ process and is implemented following the recommendations of the ATLAS Physics Modeling Group (PMG). The uncertainties arising from QCD scale, mass, PDF & α_S choice were taken into account. The values used are listed in Table 7.2.

NP name	Description	size [%]
`sig_scale`	QCD scale	3.5
`sig_PDF`	PDF & α_S	4
`sig_mass`	mass	3.0

Table 7.2 – Theory uncertainties used on the signal cross-section

7.4.2 Interpolation error

The systematic uncertainty for the interpolation of signal yields is determined by comparing the difference between a simple linear interpolation and the spline interpolation. The difference is assessed for each mass point and the largest difference is taken to be the uncertainty for the mass window being studied. The difference in the spline and linear interpolations can be seen visually in Figure 7.4. The uncertainties are summarized in Table 7.3. Additionally, a flat 1.5 % uncertainty is applied to the interpolated yields which is averaged from the MC statistical error of the generated signal mass points.

Mass Window (GeV)	Interpolation Uncertainty (%)
1.5	1.4
2	1.14
3	0.66
4	0.86

Table 7.3 – Interpolation uncertainties for various mass windows

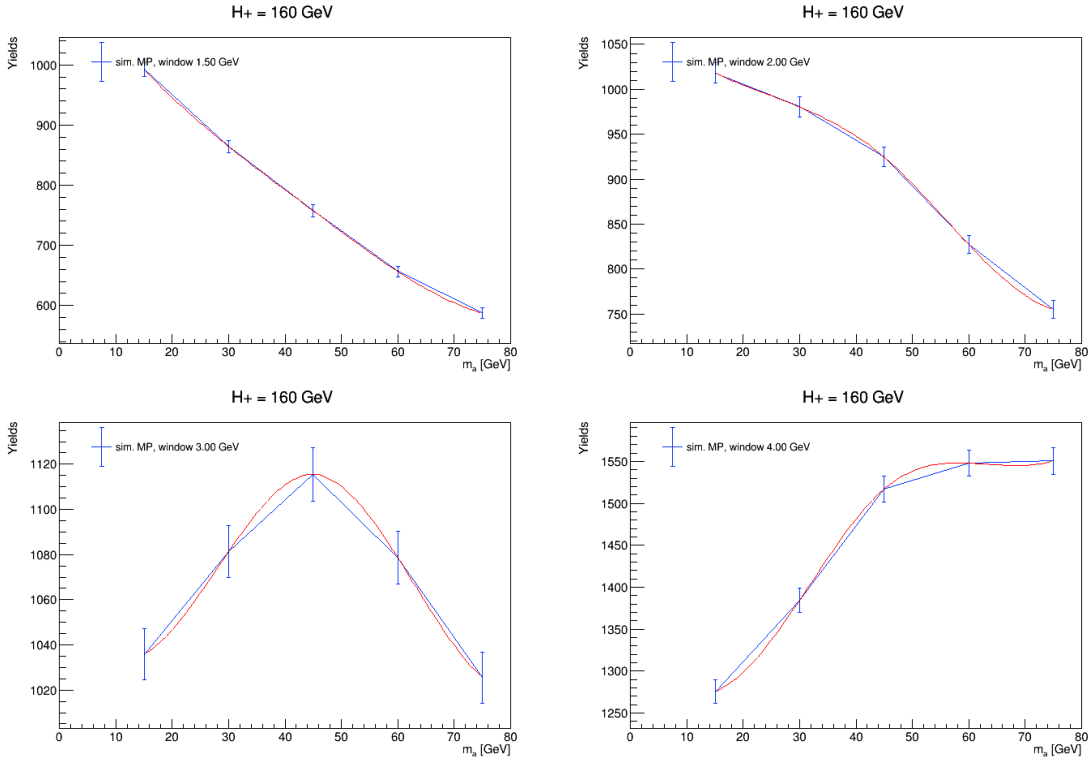

Figure 7.4 – Signal Interpolation Error: Plots showing the difference in yields between the linear and spline interpolation for H^+ = 160 GeV. The largest difference is used as the error for the interpolation.

7.5 Breakdown of Uncertainties on the Background

The post-fit systematic uncertainties on the estimated background is shown in Table 7.4. The width of the SR windows are discussed in section 6.4. For example, SR31 represents a 2 GeV window $30 \leq m_{\mu\mu} \leq 32$ GeV. The dominant uncertainties arise from the $\mu_{t\bar{t}}$ and μ_{ttZ} normalizations, $t\bar{t}$ generator and $t\bar{t}$ shower (theory), and the error due to MC statistics.

Breakdown of the uncertainties in the CRs and VR can be seen in Table 7.5. Pull plots for the NPs post-fit can be found in Figure 7.5. None of the NPs are constrained or being pulled; this is expected behaviour given that a single-bin fit is used for the CRs.

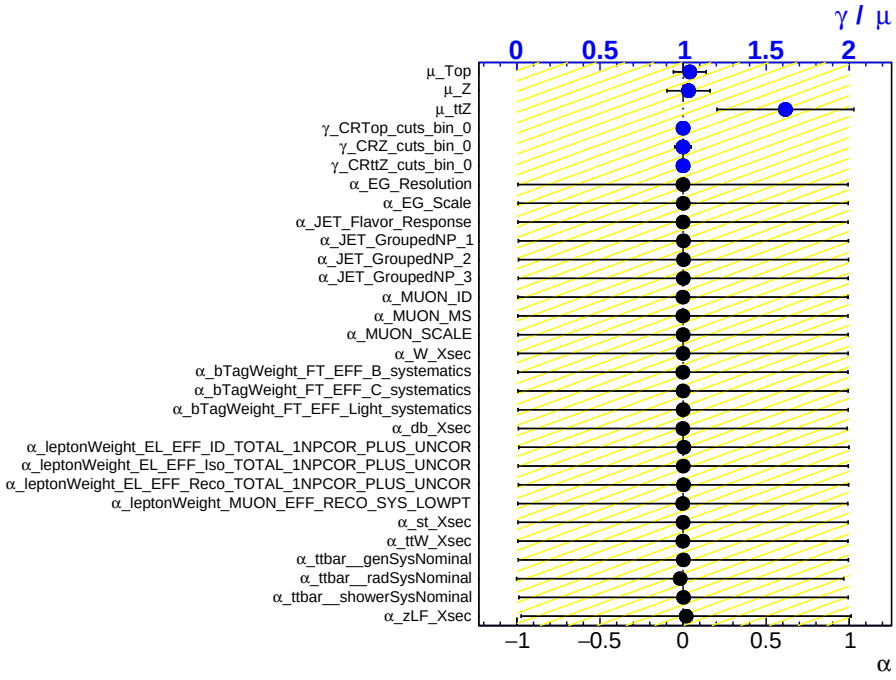

Figure 7.5 – Post-Fit pulls for a list of major systematics using the CR-only mode of the fit. None of the NPs are constrained or being pulled.

Uncertainty of channel	SR15	SR31	SR48	SR70
Total background expectation	5.47	13.54	21.88	32.49
Total statistical ($\sqrt{N_{exp}}$)	±2.34	±3.68	±4.68	±5.70
Total background systematic	±1.04 [18.96%]	±2.85 [21.04%]	±4.89 [22.35%]	±6.52 [20.07%]
MC_gamma_stat_SR15_	±0.49 [8.9%]	±0.00 [0.00%]	±0.00 [0.00%]	±0.00 [0.00%]
MC_gamma_stat_SR48_	±0.00 [0.00%]	±0.00 [0.00%]	±0.94 [4.3%]	±0.00 [0.00%]
MC_gamma_stat_SR31_	±0.00 [0.00%]	±0.74 [5.5%]	±0.00 [0.00%]	±0.00 [0.00%]
MC_gamma_stat_SR70_	±0.00 [0.00%]	±0.00 [0.00%]	±0.00 [0.00%]	±1.32 [4.1%]
alpha_ttbartheory__showerSys	±0.49 [9.0%]	±2.10 [15.5%]	±3.65 [16.7%]	±4.88 [15.0%]
mu_ttZ	±0.45 [8.3%]	±0.45 [3.3%]	±0.64 [2.9%]	±1.16 [3.6%]
alpha_db_Xsec	±0.39 [7.1%]	±0.32 [2.3%]	±0.30 [1.4%]	±0.95 [2.9%]
alpha_ttbartheory__genSys	±0.38 [7.0%]	±1.62 [12.0%]	±2.82 [12.9%]	±3.78 [11.6%]
alpha_JET_JER_EffectiveNP_2	±0.34 [6.3%]	±0.08 [0.57%]	±0.49 [2.2%]	±0.29 [0.90%]
alpha_JET_JER_EffectiveNP_4	±0.29 [5.4%]	±0.04 [0.28%]	±0.60 [2.7%]	±0.25 [0.78%]
mu_Top	±0.23 [4.2%]	±0.97 [7.2%]	±1.69 [7.7%]	±2.27 [7.0%]
alpha_JET_JER_EffectiveNP_7restTerm	±0.23 [4.2%]	±0.07 [0.55%]	±0.34 [1.5%]	±0.24 [0.73%]
alpha_JET_JER_EffectiveNP_1	±0.23 [4.1%]	±0.02 [0.16%]	±0.23 [1.0%]	±0.13 [0.41%]
alpha_JET_JER_EffectiveNP_6	±0.20 [3.6%]	±0.07 [0.53%]	±0.03 [0.16%]	±0.25 [0.77%]
alpha_JET_JER_EffectiveNP_3	±0.18 [3.4%]	±0.05 [0.36%]	±0.34 [1.6%]	±0.34 [1.0%]
alpha_JET_JER_EffectiveNP_5	±0.15 [2.8%]	±0.07 [0.55%]	±0.06 [0.27%]	±0.26 [0.80%]
alpha_MUON_SCALE	±0.12 [2.1%]	±0.17 [1.3%]	±0.27 [1.3%]	±0.56 [1.7%]
alpha_ttbartheory__radSys	±0.08 [1.4%]	±0.33 [2.4%]	±0.57 [2.6%]	±0.77 [2.4%]
alpha_JET_Flavor_Response	±0.06 [1.1%]	±0.08 [0.62%]	±0.12 [0.55%]	±0.00 [0.00%]
alpha_zLF_Xsec	±0.06 [1.1%]	±0.06 [0.42%]	±0.06 [0.26%]	±0.06 [0.18%]
alpha_JET_GroupedNP_2	±0.05 [0.96%]	±0.02 [0.16%]	±0.22 [1.00%]	±0.03 [0.11%]
mu_Z	±0.05 [0.90%]	±0.06 [0.42%]	±0.08 [0.37%]	±0.19 [0.57%]
alpha_pileupWeight	±0.04 [0.81%]	±0.02 [0.18%]	±0.04 [0.20%]	±0.08 [0.24%]
alpha_MUON_ID	±0.03 [0.63%]	±0.11 [0.85%]	±0.17 [0.80%]	±0.06 [0.19%]
alpha_MUON_MS	±0.03 [0.62%]	±0.11 [0.85%]	±0.62 [2.8%]	±0.01 [0.02%]
alpha_JET_GroupedNP_1	±0.03 [0.56%]	±0.03 [0.21%]	±0.20 [0.92%]	±0.07 [0.20%]
alpha_EG_Resolution	±0.03 [0.55%]	±0.10 [0.77%]	±0.06 [0.26%]	±0.05 [0.17%]
alpha_JET_EtaIntercalibration_NonClosure_negEta	±0.02 [0.40%]	±0.01 [0.04%]	±0.01 [0.04%]	±0.01 [0.04%]
alpha_leptonWeight_EL_EFF_ID_TOTAL_1NPCOR	±0.02 [0.36%]	±0.12 [0.92%]	±0.15 [0.67%]	±0.19 [0.58%]
alpha_MUON_SAGITTA_RESBIAS	±0.02 [0.35%]	±0.00 [0.00%]	±0.03 [0.16%]	±0.13 [0.41%]
alpha_bTagWeight_FT_EFF_B_systematics	±0.02 [0.34%]	±0.00 [0.03%]	±0.02 [0.09%]	±0.05 [0.15%]
alpha_leptonWeight_EL_EFF_Reco_TOTAL_1NPCOR	±0.02 [0.32%]	±0.08 [0.59%]	±0.13 [0.61%]	±0.18 [0.55%]
alpha_EG_Scale	±0.01 [0.26%]	±0.14 [1.0%]	±0.06 [0.29%]	±0.03 [0.09%]
alpha_bTagWeight_FT_EFF_Light_systematics	±0.01 [0.23%]	±0.01 [0.07%]	±0.06 [0.25%]	±0.07 [0.22%]
alpha_ttW_Xsec	±0.01 [0.21%]	±0.05 [0.34%]	±0.10 [0.48%]	±0.19 [0.58%]
alpha_leptonWeight_MUON_EFF_RECO_SYS_LOWPT	±0.01 [0.21%]	±0.05 [0.38%]	±0.03 [0.16%]	±0.04 [0.12%]
alpha_SF_SLORDLMUON_EFF_TrigSystUncertainty	±0.01 [0.16%]	±0.02 [0.12%]	±0.04 [0.20%]	±0.03 [0.09%]
alpha_leptonWeight_EL_EFF_Iso_TOTAL_1NPCOR	±0.01 [0.14%]	±0.03 [0.25%]	±0.06 [0.26%]	±0.08 [0.23%]
alpha_JET_GroupedNP_3	±0.01 [0.14%]	±0.04 [0.30%]	±0.00 [0.01%]	±0.02 [0.08%]
alpha_jvtWeight_JET_JvtEfficiency	±0.01 [0.13%]	±0.02 [0.17%]	±0.01 [0.06%]	±0.04 [0.13%]
alpha_leptonWeight_MUON_EFF_RECO_SYS	±0.01 [0.10%]	±0.01 [0.09%]	±0.01 [0.06%]	±0.00 [0.00%]
alpha_leptonWeight_MUON_EFF_TTVA_SYS	±0.00 [0.09%]	±0.01 [0.07%]	±0.01 [0.04%]	±0.01 [0.02%]
alpha_leptonWeight_MUON_EFF_ISO_SYS	±0.00 [0.09%]	±0.01 [0.11%]	±0.00 [0.01%]	±0.01 [0.03%]
alpha_bTagWeight_FT_EFF_C_systematics	±0.00 [0.04%]	±0.00 [0.02%]	±0.03 [0.15%]	±0.01 [0.02%]
alpha_leptonWeight_MUON_EFF_ISO_STAT	±0.00 [0.04%]	±0.01 [0.05%]	±0.00 [0.01%]	±0.00 [0.01%]
alpha_leptonWeight_MUON_EFF_TTVA_STAT	±0.00 [0.03%]	±0.01 [0.06%]	±0.01 [0.03%]	±0.01 [0.02%]
alpha_leptonWeight_MUON_EFF_RECO_STAT_LOWPT	±0.00 [0.03%]	±0.01 [0.07%]	±0.01 [0.04%]	±0.01 [0.02%]
alpha_JET_EtaIntercalibration_NonClosure_posEta	±0.00 [0.01%]	±0.00 [0.02%]	±0.01 [0.06%]	±0.01 [0.04%]
alpha_MUON_SAGITTA_RHO	±0.00 [0.01%]	±0.00 [0.03%]	±0.01 [0.02%]	±0.00 [0.01%]
alpha_JET_EtaIntercalibration_NonClosure_highE	±0.00 [0.01%]	±0.00 [0.02%]	±0.00 [0.02%]	±0.00 [0.01%]
alpha_bTagWeight_FT_EFF_extrapolation	±0.00 [0.01%]	±0.00 [0.01%]	±0.00 [0.00%]	±0.00 [0.00%]
alpha_SF_SLORDLMUON_EFF_TrigStatUncertainty	±0.00 [0.01%]	±0.01 [0.04%]	±0.00 [0.01%]	±0.00 [0.00%]
alpha_bTagWeight_FT_EFF_extrapolation_from_charm	±0.00 [0.01%]	±0.00 [0.02%]	±0.00 [0.00%]	±0.00 [0.00%]
alpha_leptonWeight_MUON_EFF_RECO_STAT	±0.00 [0.00%]	±0.00 [0.02%]	±0.00 [0.01%]	±0.00 [0.00%]
alpha_st_Xsec	±0.00 [0.00%]	±0.03 [0.20%]	±0.02 [0.10%]	±0.03 [0.08%]
alpha_W_Xsec	±0.00 [0.00%]	±0.00 [0.00%]	±0.00 [0.00%]	±0.00 [0.00%]

Table 7.4 – Post-Fit breakdown of the dominant systematic uncertainties on the background estimates in some representative bins in the SR. The width of the SR windows are discussed in section 6.4. Note that the individual uncertainties can be correlated, and do not necessarily add up quadratically to the total background uncertainty.

Uncertainty of channel	CRZ	CR$t\bar{t}$	CRttZ	VR
Total background expectation	802.97	190.00	634.98	541.03
Total statistical ($\sqrt{N_{exp}}$)	±28.34	±13.78	±25.20	±23.26
Total background systematic	±28.45 [3.54%]	±13.78 [7.25%]	±25.24 [3.98%]	±42.92 [7.93%]
mu_Z	±98.91 [12.3%]	±0.14 [0.08%]	±8.76 [1.4%]	±3.69 [0.68%]
MC_stat_gamma_CRZ	±39.30 [4.9%]	±0.00 [0.00%]	±0.00 [0.00%]	±0.00 [0.00%]
MC_stat_gamma_CRTop	±0.00 [0.00%]	±2.78 [1.5%]	±0.00 [0.00%]	±0.00 [0.00%]
MC_stat_gamma_CRttZ	±0.00 [0.00%]	±0.00 [0.00%]	±9.61 [1.5%]	±0.00 [0.00%]
MC_stat_gamma_VR	±0.00 [0.00%]	±0.00 [0.00%]	±0.00 [0.00%]	±7.72 [1.4%]
alpha_JET_JER_EffectiveNP_4	±38.41 [4.8%]	±3.20 [1.7%]	±2.99 [0.47%]	±9.11 [1.7%]
alpha_JET_JER_EffectiveNP_2	±34.25 [4.3%]	±2.86 [1.5%]	±2.72 [0.43%]	±8.03 [1.5%]
alpha_JET_JER_EffectiveNP_3	±33.00 [4.1%]	±2.33 [1.2%]	±2.35 [0.37%]	±7.20 [1.3%]
alpha_zLF_Xsec	±29.18 [3.6%]	±0.14 [0.07%]	±4.08 [0.64%]	±0.98 [0.18%]
alpha_JET_JER_EffectiveNP_7restTerm	±28.18 [3.5%]	±2.16 [1.1%]	±3.02 [0.48%]	±6.60 [1.2%]
alpha_JET_JER_EffectiveNP_1	±27.48 [3.4%]	±1.73 [0.91%]	±1.09 [0.17%]	±3.58 [0.66%]
alpha_JET_JER_EffectiveNP_5	±22.88 [2.8%]	±1.63 [0.86%]	±2.76 [0.43%]	±5.44 [1.0%]
alpha_JET_JER_EffectiveNP_6	±19.86 [2.5%]	±1.51 [0.79%]	±2.79 [0.44%]	±4.82 [0.89%]
alpha_db_Xsec	±16.91 [2.1%]	±0.29 [0.15%]	±72.70 [11.4%]	±15.93 [2.9%]
mu_Top	±13.82 [1.7%]	±17.18 [9.0%]	±9.83 [1.5%]	±39.33 [7.3%]
mu_ttZ	±13.29 [1.7%]	±1.63 [0.86%]	±83.23 [13.1%]	±19.34 [3.6%]
alpha_ttbar_theory_genSysNominal	±11.67 [1.5%]	±2.85 [1.5%]	±8.82 [1.4%]	±0.00 [0.00%]
alpha_ttbar_theory_howerSysNominal	±5.94 [0.74%]	±5.43 [2.9%]	±11.38 [1.8%]	±17.46 [3.2%]
alpha_leptonWeight_EL_EFF_ID_TOTAL_1NPCOR	±3.23 [0.40%]	±2.45 [1.3%]	±0.78 [0.12%]	±3.53 [0.65%]
alpha_JET_EtaIntercalibration_NonClosure_negEta	±3.00 [0.37%]	±0.01 [0.01%]	±2.99 [0.47%]	±1.94 [0.36%]
alpha_leptonWeight_EL_EFF_Reco_TOTAL_1NPCOR	±2.21 [0.28%]	±1.44 [0.76%]	±0.77 [0.12%]	±3.13 [0.58%]
alpha_ttbar_theory_radSysNominal	±2.05 [0.25%]	±0.80 [0.42%]	±2.85 [0.45%]	±3.44 [0.64%]
alpha_EG_Scale	±1.78 [0.22%]	±0.90 [0.47%]	±0.88 [0.14%]	±2.51 [0.46%]
alpha_JET_GroupedNP_2	±1.73 [0.22%]	±0.77 [0.41%]	±0.96 [0.15%]	±2.62 [0.48%]
alpha_SF_SLORDLMUON_EFF_TrigSystUncertainty	±1.18 [0.15%]	±0.28 [0.15%]	±1.46 [0.23%]	±1.18 [0.22%]
alpha_JET_GroupedNP_3	±1.02 [0.13%]	±0.02 [0.01%]	±1.04 [0.16%]	±0.89 [0.16%]
alpha_JET_Flavor_Response	±0.96 [0.12%]	±0.25 [0.13%]	±0.72 [0.11%]	±1.18 [0.22%]
alpha_JET_GroupedNP_1	±0.96 [0.12%]	±1.20 [0.63%]	±0.24 [0.04%]	±2.45 [0.45%]
alpha_leptonWeight_EL_EFF_Iso_TOTAL_1NPCOR	±0.90 [0.11%]	±0.58 [0.30%]	±0.32 [0.05%]	±1.32 [0.24%]
alpha_bTagWeight_FT_EFF_Light_systematics	±0.70 [0.09%]	±0.06 [0.03%]	±0.65 [0.10%]	±0.09 [0.02%]
alpha_MUON_SCALE	±0.59 [0.07%]	±0.26 [0.14%]	±0.33 [0.05%]	±0.54 [0.10%]
alpha_bTagWeight_FT_EFF_B_systematics	±0.57 [0.07%]	±0.14 [0.07%]	±0.71 [0.11%]	±0.65 [0.12%]
alpha_leptonWeight_MUON_EFF_RECO_SYS_LOWPT	±0.38 [0.05%]	±0.63 [0.33%]	±0.25 [0.04%]	±0.37 [0.07%]
alpha_pileupWeight	±0.34 [0.04%]	±0.51 [0.27%]	±0.17 [0.03%]	±0.54 [0.10%]
alpha_MUON_MS	±0.27 [0.03%]	±0.35 [0.19%]	±0.09 [0.01%]	±0.06 [0.01%]
alpha_MUON_SAGITTA_RESBIAS	±0.23 [0.03%]	±0.08 [0.04%]	±0.16 [0.02%]	±0.00 [0.00%]
alpha_st_Xsec	±0.21 [0.03%]	±0.22 [0.11%]	±0.12 [0.02%]	±0.45 [0.08%]
alpha_EG_Resolution	±0.18 [0.02%]	±0.09 [0.05%]	±0.27 [0.04%]	±0.18 [0.03%]
alpha_ttW_Xsec	±0.14 [0.02%]	±0.96 [0.51%]	±0.83 [0.13%]	±1.85 [0.34%]
alpha_MUON_SAGITTA_RHO	±0.10 [0.01%]	±0.08 [0.04%]	±0.08 [0.01%]	±0.07 [0.01%]
alpha_leptonWeight_MUON_EFF_RECO_SYS	±0.10 [0.01%]	±0.16 [0.09%]	±0.06 [0.01%]	±0.16 [0.03%]
alpha_leptonWeight_MUON_EFF_ISO_SYS	±0.10 [0.01%]	±0.17 [0.09%]	±0.07 [0.01%]	±0.11 [0.02%]
alpha_leptonWeight_MUON_EFF_TTVA_SYS	±0.09 [0.01%]	±0.13 [0.07%]	±0.04 [0.01%]	±0.07 [0.01%]
alpha_jvtWeight_JET_JvtEfficiency	±0.08 [0.01%]	±0.04 [0.02%]	±0.12 [0.02%]	±0.07 [0.01%]
alpha_leptonWeight_MUON_EFF_TTVA_STAT	±0.07 [0.01%]	±0.11 [0.06%]	±0.03 [0.01%]	±0.06 [0.01%]
alpha_leptonWeight_MUON_EFF_RECO_STAT_LOWPT	±0.07 [0.01%]	±0.12 [0.06%]	±0.05 [0.01%]	±0.08 [0.01%]
alpha_JET_EtaIntercalibration_NonClosure_posEta	±0.06 [0.01%]	±0.04 [0.02%]	±0.02 [0.00%]	±0.02 [0.00%]
alpha_JET_EtaIntercalibration_NonClosure_highE	±0.05 [0.01%]	±0.06 [0.03%]	±0.06 [0.01%]	±0.11 [0.02%]
alpha_MUON_ID	±0.05 [0.01%]	±0.25 [0.13%]	±0.21 [0.03%]	±0.30 [0.05%]
alpha_bTagWeight_FT_EFF_C_systematics	±0.05 [0.01%]	±0.02 [0.01%]	±0.03 [0.00%]	±0.11 [0.02%]
alpha_leptonWeight_MUON_EFF_ISO_STAT	±0.04 [0.01%]	±0.08 [0.04%]	±0.03 [0.00%]	±0.05 [0.01%]
alpha_leptonWeight_MUON_EFF_RECO_STAT	±0.02 [0.00%]	±0.02 [0.01%]	±0.01 [0.00%]	±0.00 [0.00%]
alpha_bTagWeight_FT_EFF_extrapolation	±0.01 [0.00%]	±0.01 [0.00%]	±0.00 [0.00%]	±0.01 [0.00%]
alpha_bTagWeight_FT_EFF_extrapolation_from_charm	±0.01 [0.00%]	±0.01 [0.00%]	±0.01 [0.00%]	±0.01 [0.00%]
alpha_W_Xsec	±0.01 [0.00%]	±0.20 [0.10%]	±0.00 [0.00%]	±0.04 [0.01%]
alpha_SF_SLORDLMUON_EFF_TrigStatUncertainty	±0.00 [0.00%]	±0.06 [0.03%]	±0.05 [0.01%]	±0.02 [0.00%]

Table 7.5 – Post-Fit Breakdown of the dominant systematic uncertainties on background estimates in the Control Regions. Note that the individual uncertainties can be correlated, and do not necessarily add up quadratically to the total background uncertainty. The percentages show the size of the uncertainty relative to the total expected background.

7.6 Breakdown of Uncertainties on the Signal

The breakdown of the systematic uncertainties on signal yields is shown in Table 7.6 for sample mass points. The dominant uncertainties arise from the uncertainties on the cross-section, jet energy scale and the error due to MC statistics.

Post-fit pulls for a sample mass point are shown in Figure 7.6. This indicates the same expected behaviour observed earlier using the CR-only fit. The effect of the uncertainties on μ_{Sig} is shown in Figure 7.7 for a sample mass point. The largest systematic effect is from $t\bar{t}$ theory uncertainties. The effect of the data statistical uncertainty on μ_{Sig} is also shown; it can be seen here that the statistical error dominates the systematic error.

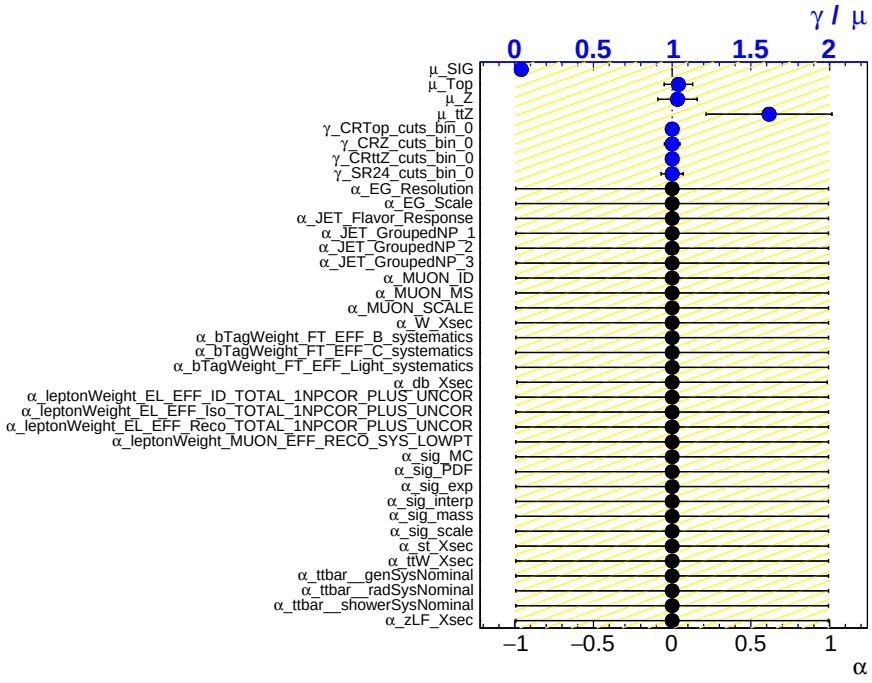

Figure 7.6 – Post-fit pulls using the signal+background mode of the fit for H^+ =160, A= 24 GeV mass point. None of the NPs are being pulled or constrained.

Signal	H160a15
Total uncertainty	[7.50%]
alpha_sig_PDF	[4.2%]
alpha_sig_scale	[3.5%]
alpha_sig_mass	[3.0%]
alpha_JET_GroupedNP_1	[2.8%]
alpha_JET_GroupedNP_2	[2.3%]
gamma_stat_SR15_cuts_bin_0	[1.1%]
alpha_JET_Flavor_Response	[1.1%]
alpha_bTagWeight_FT_EFF_B_systematics	[1.1%]
alpha_bTagWeight_FT_EFF_Light_systematics	[0.47%]
alpha_SF_SLORDLMUON_EFF_TrigSystUncertainty	[0.44%]
alpha_leptonWeight_MUON_EFF_RECO_SYS	[0.44%]
alpha_leptonWeight_MUON_EFF_RECO_SYS_LOWPT	[0.37%]
alpha_bTagWeight_FT_EFF_C_systematics	[0.35%]
alpha_jvtWeight_JET_JvtEfficiency	[0.32%]
alpha_JET_JER_EffectiveNP_4	[0.23%]
alpha_JET_GroupedNP_3	[0.19%]
alpha_leptonWeight_MUON_EFF_ISO_SYS	[0.12%]
alpha_leptonWeight_MUON_EFF_TTVA_STAT	[0.12%]
alpha_SF_SLORDLMUON_EFF_TrigStatUncertainty	[0.11%]
alpha_leptonWeight_MUON_EFF_TTVA_SYS	[0.10%]
alpha_leptonWeight_MUON_EFF_RECO_STAT	[0.10%]
alpha_leptonWeight_MUON_EFF_RECO_STAT_LOWPT	[0.07%]
alpha_JET_JER_EffectiveNP_6	[0.06%]
alpha_leptonWeight_MUON_EFF_ISO_STAT	[0.05%]
alpha_bTagWeight_FT_EFF_extrapolation_from_charm	[0.04%]
alpha_JET_JER_EffectiveNP_7restTerm	[0.03%]
alpha_JET_JER_EffectiveNP_2	[0.03%]
alpha_MUON_SAGITTA_RESBIAS	[0.03%]
alpha_JET_JER_EffectiveNP_5	[0.03%]
alpha_pileupWeight	[0.02%]
alpha_JET_JER_EffectiveNP_3	[0.02%]
alpha_JET_JER_EffectiveNP_1	[0.01%]
alpha_MUON_SAGITTA_RHO	[0.01%]
alpha_bTagWeight_FT_EFF_extrapolation	[0.01%]
alpha_JET_EtaIntercalibration_NonClosure_posEta	[0.00%]
mu_Z	[0.00%]
alpha_JET_EtaIntercalibration_NonClosure_negEta	[0.00%]
alpha_ttbar__showerSysNominal	[0.00%]
alpha_db_Xsec	[0.00%]
alpha_leptonWeight_MUON_EFF_BADMUON_SYS	[0.00%]
gamma_stat_CRTop_cuts_bin_0	[0.00%]
alpha_st_Xsec	[0.00%]
alpha_ttbar__genSysNominal	[0.00%]
mu_ttZ	[0.00%]
alpha_ttW_Xsec	[0.00%]
alpha_ttbar__radSysNominal	[0.00%]
gamma_stat_CRZ_cuts_bin_0	[0.00%]
alpha_W_Xsec	[0.00%]
mu_Top	[0.00%]
gamma_stat_CRttZ_cuts_bin_0	[0.00%]
alpha_JET_EtaIntercalibration_NonClosure_highE	[0.00%]

Signal	160a45
Total uncertainty	[7.44%]
alpha_sig_PDF	[4.2%]
alpha_sig_scale	[3.5%]
alpha_sig_mass	[3.0%]
alpha_JET_GroupedNP_1	[2.7%]
alpha_JET_GroupedNP_2	[2.2%]
gamma_stat_SR45_cuts_bin_0	[1.2%]
alpha_JET_Flavor_Response	[1.1%]
alpha_bTagWeight_FT_EFF_B_systematics	[1.1%]
alpha_SF_SLORDLMUON_EFF_TrigSystUncertainty	[0.47%]
alpha_leptonWeight_MUON_EFF_RECO_SYS	[0.45%]
alpha_leptonWeight_MUON_EFF_RECO_SYS_LOWPT	[0.36%]
alpha_jvtWeight_JET_JvtEfficiency	[0.31%]
alpha_bTagWeight_FT_EFF_Light_systematics	[0.30%]
alpha_bTagWeight_FT_EFF_C_systematics	[0.28%]
alpha_JET_GroupedNP_3	[0.21%]
alpha_JET_JER_EffectiveNP_4	[0.16%]
alpha_JET_JER_EffectiveNP_1	[0.14%]
alpha_leptonWeight_MUON_EFF_TTVA_STAT	[0.12%]
alpha_leptonWeight_MUON_EFF_TTVA_SYS	[0.11%]
alpha_SF_SLORDLMUON_EFF_TrigStatUncertainty	[0.11%]
alpha_leptonWeight_MUON_EFF_ISO_SYS	[0.10%]
alpha_leptonWeight_MUON_EFF_RECO_STAT	[0.10%]
alpha_JET_JER_EffectiveNP_2	[0.10%]
alpha_pileupWeight	[0.09%]
alpha_leptonWeight_MUON_EFF_RECO_STAT_LOWPT	[0.07%]
alpha_bTagWeight_FT_EFF_extrapolation_from_charm	[0.07%]
alpha_JET_JER_EffectiveNP_6	[0.05%]
alpha_JET_JER_EffectiveNP_5	[0.05%]
alpha_leptonWeight_MUON_EFF_ISO_STAT	[0.05%]
alpha_JET_JER_EffectiveNP_3	[0.03%]
alpha_MUON_SAGITTA_RESBIAS	[0.02%]
alpha_MUON_SAGITTA_RHO	[0.01%]
alpha_JET_EtaIntercalibration_NonClosure_negEta	[0.01%]
alpha_JET_EtaIntercalibration_NonClosure_posEta	[0.01%]
alpha_JET_JER_EffectiveNP_7restTerm	[0.01%]
alpha_bTagWeight_FT_EFF_extrapolation	[0.00%]
mu_Z	[0.00%]
alpha_ttbar__showerSysNominal	[0.00%]
alpha_db_Xsec	[0.00%]
alpha_leptonWeight_MUON_EFF_BADMUON_SYS	[0.00%]
gamma_stat_CRTop_cuts_bin_0	[0.00%]
alpha_st_Xsec	[0.00%]
alpha_ttbar__genSysNominal	[0.00%]
mu_ttZ	[0.00%]
alpha_ttW_Xsec	[0.00%]
alpha_ttbar__radSysNominal	[0.00%]
gamma_stat_CRZ_cuts_bin_0	[0.00%]
alpha_W_Xsec	[0.00%]
mu_Top	[0.00%]
gamma_stat_CRttZ_cuts_bin_0	[0.00%]
alpha_JET_EtaIntercalibration_NonClosure_highE	[0.00%]

Table 7.6 – Breakdown of systematic uncertainties on the signal yields in the corresponding SR bin. The percentages show the size of the uncertainty relative to the total expected pre-fit signal rate.

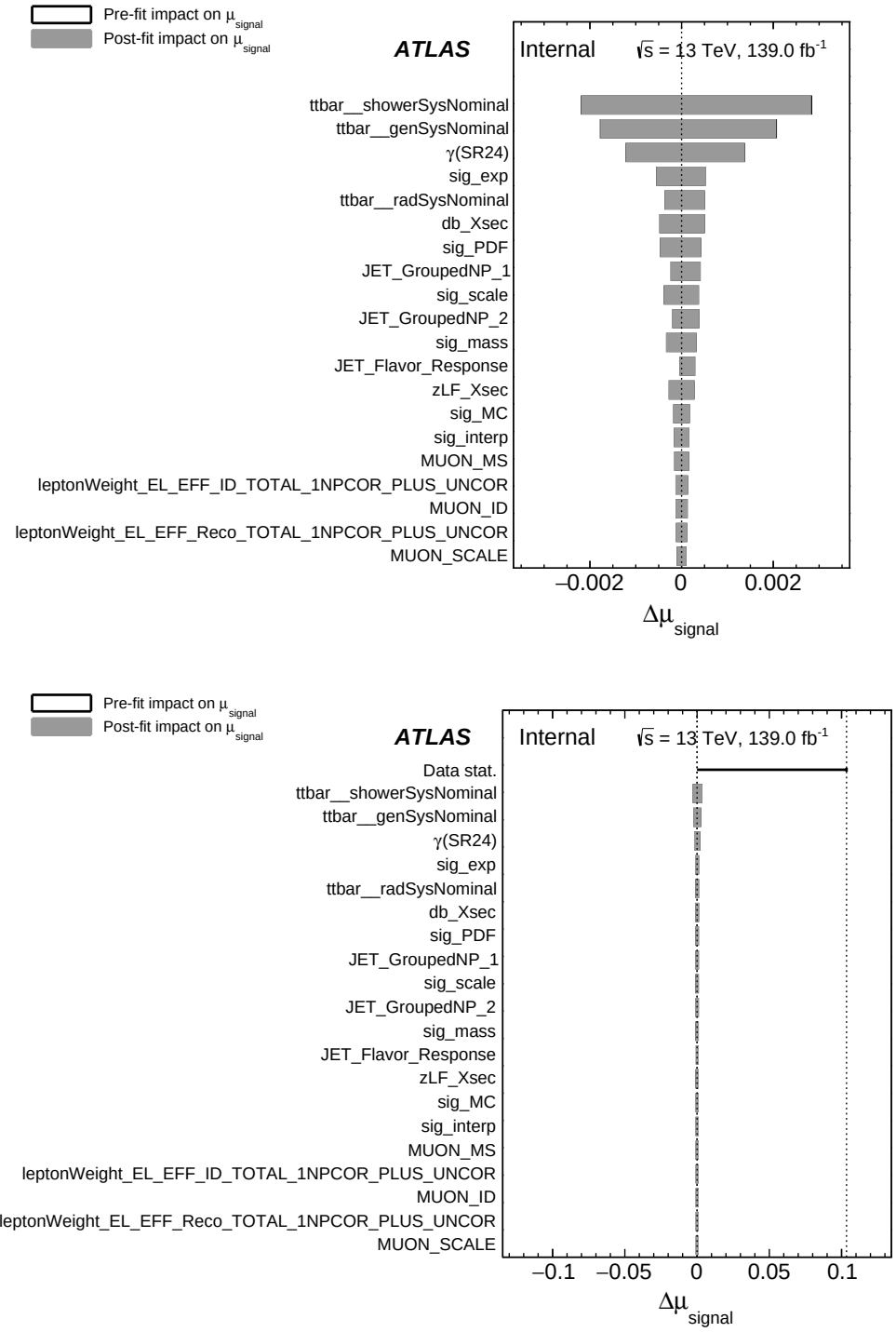

Figure 7.7 – Impact of uncertainties on μ_{Sig} for H^+ =160, A= 24 GeV. The first plot highlights the systematic uncertainties while the bottom shows that the data statistical uncertainty dominates. The impact on the signal strength, $\Delta\mu$, is given by the shift in the value of μ between a nominal fit and a fit with the nuisance parameter set to its best-fit value and associated uncertainty.

8

Results

8.1 CR-only Fit

The post-fit unblinded dimuon spectrum in the inclusive SR is shown in Figure 8.1. The data is in agreement with predictions of the simulation and an overall smooth spectrum is seen. The observed data and the estimated backgrounds in the individual SR regions, after application of the dimuon mass window cuts, can be seen in Figure 8.2.

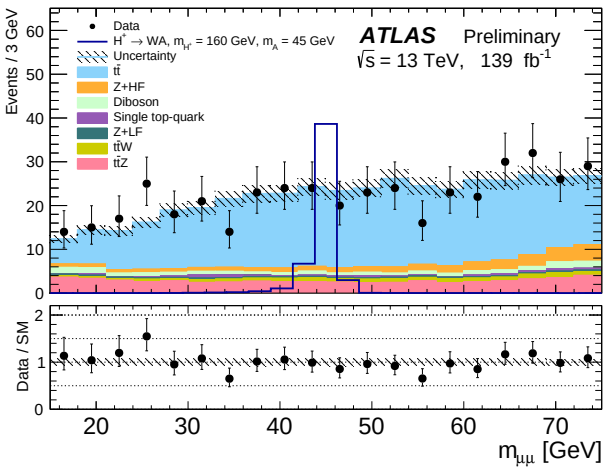

Figure 8.1 – Post-fit plot for the observed di-muon mass spectrum in the inclusive SR using the CR-only fit. The expected signal distribution for $m_{H^+} = 160$ GeV, $m_A = 45$ GeV is overlaid on top of the background to indicate the signal shape; the signal is not used in this fit configuration. Assumptions on the signal are: $\sigma(t\bar{t})$ = 832 pb, $\mathcal{B}(t \to bH^{\pm}) = 0.03$, $\mathcal{B}(H^{\pm} \to W^{\pm}A) = 1$ and $\mathcal{B}(A \to \mu^+\mu^-) = 3 \times 10^{-4}$.

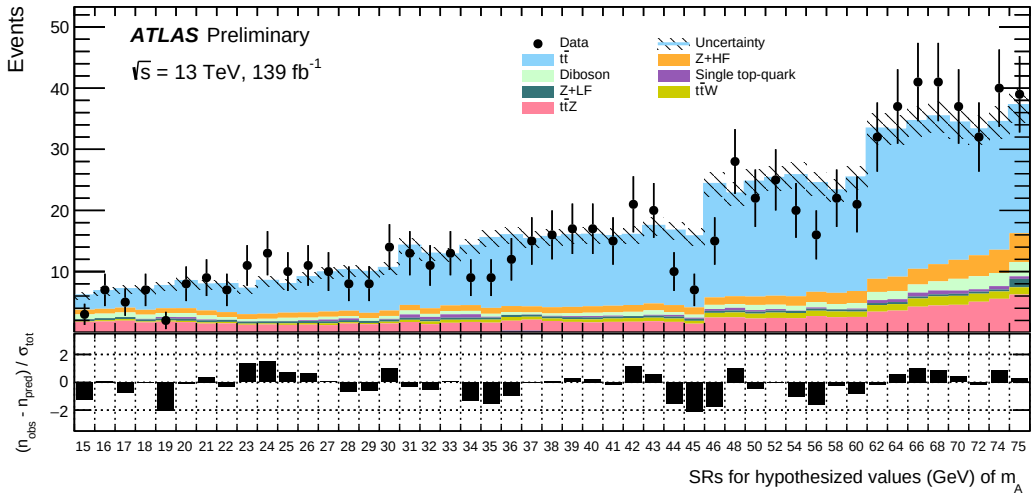

Figure 8.2 – Data and predicted background yields using the CR-only fit in individual SRs after application of the di-muon mass window cuts to the inclusive SR. Events in neighbouring bins partially overlap. The bin widths used for the search are described in Section 6. The width changes at 30 GeV, 45 GeV and 60 GeV, explaining the steps observed in the spectrum. The bottom panel shows the pull in each bin, defined as $(n_{\text{obs}}-n_{\text{pred}})/\sigma_{\text{tot}}$, where n_{obs} is the number of events in the data, n_{pred} is the number of the fitted background events and σ_{tot} is the total (systematic and statistical, added in quadrature) uncertainty on the fitted background yield.

8.2 Signal + Background Fit

This section shows the results with the signal+background mode of the fit. Using the method described previously in Section 6, the fit scans the dimuon spectrum and generates the exclusion limits shown in Figure 8.3. The limits for m_A = 15, 30, 45, 60, 75 GeV are using yields directly from the signal MC while the remainder of the mass points use the interpolated yields.

No significant excess above SM predictions is observed. The largest excess is found at a mass of 24 GeV and corresponds to a local p-value of 0.106 and significance of 1.24σ under the background-only hypothesis. Limits are set at 95% CL on the product of the branching ratios $t \to bH^{\pm}$, $H^{\pm} \to W^{\pm}A$ and $A \to \mu^{+}\mu^{-}$. The observed (expected) upper limits for a H^{+} mass of 160 GeV range from 1.0 (1.57) $\times 10^{-6}$ to 3.6 (3.21) $\times 10^{-6}$. These can be found in Tables 8.1 and 8.2. A 2D-representation of the limits are found in Figure 8.4 which is obtained by a linear interpolation between the tested points. The sensitivity represents an advance over the CMS results [63], as discussed in the next section.

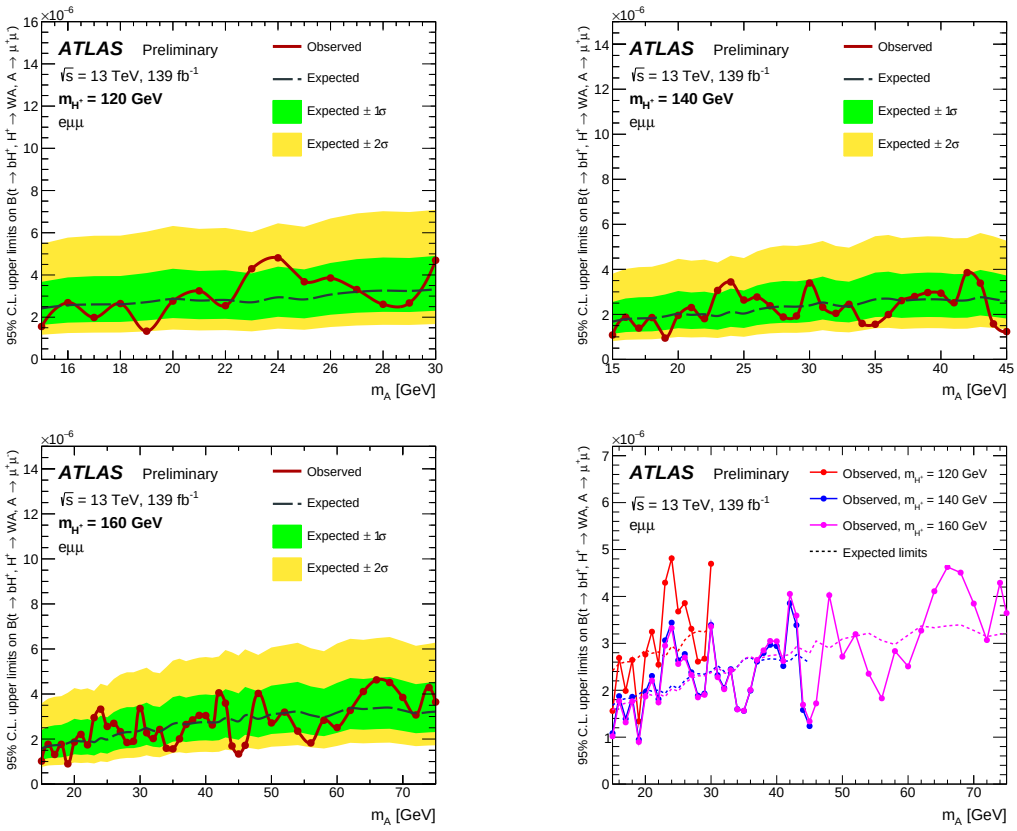

Figure 8.3 – Expected and observed upper limits for the signal using the signal+background mode of the fit. Limits are shown for several H^+ masses. The limits for m_A = 15, 30, 45, 60, 75 GeV are using yields directly from the signal MC while the remainder of the mass points use the interpolated yields. The fourth panel overlays the limits from the other three, for easier comparison.

Masses, GeV		Upper limits, 95% CL, $\times 10^{-6}$					
m_{H^+}	m_A	observed	-2 σ	-1 σ	expected	+1 σ	+2 σ
100	15	6.85	5.11	7.17	9.96	12.61	18.53
120	15	1.55	1.16	1.62	2.40	3.65	5.45
120	16	2.67	1.24	1.73	2.55	3.87	5.75
120	17	1.99	1.27	1.77	2.60	3.94	5.86
120	18	2.64	1.27	1.77	2.61	3.95	5.86
120	19	1.34	1.33	1.85	2.71	4.09	6.05
120	20	2.76	1.41	1.96	2.86	4.29	6.32
120	21	3.25	1.37	1.90	2.79	4.19	6.18
120	22	2.55	1.39	1.92	2.81	4.23	6.23
120	23	4.28	1.32	1.84	2.70	4.07	6.02
120	24	4.81	1.46	2.02	2.94	4.39	6.45
120	25	3.68	1.40	1.94	2.84	4.26	6.28
120	26	3.83	1.52	2.10	3.06	4.55	6.66
120	27	3.31	1.61	2.21	3.20	4.75	6.91
120	28	2.61	1.64	2.25	3.26	4.83	7.02
120	29	2.67	1.63	2.24	3.24	4.80	6.97
120	30	4.69	1.67	2.30	3.32	4.89	7.08
140	15	1.08	0.80	1.12	1.67	2.54	3.79
140	16	1.86	0.86	1.21	1.78	2.69	4.01
140	17	1.39	0.89	1.24	1.82	2.76	4.10
140	18	1.86	0.89	1.24	1.83	2.77	4.12
140	19	0.95	0.94	1.30	1.91	2.88	4.26
140	20	1.95	1.00	1.39	2.03	3.04	4.47
140	21	2.30	0.97	1.35	1.98	2.97	4.38
140	22	1.81	0.99	1.37	2.00	3.01	4.43
140	23	3.05	0.95	1.31	1.92	2.90	4.29
140	24	3.44	1.05	1.45	2.11	3.14	4.61
140	25	2.64	1.00	1.40	2.04	3.06	4.50
140	26	2.75	1.10	1.51	2.20	3.27	4.78
140	27	2.38	1.16	1.59	2.30	3.42	4.97
140	28	1.88	1.18	1.63	2.35	3.48	5.06
140	29	1.92	1.18	1.62	2.34	3.46	5.03
140	30	3.39	1.21	1.66	2.40	3.54	5.11
140	31	2.32	1.30	1.77	2.53	3.68	5.26
140	32	2.05	1.23	1.68	2.40	3.51	5.04
140	33	2.45	1.20	1.64	2.36	3.45	4.96
140	34	1.60	1.29	1.75	2.50	3.65	5.21
140	35	1.56	1.38	1.88	2.66	3.85	5.47
140	36	1.99	1.40	1.90	2.70	3.90	5.53
140	37	2.61	1.35	1.84	2.61	3.79	5.39
140	38	2.79	1.38	1.87	2.65	3.83	5.43
140	39	2.97	1.39	1.88	2.67	3.86	5.47
140	40	2.94	1.38	1.88	2.66	3.84	5.45
140	41	2.52	1.36	1.85	2.62	3.79	5.38
140	42	3.85	1.36	1.85	2.62	3.80	5.39
140	43	3.39	1.44	1.95	2.76	3.97	5.61
140	44	1.58	1.40	1.89	2.68	3.86	5.46
140	45	1.24	1.34	1.82	2.58	3.72	5.27

Table 8.1 – Observed and expected limits on the product of the branching ratios $t \to bH^{\pm}$, $H^{\pm} \to W^{\pm}A$ and $A \to \mu^{+}\mu^{-}$ for m_{H^+} 100 to 140 GeV.

Masses, GeV		Upper limits, 95% CL, $\times 10^{-6}$					
m_{H^+}	m_A	observed	-2 σ	-1 σ	expected	+1 σ	+2 σ
160	15	1.01	0.75	1.06	1.57	2.39	3.57
160	16	1.75	0.82	1.14	1.68	2.54	3.78
160	17	1.32	0.84	1.17	1.72	2.61	3.88
160	18	1.76	0.85	1.18	1.74	2.63	3.90
160	19	0.90	0.89	1.24	1.82	2.74	4.05
160	20	1.87	0.96	1.32	1.93	2.90	4.26
160	21	2.21	0.93	1.30	1.89	2.84	4.20
160	22	1.74	0.95	1.32	1.92	2.89	4.25
160	23	2.94	0.91	1.27	1.86	2.80	4.13
160	24	3.32	1.01	1.40	2.03	3.04	4.46
160	25	2.56	0.98	1.35	1.98	2.96	4.36
160	26	2.68	1.07	1.47	2.14	3.18	4.65
160	27	2.33	1.13	1.56	2.25	3.34	4.86
160	28	1.85	1.16	1.59	2.31	3.42	4.96
160	29	1.90	1.16	1.59	2.30	3.41	4.96
160	30	3.35	1.20	1.65	2.37	3.50	5.06
160	31	2.28	1.28	1.74	2.48	3.62	5.17
160	32	2.02	1.21	1.66	2.37	3.47	4.97
160	33	2.43	1.19	1.63	2.34	3.42	4.92
160	34	1.59	1.28	1.75	2.49	3.63	5.19
160	35	1.56	1.39	1.88	2.67	3.86	5.48
160	36	2.01	1.41	1.92	2.72	3.93	5.57
160	37	2.65	1.37	1.87	2.65	3.84	5.46
160	38	2.85	1.40	1.90	2.70	3.91	5.54
160	39	3.05	1.43	1.93	2.74	3.96	5.61
160	40	3.04	1.43	1.94	2.75	3.98	5.64
160	41	2.62	1.42	1.92	2.73	3.95	5.61
160	42	4.05	1.43	1.95	2.76	3.99	5.66
160	43	3.59	1.53	2.07	2.92	4.21	5.94
160	44	1.69	1.49	2.02	2.86	4.13	5.85
160	45	1.34	1.45	1.97	2.79	4.02	5.70
160	46	1.72	1.63	2.19	3.05	4.31	5.98
160	48	4.02	1.54	2.07	2.90	4.11	5.73
160	50	2.71	1.66	2.22	3.09	4.37	6.06
160	52	3.19	1.69	2.27	3.15	4.45	6.17
160	54	2.35	1.73	2.32	3.22	4.54	6.28
160	56	1.83	1.63	2.19	3.06	4.34	6.03
160	58	2.83	1.58	2.13	2.98	4.23	5.90
160	60	2.51	1.69	2.27	3.17	4.49	6.24
160	62	3.27	1.83	2.44	3.37	4.71	6.45
160	64	4.11	1.81	2.41	3.33	4.66	6.40
160	66	4.63	1.83	2.44	3.37	4.72	6.48
160	68	4.51	1.84	2.46	3.39	4.75	6.53
160	70	3.85	1.77	2.36	3.27	4.60	6.34
160	72	3.07	1.68	2.26	3.14	4.43	6.13
160	74	4.29	1.71	2.30	3.19	4.51	6.23
160	75	3.64	1.72	2.31	3.21	4.54	6.28

Table 8.2 – Observed and expected limits on the product of the branching ratios $t \to bH^{\pm}$, $H^{\pm} \to W^{\pm}A$ and $A \to \mu^{+}\mu^{-}$ for m_{H^+} 160 GeV.

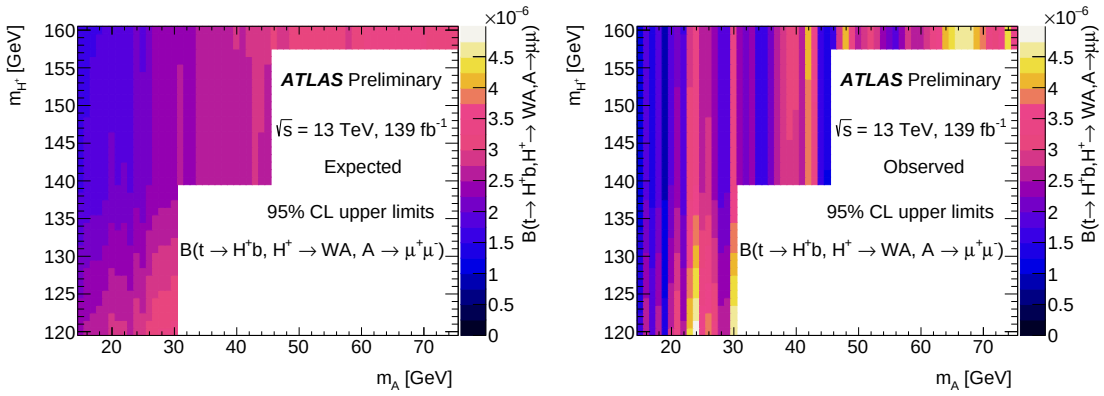

Figure 8.4 – Expected (a) and observed (b) upper limits on the branching ratios, shown as a function of m_A and m_{H^+}. The limits are evaluated at 120, 140 and 160 GeV in m_{H^+} and linearly interpolated in 1 GeV steps between the tested points, except above 45 GeV in m_A, where only m_{H^+}=160 GeV is tested, the results are displayed against 157-160 GeV for legibility. The empty region corresponding to an off-shell W boson is not tested in this analysis.

9

Discussion and Outlook

The analysis presented in this thesis is the first ATLAS result for the $H^+ \to WA$ process at $\sqrt{s} = 13$ TeV. The search was carried out by looking for an excess in the dimuon mass spectrum. The backgrounds were estimated by constraining and validating simulations in kinematic regions close to the signal region. A low mass charged Higgs boson produced in association with top quark pairs was simulated for the signal. Upper limits on the product of the branching ratios $t \to bH^{\pm}$, $H^{\pm} \to W^{\pm}A$ and $A \to \mu^+\mu^-$ are calculated.

As seen earlier in Section 8, data shows excellent agreement with SM predictions and no significant excess is observed. The largest excess is found at a mass of 24 GeV and corresponds to a significance of 1.24σ. Small deficits at 35, 45 and 55 GeV are observed which is expected behavior due to statistical fluctuations when scanning a wide mass range.

Another low mass dimuon resonance search by ATLAS, published around the same time as this analysis, is the $bb\mu\mu$ analysis [204]. Using Run-2 data, it searches for CP-odd scalar particles with 2 b-jets and 2 muons in the final state. A local excess of 3.3σ is seen by the analysis at $m_{\mu\mu}$ = 52 GeV but this does not appear in our search. Both analyses, however, show a smooth dimuon mass spectrum in the inclusive signal region as seen in Figure 9.1. Additionally, the analysis does not see the $\approx$ 30 GeV dimuon excess, in association with b-quarks, reported at the LEP [205], and then again by the CMS experiment [206]. Our results here are congruent with the ATLAS cross-check which did not find evidence for it [207].

The $H^{\pm} \to W^{\pm}A$ signal model was searched by the CMS experiment [63] as highlighted earlier. The limits presented here are an improvement by an average

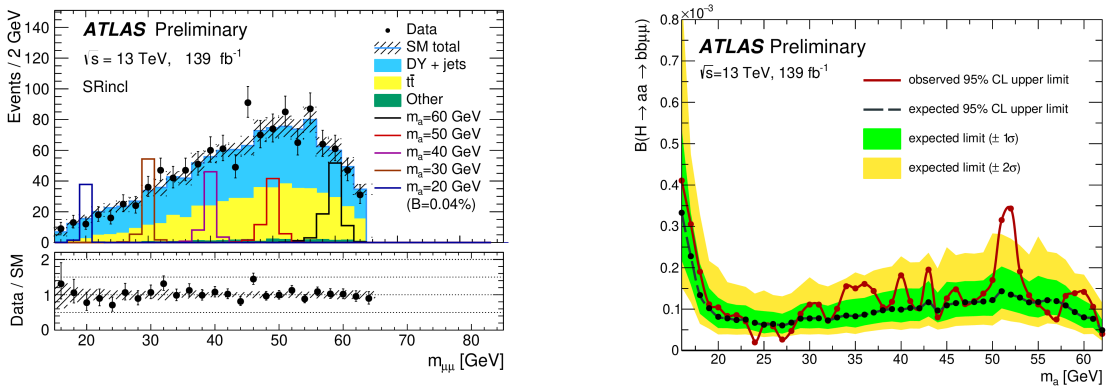

Figure 9.1 – Results of the $bb\mu\mu$ analysis [204]. Left: the dimuon mass spectrum in the inclusive signal region. Right: Upper limits on the signal model highlighting an excess at a dimuon mass of 52 GeV.

factor of ≈ 2 compared to the existing results for the $e\mu\mu$ channel as seen in Figure 9.2. Additionally, it has been noted [49] that the CMS result was of limited use as the upper limits were not released for the full two-dimensional mass plane, but for one-dimensional slices, assuming either $m_{H^\pm} = 160$ GeV or $m_{H^\pm} = m_A + 85$ GeV. By providing a scan over the $(m_{H^\pm}, m_A)$ parameter space, this work adds another improvement to existing literature.

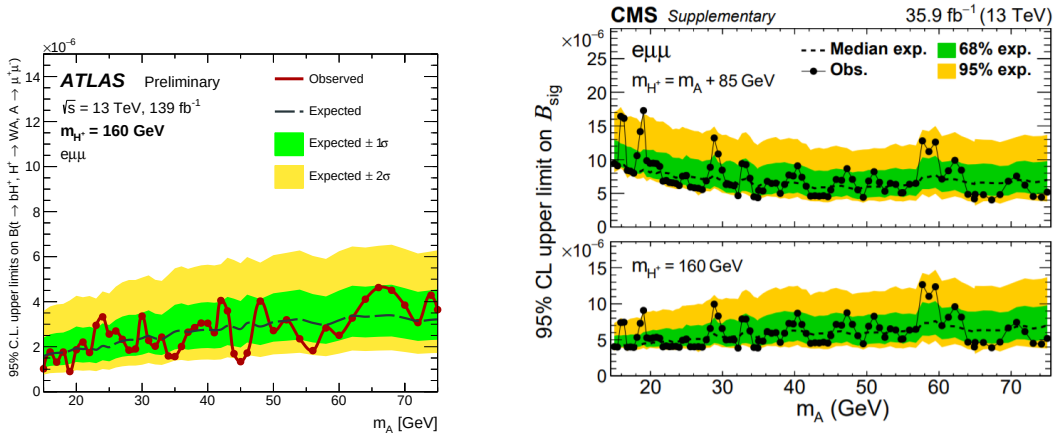

Figure 9.2 – A comparison of the ATLAS and CMS results [63] for the $e\mu\mu$ channel.

The systematic uncertainties on the background and signal were thoroughly evaluated in Section 7. The typical magnitude of the uncertainty on the back-

ground yield was found to be $\approx 20\%$, while for the signal it was $\approx 7\%$. This is an improvement from CMS which reports a background uncertainty of 30%. The impact of the systematic uncertainties on the result, however, is small because of the large statistical error of the data. The dominant sources of uncertainty are due to the $\mu_{t\bar{t}}$ and μ_{ttZ} normalizations, $t\bar{t}$ theory contributions, and the error due to MC statistics.

The impact on the NPs in the fit is also shown in Figure 7.6. If any of the uncertainties are over-estimated, the fit in principle can constrain it with data. Similarly, if the fit is over-constrained, some of the NPs could shift away from their central values i.e. 'pulled' in order to find better agreement. In this analysis it is found that the post-fit values of the NPs are centered at the input value of zero with the error bars still having $\pm 1\sigma$ size. This means that none of the NPs are being pulled or constrained. This is expected as the analysis uses a single-bin design and there is limited information available to constrain the NPs.

This analysis also provides an important validation of the use of MC templates for the purposes of background modeling. Employing the use of transfer factors to extrapolate from CRs, excellent Data/MC agreement in the VR and SR is shown in Section 6.7. Lastly, potential areas of improving this analysis are discussed below.

9.1 Charged Higgs reconstruction

In principle, there are two resonant peaks which could be searched for in this analysis: the H^+ and the A. Searching in the H^+ spectrum was attempted, but it was not effective as the reconstruction resolution for the charged Higgs is quite poor.

Difficulties in the reconstruction arise due to several reasons. While the muon pair comes from the A, the electron's parent W could come from either $t \to Wb$ or $H^+ \to WA$. An ambiguity therefore arises about whether to reconstruct the H^+ by combining the A candidate with the electron and MET, or with a pair of light jets. The jet pairing is also ambiguous because only one b-jet is required; requiring a second one would cause a substantial drop in efficiency. Reconstructing the neutrino four-vector also involves the poor MET resolution and an ambiguity in the z component.

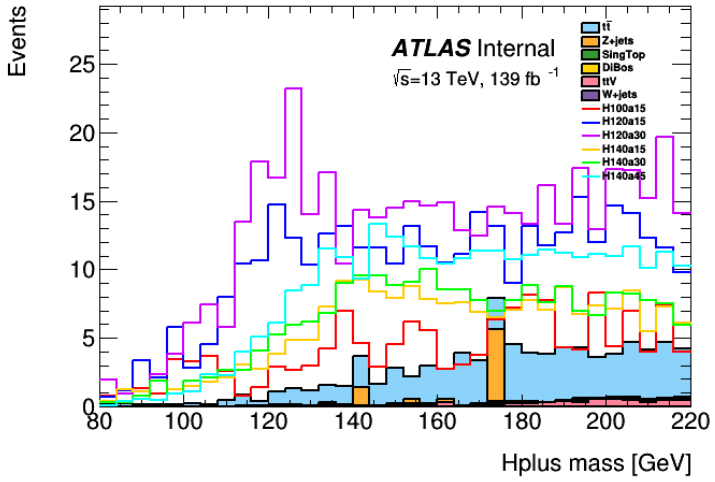

Figure 9.3 – Reconstruction of the charged Higgs invariant mass.

The attempt to reconstruct the H^+ was made using the jet pair with a mass closest to the W boson mass. This might be expected to show a peak for about half the events. However, the distributions obtained show only a small fraction of the H^+ signal contributes to a resonance peak, as seen in Figure 9.3, and thus searching this spectrum has limited advantage. A future analysis could improve on the attempt at building the mass estimator. This could be done by developing

a W-tagging algorithm which would be able to resolve the ambiguity about the electron's parent. Supervised machine learning techniques can play an important role in this improvement.

9.2 $\mu\mu\mu$ mode: reconstruction algorithm

The $e\mu\mu$ final states were chosen for this search as this channel has a simple reconstruction algorithm for the A particle, offers low backgrounds and a competitive sensitivity. In order to improve the results in the 3-lepton channel, the $\mu\mu\mu$ mode would be the next channel to study.

In the trimuon mode, there is an ambiguity about assigning muons to the A in order to create the dimuon mass spectrum. A study was conducted with several algorithms to test which one gives the best accuracy. Events are selected with exactly three muons which have atleast one opposite-sign (OS) charge pair. Thus, the charge configuration of the trio involve two same-sign muons and one muon which is opposite to the other two. Example of the charge configurations are : (+, -, -) (-,+,-) (+,+,-).

The transverse mass was used in these algorithms. It is defined as: $m_T = \sqrt{2|p_T^{\mu}|E_T^{miss}|(1-\cos\phi)}$. If a muon's p_{T} can yield a m_T between 45 GeV and 130 GeV, it is tagged as originating from the W boson instead of the A. Description of the algorithms to select two out of the three muons to build the dimuon mass spectrum are below; the results of the study are summarized in Table 9.1.

Algorithm 1: The first candidate is the OS muon i.e. it has the opposite-sign to the other two muons in the set. It is then paired with the lower p_{T} muon of the remaining two.

Algorithm 2: The first candidate is the OS muon. It is then paired with the muon which gives a lower ΔR value.

Algorithm 3: The first candidate is the OS muon. It is then paired with the lower p_{T} muon of the remaining two - except if the lower p_{T} muon gives the W transverse mass and the other muon does not.

Algorithm 4: The first candidate is the OS muon. The invariant mass for each of the two possible pairing is calculated. If one of the two gives an exceedingly large dimuon mass of > 140 GeV and the other pair gives a mass of < 120 GeV, then the candidate is paired with the muon giving the lower mass. If this condition is not met, resort back to Algorithm 3 i.e. pair with the lower p_{T} muon of the remaining two - except if the lower p_{T} muon gives the W transverse mass and the other muon does not.

mass	Algorithm 1	Algorithm 2	Algorithm 3	Algorithm 4
H^+100a15	95.8	50.1	92.0	92.1
H^+120a30	83.7	49.4	80.3	81.1
H^+160a60	56.8	46.8	59.7	61.8
H^+160a75	52.8	36.3	58.1	60.8

Table 9.1 – $\mu\mu\mu$ reconstruction: accuracy (in %) of correctly assigning the muons to the A particle in trimuon events using various algorithms.

This study shows that Algorithm 4 should be chosen as the preferred method for reconstructing the A. It gives an accuracy between 92% - 61%, an improvement on the CMS algorithm which gives an accuracy between 84% - 59% [63].

9.3 Extensions of the mass grid

The mass range for this analysis can be extended to further improve the search for this signal model. There is particular motivation for extending the search to lower masses in the range of 2 to 12 GeV. While this region poses several challenges in background modelling due to the Upsilon resonances, phenomenological studies show that such a low mass resonance could account for the $g-2$ anomaly [208, 209]. This is especially relevant in light of the recent results for the muon magnetic moment measurement showing a 4.2 σ deviation from Standard Model predictions [44].

To study the feasibility of extending this search, signal simulations for lower m_A masses were produced. The samples were produced in the same way as for the main analysis and processed through the ATLAS detector simulation. The mass points generated were m_A = 4, 7, 10 GeV, while the charged Higgs mass was kept the same i.e. m_H^+ = 100, 120, 140, 160 GeV. The object definitions and isolation requirements were kept the same, but a looser selection with the lepton p_{T} cuts relaxed was used as shown in Table 9.2. Key variables showing the characteristics of the signal at low masses were then plotted with these cuts applied as shown in Figures 9.4, 9.5, 9.6.

	Event selection	
Trigger	single muon	di-muon
Muons	$p_{\mathrm{T}}^{\text{leading}} > 27$ GeV, $p_{\mathrm{T}}^{\text{subleading}} > 5$ GeV	$p_{\mathrm{T}}^{\text{leading}} > 15$ GeV, $p_{\mathrm{T}}^{\text{subleading}} > 15$ GeV
	exactly 2, opposite sign $0 < m_{\mu\mu}$ [GeV] < 15	
Electrons	exactly 1	
Jets	≥ 3, $p_{\mathrm{T}} > 20$ GeV ≥ 1 b-tagged jet	

Table 9.2 – Summary of selection cuts used to study the kinematics of low mass resonances ranging from m_A = 4 to 10 GeV.

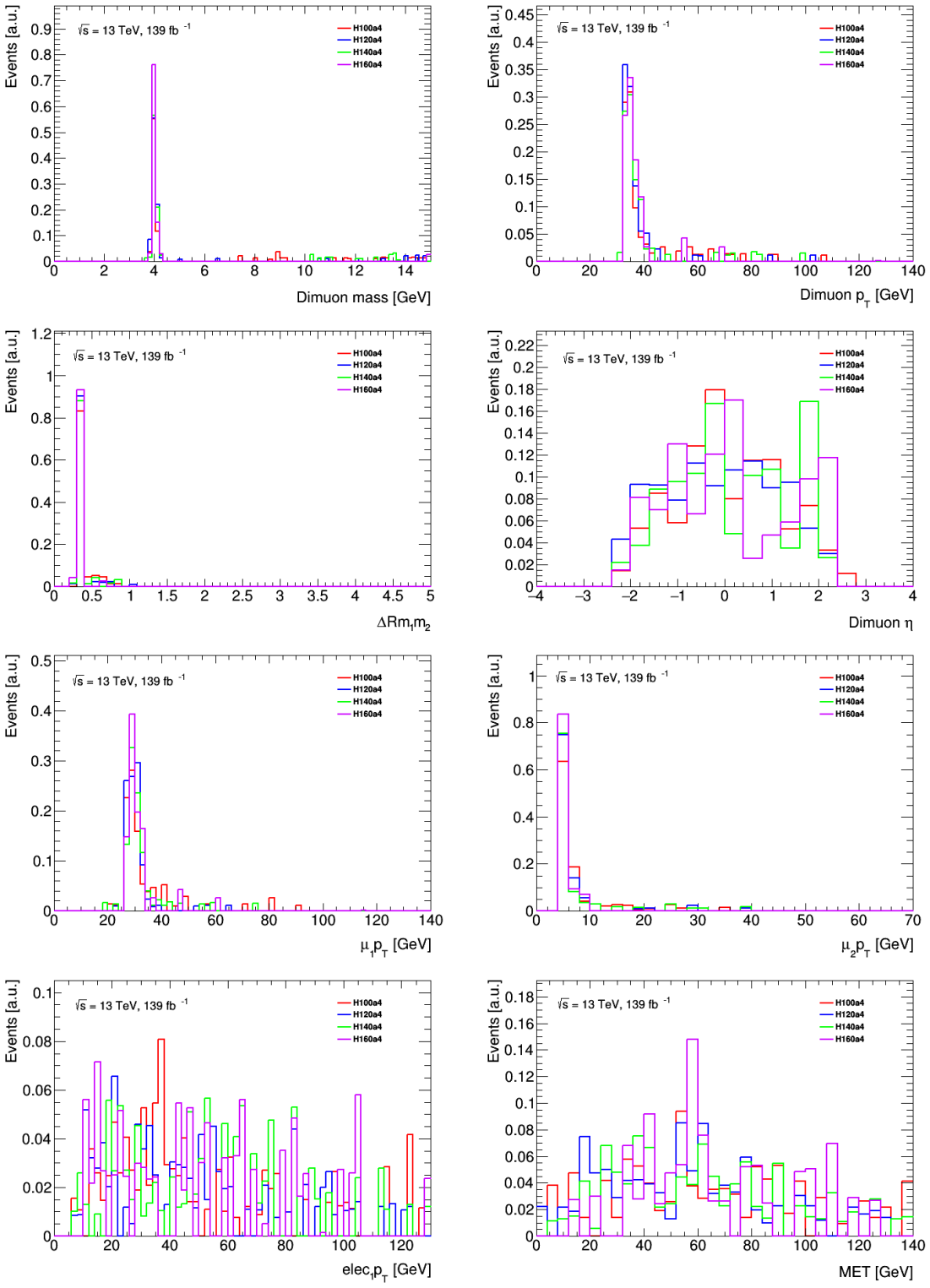

Figure 9.4 – Extensions to lower masses: kinematic quantities for the m_A= 4 GeV simulated signal with varying masses of the charged Higgs boson.

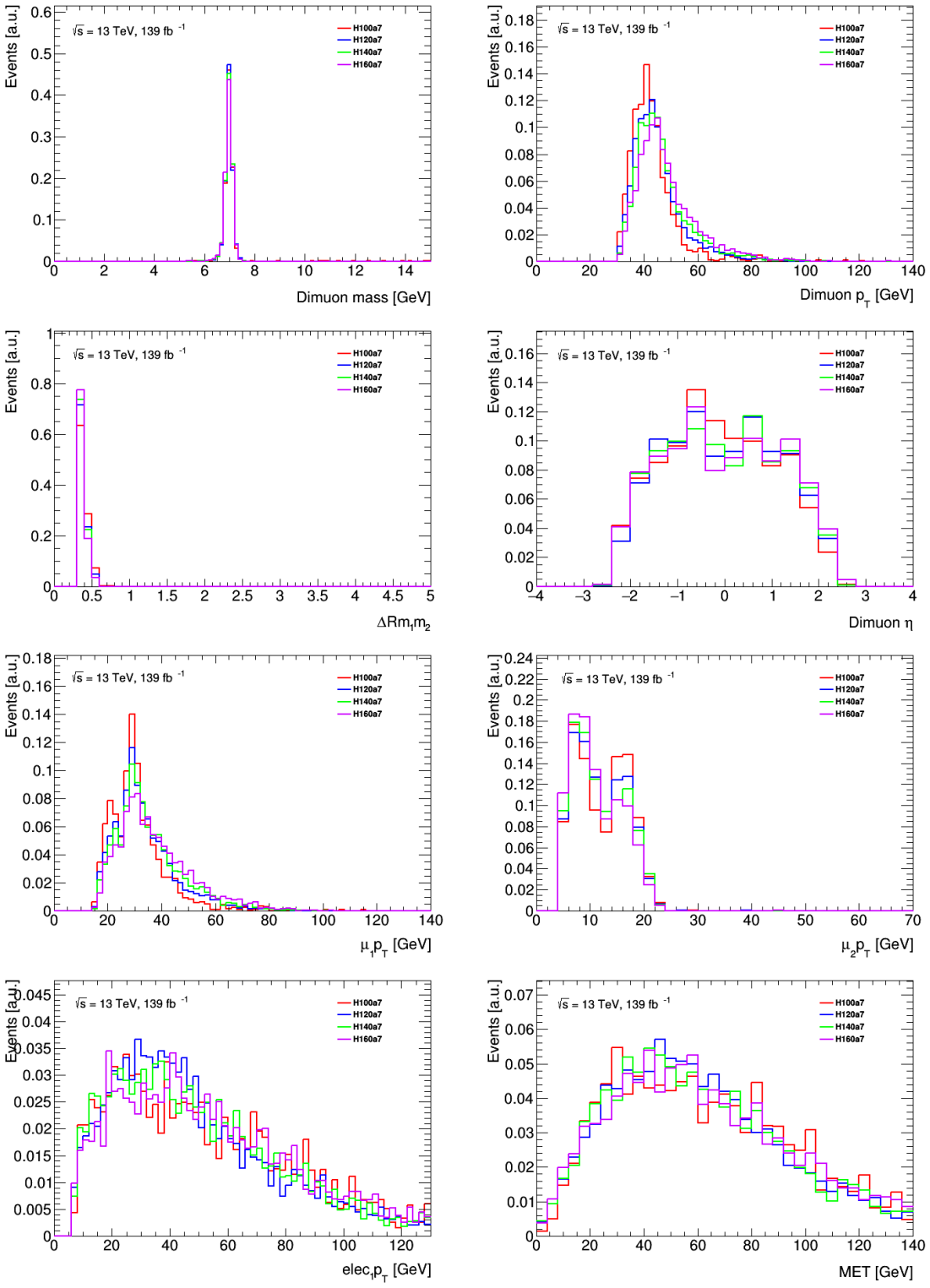

Figure 9.5 – Extensions to lower masses: kinematic quantities for the m_A= 7 GeV simulated signal with varying masses of the charged Higgs boson.

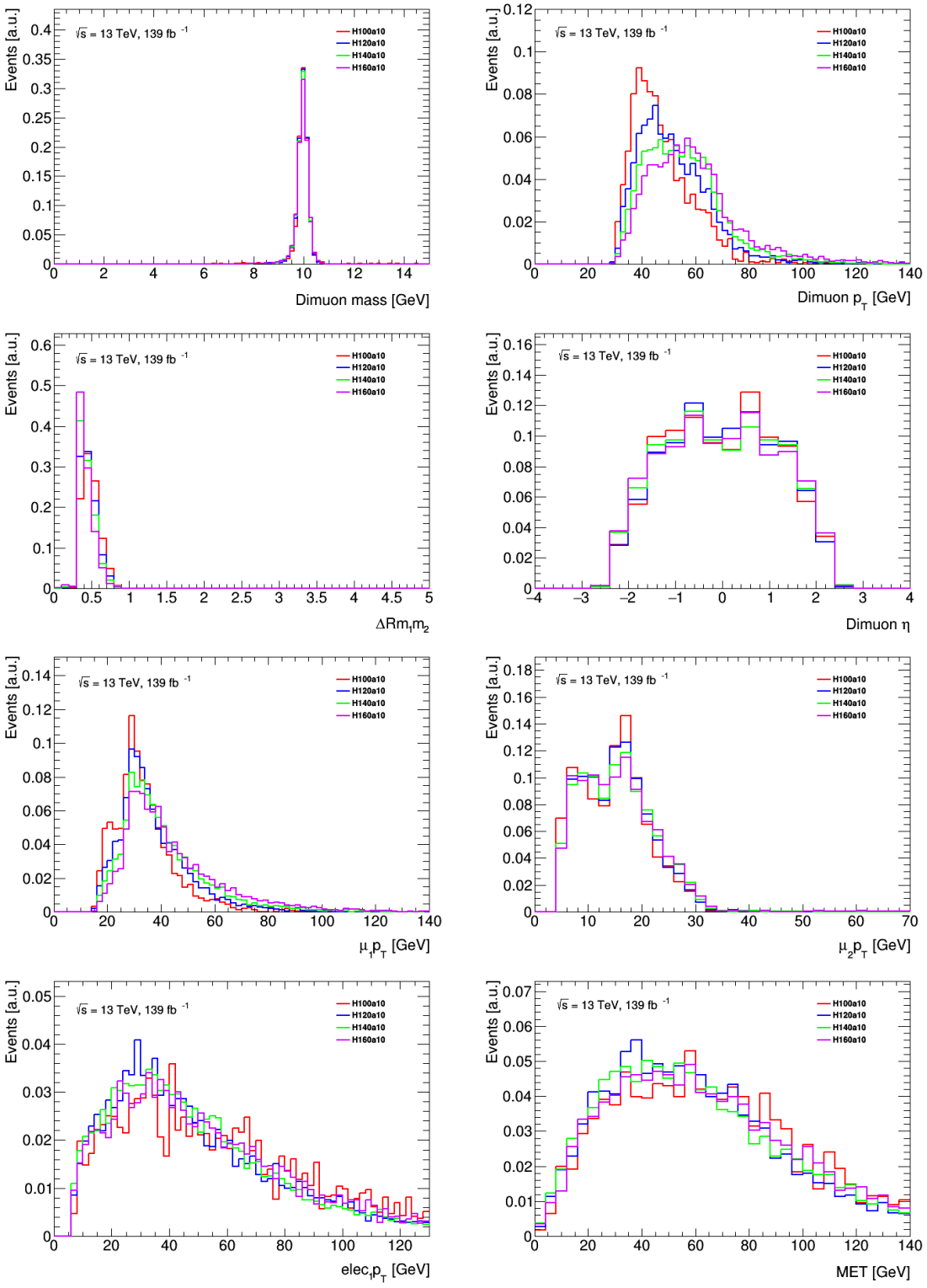

Figure 9.6 – Extensions to lower masses: kinematic quantities for the m_A= 10 GeV simulated signal with varying masses of the charged Higgs boson.

These distributions of the signal kinematics show a number of important features. It can be observed that the kinematics at this mass range (m_A = 4-10 GeV) are not as dependent on the charged Higgs mass as they were for higher and wider mass range (m_A = 15 - 75 GeV). For example, the ΔR profile shows little change as the H^+ mass is increased. This could provide motivation for implementing a $\Delta R < 1$ cut as the dimuon system is quite collimated due to the boost of the light A. It can also be seen that the dimuon mass resolution gets very small and it is unlikely the search could be extended below 4 GeV due to difficulties in resolving the two muons as separate objects.

The plots also show lower statistics for m_A = 4 GeV compared to the other masses. The selection efficiency of the triggers (a combination of the single muon and dimuon triggers) was thus compared between the mass points. Events were selected with atleast two muons, an electron and a jet. The identification and isolation requirement for objects are the same as the main analysis. As can be seen in the Table 9.3, there is a large drop in selection efficiency at the very low mass point of 4 GeV. This occurs as the muons at low masses don't have the energy needed to make it past the p_{T} threshold for the muon triggers, thus leading to inefficiencies in the selection.

	a4	a7	a10
H^+100	0.98 %	2.0 %	2.1 %
H^+120	0.93 %	3.1 %	4.3 %
H^+140	0.77 %	3.3 %	5.5 %
H^+160	0.74 %	3.4 %	6.4 %

Table 9.3 – Signal selection efficiencies with the single muon and dimuon triggers. Events are required to have at least two muons, one electron and one jet. An offline requirement of $p_{\mathrm{T}}^{\mu_1} > 27$ GeV and $p_{\mathrm{T}}^{\mu_{1,2}} > 15$ GeV is used for events passing the single muon and dimuon triggers respectively.

The selection efficiency could be improved by triggering on the high p_{T} electron from the W boson in the event. A study was done to check the potential for improvement by using the electron and muon triggers together in a logical "OR". The results are summarized in Table 9.4. As the table shows, significant gains can be made when the electron trigger is used in combination with the muon triggers;

an improvement factor ranging from 1.4 to 3.8 is seen.

While the gain from such a trigger strategy is impressive, implementing it for analysis purposes can pose a technical challenge. This is because the overall trigger scale factors for correcting the mismodeling of the trigger efficiency, defined as the trigger efficiency on data divided by the trigger efficiency on MC, have to be calculated for the OR between electron and muon triggers. This calculation can become quite challenging when using a complicated trigger list that involves mixing triggers. While this preliminary trigger study was done simply by using the information stored on the trigger decisions by the MC processing framework, the scale factor calculation would need to be done carefully and validated against data for a formal analysis.

	a4	gain factor	a7	gain factor	a10	gain factor
H^+100	3.7 %	3.8	5.5 %	2.8	5.6 %	2.7
H^+120	2.9 %	3.1	6.3 %	2.0	7.7 %	1.8
H^+140	2.1 %	2.7	5.8 %	1.8	8.1 %	1.5
H^+160	1.6 %	2.2	5.5 %	1.6	8.7 %	1.4

Table 9.4 – Signal selection efficiencies for events with the single muon, dimuon and electron triggers implemented in a logical OR. Events are required to have at least two muons, one electron and one jet. An offline requirement of $p_{\mathrm{T}}^{\mu_1} > 27$ GeV, $p_{\mathrm{T}}^{\mu_{1,2}} > 15$ GeV, $p_{\mathrm{T}}^{e} > 27$ GeV is used for events passing that single muon, dimuon and electron triggers respectively.

In addition to a low mass extension of the analysis, there is also reason to consider increasing to higher masses above the Z peak. This is motivated by an excess observed at ≈ 96 GeV both at the LHC and the original LEP collider. At LEP, a 2.3 σ local excess was observed around a mass of 98 GeV in the $e^+e^- \to Z(H \to bb)$ search [210]. At the LHC, the CMS experiment has reported an excess in two channels. In $H \to \gamma\gamma$, a local (global) excess of $2.8(1.3)\sigma$ is reported at a mass hypothesis of 95.3 GeV [211]. Most recently, they have also reported an excess in the $gg\phi \to \tau\tau$ channel with a local (global) p-value equivalent to 3.1 (2.7) standard deviations at a mass of 100 GeV [212]. This excess coincides with the 95 GeV $\gamma\gamma$ bump as it is within the resolution of the reconstructed invariant $\tau^+\tau^-$ mass. ATLAS has previously investigated this excess in the diphoton channel, but

was not able to find similar evidence using partial Run-2 data [213].

Phenomenological studies have used this excess to study the 2HDM parameter space by identifying the 96 GeV bump as the light CP-even state h in the model. As seen in Figure 9.7, these studies show that the $BR(H^+ \to WA)$ can reach an impressive 82% for $m_{H^+} > 165$ GeV in such scenarios ; exceeding the fermionic decay modes $c\bar{s}$ and $\tau\nu$ considerably [214]. This provides strong motivation to continue looking for this channel during Run-3 of the LHC as it offers a smoking gun signature. Furthermore, a future analysis should also consider off-shell W decays as it has been shown that the branching ratio can be substantial even when it is off mass shell [49].

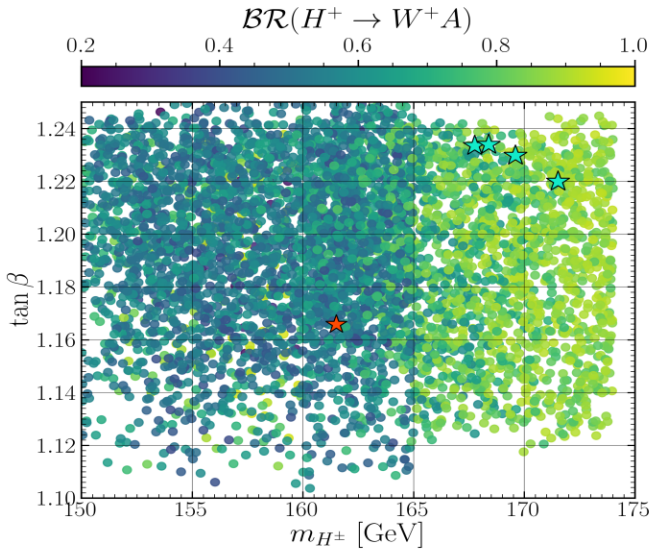

Figure 9.7 – Scan of the 2HDM parameter space with benchmark points (indicated with stars) in which a light CP-even state is used to explain the 96 GeV excess at the LHC and LEP. These studies show that $BR(H^+ \to WA)$ can be substantial in these scenarios, motivating the continued search for this channel. The tan β is a parameter in the theory representing the ratio of the vacuum expectation values of the two Higgs doublet fields [214].

10

Conclusions

A search for a charged Higgs decay to a W boson and a pseudoscalar particle A was presented in this thesis. The data analysis was conducted using 139 fb^{-1} of proton-proton (pp) collision data at $\sqrt{s} = 13$ TeV collected by the ATLAS experiment during Run 2 of the LHC. The analysis relies on a combination of muon triggers and is designed to look for a narrow dimuon resonance in the range 15 GeV $\leq m_{\mu\mu} \leq$ 75 GeV. The mass range for the H^+ is between 100 GeV and 160 GeV. The presence of signal is investigated by comparing predicted and observed event yields in mass windows with widths that maximize the sensitivity. Monte Carlo simulations that are normalized to data with profile likelihood fits are used to estimate the main backgrounds: $t\bar{t}$, ttZ and Z+jets. The effect of systematic uncertainties on the background and signal modelling is evaluated. Data shows agreement with SM predictions and no significant excess is observed. Upper limits at the 95% confidence level using the CL$_s$ method are set on the product of the branching ratios $t \to bH^{\pm}$, $H^{\pm} \to W^{\pm}A$ and $A \to \mu^+\mu^-$. The observed (expected) limits vary from 0.9 (1.6) $\times 10^{-6}$ to 6.9 (9.9) $\times 10^{-6}$. The results are discussed in the context of recent low mass resonance searches and prospects for improving a future analysis are highlighted.

A

Appendix

A.1 Cutflow for signal samples

Signal efficiency for various mass points using weighted events is shown in Table A.1. The weighted sample is scaled to the effective luminosity of 2017, 44.3 fb^{-1}, and includes weights from the generator and from matching data and simulation in lepton identification, flavour tagging, primary vertex identification, pileup and trigger efficiency.

The reference signal cross-section is found using a set of nominal branching ratios: $\mathcal{B}(t \rightarrow H^{+})$ of 1%, $\mathcal{B}(H^{+} \rightarrow WA)$ of 100% and $\mathcal{B}(A \rightarrow \mu\mu)$ of 3×10^{-4}. Using a top-quark pair production cross-section of 831.76 pb, and a factor 2 for two possible top-quark decays per event, (neglecting the possibility of both top-quark decays to H^{+}), and an average filter efficiency, ϵ_{gen}, of 0.63 gives a cross-section of 3.18 fb. The filter efficiency comes from requiring three charged leptons in the generated events, to match the $e\mu\mu$ topology considered.

Table A.1 – Weighted cutflow table for several signal samples in simulation modelling 2017 data-taking conditions. The relative efficiency is given in percent. Signal rates are quoted assuming that $\mathcal{B}(t \to H^+b)$ is 1%, $\mathcal{B}(H^+ \to WA)$ is 100% and $\mathcal{B}(A \to \mu\mu)$ is 3×10^{-4}. The ϵ_{gen} represents the filter efficiency from requiring three charged leptons in the generated events.

	H^+160a15		H^+160a45		H^+160a75		H^+140a15		H^+120a15		H^+120a30	
	events	eff., %	events	eff., %	events	eff., %	events	eff., %	events	eff., %	events	eff., %
$\mathcal{L} \times \sigma \times \mathcal{B}$	222.1	100	224.4	100	220.1	100	222.9	100	222.1	100	216.4	100
$\mathcal{L} \times \sigma \times \mathcal{B} \times \epsilon_{gen}$	135.5	61.0	141.4	63.0	140.9	64.0	138.2	62.0	142.1	64.0	145.0	67.0
= 2 muons	55.8	25.1	62.3	27.7	68.8	31.2	51.1	22.9	43.6	19.6	50.3	23.2
muon p_T selection	45.0	20.3	54.0	24.1	63.2	28.7	37.8	17.0	27.6	12.4	30.6	14.2
$\geq$ 3 jets, 20 GeV	36.7	16.5	44.4	19.8	52.0	23.6	32.6	14.6	24.1	10.9	27.0	12.5
$\geq$1 b-jet	26.9	12.1	32.5	14.5	38.5	17.5	26.6	12.0	20.7	9.3	23.1	10.7
OS muons	24.2	10.9	29.9	13.3	36.1	16.4	23.3	10.4	16.7	7.5	19.1	8.8
=1 electron	5.3	2.4	6.8	3.0	8.2	3.7	4.9	2.2	3.4	1.5	4.1	1.9
electron $p_T > 20$ GeV	4.6	2.1	5.9	2.6	7.2	3.3	4.2	1.9	3.0	1.4	3.5	1.6
mass window	4.2	1.9	4.8	2.1	5.2	2.4	3.8	1.7	2.6	1.2	2.9	1.3
$\frac{p_T(\mu^{SS})}{p_T(\mu^{OS})} > 0.2$	3.8	1.7	4.4	2.0	4.9	2.2	3.5	1.6	2.4	1.1	2.6	1.2

A.2 Reference Plots

A.2.1 Smoothing Z+jets

Bin-to-bin statistical fluctuations were seen in the Z + jets sample which was creating non-physical bumps in the exclusion limits. Both the Z + HF and Z + LF MC sample was thus smoothed. Z + HF was fitted with a constant + exponential function while the Z + LF was fitted with a straight line as shown in Figure A.1. From the fitted functions a new smoothed histogram is produced by integrating the fit function over the bin size and by assigning the stat error on that bin with the `IntegralError()` [1] function in `Root`. The yields from this new histogram are used as the Z + jets inputs to the fit in S + B mode.

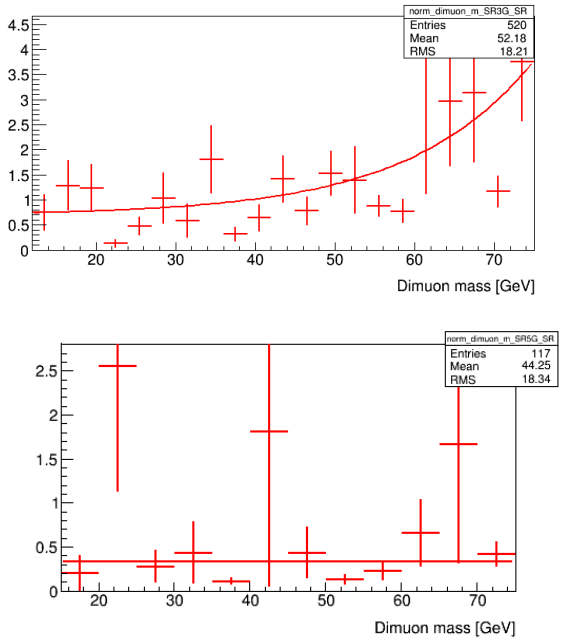

Figure A.1 – Smoothing of Z + HF and Z + LF MC was done to reduced bin-by-bin fluctuations. Z + HF was fitted with a constant + exponential function while the Z + LF was fitted with a straight line. For Z + HF, the fit parameters are p_0 = 0.68, p_1 = 0.063, p_2 = 57.32 while for Z + LF they are p_0 = 0.33

1. https://root.cern.ch/doc/master/classTF1.html

A.3 Signal Window Optimization Study

The optimized signal windows, discussed in Section 6.4.2, were determined by comparing the expected upper limits on BR($t \to bH^+$) for various mass windows using the signal + background fit. The results of the study are summarized in Table A.2. In general, this study showed that narrow binning at the low end of the mass spectrum gave the tightest limits, while wider binning is preferred at the high end. This follows from the dimuon resolution in this mass range.

	4 GeV [%]	3 GeV [%]	2 GeV [%]	1 GeV [%]
H160a15	0.96	0.85	0.71	0.61
H160a30	1.22	1.12	1.07	1.16
H160a45	1.23	1.15	1.15	1.50
H160a60	1.23	1.25	1.26	1.72
H160a75	1.32	1.40	1.61	2.17

Table A.2 – Optimization of signal mass windows: Expected upper limits on BR($t \to bH^+$) are calculated for various window widths using the signal+ background fit. Events were chosen with three leptons and atleast three jets.

A.4 Closure Test for Signal Interpolation

In order to validate the interpolation procedure for signal efficiencies, a closure test was conducted. This was done by removing one of the simulated mass points from the spline for the 4 GeV window and then comparing the predicted efficiencies to the actual ones. The results are summarized in Table A.3 and confirm that the interpolation procedure is working well.

mass point removed	Interpolated efficiency [%]	Efficiency from simulation [%]
H160a30	$3.31 \pm .08$	3.22
H160a45	$3.41 \pm .09$	3.47
H160a60	$3.61 \pm .09$	3.53

Table A.3 – Closure Test for Signal Interpolation error.

A.5 Closure Test for Exclusion Limits

In order to validate the limit setting code, a closure test was conducted. This was done by using the 'blinded' feature in Histfitter which is designed to test the limiting setting method prior to unblinding the analysis. Using this feature, pseudo data is injected into the blinded signal region windows and the 'observed' limits are determined. Agreement of these 'observed' and expected limits serve as validation of the fit machinery. The results are summarized in Table A.4 and confirm that the limiting setting code is working well.

mass point	Expected limits [%]	'Observed' limits [%]
H140a18	$0.72 \pm .23$	0.64
H140a24	$0.86 \pm .27$	0.78
H140a33	$0.93 \pm .28$	0.85
H140a42	$0.98 \pm .30$	0.89

Table A.4 – Closure test to validate the limiting setting code.

A.6 Samples

The simulated background and samples used in the analysis are listed in Table. A.5.

Process	Generator (+ Shower)	DSID
$t\bar{t}$	Powheg+Pythia8+EvtGen	410472
single-t schan_lept_top	Powheg+Pythia8+EvtGen	410644
single-t schan_lept_antitop	Powheg+Pythia8+EvtGen	410645
single-t tchan_BW50_lept_top	Powheg+Pythia8+EvtGen	410658
single-t tchan_BW50_lept_antitop	Powheg+Pythia8+EvtGen	410659
single-t Wt_DR_dilepton_top	Powheg+Pythia8+EvtGen	410648
single-t Wt_DR_dilepton_antitop	Powheg+Pythia8+EvtGen	410649
$t\bar{t}$ +V ttee	aMcAtNlo+Pythia8+EvtGen	410218
$t\bar{t}$ +V ttmumu	aMcAtNlo+Pythia8+EvtGen	410219
$t\bar{t}$ +V tttautau	aMcAtNlo+Pythia8+EvtGen	410220
$t\bar{t}$ +V ttW	aMcAtNlo+Pythia8+EvtGen	410155
$t\bar{t}$ +V ttZnunu	aMcAtNlo+Pythia8+EvtGen	410156
$t\bar{t}$ +V ttZqq	aMcAtNlo+Pythia8+EvtGen	410157
DB lllv	Sherpa 222	364253
DB llvv	Sherpa 222	364254
DB lvvv	Sherpa 222	364255
DB ZqqZvv	Sherpa 221	363355
DB ZqqZll	Sherpa 221	363356
DB WqqZvv	Sherpa 221	363357
DB WqqZll	Sherpa 221	363358
DB WpqqWmlv	Sherpa 221	363359
DB WplvWmqq	Sherpa 221	363360
DB WlvZqq	Sherpa 222	363489
DB llll	Sherpa 222	364250
W+jets Wmunu	Sherpa 221	364156 - 364169
W+jets Wenu	Sherpa 221	364170 - 364183
W+jets Wtaunu	Sherpa 221	364184 - 364197
default max{Ht,ptV} sliced samples		
Z+jets Zmumu	Sherpa 221	364100 - 364113
Z+jets Zee	Sherpa 221	364114 - 364127
Z+jets Ztautau	Sherpa 221	364128 - 364141
Z+jets Zmumu Mll10_40	Sherpa 221	364198 - 364203
Z+jets Zee Mll10_40	Sherpa 221	364204 - 364209
Z+jets Ztautau Mll10_40	Sherpa 221	364210 - 364215
Z+jets Zmumu mu24_2_Mll15_50	Sherpa 221	450581 - 450582
$H^+ \to WA$	MGPy8 EvtGen NNPDF23LO	451024-451046

Table A.5 – List of background and signal MC samples used in the analysis.

List of Abbreviations

2HDM Two-Higgs-Doublet Model

ALICE A Large Ion Collider Experiment

ATLAS A Toroidal LHC ApparatuS Experiment

BSM Beyond the Standard Model

CL Confidence Limit

CMS Compact Muon Solenoid Experiment

CR Control Region

CSC Cathode Strip Chambers

EMB EM Barrel Calorimeter

EMEC Electromagnetic Endcap Calorimeter

FCal Forward Calorimeters

FSR Final-State Radiation

HCAL Hadronic Calorimeters

HEC Hadronic End-cap Calorimeters

HLT High Level Trigger

IBL Insertable B-layer

ID Inner Detector

IP Interaction Point

ISR Initial-State Radiation

JER Jet Energy Resolution

JES Jet Energy Scale

JVT Jet Vertex Tagger

LAr Liquid Argon

LEP Large Electron–Positron Collider

LHC Large Hadron Collider

LO Leading Order

MC Monte Carlo

MDT Monitored Drift Tubes

MPI Multiple Parton Interactions

MS Muon Spectrometer

NLO Next-to-Leading Order

NNLO Next-to-Next-to-Leading Order

N3LO Next-to-Next-to-Next-to-leading Order

NP Nuisance Parameter

PDF Probability Density Function

PDF Parton Density Function

PLR Profile Likelihood Ratio

POI Parameter of Interest

PS Proton Synchrotron

PSB Proton Synchrotron Booster

QCD Quantum Chromodynamics

QED Quantum Electrodynamics

RPC Resistive Plate Chambers

SCT Semiconductor Tracker

SM Standard Model

SPS Super Proton Synchrotron

SR Signal Region

TDAQ Trigger and Data Acquisition

TGC Thin Gap Chambers

TRT Transition Radiation Tracker

UE Underlying Event

VR Validation Region

Bibliography

[1] ATLAS Collaboration. Search for $H^{\pm} \to W^{\pm}A \to W^{\pm}\mu\mu$ in $pp \to t\bar{t}$ events using an $e\mu\mu$ signature with the ATLAS detector at $\sqrt{s} = 13$ TeV. Sep 2021.

[2] G.C. Branco et al. Theory and phenomenology of two-Higgs-doublet models. *Phys. Rept.*, 516:1–102, 2012.

[3] T. Ferbel. *The Standard Model: Techniques and Concepts of High Energy Physics*. Kluwer Acad. Publ., 1999.

[4] D. Griffiths. *Introduction to Elementary Particles*. Wiley, 2008.

[5] M.D. Schwartz. *Quantum Field Theory and the Standard Model*. Cambridge University Press, 2014.

[6] T. Lancaster and S.J Blundell. *Quantum Field Theory for the Gifted Amateur*. OUP Oxford, 2014.

[7] M. Srednicki. *Quantum Field Theory*. Cambridge University Press, 2007.

[8] L.H. Ryder. *Quantum Field Theory*. Cambridge University Press, 1996.

[9] W. Greiner and B. Müller. *Gauge Theory of Weak Interactions*. Springer Berlin Heidelberg, 2009.

[10] C. Burgess and G. Moore. *The Standard Model: A Primer*. Cambridge University Press, 2007.

[11] M.E. Peskin. *An Introduction To Quantum Field Theory*. CRC Press, 2018.

[12] R. Brandelik *et al.* Evidence for a spin-1 gluon in three-jet events. *Physics Letters B*, 97(3):453–458, 1980.

[13] Wikipedia. Overview of the Standard Model, 2022. [Online; accessed 28-February-2022].

[14] Bernard de Wit. Introduction to gauge theories and the Standard Model. Oct 1995.

[15] G.T. Hooft. *Under The Spell Of The Gauge Principle*. Advanced Series In Mathematical Physics. World Scientific Publishing Company, 1994.

[16] S. L. Glashow. *Partial-symmetries of weak interactions*. Nuclear Physics, 22(4):579 - 588, 1961.

[17] Steven Weinberg. A model of leptons. *Phys. Rev. Lett.*, 19:1264–1266, Nov 1967.

[18] Abdus Salam. Weak and Electromagnetic Interactions. *Conf. Proc. C*, 680519:367–377, 1968.

[19] Michael E. Peskin. Lectures on the theory of the weak interaction, 2017.

[20] Ben Gripaios. Lectures: From quantum mechanics to the Standard Model. 2020.

[21] Heather E. Logan. TASI 2013 lectures on Higgs physics within and beyond the Standard Model. 2014.

[22] Timo Weigand. *Lectures on Quantum Field Theory I + II*. Institute for Theoretical Physics, Heidelberg University.

[23] P.W. Higgs. Broken symmetries, massless particles and gauge fields. *Physics Letters*, 12(2):132–133, 1964.

[24] Peter W. Higgs. Broken symmetries and the masses of gauge bosons. *Phys. Rev. Lett.*, 13:508–509, Oct 1964.

[25] F. Englert and R. Brout. Broken symmetry and the mass of gauge vector mesons. *Phys. Rev. Lett.*, 13:321–323, Aug 1964.

[26] G. S. Guralnik, C. R. Hagen, and T. W. B. Kibble. Global conservation laws and massless particles. *Phys. Rev. Lett.*, 13:585–587, Nov 1964.

[27] T. W. B. Kibble. Symmetry breaking in non-abelian gauge theories. *Phys. Rev.*, 155:1554–1561, Mar 1967.

[28] Wikipedia. Mathematical formulation of the Standard Model, 2022. [Online; accessed 28-February-2022].

[29] Georges Aad et al. Observation of a new particle in the search for the Standard Model Higgs boson with the ATLAS detector at the LHC. *Phys. Lett. B*, 716:1–29, 2012.

[30] Serguei Chatrchyan et al. Observation of a New Boson at a Mass of 125 GeV with the CMS Experiment at the LHC. *Phys. Lett. B*, 716:30–61, 2012.

[31] ATLAS Collaboration. A detailed map of Higgs boson interactions by the ATLAS experiment ten years after the discovery. *Nature*, 607(7917):52–59, 2022. [Erratum: Nature 612, E24 (2022)].

[32] Otto Eberhardt, Ulrich Nierste, and Martin Wiebusch. Status of the two-Higgs-doublet model of type II. *JHEP*, 07:118, 2013.

[33] K. A. Olive *et al*. *Review of Particle Physics*. Chin. Phys., C38:090001, 2014.

[34] Hans Peter Nilles. Supersymmetry, Supergravity and Particle Physics. *Phys. Rept.*, 110:1–162, 1984.

[35] H.E. Haber and G.L. Kane. The search for supersymmetry: Probing physics beyond the standard model. *Physics Reports*, 117(2):75–263, 1985.

[36] Riccardo Barbieri. Looking Beyond the Standard Model: The Supersymmetric Option. *Riv. Nuovo Cim.*, 11N4:1–45, 1988.

[37] J. Ellis, J. F. Gunion, H. E. Haber, L. Roszkowski, and F. Zwirner. Higgs bosons in a nonminimal supersymmetric model. *Phys. Rev. D*, 39:844–869, Feb 1989.

[38] Manuel Drees. Supersymmetric Models with Extended Higgs Sector. *Int. J. Mod. Phys. A*, 4:3635, 1989.

[39] Jihn E. Kim. Light Pseudoscalars, Particle Physics and Cosmology. *Phys. Rept.*, 150:1–177, 1987.

[40] Domènec Espriu, Federico Mescia, and Albert Renau. Axion-higgs interplay in the two-higgs-doublet model. *Phys. Rev. D*, 92:095013, Nov 2015.

[41] Giorgio Arcadi, Abdelhak Djouadi, and Martti Raidal. Dark Matter through the Higgs portal. *Phys. Rept.*, 842:1–180, 2020.

[42] M. Ackermann and M. Ajello *et al.* TheFermiGalactic center GeV excess and implications for dark matter. *The Astrophysical Journal*, 840(1):43, 2017.

[43] Adriano Cherchiglia, Dominik Stöckinger, and Hyejung Stöckinger-Kim. The muon g–2 for low-mass pseudoscalar Higgs in the general 2HDM. *EPJ Web Conf.*, 179:01022, 2018.

[44] B. Abi et al. Measurement of the Positive Muon Anomalous Magnetic Moment to 0.46 ppm. *Phys. Rev. Lett.*, 126(14):141801, 2021.

[45] G.C. Branco, P.M. Ferreira, L. Lavoura, M.N. Rebelo, Marc Sher, and João P. Silva. Theory and phenomenology of two-higgs-doublet models. *Physics Reports*, 516(1-2):1–102, Jul 2012.

[46] H. E. Haber, Gordon L. Kane, and T. Sterling. The Fermion Mass Scale and Possible Effects of Higgs Bosons on Experimental Observables. *Nucl. Phys. B*, 161:493–532, 1979.

[47] A. Arhrib, R. Benbrik, M. Krab, B. Manaut, S. Moretti, Yan Wang, and Qi-Shu Yan. New discovery modes for a light charged Higgs boson at the LHC. *JHEP*, 10:073, 2021.

[48] A. G. Akeroyd et al. Prospects for charged Higgs searches at the LHC. *Eur. Phys. J. C*, 77(5):276, 2017.

[49] Henning Bahl, Tim Stefaniak, and Jonas Wittbrodt. The forgotten channels: charged Higgs boson decays to a $W^{\pm}$ and a non-SM-like Higgs boson. 2021.

[50] Felix Kling, Adarsh Pyarelal, and Shufang Su. Light charged higgs bosons to AW/HW via top decay. *Journal of High Energy Physics*, 2015(11), Nov 2015.

[51] Abdesslam Arhrib, Rachid Benbrik, and Stefano Moretti. Bosonic Decays of Charged Higgs Bosons in a 2HDM Type-I. *Eur. Phys. J. C*, 77(9):621, 2017.

[52] A.G. Akeroyd. Three−body decays of higgs bosons at LEP-2 and application to a hidden fermiophobic higgs. *Nuclear Physics B*, 544(3):557–575, Apr 1999.

[53] Radovan Dermisek, Enrico Lunghi, and Aditi Raval. Trilepton Signatures of Light Charged and CP-odd Higgs Bosons in Top Quark Decays. *JHEP*, 04:063, 2013.

[54] Morad Aaboud et al. Search for charged Higgs bosons decaying via $H^{\pm} \to \tau^{\pm}\nu_{\tau}$ in the τ+jets and τ+lepton final states with 36 fb^{-1} of pp collision data recorded at $\sqrt{s} = 13$ TeV with the ATLAS experiment. *JHEP*, 09:139, 2018.

[55] Albert M Sirunyan et al. Search for charged Higgs bosons in the $H^{\pm} \to \tau^{\pm}\nu_{\tau}$ decay channel in proton-proton collisions at $\sqrt{s} = 13$ TeV. *JHEP*, 07:142, 2019.

[56] Albert M Sirunyan et al. Search for a light charged Higgs boson in the $H^{\pm}$ $\to$ cs channel in proton-proton collisions at $\sqrt{s} = 13$ TeV. *Phys. Rev. D*, 102(7):072001, 2020.

[57] Georges Aad et al. Search for a light charged Higgs boson in the decay channel $H^+ \to c\bar{s}$ in $t\bar{t}$ events using pp collisions at $\sqrt{s}$ = 7 TeV with the ATLAS detector. *Eur. Phys. J. C*, 73(6):2465, 2013.

[58] ATLAS Collaboration. Search for a light charged Higgs boson in t $\to H^+b$ decays, with $H^+ \to cb$, in the lepton+jets final state in proton-proton collisions at $\sqrt{s} = 13$ TeV with the ATLAS detector. Technical report, CERN, Geneva, 2021.

[59] Albert M Sirunyan et al. Search for a charged Higgs boson decaying to charm and bottom quarks in proton-proton collisions at $\sqrt{s} = 8$ TeV. *JHEP*, 11:115, 2018.

[60] Aleph, Delphi, L3, OPAL Collaborations, and the LEP working group for Higgs boson searches. Search for charged higgs bosons: Combined results using LEP data, 2013.

[61] Spencer Chang, Radovan Dermisek, John F. Gunion, and Neal Weiner. Nonstandard Higgs Boson Decays. *Ann. Rev. Nucl. Part. Sci.*, 58:75–98, 2008.

[62] T. Aaltonen et al. Search for a very light cp-odd higgs boson in top quark decays from pp collisions at $\sqrt{s}$ = 1.96 TeV. *Physical Review Letters*, 107(3).

[63] A. M. Sirunyan et al. Search for a light charged higgs boson decaying to a w boson and a cp-odd higgs boson in final states with $e\mu\mu$ or $\mu\mu\mu$ in proton-proton collisions at $\sqrt{s} = 13$ tev. *Physical Review Letters*, 123(13), Sep 2019.

[64] M. Aaboud et al. Search for resonant WZ production in the fully leptonic final state in proton-proton collisions at $\sqrt{s} = 13$ TeV with the ATLAS detector. *Phys. Lett. B*, 787:68–88, 2018.

[65] A. M. Sirunyan et al. Search for charged higgs bosons produced via vector boson fusion and decaying into a pair of w and z bosons using pp collisions at $\sqrt{s} = 13$ TeV. *Phys. Rev. Lett.*, 119:141802, Oct 2017.

[66] J. D. Bjorken and E. A. Paschos. Inelastic electron-proton and γ-proton scattering and the structure of the nucleon. *Phys. Rev.*, 185:1975–1982, Sep 1969.

[67] Richard P. Feynman. Very high-energy collisions of hadrons. *Phys. Rev. Lett.*, 23:1415–1417, Dec 1969.

[68] F Close. The quark parton model. *Reports on Progress in Physics*, 42(8):1285–1335, 1979.

[69] David J. Gross and Frank Wilczek. Ultraviolet behavior of non-abelian gauge theories. *Phys. Rev. Lett.*, 30:1343–1346, Jun 1973.

[70] George F. Sterman. Partons, factorization and resummation. *Theoretical Advanced Study Institute in Elementary Particle Physics (TASI 95): QCD and Beyond*, 1995.

[71] Del Debbio, Luigi. Parton distributions in the LHC era. *EPJ Web Conf.*, 175:01006, 2018.

[72] Eva Halkiadakis. Introduction to the LHC Experiments. *Theoretical Advanced Study Institute in Elementary Particle Physics: Physics of the Large and the Small*, 2011.

[73] Peter Skands. Introduction to QCD. 2013.

[74] John M. Campbell, J. W. Huston, and W. J. Stirling. Hard Interactions of Quarks and Gluons: A Primer for LHC Physics. *Rept. Prog. Phys.*, 70:89, 2007.

[75] CMS Collaboration. How CMS weeds out particles that pile up, 2022. [Online; accessed 20-May-2022].

[76] Xabier Cid Vidal and Ramon Cid Manzano. Taking a closer look at LHC, 2022. [Online; accessed 20-May-2022].

[77] ATLAS Collaboration. Public ATLAS luminosity results for run-2 of the LHC. [Online; accessed 20-May-2022].

[78] Grégory Soyez. Pileup mitigation at the LHC: A theorist's view. *Phys. Rept.*, 803:1–158, 2019.

[79] Torbjorn Sjostrand. Monte Carlo Generators. 2006.

[80] Torbjorn Sjostrand, Stephen Mrenna, and Peter Z. Skands. PYTHIA 6.4 Physics and Manual. *JHEP*, 05:026, 2006.

[81] M. A. Dobbs et al. Les Houches guidebook to Monte Carlo generators for hadron collider physics. In *3rd Les Houches Workshop on Physics at TeV Colliders*, 2004.

[82] Stefan Höche. Introduction to parton-shower event generators. 2015.

[83] Andy Buckley, Jonathan Butterworth, et al. General-purpose event generators for lhc physics. *Physics Reports*, 504(5):145–233, 2011.

[84] Michael H. Seymour and Marilyn Marx. Monte Carlo Event Generators. In *69th Scottish Universities Summer School in Physics: LHC Physics*, pages 287–319, 4 2013.

[85] Etienne Dreyer. The search for new high-mass resonances in the dilepton final state using the full Run-2 ATLAS dataset of 13 TeV proton-proton collisions, Aug 2021.

[86] G. Aad et al. The ATLAS Experiment at the CERN Large Hadron Collider. *JINST*, 3:S08003, 2008.

[87] Lyndon Evans and Philip Bryant. LHC machine. *Journal of Instrumentation*, 3(08):S08001, aug 2008.

[88] CERN Website. Radiofrequency cavities. 2012. [Online; accessed Jan-2023].

[89] CERN Website. Linear Accelerator 2. 2012. [Online; accessed Jan-2023].

[90] Jason Nielsen. Fundamentals of LHC Experiments. In *Theoretical Advanced Study Institute in Elementary Particle Physics: String theory and its Applications: From meV to the Planck Scale*, pages 127–152, 6 2011.

[91] Sascha Mehlhase. ATLAS detector slice (and particle visualisations). May 2021.

[92] Eduardo Simas, Jose M. Seixas, and Luiz Caloba. Self-organized mapping of calorimetry information for high efficient online electron / jet identification in ATLAS. *PoS*, ACAT:055, 2007.

[93] *ATLAS inner detector: Technical Design Report, 1*. Technical design report. ATLAS. CERN, Geneva, 1997.

[94] G. Aad et al. The ATLAS Inner Detector commissioning and calibration. *Eur. Phys. J. C*, 70:787–821, 2010.

[95] *ATLAS magnet system: Technical Design Report, 1*. Technical design report. ATLAS. CERN, Geneva, 1997.

[96] Sally Seidel. Silicon strip and pixel detectors for particle physics experiments. *Physics Reports*, 828:1–34, 2019.

[97] G. Aad et al. ATLAS pixel detector electronics and sensors. *JINST*, 3:P07007, 2008.

[98] M Capeans, G Darbo, K Einsweiller, M Elsing, T Flick, M Garcia-Sciveres, C Gemme, H Pernegger, O Rohne, and R Vuillermet. ATLAS Insertable B-Layer Technical Design Report. Technical report, Sep 2010.

[99] Track Reconstruction Performance of the ATLAS Inner Detector at $\sqrt{s} = 13$ TeV. Technical report, CERN, Geneva, Jul 2015.

[100] Joao Pequenao. Computer generated image of the ATLAS inner detector. Mar 2008.

[101] Manuel Kayl. Tracking Performance of the ATLAS Inner Detector and Observation of Known Hadrons. 2010.

[102] Particle Identification Performance of the ATLAS Transition Radiation Tracker. Technical report, CERN, Geneva, Sep 2011.

[103] Bartosz Mindur. ATLAS Transition Radiation Tracker (TRT): Straw tubes for tracking and particle identification at the Large Hadron Collider. Technical report, CERN, Geneva, 2017.

[104] Christian Wolfgang Fabjan and F Gianotti. Calorimetry for Particle Physics. *Rev. Mod. Phys.*, 75:1243–1286. 96 p, Oct 2003.

[105] ATLAS Liquid Argon Calorimeter Phase-II Upgrade: Technical Design Report. Sep 2017.

[106] B Di Girolamo. An overview of the ATLAS TILECAL hadronic calorimeter. Technical report, CERN, Geneva, 1997.

[107] Ana Maria Henriques Correia. The ATLAS Tile Calorimeter. Technical report, CERN, Geneva, 2015.

[108] T. Barillari. The ATLAS liquid argon hadronic end-cap calorimeter: Construction and selected beam test results. *Nucl. Phys. B Proc. Suppl.*, 150:102–105, 2006.

[109] Dag Gillberg et al. Performance of the ATLAS Forward Calorimeters in First LHC Data. *Journal of Physics: Conference Series*, 293(1):012041, apr 2011.

[110] L. Pontecorvo. The ATLAS muon spectrometer. *Eur. Phys. J. C*, 34:S117–S128, 2004.

[111] ATLAS Collaboration. ATLAS Fact Sheet : To raise awareness of the ATLAS detector and collaboration on the LHC. 2010.

[112] Michele Livan. Monitored drift tubes in atlas. *Nuclear Instruments and Methods in Physics Research Section A: Accelerators, Spectrometers, Detectors and Associated Equipment*, 384(1):214–218, 1996. BEAUTY '96.

[113] T. Argyropoulos et al. Cathode strip chambers in ATLAS : Installation, commissioning and in situ performance. In *2008 IEEE Nuclear Science Symposium Conference Record*, pages 2819–2824, 2008.

[114] R. Santonico and R. Cardarelli. Development of resistive plate counters. *Nuclear Instruments and Methods in Physics Research*, 187(2):377–380, 1981.

[115] Koichi Nagai. Thin gap chambers in ATLAS. *Nuclear Instruments and Methods in Physics Research Section A: Accelerators, Spectrometers, Detectors and Associated Equipment*, 384(1):219–221, 1996. BEAUTY '96.

[116] ATLAS Collaboration. Trigger menu in 2018. Technical report, CERN, Geneva, Oct 2019.

[117] Georges Aad et al. Operation of the ATLAS trigger system in Run 2. *JINST*, 15(10):P10004, 2020.

[118] ATLAS Collaboration. Statistical methods for the **LHC**: A roofit and roostats workbook, 2019.

[119] Glen Cowan. Statistics for Searches at the LHC. In *69th Scottish Universities Summer School in Physics: LHC Physics*, 2013.

[120] Glen Cowan, Kyle Cranmer, Eilam Gross, and Ofer Vitells. Asymptotic formulae for likelihood-based tests of new physics. *The European Physical Journal C*, 71(2), Feb 2011.

[121] M. Baak, G. J. Besjes, D. Côte, A. Koutsman, J. Lorenz, and D. Short. HistFitter software framework for statistical data analysis. *Eur. Phys. J.*, C75:153, 2015.

[122] Kyle Cranmer. Practical Statistics for the LHC. In *2011 European School of High-Energy Physics*, 2014.

[123] Procedure for the LHC Higgs boson search combination in Summer 2011. Technical report, CERN, Geneva, Aug 2011.

[124] Kyle Cranmer, George Lewis, Lorenzo Moneta, Akira Shibata, and Wouter Verkerke. HistFactory: A tool for creating statistical models for use with RooFit and RooStats. Technical report, New York U., New York, Jan 2012.

[125] Simone Amoroso, Christian Gutschow, Richard Hawkings, Zach Marshall, Bogdan Malaescu, and Wouter Verkerke. Recommendations on the treatment of theoretical systematic uncertainties in statistical analysis of ATLAS data. Technical report, CERN, Geneva, Apr 2020.

[126] Luca Lista. Practical Statistics for Particle Physicists. In *2016 European School of High-Energy Physics*, 2017.

[127] Georges Aad et al. Combined search for the Standard Model Higgs boson in pp collisions at $\sqrt{s} = 7$ TeV with the ATLAS detector. *Phys. Rev. D*, 86:032003, 2012.

[128] Michele Pinamonti. Statistical methods at ATLAS and CMS. June 2018.

[129] Olaf Behnke, Kevin Kröninger, Grégory Schott, and Thomas Schörner-Sadenius. *Data analysis in high energy physics: a practical guide to statistical methods*. Wiley-VCH, Weinheim, 2013.

[130] Georges Aad et al. Search for the $b\bar{b}$ decay of the Standard Model Higgs boson in associated $(W/Z)H$ production with the ATLAS detector. *JHEP*, 01:069, 2015.

[131] Wouter Verkerke. Advanced Statistics Lectures: Systematic Uncertainties and Profiling. June 2020.

[132] J. Neyman and E. S. Pearson. On the problem of the most efficient tests of statistical hypotheses. *Philosophical Transactions of the Royal Society of London. Series A, Containing Papers of a Mathematical or Physical Character*, 231:289–337, 1933.

[133] S. S. Wilks. The large-sample distribution of the likelihood ratio for testing composite hypotheses. *The Annals of Mathematical Statistics*, 9(1):60–62, 1938.

[134] Nicolas Berger. Lecture on Statistical analysis methods by ATLAS. Sep 2017.

[135] Alexander L. Read. Presentation of search results: The CL(s) technique. *J. Phys. G*, 28:2693–2704, 2002.

[136] Eilam Gross and Ofer Vitells. Trial factors for the look elsewhere effect in high energy physics. *The European Physical Journal C*, 70(1-2):525–530, Oct 2010.

[137] Ayana Arce et al. Search for $Z\gamma$, $W\gamma$ and $H\gamma$. Technical Report ATL-COM-PHYS-2016-1509, CERN, Geneva, Oct 2016.

[138] Wouter Verkerke and David Kirkby. The roofit toolkit for data modeling, 2003.

[139] Lorenzo Moneta, Kevin Belasco, Kyle Cranmer, Sven Kreiss, Alfio Lazzaro, Danilo Piparo, Gregory Schott, Wouter Verkerke, and Matthias Wolf. The roostats project, 2010.

[140] Jeanette Lorenz. Histfitter: Advanced tutorial. [Online; accessed 20-June-2022].

[141] Georges Aad et al. ATLAS data quality operations and performance for 2015–2018 data-taking. *JINST*, 15(04):P04003, 2020.

[142] ATLAS Collaboration. The ATLAS Simulation Infrastructure. *Eur. Phys. J. C*, 70:823, 2010.

[143] Stefano Frixione, Paolo Nason, and Carlo Oleari. Matching NLO QCD computations with Parton Shower simulations: the POWHEG method. *JHEP*, 11:070, 2007.

[144] Paolo Nason. A new method for combining NLO QCD with shower Monte Carlo algorithms. *JHEP*, 11:040, 2004.

[145] Simone Alioli, Paolo Nason, Carlo Oleari, and Emanuele Re. A general framework for implementing NLO calculations in shower Monte Carlo programs: the POWHEG BOX. *JHEP*, 06:043, 2010.

[146] Stefano Frixione, Paolo Nason, and Giovanni Ridolfi. A positive-weight next-to-leading-order Monte Carlo for heavy flavour hadroproduction. *JHEP*, 09:126, 2007.

[147] Emanuele Re. Single-top Wt-channel production matched with parton showers using the POWHEG method. *Eur. Phys. J. C*, 71:1547, 2011.

[148] Richard D. Ball et al. Parton distributions for the LHC Run II. *JHEP*, 04:040, 2015.

[149] Torbjörn Sjöstrand, Stefan Ask, Jesper R. Christiansen, Richard Corke, Nishita Desai, Philip Ilten, Stephen Mrenna, Stefan Prestel, Christine O. Rasmussen, and Peter Z. Skands. An introduction to PYTHIA 8.2. *Comput. Phys. Commun.*, 191:159, 2015.

[150] ATLAS Collaboration. ATLAS Run 1 Pythia8 tunes. Technical report, CERN, Geneva, Nov 2014.

[151] Richard D. Ball et al. Parton distributions with LHC data. *Nucl. Phys. B*, 867:244, 2013.

[152] J. Alwall, R. Frederix, S. Frixione, V. Hirschi, F. Maltoni, O. Mattelaer, H. S. Shao, T. Stelzer, P. Torrielli, and M. Zaro. The automated computation of tree-level and next-to-leading order differential cross sections, and their matching to parton shower simulations. *JHEP*, 07:079, 2014.

[153] T. Gleisberg, S. Höche, F. Krauss, M. Schönherr, S. Schumann, et al. Event generation with SHERPA 1.1. *JHEP*, 02:007, 2009.

[154] Enrico Bothmann et al. Event generation with Sherpa 2.2. *SciPost Phys.*, 7(3):034, 2019.

[155] Steffen Schumann and Frank Krauss. A parton shower algorithm based on Catani–Seymour dipole factorisation. *JHEP*, 03:038, 2008.

[156] Stefan Höche, Frank Krauss, Marek Schönherr, and Frank Siegert. A critical appraisal of NLO+PS matching methods. *JHEP*, 09:049, 2012.

[157] Stefan Höche, Frank Krauss, Marek Schönherr, and Frank Siegert. QCD matrix elements + parton showers. The NLO case. *JHEP*, 04:027, 2013.

[158] S. Catani, F. Krauss, R. Kuhn, and B. R. Webber. QCD Matrix Elements + Parton Showers. *JHEP*, 11:063, 2001.

[159] Stefan Höche, Frank Krauss, Steffen Schumann, and Frank Siegert. QCD matrix elements and truncated showers. *JHEP*, 05:053, 2009.

[160] Tanju Gleisberg and Stefan Höche. Comix, a new matrix element generator. *JHEP*, 12:039, 2008.

[161] F. Cascioli, P. Maierhöfer, and S. Pozzorini. Scattering amplitudes with open loops. *Phys. Rev. Lett.*, 108(11), Mar 2012.

[162] Ansgar Denner, Stefan Dittmaier, and Lars Hofer. Collier: A fortran-based complex one-loop library in extended regularizations. *Comput. Phys. Commun.*, 212:220–238, Mar 2017.

[163] D. J. Lange. The EvtGen particle decay simulation package. *Nucl. Instrum. Meth. A*, 462:152, 2001.

[164] Celine Degrande, Rikkert Frederix, Valentin Hirschi, Maria Ubiali, Marius Wiesemann, and Marco Zaro. Accurate predictions for charged Higgs production: Closing the $m_{H^\pm} \sim m_t$ window. *Phys. Lett. B*, 772:87–92, 2017.

[165] S. Agostinelli et al. GEANT4 – a simulation toolkit. *Nucl. Instrum. Meth. A*, 506:250, 2003.

[166] ATLAS Collaboration. The simulation principle and performance of the ATLAS fast calorimeter simulation FastCaloSim, 2010.

[167] M. Aaboud et al. Performance of the ATLAS Track Reconstruction Algorithms in Dense Environments in LHC Run 2. *Eur. Phys. J. C*, 77(10):673, 2017.

[168] T Cornelissen, M Elsing, S Fleischmann, W Liebig, E Moyse, and A Salzburger. Concepts, Design and Implementation of the ATLAS New Tracking (NEWT). Technical report, CERN, Geneva, Mar 2007.

[169] ATLAS Collaboration. Performance of the reconstruction of large impact parameter tracks in the ATLAS inner detector. Technical report, CERN, Geneva, Jul 2017.

[170] Kyungeon Choi. Tracking and Vertexing with the ATLAS Inner Detector in the LHC Run-2. Technical report, CERN, Geneva, Jun 2017.

[171] Morad Aaboud et al. Reconstruction of primary vertices at the ATLAS experiment in Run 1 proton–proton collisions at the LHC. *Eur. Phys. J. C*, 77(5):332, 2017.

[172] ATLAS Collaboration. Pile-up subtraction and suppression for jets in ATLAS. Technical report, CERN, Geneva, Aug 2013.

[173] S. Boutle et al. Primary vertex reconstruction at the ATLAS experiment. *J. Phys. Conf. Ser.*, 898(4):042056, 2017.

[174] Liza Mijovic. Measurement of cross sections and properties of the Higgs boson in decays to two photons using the ATLAS detector. 2018.

[175] Performance of the ATLAS Inner Detector Track and Vertex Reconstruction in the High Pile-Up LHC Environment. Technical report, CERN, Geneva, Mar 2012.

[176] ATLAS Collaboration. ATLAS beamspot public results Run-2. [Online; accessed 20-June-2022].

[177] ATLAS Collaboration. Muon reconstruction and identification efficiency in ATLAS using the full Run 2 pp collision data set at $\sqrt{s} = 13$ TeV. *Eur. Phys. J. C*, 81(7):578, 2020.

[178] Morad Aaboud et al. Electron reconstruction and identification in the ATLAS experiment using the 2015 and 2016 LHC proton-proton collision data at $\sqrt{s}$ = 13 TeV. *Eur. Phys. J. C*, 79(8):639, 2019.

[179] ATLAS Collaboration. Electron and photon performance measurements with the ATLAS detector using the 2015–2017 LHC proton–proton collision data. *JINST*, 14:P12006, 2019.

[180] W. Lampl et al. Calorimeter clustering algorithms: Description and performance. Technical report, CERN, Geneva, 2008.

[181] Electron and photon reconstruction and performance in ATLAS using a dynamical, topological cell clustering-based approach. Technical report, CERN, Geneva, Dec 2017.

[182] Georges Aad et al. Jet energy scale and resolution measured in proton–proton collisions at $\sqrt{s} = 13$ TeV with the ATLAS detector. *Eur. Phys. J. C*, 81(8):689, 2021.

[183] Matteo Cacciari, Gavin P. Salam, and Gregory Soyez. FastJet User Manual. *Eur. Phys. J. C*, 72:1896, 2012.

[184] Matteo Cacciari, Gavin P. Salam, and Gregory Soyez. The Anti-k_t jet clustering algorithm. *JHEP*, 0804:063, 2008.

[185] ATLAS Collaboration. Jet reconstruction and performance using particle flow with the ATLAS Detector. *Eur. Phys. J. C*, 77:466, 2017.

[186] ATLAS Collaboration. Tagging and suppression of pileup jets with the ATLAS detector. Technical report, CERN, Geneva, May 2014.

[187] Georges Aad et al. Performance of b-Jet Identification in the ATLAS Experiment. *JINST*, 11(04):P04008, 2016.

[188] Georges Aad et al. Configuration and performance of the ATLAS b-jet triggers in Run 2. *Eur. Phys. J. C*, 81(12):1087, 2021.

[189] Optimisation and performance studies of the ATLAS b-tagging algorithms for the 2017-18 LHC run. Technical report, CERN, Geneva, 2017.

[190] Morad Aaboud et al. Measurements of b-jet tagging efficiency with the ATLAS detector using $t\bar{t}$ events at $\sqrt{s} = 13$ TeV. *JHEP*, 08:089, 2018.

[191] ATLAS Collaboration. ATLAS b-jet identification performance and efficiency measurement with $t\bar{t}$ events in pp collisions at $\sqrt{s} = 13$ TeV. *Eur. Phys. J. C*, 79:970, 2019.

[192] Vazquez Schroeder *et al.* Search for the Associated Production of a Higgs Boson and a Top Quark Pair in multilepton final states in 80 fb^{-1} pp Collisions at $\sqrt{s}$ = 13 TeV with the ATLAS Detector. Technical report, CERN, Geneva, Apr 2018.

[193] Analysis of $t\bar{t}H$ and $t\bar{t}W$ production in multilepton final states with the ATLAS detector. Technical report, CERN, Geneva, Oct 2019.

[194] ATLAS Collaboration. Recommendations for the Modeling of Smooth Backgrounds. 2020.

[195] Morad Aaboud et al. Search for Higgs boson decays into a pair of light bosons in the $bb\mu\mu$ final state in pp collision at $\sqrt{s}$ =13 TeV with the ATLAS detector. *Phys. Lett. B*, 790:1–21, 2019.

[196] ATLAS Collaboration. Measurements of the inclusive and differential production cross sections of a top-quark-antiquark pair in association with a Z boson at $\sqrt{s} = 13$ TeV with the ATLAS detector. *Eur. Phys. J. C*, 81:737, 2021.

[197] Georges Aad et al. ATLAS b-jet identification performance and efficiency measurement with $t\bar{t}$ events in pp collisions at $\sqrt{s} = 13$ TeV. *Eur. Phys. J. C*, 79(11):970, 2019.

[198] Luminosity determination in pp collisions at $\sqrt{s} = 13$ TeV using the ATLAS detector at the LHC. Technical report, CERN, Geneva, Jun 2019.

[199] Roger Barlow and Christine Beeston. Fitting using finite monte carlo samples. *Computer Physics Communications*, 77(2):219–228, 1993.

[200] M. Bähr et al. Herwig++ physics and manual. *Eur. Phys. J. C*, 58:639, 2008.

[201] Johannes Bellm et al. Herwig 7.0/Herwig++ 3.0 release note. *Eur. Phys. J. C*, 76(4):196, 2016.

[202] ATLAS Collaboration. ATLAS Pythia 8 tunes to 7 TeV data. Technical report, CERN, Geneva, Nov 2014.

[203] Michiel Botje et al. The PDF4LHC Working Group Interim Recommendations. 2011.

[204] Georges Aad et al. Search for Higgs boson decays into a pair of pseudoscalar particles in the $bb\mu\mu$ final state with the ATLAS detector in pp collisions at $\sqrt{s}$=13 TeV. *Phys. Rev. D*, 105(1):012006, 2022.

[205] Arno Heister. Observation of an excess at 30 GeV in the opposite sign dimuon spectra of $\mathrm{Z} \to b\bar{b} + \mathrm{X}$ events recorded by the ALEPH experiment at LEP. 10 2016.

[206] A. M. Sirunyan et al. Search for resonances in the mass spectrum of muon pairs produced in association with b quark jets in proton-proton collisions at $\sqrt{s} = 8$ and 13 TeV. *JHEP*, 11:161, 2018.

[207] Search for a new resonance in the $bj\mu\mu$ final state at a dimuon invariant mass around 28 GeV with ATLAS pp data collected at $\sqrt{s} = 8$ and 13 TeV. Technical report, CERN, Geneva, 2019.

[208] John F. Gunion. A Light CP-odd Higgs boson and the muon anomalous magnetic moment. *JHEP*, 08:032, 2009.

[209] C. T. Potter. Natural NMSSM with a Light Singlet Higgs and Singlino LSP. *Eur. Phys. J. C*, 76(1):44, 2016.

[210] R. Barate et al. Search for the standard model Higgs boson at LEP. *Phys. Lett. B*, 565:61–75, 2003.

[211] Albert M Sirunyan et al. Search for a standard model-like Higgs boson in the mass range between 70 and 110 GeV in the diphoton final state in proton-proton collisions at $\sqrt{s} = 8$ and 13 TeV. *Phys. Lett. B*, 793:320–347, 2019.

[212] CMS Collaboration. Searches for additional Higgs bosons and for vector leptoquarks in $\tau\tau$ final states in proton-proton collisions at $\sqrt{s}$ = 13 TeV. 2022.

[213] ATLAS Collaboration. Search for resonances in the 65 to 110 GeV diphoton invariant mass range using 80 fb^{-1} of pp collisions collected at $\sqrt{s} = 13$ TeV with the ATLAS detector. Technical report, CERN, Geneva, 2018.

[214] Rachid Benbrik, Mohammed Boukidi, Stefano Moretti, and Souad Semlali. Explaining the 96 GeV Di-photon anomaly in a generic 2HDM Type-III. *Phys. Lett. B*, 832:137245, 2022.